

Alma Mater Studiorum – Università di Bologna

**DOTTORATO DI RICERCA IN
SCIENZE CHIMICHE**

Ciclo XXVII

Settore Concorsuale di afferenza: 03/A1 – CHIMICA ANALITICA

**Settore Scientifico disciplinare: CHIM/12 - CHIMICA DELL'AMBIENTE E
DEI BENI CULTURALI**

**DEVELOPMENT OF NEW ANALYTICAL
PROCEDURES AIMED AT THE
CHARACTERIZATION OF ARTISTIC
SAMPLES**

Presentata da: IRENE BONACINI

Coordinatore Dottorato

Relatore

Prof. Aldo Roda

Dott.ssa Silvia Prati

Esame finale anno 2015



The work described in this thesis was performed at:

M2ADL - Microchemistry & Microscopy Art Diagnostic Laboratory,
Università di Bologna, Ravenna Campus,
Via Guaccimanni 42, 48100 Ravenna, Italy.

Three months Marco Polo fellowship were conducted at:

Institution of the Material Structure
Consejo Superior de Investigaciones Científicas
C/ Serrano, 121
28006 Madrid, Spain.

Under the supervision of Dr S. Sanchez Cortés.



*For my father,
to my family.*

DEVELOPMENT OF NEW ANALYTICAL
PROCEDURES AIMED AT THE
CHARACTERIZATION OF ARTISTIC
SAMPLES

IRENE BONACINI

ABSTRACT

In this thesis, new advances in the development of spectroscopic based methods for the characterization of heritage materials have been achieved.

As concern FTIR spectroscopy, new approaches aimed at exploiting near and far IR region for the characterization of inorganic or organic materials have been successfully tested. Paint cross-section constituted by a complex matrix of several substances have been analysed by FTIR spectroscopy in the NIR range (8000-4000 cm^{-1}) and an ad hoc chemometric approach has been developed for the elaboration of hyperspectral maps which allowed the characterisation and the localisation of the different components within each paint section. Moreover, a new method for the characterization of calcite based on the use of grinding curves has been set up both in the MID and in the FAR region. Indeed, calcite is a material widely applied in cultural heritage field, and this spectroscopic approach is an efficient, rapid, and effective tool to distinguish between different calcite samples.

Different innovative spectroscopic methods have been tested aimed at the development of enhanced vibrational techniques for the characterisation of dyed fibres. First, a SEIRA (Surface Enhanced Infra-Red Absorption) protocol has been optimised and the analysis of colorant micro extracts have been reached thanks to the enhancement produced by the addition of gold nanoparticles. These preliminary studies permitted to identify a new enhanced FTIR method, which was named by our research group as ATR/RAS and which allowed to reach lower detection limits. Regarding Raman microscopy, the research followed two lines, which have in common the aim of avoiding the use of colloidal solutions. AgI based supports obtained after deposition in controlled conditions on a gold-coated glass slides have been developed. Spotting the colorant solution on this type of support a SERS spectrum can be obtained thanks to the photoreduction, which the laser may induce on the silver salt. Moreover, these AgI supports can be used for the TLC separation of a mixture of colorants and the analyses by means of both Raman/SERS and ATR-RAIRS can be successfully reached. In conclusion, a photoreduction method for the “on fiber” analysis of colorant without the need of any extraction have been optimised.

Contents

| | |
|---|-----------|
| ABSTRACT | 5 |
| CHAPTER 1 - INTRODUCTION | 9 |
| 1.1 Introduction | 10 |
| 1.2 Thesis objective and overview | 11 |
| 1.3 References | 15 |
| LIST OF PUBLICATIONS | 17 |
| CHAPTER 2 - NEW ADVANCES IN THE APPLICATION OF FTIR MICROSCOPY IN THE NEAR-IR RANGE. | 19 |
| 2.1 Infrared microscopy applied to cultural heritage | 20 |
| 2.2 Application to Near-IR spectroscopy to the analysis of natural resins and real samples | 25 |
| 2.2.1 Near-IR spectroscopy | 25 |
| 2.2.2 Materials and methods | 27 |
| 2.2.3 Results and discussion | 30 |
| 2.3 Conclusions | 42 |
| 2.4 References | 43 |
| CHAPTER 3 - DISCRIMINATION OF WOOL DYED FIBERS: A NEW ANALYTICAL APPROACH FOR IN SITU MICRO-RAMAN AND SERS SPECTROSCOPY. | 47 |
| 3.1 Dyeing process and wool dyeing | 48 |
| 3.2 Dyed fibres analysis: an overview | 50 |
| 3.2.1 Raman spectroscopy | 51 |
| 3.2.3 Surface Enhanced Raman Spectroscopy (SERS) | 52 |
| 3.3 A new analytical protocol for dyed fibres analysis | 63 |
| 3.3.1 Raman spectroscopy for wool dyed fibres analysis | 63 |
| 3.3.1.1 Materials and methods | 64 |
| 3.3.1.2 Results | 65 |
| 3.3.1.3 Discussion | 70 |
| 3.3.1.4 Principal Component Analysis | 81 |
| 3.3.1.5 Conclusions | 84 |

| | |
|--|------------|
| 3.2.2 SERS on wool dyed fibres using photoreduced AgNPs | 86 |
| 3.2.2.1 Ag photoreduction methods | 86 |
| 3.2.2.2 Experimental procedure and applied method | 87 |
| 3.2.2.3 Samples | 89 |
| 3.2.2.4 Results and Discussion | 90 |
| 3.2.2.5 Conclusions | 108 |
| 3.6 References | 109 |

CHAPTER 4 - SURFACE ENHANCED VIBRATIONAL SPECTROSCOPY (SEVS). DEVELOPMENT OF TWO INNOVATIVE APPROACHES IN THE IR RANGE. 116

| | |
|---|------------|
| 4.1 Surface Enhanced Infrared Absorption (SEIRA) | 118 |
| 4.1.1 SEIRA effect | 118 |
| 4.1.2 Materials and methods | 121 |
| 4.1.3 Results and discussion | 124 |
| 4.1.4 Conclusions | 133 |
| 4.2 ATR-RAIRS | 135 |
| 4.2.1 Reflection Absorption InfraRed Spectroscopy (RAIRS)and Grazing Angle (GA) | 135 |
| 4.2.3 Enhanced IR: Grazing Angle Attenuated Total Reflection (GAATR)and ATR-RAIRS | 139 |
| 4.2.4 Materials and methods | 141 |
| 4.2.6 Conclusions | 151 |
| 4.3 Conclusions | 153 |
| 4.3 References | 154 |

CHAPTER 5 - NEW DEVELOPMENT OF TLC-SERS AND TLC-FTIR METHODS.157

| | |
|--|------------|
| 3.1 Thin-Layer Chromatography (TLC) and coupled TLC-SERS and TLC-FTIR methods | 158 |
| 3.2 Materials and Methods | 162 |
| 3.2.1 Materials | 162 |
| 3.2.2 AgI synthesis | 162 |
| 3.2.3 AgI deposition methods | 163 |
| 3.2.4 TLC | 164 |
| 3.2.5 Optical Microscope and SEM | 165 |
| 3.2.6 FTIR-ATR and ATR-RAIRS | 165 |
| 3.2.7 Raman-SERS | 166 |
| 3.3 Results and discussion | 167 |
| 3.3.1 AgI | 167 |
| 3.3.2 NANO silica | 180 |
| 3.3 Conclusions | 181 |
| 3.4 References | 183 |

| | |
|--|------------|
| CHAPTER 6 - INFRARED SPECTRUM GRINDING CURVES METHOD ON MIR AND FIR RANGES. | 185 |
| 6.1 Calcium carbonate in cultural heritage | 186 |
| 6.2 Grinding curves method | 188 |
| 6.3 Materials and Methods | 190 |
| 6.3.1 Materials | 190 |
| 6.3.2 Methods | 192 |
| 6.4 Results and discussion | 193 |
| 6.5 Conclusions | 198 |
| 6.6 References | 199 |
| | |
| Acknowledgements | 202 |

Chapter 1

Introduction

1.1 Introduction

Nowadays scientific methodologies are widely used in the study of cultural heritage and in solving problems concerning its conservation. The scientific analysis allows not only the characterisation of the constitutive materials of artworks, but also to identify their distribution and alteration products during time. Moreover, important historic and artistic information can be emerged or an aid in the choosing of adequate methodologies for conservation or restoration of historical objects.

Modern sciences, such as chemistry, physics or biology, can successfully employed in this field. In the 18th century chemistry was first applied to the conservation field and gradually assumed an important role due to the increase number of collections exposed in museum all around the Europe [1]. Through the past decades, the field of conservation science has become an interdisciplinary subject, using scientific investigation and analytical equipment applied to the wide area of studies including the technology, structure and materials of artworks and their historical background.

Ancient artworks can be considered as heterogeneous systems where several interactions between substances present in the complex matrix, as well as degradation and aging phenomena, can occur. For example, samples collected from a painting usually show a multilayered structure composed by the superimposition of different components, which constitute the preparation, priming, paint and varnish layers, depending on the working practices and techniques of the artist, as well as on the state of conservation of the object and mainly constituted of a mixtures of organic and inorganic substances (Fig. 1).

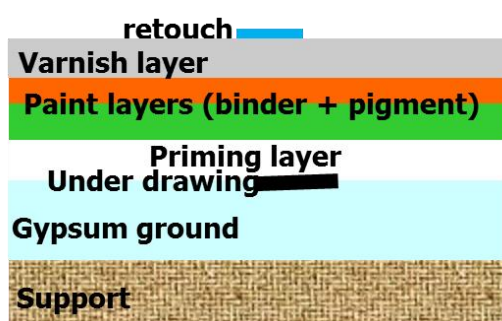


Fig. 1: Schematic view of a paint stratigraphy structure

The comprehensive characterisation of different artistic materials – and in particular the spatial location within the layer structure and even within a single paint layer – is fundamental in the determination of adequate methodologies for conservation and restoration practices.

For these reasons, over recent times analytical protocols, which make use of several techniques in an integrated way, have been proposed. Spectroscopic techniques are widely used in this field since they can be applied either in situ for non-invasive analyses or, easily coupled to a microscope for cross sections analyses of multi-layered samples.

The use of non-invasive techniques have been recently strongly developed, with the aim of characterise the whole artwork surface without damages. For this purpose, spectroscopic techniques and imaging systems such as Xray radiography, X-ray fluorescence (XRF), multispectral imaging system, and portable FTIR (Fourier transform infrared) or Raman spectroscopies are widely employed for investigation of artworks. Unfortunately, non-destructive approaches alone are often insufficient for fully characterising the complex historical objects and, as a consequence, a sample – or micro-sample - collection is required for achieved a detailed comprehensive stratigraphical characterisation. For this reason, it is recommendable to follow a methodological approach, combining non-destructive and microdestructive techniques in an integrated way.

1.2 Thesis objective and overview

In this thesis different new spectroscopic approaches have been developed in order to characterize organic substances in sample cross sections, organic synthetic dyes on fibres and some inorganic materials commonly used to realize art objects. In order to overcome drawbacks and limits of the traditional techniques in terms of selectivity and response, different analytical purposes have been followed to optimise and define innovative methodologies addressing specific conservation issues.

An overview of the recent advances of FTIR microscopy in artwork diagnostic is provided. Considering the main drawbacks that can be possibly encountered in the FTIR analysis usually employed, two different infrared ranges have been evaluated and compared (Chapter 2). Indeed, the application of near infrared (NIR) spectroscopy in artwork diagnostic has been demonstrated to be a very convenient technique, and it has been proposed as an alternative method for the characterization of paint cross-sections. NIR spectra result useful to characterize the different artworks materials and allowing non-contact measurements in reflectance mode overcome the main drawbacks of FTIR-ATR analysis. Although the use of this spectral range may be extremely useful, the combination and overtone bands are generally broader and less resolved than the fundamental bands and overlapped with one another. For this reasons the information achieved in this range may be less specific than the ones obtained in the mid-infrared and mixtures of organic substances may be extremely difficult to be distinguished. For this reasons, a multivariate approach is usually required in order to extract useful information from spectra [2]. An integrated use of information recorded in the NIR and in the MIR region is here proposed, and the molecular investigation of both organic and

inorganic substances, through chemical maps, have been successfully performed. In order to extract the maximum useful information embodied in the hyperspectral data, an exploratory multivariate approach has been adopted. Principal component analysis (PCA) was performed, after application of proper signal preprocessing, and the score values were converted into chemical maps.

A core part of the thesis is dedicated to the development of different analytical approaches aimed at investigating organic synthetic dyes (Chapters 3, 4 and 5). Indeed, the characterization of organic colorants still represents a very challenging task in scientific analysis of artistic samples, due to the fact that they are commonly present in mixtures with other components and in very little amounts and concentrations.

Chapter 3 aims at the elaboration and optimization of an analytical methodology for the characterization of organic synthetic dyes in wool matrices employing Raman and/or SERS spectroscopy. In particular, given the challenges in the detection and characterization of dyes and the relative low amount of literature on synthetic ones, the efforts will be directed on the specific optimization of an ad hoc approach for the in situ identification of dyes.

First of all, micro-Raman spectroscopy has been tested as a possible technique of examining wool dyed fibres, and different analytical conditions have been compared (Chapter 3.1). Indeed, Raman spectroscopy has a large variety of parameters, designs and sampling procedures which has rendered a clear evaluation of the technique difficult until now. Positive results have been achieved directly analysing wool dyed fibres: employing different excitation wavelengths meaningful spectra have been acquired and this allows to try, for the first time, to identify and distinguish what laser excitation wavelength applies on the basis of different colour fibres. The use of different lasers and the large number of wool dyed fibres analysed might allow to create a database on the wool dyed fibres and to promote a sort of guidelines on micro-Raman parameters to be applied in the analysis directly on fibres depending on colours. If the dye does not permit to achieve a meaningful Raman spectrum due to the low amount of dyestuff or to fluorescence effect, SERS spectroscopy can be performed.

SERS can overcome the above disadvantages because of the fluorescence quenching of the analyte, as well as the high sensitivity provided by the giant intensification of the radiation intensity in the presence of the metal nanoparticle. Therefore, SERS is being developed as a promising micro or non-destructive technique for characterizing natural or synthetic organic pigments and dyes in works of art and cultural heritage materials [3].

A new method for the in situ production of Ag nanoparticles [4], for the “on fibre” SERS detection of synthetic organic dyes has been developed (Chapter 3.2). Immobilized AgNPs have been prepared (Jurasekova et al. [5, 6] method) by photoreduction of Ag⁺ by using a laser/micro-Raman coupled system, and the SERS efficiency of AgNPs prepared at different experimental conditions has been evaluated changing the excitation wavelength, the laser power and the laser irradiation time. Indeed, in order to achieve good SERS signals by photoreduced and immobilized AgNPs on fibre without burning the sample, two different experimental methods have been developed using two excitation wavelengths (442 nm and

532 nm). Photoreduction has the advantage of avoiding the use of nano-metal colloidal solutions which have to be prepared and whose stability is reduced with passing of time. Usually, the AgNPs produced on fiber were photoreduced using a laser wavelength of 532 nm [5, 6], metal nanoparticles obtained in these conditions produce a SERS effect only when the 532 nm laser is employed as excitation wavelength. Otherwise, it is found that AgNPs photoreduced focalizing 442 nm laser, allow the analyses of the dyed fibres with different excitation wavelengths (442 nm, 532 nm, 785 nm), thus improving the identification of the dye. The development of a versatile photo reduction method with 442 nm excitation wavelength is the main novelty of this part of research.

Surface Enhanced Vibrational Spectroscopy (SEVS) mainly focused at the Infrared spectroscopy are the subject of Chapter 4, in particular two different analytical approaches have been developed: SEIRA and ATR-RAIRS. Both the presented techniques work on solution, and Acid Orange 7 (AO7), a synthetic colorant used for dyeing, has been selected in order to develop the analytical protocols. Moreover, the necessity to work in solution means a compulsory sample pretreatment for dyed fibres. Using the micro extraction method, the limitations inherent to IR spectroscopy which do not allow the obtainment of clear vibrational spectra from minor analytes in a protein matrix such as wool, has been overcome.

In Chapter 4.1 SEIRA based methods for the characterization of synthetic colorants have been tested and improved. Two different colloidal solutions (Ag-hydroxylamine and Au obtained by laser ablation) have been tested with and without aggregation. The method set up using naked AuNPs produced by means of laser ablation, allows to strongly enhance the signals, without the presence of spurious by-products - found employing Ag colloid - which may affect the results. SEIRA has been applied for the analyses of extracted dyed wool samples after the setting up of a suitable micro extraction method aimed at avoiding hydrolysis of wool and the presence of by-products which can hinder the colorant absorption bands. The extraction with MeOH, which provided the most effective results among three extraction methods tested, was applied for the analysis of a few pieces of fiber. SEIRA spectra obtained mixing the extract with the unaggregated AuNPs allowed to recognize bands of the colorant, even if present in low concentration.

Even though SEIRA method has been demonstrated to be useful in the identification of small quantities of synthetic organic dyes of standard solutions and also, micro extracted from standard fibres, the necessary use of metal colloids and the spectra resolution to be improved make this analytical approach difficult and costly due to the employment of naked AuNPs created by means of laser ablation. For these reasons another approach has been experimented, with the aim of reaching the enhancement without the use of metal colloids. Experimental data allowed to identify a new enhanced vibrational technique which we have named ATR-RAIRS (Chapter 4.2): this technique is performed with commercial instrumentations available in conservation departments, coupling ATR and RAIRS methods with a fixed incident angle.

Due to the good reproducibility of the ATR-RAIRS analytical approach revealed for AO7, and the good consistency with conventional IR reference data when concentrations in the range of

10^{-4} - 10^{-5} M are submitted to analysis, several other solution of synthetic organic standard dyes belonging to xanthene, triarylmenthane, nitro and azo classes have been successfully analysed. The spectra achieved from the analysis of these standard dyes solution have been processed with PCA. The multivariate analysis demonstrate that all these dyes categories can be correctly discriminate. The positive results obtained on standard solution, have been encouraged to further explore this method on micro-extraction of standard and real fibres samples, and, a worthy degree of discrimination identified with PCA have been achieved.

Moreover, for the analysis of mixture of dyes the analytical approaches before mentioned present difficulties in the exactly detection of all components, for this reason a third analytical method has been developed.

Mixtures of dyes can be easily separated via thin layer chromatography [7, 8]. The separated TLC spots can then be analyzed by means of vibrational techniques, which can be efficiently employed for the characterization of organic molecules such as synthetic dyes.

In this general frame, the Chapter 5 of this thesis has been focused on the development of an advanced analytical system based on the combination of an improved thin layer chromatography plate coupled with ATR-RAIRS and SERS-Raman microscopies for the detection and the analysis of organic synthetic dyes. The research is aimed at making possible the performance of both analyses on the same separated TLC spot, allowing for taking advantage of the complementarity of the two techniques.

As stationary phases, golden slides coated with silver iodide (AgI) are proposed. this inorganic salt has been chosen due to its transparency in the mid-IR range, thanks to which it does not interfere in the FTIR analyses. Indeed, it forms a thin layer on the golden slide that does not decrease the enhancement given by the Au underlayer in the ATR-RAIRS analysis. AgI has already been used as a novel stationary phase for TLC/FTIR experiments, not only because it removes problems of interference caused by IR absorption, but also because thanks to its insolubility it precludes the possibility that the stationary phase is destroyed by the mobile phase. As far as enhanced Raman in concern, AgI was chosen considering the already reported SERS activity given by silver halides [9]; the Au-AgI plates indeed showed to bring an enhancement to the Raman signal, probably linked to the coexistence of AgI and gold. The method has been successfully tested for the characterization of a mixture of three synthetic organic colorants: Diamond green (BG 1), Rhodamine B (BV 10) and Methylene blue (BB 9). Those have been chosen being all basic colorants widely used in dyeing processes.

The last chapter of this work (Chapter 6) is dedicated to test and to develop an elaboration of IR spectra achieved in MIR and FIR range named the Grinding Curves Method [10-13]. A new method for calcite analysis has been performed with the aim to investigate the crystals size, the atomic order and to differentiate morphological structure arising from different crystallization process. Calcium carbonate in various forms has had from earliest times a wide role in art as a pigment (i.e. Saint John's white), as a raw matter in sculptures (i.e. marble as Carrara marble), as a substrate for wall paintings and also as a treatment for artworks restoration in consolidation procedure for wall or stones and in paper de-acidification practice.

For this reason, it was decided to develop also new spectroscopic approaches applying the method both on MIR and FIR range, in order to improve knowledge on this mineral. As concerned grinding curves in MIR region, the results achieved for different calcite samples ground is an efficient, rapid, and effective tool to distinguish between calcites formed by different processes. The basis for this differentiation correlates with characteristic differences of local and extended atomic order in the calcite. Moreover, the possibility to use grinding curves method also in spectra acquired in FIR region is the real novelty. FIR grinding curves might allow to differentiate calcite samples depending on their lactone vibrations.

1.3 References

- [1] G. Spoto, *Acc. Chem. Res.*, 2002; 35, 652-659
- [2] M. Vagnini, C. Miliani, L. Cartechini, P. Rocchi, B.G. Brunetti, A. Sgamellotti, *Anal Bioanal Chem*, 2009; 395, 2107–2118
- [3] K. Chen, M. Leona, T. Vo-Dinh, *Sens. Rev.*, 2007; 27.
- [4] M. V. Canameres, J. V. Garcia-Ramos, J. D. Gomez-Varga, C. Domingo, S. Sanchez-Cortes, *Langmuir*, 2007; 23.
- [5] Z. Jurasekova, C. Domingo, J. V. Garcia-Ramos and S. Sanchez-Cortes, *J. Raman Spectrosc.*, 2008; 39.
- [6] Z. Jurasekova, E. del Puerto, G. Bruno, J. V. García-Ramos, S. Sanchez-Cortes, C. Domingo, *J. Raman Spectrosc.*, 2010; 4.
- [7] F. Wang, H. Wu, Q. Zhu, K. Huan g , Y. Wei, C. Liu, Y. Zhai, Z. Yang, S. Weng, Y. Xu, I. Noda, J. Wu, *Anal. Methods*, 2013; 5, 4138-4144
- [8] K. Tsutsumi, K. Ohga, *Analytical Sciences*, 1998; 4
- [9] X. Wang, W. Shi, G. She, L. Mua, *Phys. Chem. Chem. Phys.*, 2012; 14, 5891–5901
- [10] V. Chu, L. Regev, S. Weiner, E. Boaretto, *Journal of Archaeological Science*, 2008; 35, 905-911.
- [11] L. Regev, K. M. Poduska, L. Addadi, S. Weiner, E. Boaretto , *Journal of Archaeological Science*, 2010; 37, 3022-3029
- [12] M. Suzuki, Y. Dauphin, L. Addadi, S. Wainer, *CrystEngComm*, 2011; 13, 6780-6786

[13] K. M. Poduska, L. Regev, E. Boaretto, L. Addadi, S. Weiner, L. Kronik, S. Curtarolo, *Advanced Materials*, 2011; 23, 550–554

LIST OF PUBLICATIONS

Publicazioni

- S. Prati, I. Bonacini, G. Sciutto, A. Genty-Vincent, M. Cotte, M. Eveno, M. Menu, R. Mazzeo, *New Insight into the degradation processes occurring on verdigris*, submitted to Dyes and Pigments;
- M. Ricci, S. Prati, B. Ballarin, I. Bonacini, M. C. Cassani, E. Castellucci, C. Lofrumento, R. Mazzeo, G. Sciutto, M. Quaranta, M. Van Bommel, *Direct observation of dyes in XIX cinematographic films by surface enhanced (resonance) Raman spectroscopy: spectroscopic evaluations*, to be submitted to J. Raman Spectroscopy;
- S. Prati, G. Sciutto, I. Bonacini, S. Kazarian, R. Mazzeo, *ATR/RAIRS as innovative approach for the analyses of colorants in micro extracts*, to be submitted to Analytica Chimica Acta;
- I. Bonacini, S. Prati, R. Mazzeo, G. Falini, *Crystallization of CaCO₃ in the Presence of Ethanolamine Reveals Transient Meso-like Crystals*, Cryst. Growth Des., 2014, 14, 11, 5922-5928;
- G. Sciutto, S. Prati, I. Bonacini, P. Olivieri, R. Mazzeo, *FT-NIR microscopy: An advanced spectroscopic approach for the characterisation of paint cross-sections*, Microchemical Journal, 2014, 112: 87–96;
- S. Prati, M. Quaranta, G. Sciutto, I. Bonacini, L. Litti, M. Meneghetti, R. Mazzeo, *Use of nano gold obtained by laser ablation for SEIRA analyses of colorants*, Heritage Science, 2014, 2, 28;
- C. Torri, A. Mangoni, R. Teta, E. Fattorusso, L. Alibardi, S. Fermani, I. Bonacini, M. Gazzano, M. Burghammer, D. Fabbri, G. Falini, *Skin lipid structure controls water permeability in snake molts*, Journal of Structural Biology, 2014, 185, 1, 99-106;
- S. Fermani, C. Vettrai, I. Bonacini, M. Marcaccio, G. Falini, J. A. Gavira, J. M. Garcia Ruiz, *Heterogeneous Crystallization of Proteins: Is it a Prenucleation Clusters Mediated Process?*, Cryst. Growth Des., 2013, 13, 3110–3115; also selected for the cover page;
- R. Mazzeo, G. Sciutto, M.L. Amadori, S. Barcelli, S. Bersani, I. Bonacini, B.G. Brunetti, L. Cartechini, E. Catelli, C. Clementi, M. Quaranta, M. Palmieri, S. Prati, M. Vagnini, *Indagini non invasive e micro-invasive per la caratterizzazione del disegno preparatorio e dei componenti pittorici nel dipinto della Città ideale*, in: A. Marchi, M.R. Vallazzi (Eds.), La città ideale, l'utopia del rinascimento ad Urbino tra Piero della Francesca e Raffaello, Electa, 2012;

- R. Mazzeo, G. Sciutto, S. Bersani, I. Bonacini, M. Quaranta, S. Prati, *Indagini chimiche e fisiche non invasive per la caratterizzazione degli inchiostri*, in: L'evangelario di papa Chiaramonti. Storia di un codice del secolo XII, a cura di Paola Errani e Marco Palma, Cesena 2012 (Stilgraf), pp. 39-45;
- R. Mazzeo, M. Menu, L. Amadori, I. Bonacini, E. Itié, M. Eveno, E. Joseph, E. Lambert, S. Prati, E. Ravaud, G. Sciutto, *Examination of the Uomini Illustri: looking for the origins of the 28 portraits in the Studiolo of the Ducal Palace of Urbino*, in *Studying Old Master Paintings: Technology and Practice*. Marika Spring (ed.). Archetype Publications. London (2011), pp.44-51 e pp.37-43.

Chapter 2

**New advances in the application of FTIR
microscopy in the near-IR range.**

2.1 Infrared microscopy applied to cultural heritage

The coupling of a microscope to the IR spectrophotometer produces a system capable of doing IR microspectroscopy. The resulting apparatus, called an IR microspectrophotometer, was first made commercially in the 1950s [1]. These instruments slowly become widely applied for the investigation of cultural heritage materials, after the advent of Fourier transform-based IR (FTIR) spectrometers (late in the 1960s, in parallel with the availability of personal computers).

Particularly useful for the field of art conservation was the coupling of the optical microscope with the IR spectrometer. Although the system performed well, the sensitivity achievable by a microscope in combination with a wavelength dispersive IR spectrometer was low, and interest in the technique waned. Revival of IR micro spectroscopy was stimulated by the development of FT-IR instrumentation, with its increased energy throughput.

In fact, IR spectroscopy for the examination of paintings and artworks has been use from its early beginning [2] due to characteristic absorptions in the mid-IR range (4000–600 cm^{-1}) of many of the inorganic and organic artworks constituents [3, 4]. In particular, the improvement concerning spectral resolution and detection limits obtained with the transition from dispersive IR to FTIR instruments, allowed their widespread use as suitable tools in conservation issues [5], overcoming drawbacks related to dispersive instruments and increasing the energy throughput. Moreover, when micro-sampling accessories for FTIR spectroscopy were introduced in the early 1980s, the following development of FTIR microscopy represented a powerful innovation for the micro-destructive analysis of small samples [6]. The recent introduction of mapping and imaging equipments allows to collect a large number of FTIR spectra on a surface, producing a distribution map of the identified compounds.

A FTIR microscope consists of a FTIR spectrophotometer combined with an optical microscope, which incorporates all-reflecting optics and a spherical surfaces adapted to the infrared radiation for minimising optical aberrations. The conventional infrared light source (typically a Globar silicon bar heated to 1500 K), which emits radiation from 1.5 μm up to a few tens of micrometers, is directly directed to the microscope rather than to the spectrophotometer sample chamber, without any modification to the interferometer. The user interface for data acquisition and processing is also the same as for conventional FTIR spectroscopy. The microscope is designed for observation both in transmission and in reflection mode. A system of dichroic mirrors allows the visible light and the IR radiation to pass through the same optical system, permitting to first visually observe the region of interest and then to record the corresponding IR spectra.

The radiation can be focused on small areas, reducing the amount of material necessary for the analysis and allowing to isolate different regions of heterogeneous samples, which cannot be physically separated.

Several modes, depending on the amount and type (powder or fragment) of the available samples can be choose for FTIR spectroscopy and microscopy analysis. In order to achieve the largest amount of information, our laboratory has developed an analytical protocol giving priority to sample conservative techniques within the frame of micro-destructive FTIR spectroscopy techniques [7] (Fig. 1)

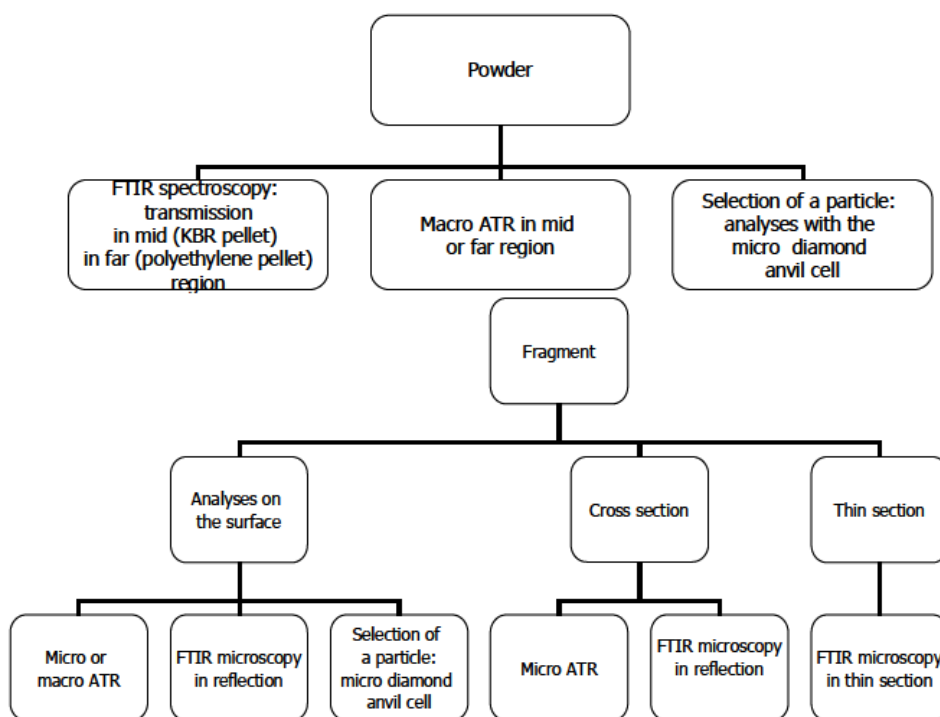


Figure 1: Scheme of the possible analysis in FTIR spectroscopy and microscopy on powder or fragments

Until thirty-five years ago, transmission measurement was the only method of IR analysis. Because of its versatility, IR transmission was used for both qualitative and quantitative analysis of gas, liquid, and solid samples. In the transmission measurements, the IR beam passing through the sample benefits of a high energy throughput and a resulting high sensitivity. This explain the large collections of IR transmission spectra produced in the past and their use as reference for comparison with other infrared methods.

The absorption spectra report at each wavelength the absorbance value ($A = -\log T$), which is proportional to both the concentration of the analyte in the sample (c) and the sample thickness (l), (Lambert-Beer's law) in the Equation 1.1 where the extinction coefficient ϵ is a characteristic property of the absorbing material.

$$A = \epsilon c l = -\log T \quad (1.1)$$

In transmission analysis, particularly appropriate for small particles (sampled from bigger fragments under the stereomicroscope), or for thin film, the sample can be placed freestanding in the IR beam, or it may be held in place by a supporting material. Ideally, the supporting material would not, in itself, absorb any of the IR radiation, normally transparent salt as support (i.e., NaCl window) [8], or the diamond anvil cell are used. The diamond anvil cell consists of two industrial-grade diamonds, each with a flat, polished face, that are carefully aligned in a steel compression cell. The diamonds serve as windows, on which the sample is placed and through which the IR beam travels. The sample is placed on the clean diamond facet, the opposing diamond is positioned on top, the cell is closed, and pressure is applied to flatten the sample. This is a simple device that can be placed directly on the stage of a FTIR microscope and, for this reason, it is widely employed to analyse paintings or archaeological materials as single organic colorants particles mixed with strongly absorbent inorganic salts and organic binders to reduce influence by other components [9] or for the study of multilayered samples [10]. After careful positioning on a diamond window followed by compression, the sample stratigraphy can be preserved with only an expansion of each individual layers.

Reflection methods can be applied for the analysis of either the sample surface or its cross section and they can also be performed directly on the surface of an object without any sample removal and, thus, they have been applied on a large variety of materials. If the object is small enough, it can be placed directly on the microscope stage, otherwise a side port reflectance accessory can be used. Different the beam reflection paths are used by different types of IR reflection devices (fig. 2).

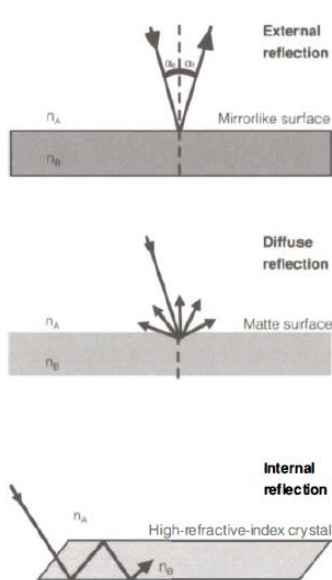


Fig. 2: Three different reflection types
 n_A = refractive index of air;
 n_B = refractive index of the reflecting material;
 α = angle of incidence).

At any interface between two materials, an incident radiation is split into a specular reflected light and transmitted beams, in different proportions according to the refractive index ratio of the two materials involved, as described by the Fresnel's equations [11]

If a sample cross section surface is not optically flat, the diffuse reflection component has to be considered. In fact, the diffuse reflected light travels through the sample before being scattered or reflected from internal surfaces. Consequently, reststrahlen effects and diffuse reflection may arise and the Kramers-Kronig transformation cannot be applied [12]. Thus the resulted spectra may be of very difficult interpretation. In order to obtain a highly reflecting surface, a perfect sample planarity has to be achieved by using adequate and strenuous mechanical polishing methods [13], costly advanced techniques such as ion milling system, focused ion beam [14, 15], or ultramicrotomy [16, 17]. As a consequence, very few publications have been so far reported concerning the study of paint cross sections by FTIR microscopy in specular

reflection mode [18, 19].

Reflection-absorption occurs when the IR beam passes through a thin film of sample (no more than 15 μm) and is reflected from a nonabsorbing substrate as a metal surface. When the incident radiation enters the thin layer at a near-normal angle (90°), the method is essentially a double-pass transmission experiment. Reflection-absorption experiments can also be conducted at a greater angle of incidence (65° - 85°), thereby increasing the effective path length of the sample. This is called grazing-angle spectroscopy and is used to detect and analyze very thin films. Nevertheless, reflection-absorption spectrometry (RAS) can be applied in some restricted cases, such as the study of protective coatings on metal artworks [20], for the characterization of varnish layers on gilded art objects or for the identification of organic dyes extracted from fibres. Moreover, it is a simple method, which can be proposed as an alternative to transmission measurements. In fact, samples (films, powders, particles or fibres, etc...) can be easily prepared by flattening in the same way as for the analysis with NaCl windows.

Attenuated total reflection (ATR) is based on the principle that total reflection is produced when the incident radiation passes from a higher refractive index material to a lower one with a particular incidence angle, called critical angle. When the incident angle is greater than the critical one, an evanescent wave forms up on the surface of the higher refractive index material (IRE, internal reflection element) and can penetrate the optically less dense medium placed in contact with it, resulting therefore attenuated. The use of ATR has been successfully reported for a large variety of samples, due to the fact that the spectra so obtained are similar to those recorded in the transmission mode. Nevertheless, some distortions of relative intensity and wavenumber shifts, principally at lower wavenumbers, are visible in ATR spectra, since the evanescent wave penetration depth (dp) depends on the refractive index of both the IRE and the material analysed, but is also function of the wavelength, as shown by the equation below (Equation 1.2), where λ is the wavelength of incidence radiation, n_1 the refractive index of IRE, n_2 the refractive index of the sample and θ the incidence angle of radiation on the interface [21].

$$dp = \frac{\lambda}{2\pi n_1 \sqrt{\sin^2 \theta - (n_1 - n_2)^2}} \quad (1.2)$$

The sample refractive index is function of wavelength, and frequency shifts are also observed, principally at lower wavenumbers.

ATR correction algorithms, proposed by most of the commercially available FTIR software, proved to be not effective in the case of analysis of mixtures, like samples from cultural artworks. The simplest way to compare ATR and transmission spectra is therefore to create a reference library of known compounds, whose spectra can be subsequently compared with unknown samples. An important advantage of ATR investigation is that it allows the investigation of smaller area maintaining the same aperture, thanks to the magnification factor of the IRE [22]. As an example, the actual investigated area is 25 x 25 μm , in the case for an aperture of 100 μm x 100 μm and an IRE of germanium (refractive index = 4).

In the last decades, mapping and imaging equipments for FTIR microscopy allow to analyse a surface collecting a considerable number of FTIR spectra and obtaining a pattern showing the distribution of different compounds. FTIR mapping systems produce a sequential data collection, using a single-element mercury-cadmium-telluride (MCT) detector, adjustable apertures to select the investigated area and a motorised stage. The spatial resolution is related to the aperture dimensions and to the acquisition method (reflection, transmission or ATR). Furthermore, the overlap between two adjacent surface areas during data collection allows further increasing the spatial resolution. The main disadvantage of the mapping systems is the long time required for acquisition (hours), which may be, however, not so relevant when dealing with important cultural heritage samples.

FTIR imaging consists of a simultaneous and, therefore, faster data collection performed by a multichannel detector where small pixels of about 6 μm are distributed over a grid pattern (FPA, focal plane array) [23, 24]. This type of detectors allows to record the optical signal entire field of view (FOV) and requires no aperture. Typical IR sensitive focal plane array (FPA) detectors include 64 x 64, 128 x 128 and 256 x 256 elements (pixels) arranged in a regular pattern. Compared to the mapping system, where geometrical apertures are used, the spatial resolution is in this case determined by the pixel dimension. Unfortunately, this yields also a poor spectral quality (low signal-to-noise ratio, S/N) since the photons quantity received by each pixel is inversely related to the number of pixels. For large detectors, this means a low photon quantity. The ATR configuration can provide increased spatial resolution of approximately 5 μm compared to transmission or reflection imaging. Moreover, the cut-off of the focal plane array detector at 900 cm^{-1} is a significant disadvantage in distinguishing several inorganic compounds with characteristic absorptions below 650 cm^{-1} (i.e., calcite and lead white).

Linear array detectors (raster scanning) have been recently developed combining several MCT detectors with a motorised stage to sequentially scan lines. This system reduces the acquisition time by a factor corresponding to the number of detector elements. The size of individual elements is 25 μm , permitting to obtain high quality spectra. In transmission or reflection mode, the achieved resolution of 25 μm can be reduced to 6.25 μm using an optical zoom, while in ATR the spatial resolution is reduced by the crystal magnification ($\sim 6 \mu\text{m}$ with a germanium crystal).

In recent times, a new integrated FTIR microscope has been designed, offering the powerful combination of a microscope with an incorporated FTIR spectrometer (interferometer, source, laser and detector). The main advantage of this setting is the higher energy compared to conventional systems, where energy losses are due to the radiation optical path from spectrometer to microscope [25].

2.2 Application to Near-IR spectroscopy to the analysis of natural resins and real samples

2.2.1 Near-IR spectroscopy

The near-infrared spectral region was first discovered by Herschel, in his classic experiment. Basically, Herschel trying to find out which colors of the spectrum contained the heat that is felt in sunlight, separated them with a prism and placed a black-painted thermometer in the various parts of the spectrum. This was the first indication that electromagnetic radiation. After almost 100 years, other scientists were able to obtain spectra in infrared region. In the early part of the 20th century, some scientists were active in systematically measuring the spectra of interesting molecules in the mid-infrared range; the near-infrared region was neglected due to the limitations of the equipment available at the time.

This topic remain unchanged until the 1960s when Karl Morris of the U.S. Department of Agriculture conceived the modern near-infrared spectroscopy combining: low-noise spectrometers, computerized control of the spectrometer along with computerized data acquisition, the use of multivariate approach to analyze the data and the use of diffuse reflectance measurements [26]. This last issue gave the analyst the ability to obtain useful spectra from a large variety of natural products and other problematic samples, without the necessity of a pretreatment. Starting from this point, the near-IR spectroscopy had been extensively use for different scopes.

The NIR region (13300 to 4000 cm^{-1} [27]) has been widely exploited in bench or portable systems for the macroscopic analyses of samples in different fields (pharmaceutical, forensic, polymers, food) [28-32] monitoring a variety of processes and for characterization of different substances. Indeed NIR spectroscopy is a fast, non-invasive and cost-effective analytical method which allows non-contact measurements in reflectance mode, providing molecular information on complex macromolecules. Moreover the use of this spectral range may be extremely useful as combination and overtone bands have lower absorptions and for this reason are not distorted by the specular reflection. In addition if the surface is not completely planar these bands are enhanced by the volume reflection, often resulting very useful for a chemical characterisation of the material [33]. On the other hand only functional groups containing NH, CH, OH, CO, and CC bonds can produce significant vibrational bands in the NIR range. Moreover combination and overtone bands are generally broader and less resolved than the fundamental bands and overlapped with one another. For this reasons the information achieved in this range may be less specific than the ones obtained in the mid-infrared one and mixtures of organic substances, may be extremely difficult to be

distinguished. For this reasons, a multivariate approach is usually required in order to extract useful information from spectra [34, 35].

For the analysis of art-works, FTIR microscopy has been widely applied for the characterization of painting materials thanks to its contemporary capability to characterise stratigraphically both inorganic and organic compounds [25]. Polychrome samples have been mainly analysed as cross sections, in attenuated total reflectance (ATR) or total reflectance modes mainly employing the MIR region (4000cm^{-1} - 700cm^{-1}) [7]. ATR mode is generally considered the most appropriate method to analyse cross sections [3, 36-41] thanks to its high and its capability to obtain spectra similar to those obtained in the transmission mode. However, this setup presents some limitations due to the need for a good contact between the ATR crystal and the sample surface. In addition, the surface of stratigraphies may result damaged by the pressure of the crystal and, frequently, the contact may induce displacements of the surface to be investigated [42].

Differently, FT-IR microscopy can be carried out in a non-contact mode through a Cassegrain objective. Nevertheless, the reflected light is characterised by derivative-like and reststrahlen bands generated by the highly reflecting surfaces. Moreover, broadening and shift of signals may be induced by diffuse reflection [10, 43]. As a consequence, difficulties in the interpretation of spectra may affect the reliability of the results, but on the other hand this method can be applied for analysis in MIR and NIR range allowed an integrated use of information recorded within these spectral ranges that can be extremely useful.

In the field of cultural heritage, non-invasive *in-situ* NIR spectroscopy investigations have been performed for the identification of paint materials [35, 43-46], for the evaluation of the long-term stability of historical papers [47] and for the study of degradation processes on calcareous stones [48]. Recently, Dooley et al. proposed the use of an advanced NIR reflectance imaging system for the identification of organic substances in paintings, exploiting the vibrational overtones and combination bands of fundamental absorptions, which are less affected by potential pigment interferences [49].

On the other hand, only very few studies concerning the use of FTIR microscopy in the near infrared range for the analysis of artistic multi-layered samples have been reported in the literature [50, 51]. Rosi et al. [44] reported the application of micro-IR spectroscopy in reflection mode in the $5600 - 960\text{ cm}^{-1}$ range, for discovery of the spatial distribution of organic and inorganic materials in easel painting cross sections of standard mock-ups and of a 17th century wooden sculpture. The NIR spectra achieved for the different samples have been treated with multivariate analysis and were useful for characterization of gypsum and linseed oil. Poli et al [52] carried out micro-infrared total reflection measurements in an extended IR range (from 1000 to 5266 cm^{-1}) exploiting the broad spectral response of mercury cadmium telluride detector in order to include near-infrared information without any modification of the standard mid-infrared micro-FT instrumentation. The NIR region was here employed for the exact recognition of azurite on a micro-sample of a wood polychromy from an undated historic polyptic. In conclusion, in these works on cross-sections spectra have been collected

exploiting a limited NIR range - from 5600 to 4000 cm^{-1} - for the characterisation of few compounds (such as azurite, gypsum and linseed oil) present in polychrome samples.

The use of FT-IR microscopy in the near-infrared region (NIR) in the total reflectance mode, can be a complementary technique for the characterisation of paint cross-sections. The integrated use of information recorded in the NIR and in the MIR region is extremely useful in the molecular investigation of both organic and inorganic substances, thanks to the fact that combination and overtone bands present in the NIR region, even if weaker and less selective than those on the MIR region, are not distorted by reflection phenomena. Furthermore, NIR spectra can be efficiently used as a spectral fingerprint for the stratigraphic characterisation of paint cross sections.

2.2.2 Materials and methods

2.2.2.1 Samples

All standard natural resins purchased from Kremer Pigmente (Aichstetten, Germany) were:

- Colophony;
- Copal;
- Sandarac;
- Mastic;
- Dammar;
- Shellac.

Linseed oil was purchased from Zecchi (Florence, Italy).

Resins, previously dissolved in different solvents (turpentine for triterpenic resins and colophony, ethyl alcohol for sesquiterpenic resins and sandarac), and linseed oil were applied on glass slide supports and left drying at room temperature. FTIR total reflection spectra – in the mid and near regions – were acquired on powdered resins scraped off from these films.

Three historical samples were investigated, discussing the performance and the advantages of the μ FT-NIR/MIR analysis in combination with multivariate statistical treatment. The first sample (labelled as BP3) was collected from a yellow area of “La Battaglia di Cialdiran”, an oil painting on canvas, dated back to the sixteenth century, and exhibited in the Regional Museum of Mirto Palace in Palermo, Italy. The second one (Rond25) was collected from a Renaissance wooden painting (Madonna in Trono con Santi), exhibited at the Museum of the City of Ravenna. The third sample (Civ6) was collected from a gilded area of the XV century wall paintings of the Basilica di San Frediano, Lucca (Italy).

Paint cross-sections of real samples were prepared by using the KBr/synthetic resin system [27]. Briefly, the micro-fragment was placed in a macro–micro pellet die where a KBr pellet-bed (2 t for 1 min) had been previously prepared and covered with additional KBr and finally

pressed (3 t for 2 min). Afterwards, the pellet obtained was reduced in the external part and submitted to the polyester-resin embedding procedure. Dry polishing was carried out using silica abrasive cards (purchased from Micro-Surface Finishing Products Inc., Wilton, IA) with grit from 1000 to 12000, to obtain a high-quality surface in terms of planarity and roughness. A polishing sample holder was employed in order to ensure a high level of surface planarity.

2.2.2.2 Optical microscopy

Cross-sections were observed and documented stratigraphically by means of dark field observations performed with the use of an Olympus (Olympus Optical, Tokyo, Japan) BX51 microscope equipped with an Olympus DP70 digital scanner camera. A 100-W halogen projection lamp and a Ushio Electric (USHIO Inc, Tokyo, Japan) USH102 Ultraviolet (UV) lamp were employed for the acquisition of visible and UV fluorescence images, respectively.

2.2.2.3 μ FT-NIR/MIR analysis

A Thermo Nicolet (Thermo Fisher Scientific, Waltham, MA, USA), iNTM10MX imaging microscope, fitted with a mercury–cadmium–telluride (MCT) detector cooled by liquid nitrogen, was used for single-point and mapping analyses. Spectra were recorded within the NIR and MIR ranges (8000–675 cm^{-1}) in total reflection mode with a spectral resolution of 4 cm^{-1} .

Sample Rond25 was investigated selecting an area of $25 \times 90 \mu\text{m}^2$, with an optical aperture of $50 \times 20 \mu\text{m}^2$ and step size of 25 and 10 μm for x and y axes respectively. Each spectrum was recorded as the average of 4096 scans.

Samples BP3 and Civ6 were mapped using an aperture of $20 \times 50 \mu\text{m}^2$ and a step of $10 \times 25 \mu\text{m}$ in the x–y direction. The overall area of analysis was $25 \times 90 \mu\text{m}^2$. Each spectrum was recorded as the average of 2048 scans.

A dedicated software, OMNIC PictaTM (Thermo Fisher Scientific, Waltham, MA, USA), was applied for the preliminary manipulation of the spectral data.

Analyses of powder standard resin samples were performed with an optical aperture of $200 \times 200 \mu\text{m}^2$, collecting 1024 scans for each spectrum. Nine replicate spectra were collected for each resin specimen.

2.2.2.4 Principal component analysis on single-point spectra of standard natural resins and linseed oil

PCA is an exploratory method that looks for directions of maximum variance within the multivariate data space, based on the assumption that a high variance (i.e., a high variability) is synonymous with a high amount of information. The directions searched, which are called principal components (PCs), are orthogonal. This implies that they are not inter-correlated and, therefore, that they never account for duplicate information [53].

From a mathematical point of view, the PCs are expressible as linear combinations of the original variables: the coefficients which multiply each variable are called loadings. The loading

values of the original variables on two selected PCs can be represented on bidimensional scatter plots (the loading plots), which give information about the importance of the variables and about their inter-correlation, with respect to the fraction of variance (i.e., information) explained by those PCs.

The key feature of PCA is in its high capability for representing large amounts of complex information by way of simple bidimensional or tridimensional plots. In fact, the space described by two or three PCs can be used to represent the objects (score plot), the original variables (loading plot), or both objects and variables (biplot). For instance, if the first two PCs (low-order) are drawn as axes of a Cartesian plane, we may observe in this plane a fraction of the information enclosed in the original multidimensional space which corresponds to the sum of the variance values explained by the two PCs.

Since PCs are not intercorrelated variables, no duplicate information is shown in PC plots. In the case of almost continuous signals such as IR spectra, it may be useful to represent the loading profiles, eventually superimposed to a selected signal or an average signal profile, in order to directly visualise which parts of the original signals give the highest contribution in defining a particular PC.

PCA on standard resin spectra was performed in order to verify the possibility of distinguishing between the different resin classes. Spectra in the NIR range (6400–5500, 5300–4000 cm^{-1}) were pre-processed by the standard normal variate (SNV) transform and the second-order Savitzky Golay derivative, using third order polynomials and 11 datapoint gaps.

The SNV transform is able to correct for baseline shifts and global intensity effects, while derivatives enhance details within complex spectral features (e.g. unresolved broad bands) and correct for baseline shifts (first derivative) and drifts (second derivative). In particular, the first derivative of a signal can be interpreted as the slope of the tangent to the signal at each point. It returns null segments in correspondence to constant bands of the original signal and provides a correction for additive effects. The second derivative can be considered as a further derivation of the first derivative; it represents a measure of the curvature of the original signal. The second derivative returns null segments in correspondence to bands characterised by a constant slope in the original signal and provides a correction for both additive and multiplicative effects.

2.2.2.5 Multivariate chemical mapping

Multivariate data processing and chemical mapping were performed by means of in-house Matlab routines (The Mathworks Inc., Natick, USA).

Hyperspectral data were processed using the so-called brushing procedure [54-56]. It is based on the integration of scatter plots and score maps and allows the detection of correspondences between clusters of scores and specific areas within a given PC score map, employing an interactive selection procedure. Moreover, the average spectral profiles of these points can be visualised, jointly with the analysis of the loading values, identifying the spectral features most involved in defining each investigated area and providing a consistent chemical

interpretation of the results. Finally, PC false colour images (RGB) were obtained by coding the score values on three selected PCs as the intensity of the red, green, and blue channels. This generally allowed to illustrate an overall localisation of the painting materials in a single image.

A number of common mathematical pre-processing strategies were applied on the hyperspectral data. The aim of such pretreatments was the minimisation of unwanted effects – such as baseline variations and global intensity effects – which commonly affect NIR and MIR spectra. In more detail, the standard normal variate (SNV) transform, a linear detrending and Savitzky–Golay derivation were applied, both singularly and in combination.

The MIR range considered was between 4000 and 700 cm^{-1} , while the NIR range was investigated between 7500 and 3950 cm^{-1} , for sample Rond25, and in the intervals 6500–5500 cm^{-1} and 5300–3950 cm^{-1} , for samples BP3 and Civ6. Principal component analysis (PCA) was performed on hyperspectral data and the score values were converted into chemical score maps, which represent variation of the score values in the mapped area by a chromatic scale.

2.2.3 Results and discussion

2.2.3.1 Sample BP3

The cross-section photomicrographs of BP3 sample, shown in figures 3a,b, allowed to clearly identify the presence of three layers: the ground layer (layer 0), a superimposed yellow layer (layer 1) and the uppermost layer (layer 2) probably applied as varnish, well identifiable thanks to the strong whitish fluorescence, detectable under UV illumination.

PCA was performed on both MIR and NIR data and the results were compared. A number of common mathematical pre-treatments were applied to both of the hyperspectral data arrays, in order to minimise unwanted spectral variations. In the case of the NIR region, the outcomes showed that pre-treatments are functional to exploit the extraction of useful information from spectral data. In particular, the SNV transform coupled with a linear detrending was chosen as the most effective strategy to remove slope variations and to correct for baseline shifts and global intensity variations.

The PC1 score map of sample BP3 (NIR data), reported in Fig. 3c,d,e, identified the two different layers: layer 2 (red area, corresponding to the highest score values) and layer 1 (green area). The so-called brushing approach was used to understand the correspondences between clusters of scores (detectable in the scatter plots) and the corresponding areas within a given PC score map, using an interactive manual selection procedure. In addition, the average spectral profile of the selected points was visualised, in attempt to identify the spectral bands most involved in defining each investigated area. The examination of the average spectral profile corresponding to first selected area (layer 2) suggested the presence of a triterpenic resin, as the principal constituent of layer 2 (Fig. 3f,g). Such a hypothesis was supported by the presence of the third overtone band of CC bending at 4060 cm^{-1} , a

combination band of CH₂ antisymmetric stretching and CH₂ bending at 4164 cm⁻¹ and an intense combination band of CH₂ symmetric stretching and CH₂ bending at 4345 cm⁻¹.

The results obtained are in accordance with those obtained with macro ATR FAR infrared spectroscopy and GC/MS previously reported [51]. Moreover, signal related to the presence of calcite (band at 4273 cm⁻¹, second overtone stretching CO) and probably arising from the paint matrix was detectable. Gypsum (5155 cm⁻¹, combination band of OH antisymmetric stretching and OH bending) was also identified in the same layer. Its presence is probably ascribable to deposition of materials on the external surface. In addition, the interpretation of NIR spectral outcomes suggested the presence in layer 1 of oil as binding medium, probably mixed with calcite, thanks to the well-defined bands at 4264 cm⁻¹ and 4342 cm⁻¹ due to the combination band of CH₂ stretching and bending.

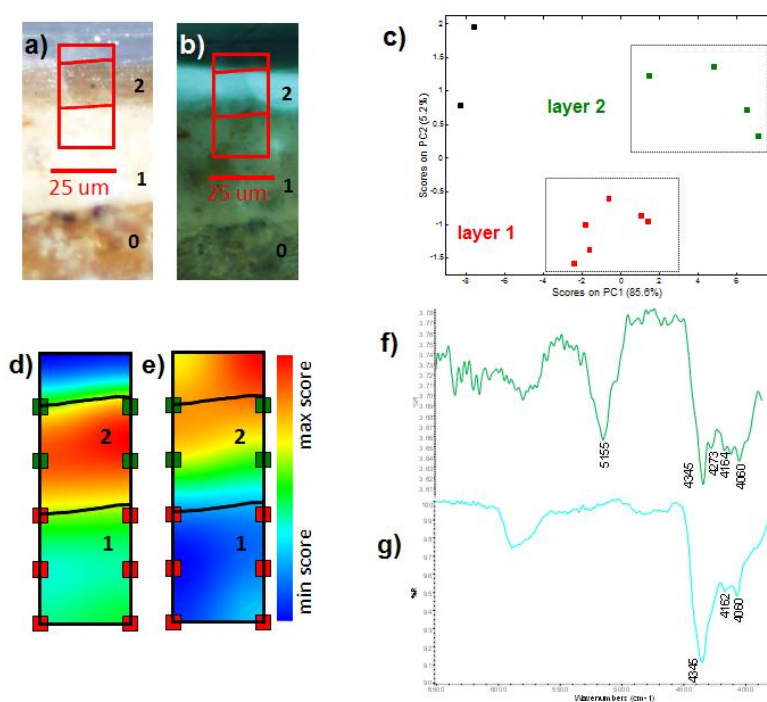


Fig. 3: Sample BP3 - cross-section microphotographs: a) image under visible light; b) image under UV illumination: the red box indicates the area selected for μ FT-NIR analysis; c) PC1/PC2 score plot: clusters highlighted in green and red indicate the objects localised within the PC1 score map: layer 1 d and layer 2 e; f) average spectral profile extracted from layer 2 and g) dammar standard reference.

As reported above, a number of mathematical pre-treatments were tested to evaluate the most suitable for data recorded in the MIR region. The MIR score maps of PC1 and PC2 (Fig. 4a,b), obtained by application of the SNV transform coupled with a linear detrending, also in this case allowed to differentiate the two layers constituting the cross-section, probably thanks to the fact that the layers presented significant differences in composition. Nevertheless, the examination of the MIR average profile of the spectra extracted from layer 2 resulted rather difficult, due to derivative-like and reststrahlen bands generated by the highly reflective surface. Indeed, the C=O stretching band (1710 cm⁻¹), ascribable to hydrogen-bonded

carboxylic acids, suggested the presence of a natural resin, without any more specific information on the terpenoid categories.

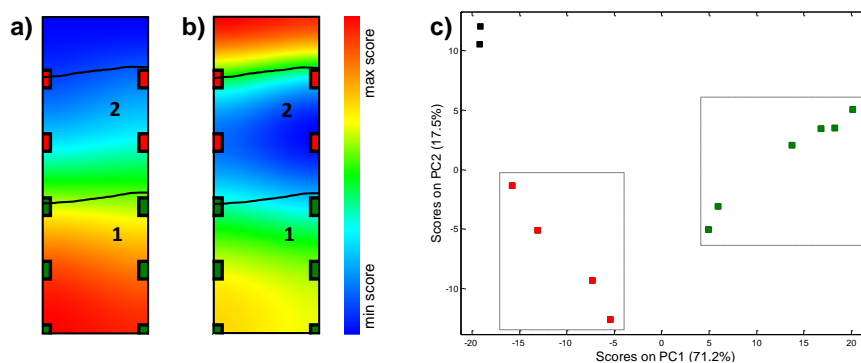


Fig. 4: Sample BP3 - a) PC1 MIR score map; b) PC2 MIR score map; c) PC1/PC2 score plot clusters highlighted in green and red indicate layers 1 and 2, respectively

2.2.3.2 Sample Rond25

The study on this historical sample was part of a project aimed at characterising painting materials, to support attribution researches and the on-going restoration intervention. Micro-FT-NIR/MIR analysis was carried out on a portion of the paint stratigraphy, containing three different layers (white boxes in Fig. 5a and b). Over a yellow layer (layer 0) a translucent brownish layer is superimposed (layer 1) and better recognisable under UV illumination thanks to its bright bluish fluorescence. A pigment layer is also observed (layer 2), characterised by the presence of small blue crystals dispersed within a white and homogeneous matrix.

Also for this sample, PCA combined with a number of common mathematical pretreatments, was performed on both MIR and NIR data and the results were compared. In the case of the NIR region, the outcomes showed that specific pre-treatments are functional to exploit the extraction of useful information from spectral data. In particular, the SNV transform coupled with a first derivative was chosen as the most effective strategy to remove slope variations and to correct for baseline shifts and global intensity effects.

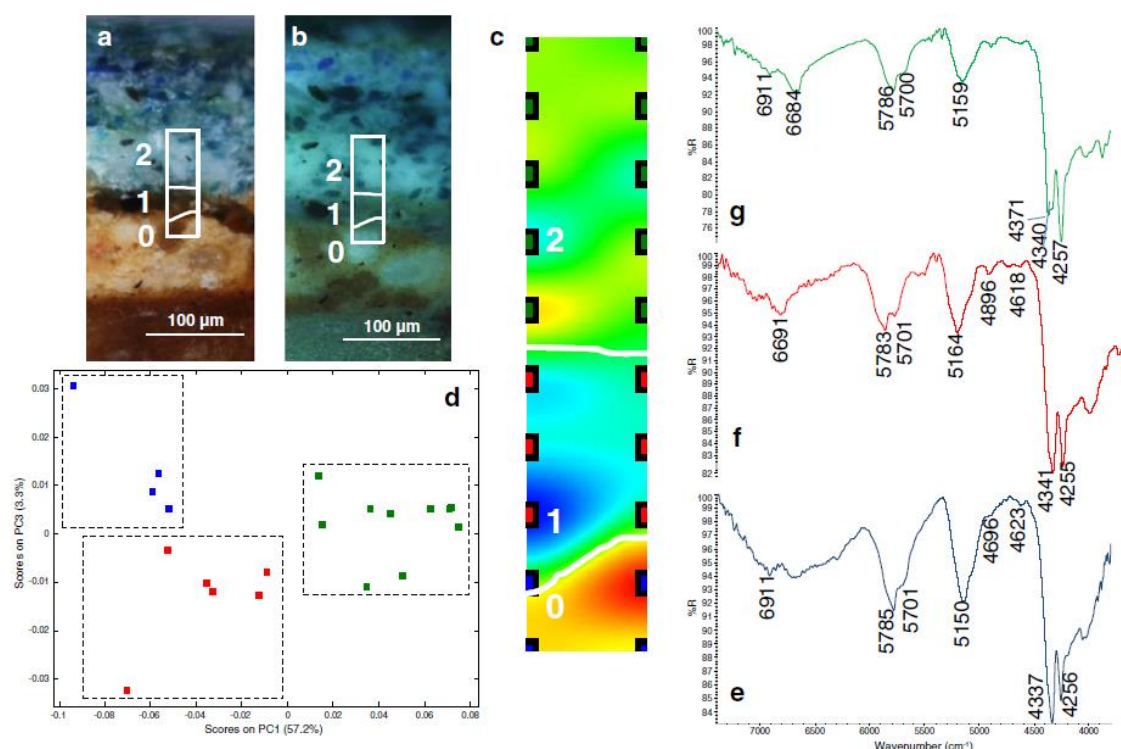


Fig. 5: Sample Rond25: a) cross-section microphotographs under visible light; b) cross-section microphotographs under UV illumination. The white boxes indicate the area selected for FTIR mapping analysis; c) score map of PC3; d) PC13 score plot: clusters in blue, red and green correspond to the points localised within the PC3 score map: layer 0, layer1 and layer 2, respectively; e) average spectral profiles extracted from layer 0; f) average spectral profiles extracted from layer 1; and g) average spectral profiles extracted from layer 2.

Interestingly, it was possible to observe that the score map of PC3 (Fig. 5c) allowed a clear identification of all the three layers present in the sample. Therefore, the PC1-3 score scatter plot (Fig. 5d) was considered and brushing was used to understand the correspondences between clusters of scores (detectable in the scatter plots) and the corresponding areas within PC3 score map. In particular, the score plot showed a group of points, related to high score values along the PC3, which corresponds to layer 0. The average spectral profile of such cluster was extracted and examined in attempt to identify all the constituents of the layer (Fig. 1e). Lead white ($2\text{PbCO}_3 \cdot \text{Pb}(\text{OH})_2$) was revealed thanks to the broad band at 6911 cm^{-1} (1st overtone of OH stretching). Furthermore, it was possible to identify peculiar spectral features ascribable to a lipidic substance (such as siccativ oil) used as binding medium (bands at 5701 and 5785 cm^{-1} corresponding to the 1st overtone of CH_2 symmetric and antisymmetric stretching, respectively; bands at 4339 and 4256 cm^{-1} corresponding to the combination of methylenic CH stretching and bending and band at 4056 cm^{-1} corresponding to the 3rd overtone of CC bending). Very weak bands ascribable to the proteinaceous fraction were observed at 4896 and 4623 cm^{-1} assigned to stretching and bending of NH and to the 1st overtone of carbonyl stretching and of amide II, respectively [43, 44]. In spite of the very low intensity of such spectral features, it is not possible to exclude the contemporary presence of proteins in the same layer, even if in a limited amount. Interestingly, the presence of proteinaceous components was clearly identified in layer 1, well described in the PC3 score map. Indeed, through the examination of the spectral profile (Fig. 5f) extracted from the

correspondent cluster of scores in the PC1-3 plot, it was possible to localise the presence of the characteristic combination band of the 1st overtone of carbonyl stretching and of amide II at 4618 cm⁻¹, and the vibrational feature assigned to stretching and bending modes of NH at 4896 cm⁻¹. In addition, a lipidic component was also identified thanks to the presence of the above mentioned bands at 4341, 4255 cm⁻¹, 5701 and 5783 cm⁻¹. This finding has been confirmed by analyses performed in FTIR microscopy in ATR mode.

Concerning the characterisation of the proteinaceous substance identified in both layers, it is worth highlighting that, even if all the different types of proteins commonly used in ancient paintings are characterised by similar spectral features in the NIR region, the possibility to distinguish between animal glue and egg tempera – thanks to the shift of NH combination bands to higher wavelengths – has been reported when using a macro-NIR imaging system [44]. Indeed, the spectrum extracted from layer 1 was compared with reference spectra obtained from standard substances (Fig. 6). By visual comparison, it was possible to notice a match with the NH band of animal glue (at around 4896 cm⁻¹) – while the marker bands of egg proteins are shifted to about 4863 cm⁻¹, according to the literature. This outcome would suggest the presence of a mixture of lipids and proteinaceous materials, such as animal glue. However, it is worth remarking that the broad shape of the above mentioned band – detected in a complex and real paint stratigraphy – hampers a definitive identification of the specific protein.

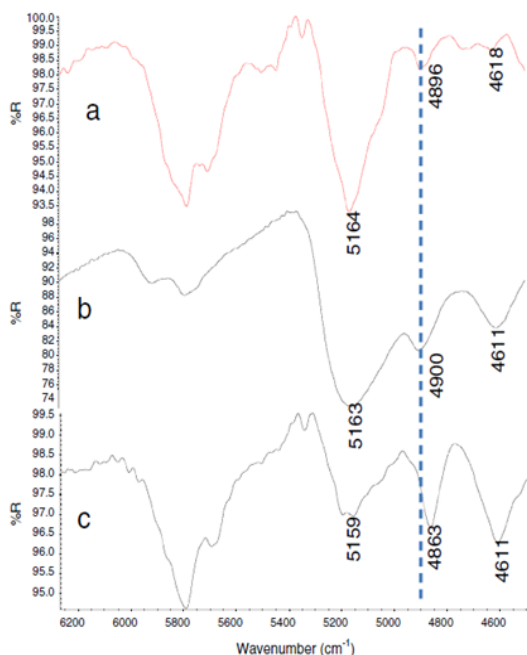


Fig. 6: Comparison among NIR spectra of: a) spectrum extracted from layer 1 of sample Rond25; b) reference spectrum animal glue; and c) reference standard of whole egg tempera.

Finally, in the PC1-3 score scatter plot, a third group of points, was recognised. This cluster described layer 2 in the PC3 score map, corresponding to the blue pigment layer (Fig. 5g). The average spectral profile corresponding to layer 2 allowed us to recognise the presence of azurite ($2\text{CuCO}_3 \cdot \text{Cu}(\text{OH})_2$), thanks to the bands at 4253 cm⁻¹ (3rd overtone of CO₃), and at 4371 cm⁻¹ (combination bands of OH symmetric and asymmetric stretching). Moreover, band at 6684 cm⁻¹ was ascribed to 2nd overtone of OH stretching, confirming the identification of the blue pigment. Despite the fact that hydroxyl and carbonate vibrational modes, partially overlapped with signals of organic materials, spectral features of lipidic substances were recognizable thanks to bands at 4340 cm⁻¹ and at 5700 and 5781 cm⁻¹. In addition, lead white was also localised in the same layer (band at 6911 cm⁻¹).

In all of the spectra extracted from paint layers, it was possible to observe a band in the region between 5150 and 5164 cm⁻¹ ascribable to OH combination stretching and bending. However, such

spectral features can neither be univocally attributed to a given component nor used as diagnostic band, due to their low selectivity.

Multivariate analyses were performed also on spectra recorded in the MIR range. Although different types of mathematical pre-treatments were considered and tested, no satisfactory differentiation among paint layers was obtained (Fig. 7a,b,c) in the PC plots.

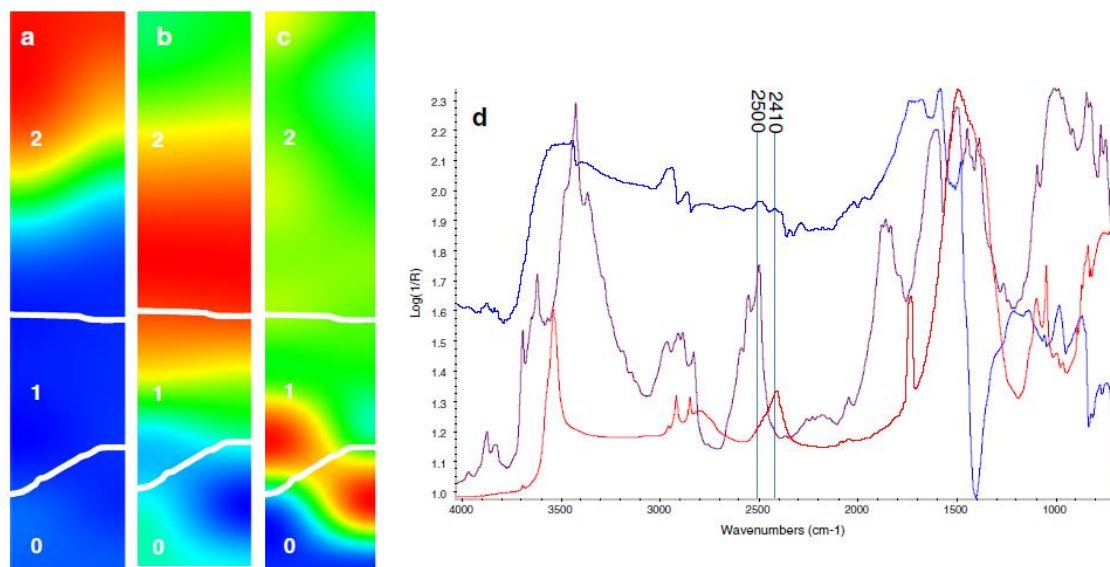


Fig. 7: Sample Rond25 — PC scoremaps obtained in the MIR range. SNV transform coupled with a first derivative was applied as mathematical pre-treatment: a) PC1 map; b) PC2 map; c) PC3 map; and d) MIR spectra. Blue profile: spectrum extracted from the blue layer 2, red profile: standard reference of lead white, violet profile: standard reference of azurite.

This result may be mainly caused by distortion of spectra and overlapping of bands. Consequently, interpretation of the spectra corresponding to the different layers of the mapped sample was complicated by the presence of derivative like and reststrahlen bands. In particular, the identification of the organic binder was uncertain and just few evidences of the presence of a lipidic material in layer 0 and of a proteinaceous material in layer 1 were found. Moreover, in layer 2 the presence of lead white masked the presence of the lipidic binder (confirmed by NIR spectra). In fact, no diagnostic signal related to the carbonyl antisymmetric stretching band of oil was observed. In addition, it is worth remarking that lead white may present a combination band of symmetric stretching and in-plan bending of CO_3^{2-} at 1733 cm^{-1} for hydrocerussite, overlapped with the carbonyl stretching of oil [12]. NIR signals suggested the simultaneous presence of lead white and azurite in layer 2 which were both identified in the MIR range thanks to the presence of weak bands at 2500 and 2410 cm^{-1} (Fig. 7d) corresponding to combination band of symmetric and antisymmetric stretching of CO_3^{2-} and/or combination of in-plan and out-of plan bending of CO_3^{2-} for azurite and cerussite, respectively. Concerning lead white, broad signals at 6911 and 2410 cm^{-1} were characterised by a very low intensity. Indeed, their simultaneous presence was extremely useful for the characterisation. MIR spectra allowed to identify the presence of calcite in layer 0, whose NIR signal at around 4260 cm^{-1} (3rd overtone of CO stretching) [43] was probably hindered by absorption related to the lipidic binder.

2.2.3.3 Sample Civ6

The cross-section of sample Civ6, shown in Fig. 8, was studied in an attempt to achieve information related to the gilding technique employed by the artist, addressing attribution purposes. Indeed, the investigation on the sample was aimed at characterising all the stratigraphic components and, in particular, the organic layer responsible for the intense fluorescence detected under UV illumination (Fig. 8b).

The hyperspectral map was acquired on a portion of the paint stratigraphy containing three different layers (white boxes in Fig. 8a and b). In more detail, over a whitish ground layer (layer 0) it is possible to identify the presence of an irregular blue paint layer (layer 1), which is covered by a thick brown layer (layer 2), characterised by the peculiar fluorescence emission mentioned above. This thick layer is probably applied as a mordant for the application of a gold leaf, which is no longer present in the fragment.

The hyperspectral data matrix of sample Civ6 was submitted to different mathematical pre-treatments. In the case of the MIR spectral region, no mathematical correction was helpful to provide a thorough characterisation of the entire cross-section by PCA. Conversely, for the NIR range, a first derivative coupled with SNV transform, provided a satisfactory resolution of all the layers of the sample by PCA. In more detail, PC2 score map allowed the complete differentiation of all the layers (Fig. 8c).

The average spectral profile extracted from points selected from the PC1-2 score scatter plot (Fig. 8d) and related to layer 0, allowed the characterisation of the ground thanks to the absorption band at 4257 cm^{-1} (Fig. 8e), which can be ascribed, according to the literature [57, 58], to the presence of calcite (3rd overtone of CO stretching). It is worth remarking that several studies have been reported concerning the spectral characterisation of calcium carbonates and their discrimination in the NIR region. In fact, calcium carbonate minerals present a diagnostic band which can vary between 4291 and 4255 cm^{-1} , depending on purity level and mineral composition [43,57-60]. In the case of sample Civ6, even if the identification can be ambiguous due to signals arising from the upper layer containing azurite (which have similar absorptions in this region) spectral signals in the MIR region related to reststrahlen bands at 1408 and 872 cm^{-1} (stretching and bending of CO, respectively) confirmed the attribution. Moreover, calcium carbonate was probably mixed with silicates (5209 cm^{-1} , combination band of OH antisymmetric stretching and OH bending) [35]. Chemometric analysis permitted to obtain a complete characterisation discrimination of layer 1 (Fig. 8c), showing the presence of azurite as blue pigment. Indeed, the bands at 4368 cm^{-1} supported the identification of such pigment (Fig. 8f). Unluckily, the weak band at higher wavenumbers (6684 cm^{-1}) was not detectable, probably due to the low signal-to-noise ratio affecting such portion of the spectral range in the map. Also in this layer the presence of silicates (band at 5206 cm^{-1}) was detected. In addition, the shoulder band at 4340 cm^{-1} suggested the presence of lipidic materials (probably oil). The detection of the organic component, probably used as binding medium, allowed us to postulate the use of the secco painting technique for the mural decoration.

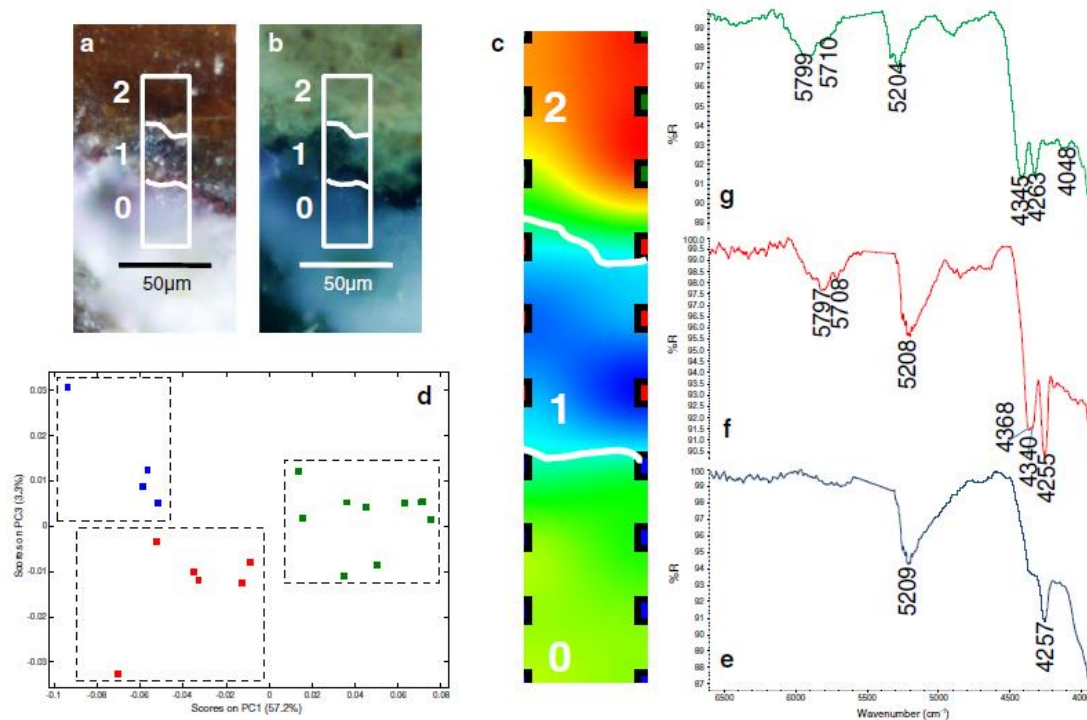


Fig. 8: Sample Civ6: a) cross-section microphotographs under visible light; and b) cross-section microphotographs under UV illumination. The white boxes indicate the area selected for FTIR mapping analysis; c) score map of PC2; d) PC12 score plot: clusters in blue, red and green correspond to the points localised within the PC2 score map: layer 0, layer 1 and layer 2, respectively; e) average spectral profiles extracted from layer 0; f) average spectral profiles extracted from layer 1; g) average spectral profiles extracted from layer 2.

Interpretation of MIR bands provided complementary information for chemical characterisation. In fact, the spectra suggested the contemporary presence of calcite (reststrahlen band at 872 cm^{-1}) and azurite (reststrahlen band at 1497 cm^{-1}), while no information was obtained on the organic binder. Conversely, for the organic binder in layer 2, the NIR spectrum proved to be more informative thanks to the presence of combination and overtone bands, which were not distorted by the specular reflection. Within the PC1-2 score plot, it was possible to identify the presence of a well clustered group of scores, characterised by high values along PC2 and corresponding to layer 2. The examination of the average spectrum of points of this layer (Fig. 8g) suggested the presence of a lipidic material, such as shellac or a siccative oil, which show similar spectral features in the NIR region [35]. Indeed, it is known that oil and/or terpenic resins could be employed as mordent. In particular, the use of shellac has been mentioned as alternative mordent for particularly porous surfaces, instead of linseed oil [61] and its occurrence was dated back to the 15th century, when the resin was introduced into Europe [62]. To tentatively identify the organic material present in this layer, different resins and linseed oil were analysed.

2.2.3.4 Standard resins

Different resin specimens were analysed in the NIR/MIR region in total reflection mode, in attempt to assess the suitability of this technique for the discrimination among different

terpenoid categories and to build a database for the identification of varnish composition in real case studies.

However, similarly to previous researches on ATR data [36], MIR spectra showed extremely similar profiles and it was therefore difficult to identify not only the individual resins but also more generic terpenoid categories: (a) sesquiterpenic resins (i.e. shellac), (b) diterpenic resins containing abietane compounds (i.e. colophony), (c) diterpenic resins containing polymerised communic acid (i.e. copal, sandarac), (d) triterpenic resins (i.e. mastic and dammar).

Conversely, FT-NIR analyses (Fig.9) revealed the presence of characterising bands for each category investigated, as shown in Table 1.

Table 1: Natural resin signals in the NIR region obtained in total reflection mode

| Colophony | Copal | Sandarac | Mastic, Dammar | Shellac | Band assignment ²⁹ |
|-----------|-------|----------|-------------------|---------|--|
| | 6,120 | 6120 | | | |
| 6,108 | | | | | 3rd overtone $\delta(\text{CC})$ |
| | 5,889 | 5,892 | | | $\nu(\text{CH}_2)+\delta(\text{CH}_2)$ |
| | | | 5,873 | | 1st overtone $\nu_a(\text{CH}_2)$ |
| 5,842 | | | | | 1st overtone $\nu_a(\text{CH}_2)$ |
| | 5,803 | 5,820 | | | 1st overtone $\nu_a(\text{CH}_2)$ |
| | | | | 5,780 | 1st overtone $\nu_a(\text{CH}_2)$ |
| | | | 5,726 | | 1st overtone $\nu_s(\text{CH}_2)$ |
| 5,707 | 5,700 | | | 5,708 | 1st overtone $\nu_s(\text{CH}_2)$ |
| | 5,201 | | 5,193 | 5,200 | $\nu(\text{OH})+\delta(\text{OH})$ |
| | | | | 4,870 | |
| | | | | 4,805 | $\nu(\text{CO})+\nu(\text{OH})$ |
| | 4,728 | 4,725 | | | $\nu(\text{CO})+ \nu(\text{OH})$ |
| | | | | 4,670 | $\nu(\text{CO})+\nu(\text{CH}_2)$ |
| | 4,612 | 4,616 | | | $\nu(\text{CO})+\nu(\text{CH}_2)$ |
| 4,348 | 4,348 | 4,348 | 4,345 | 4,342 | $\nu(\text{CH}_2)+\delta(\text{CH}_2)$ |
| | 4,292 | 4,292 | | | |

| | | | | | |
|-------|-------|-------|-------|-------|---|
| | | | | 4,261 | vs (CH ₂)+δ(CH ₂) |
| 4,238 | 4,250 | 4,250 | | | |
| | | | | 4,200 | |
| 4,147 | | | 4,162 | | va(CH ₂)+δ(CH ₂) |
| 4,060 | 4,062 | 4,062 | 4,060 | 4,050 | 3rd overtone δ(CC) |

Shellac showed very distinctive NIR spectra (Fig. 9c) allowing a clear differentiation of this resin from all the other types, thanks to the presence of the bands at 4261 (CH₂ bending and stretching combination band) and 4204 cm⁻¹. However, similar features were present also in siccative oil spectra (Fig. 9d).

Diterpenic resins (Fig. 9f,g) showed peculiar shoulder bands at 4,238 cm⁻¹ (present in the colophony spectrum) and bands at 4,250 and 4,292 cm⁻¹ (present in both the copal and the sandarac spectra) which allowed to distinguish such compounds from diterpenic resins with or without the polymerised communic acid. Moreover, some additional marker bands are identifiable in copal and sandarac spectra, namely the band at 4,612 cm⁻¹ (symmetric CO and CH₂ stretching combination band) and 4,728 cm⁻¹ (combination band of stretching of CO and OH). Indeed, all these bands allowed us to distinguish the two different classes of diterpenic resin, and these from all the other resin specimens analysed.

Some peculiar spectral features were presented also by triterpenic resins (Fig. 9a,b). In particular, band at 4162 cm⁻¹ (combination band of CH₂ antisymmetric stretching and bending) and at 5868 and 5891 cm⁻¹ (1st overtone of CH₂ symmetric and antisymmetric stretching) for dammar and mastic, respectively were revealed.

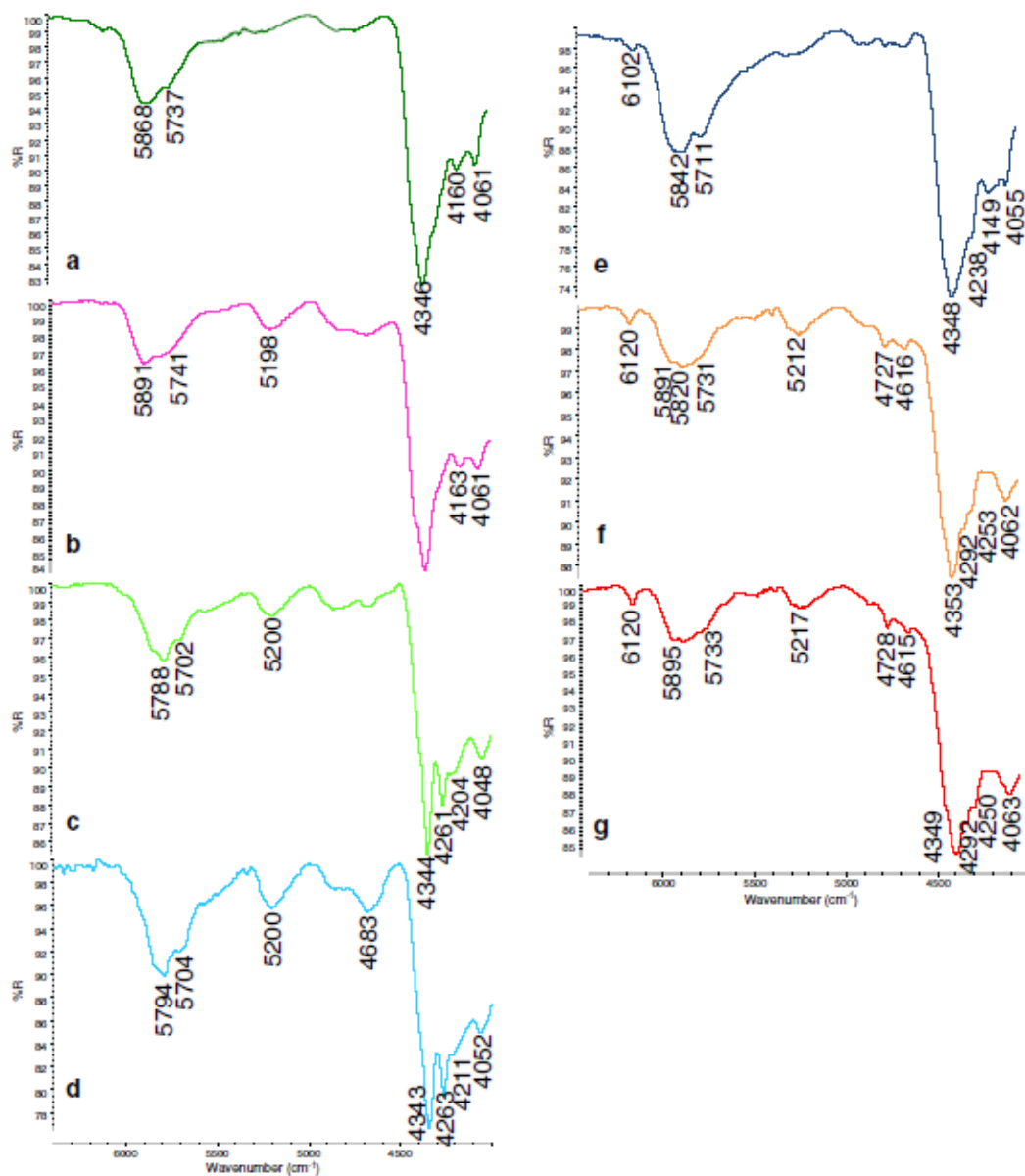


Fig. 9: NIR spectra of standard resins: a) dammar; b) mastic; c) shellac; d) oil; e) colophony; f) sandarac; and g) copal.

Multivariate analysis was performed in order to evaluate the importance of these differences in the discrimination of resins, and the possibility to distinguish shellac and linseed oil. In more detail, PCA was performed on nine replicas for each resin specimen, on both MIR and NIR data and the results were compared. Also in this case, several mathematical pre-treatments for the reduction of unwanted spectral variations were applied, evaluating the effectiveness in the extraction of useful information.

For processing the resin spectral data in the NIR region (6400–5500, 5300–4000 cm^{-1}), a second derivative (Savitzky-Golay method), using first third-order polynomials and 11 datapoint gaps, coupled with SNV transform was finally chosen.

The PC12 score scatter plot obtained from NIR spectra (Fig. 10a) was able to identify 5 cluster of scores related to: diterpenic resins, diterpenic resins with a polymerised components and triterpenic resin (mastic and dammar, which seem to be differentiated within the score space). However, it was not possible to clearly distinguish shellac from linseed oil. As expected, the average spectral profile, of points of layer 2 of the Civ6 NIR map, was positioned within the score scatter plot, close to the shellac-linseed oil dispersion area, along PC1.

Subsequently, the focus was put on the separation between shellac and linseed oil, which were therefore analysed separately. PCA performed on spectra of these two classes – treated in the same way as in the previous case – showed a clear differentiation, on PC1 (Fig. 10b), between shellac (at positive score values) and siccative oil (at negative score values). An average spectrum from layer 2 of sample Civ6, after analogous pre-treatment, was projected onto PC1: its score clearly falls in the shellac region, suggesting the presence of such terpenic resin in the real sample, even if the simultaneous presence of oil cannot be excluded.

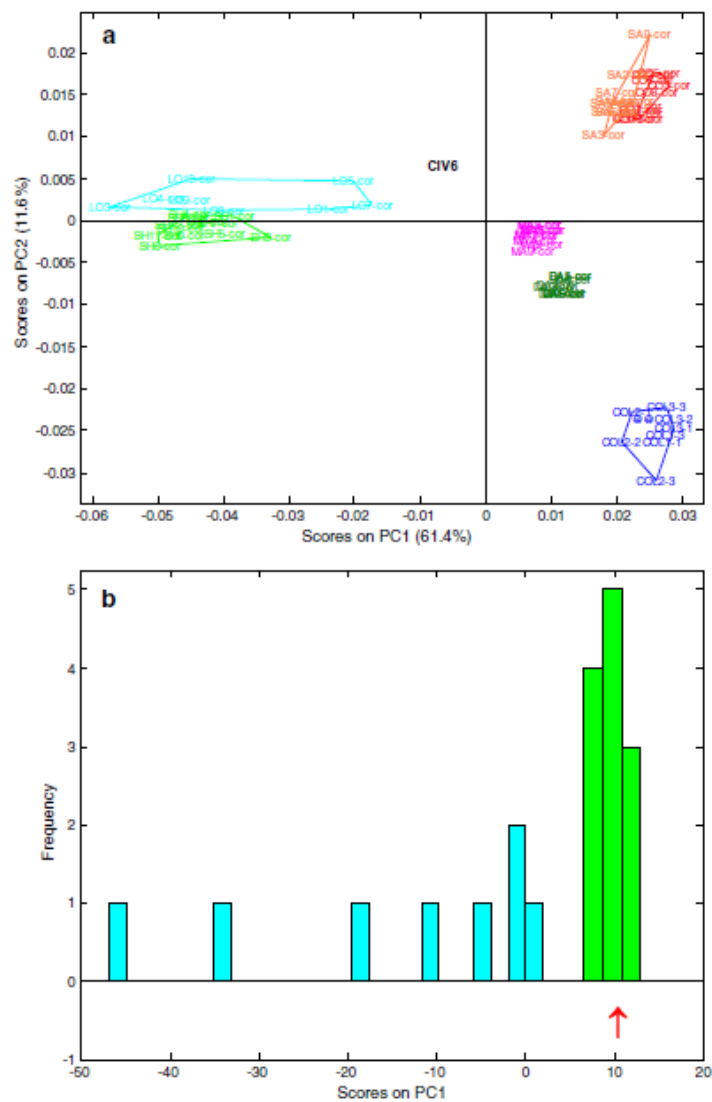


Fig. 10: a) PC12 score plot of standard resins; b) histogram of score values of shellac and linseed oil along PC1. The score projection of the average spectral profile extracted from layer 2 of Civ6 is indicated with the black arrow.

The interpretation of the spectra may be supported by the integration of the two spectral regions investigated. Indeed, considering the MIR region, it was possible to suppose the presence of a resinous material thanks to the presence of a derivative like band corresponding to the C-O stretching at 1710 cm^{-1} . However, by examination of this region, it was not possible to selectively identify any particular natural resin.

To confirm the identification of the sesquiterpenic resin, macro-ATR analysis in the FIR range has been performed on the external surface of the sample [63]. The spectrum acquired revealed several analogies in the position and shape of the bands at 524 cm^{-1} and 216 cm^{-1} , compared with those of standard shellac spectral profile (Fig. 11). Probably, signals arising from the blue layer were also detectable: azurite could be revealed thanks to the bands at 453 cm^{-1} and 395 cm^{-1} . Moreover, the broad band at about 285 cm^{-1} could be indicative for the presence of calcium carbonate [63].

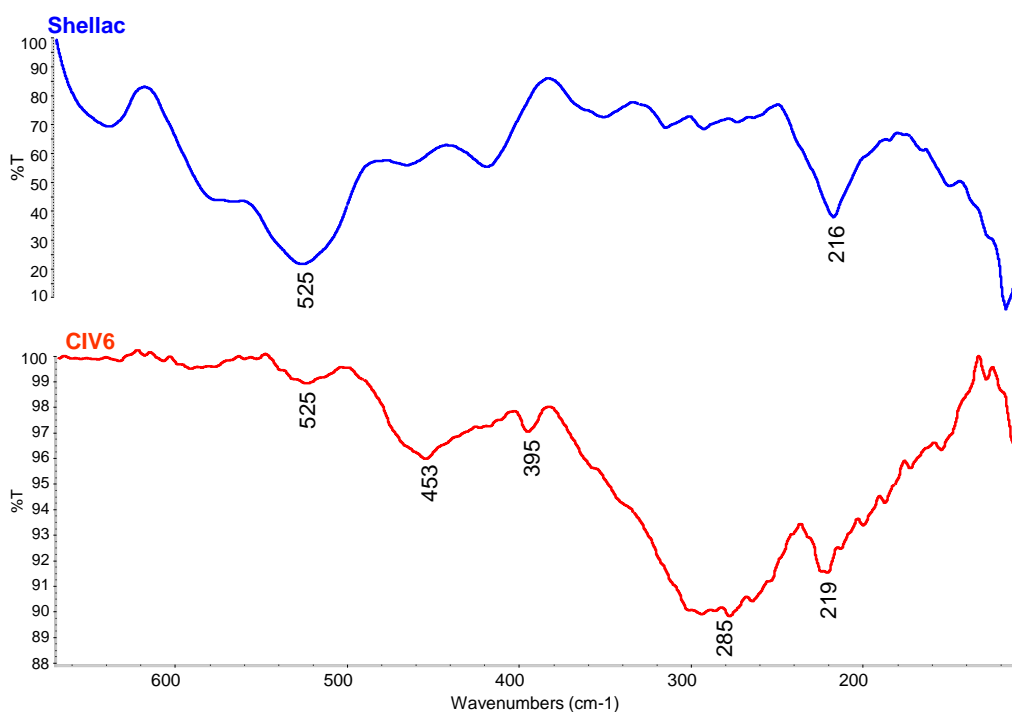


Fig. 11: Comparison between spectra obtained by FIR spectroscopy in macro-ATR mode of: a) standard shellac specimen (blue profile) and b) mordant layers 3 of sample CIV6 (red profile).

2.3 Conclusions

The present study presents a suitable application of FTIR microscopy in the NIR range, using the total reflection mode, able to provide useful information for the characterisation of both organic and inorganic substances within complex paint stratigraphies.

Such a type of micro-spectroscopy has been underemployed so far and its potentialities have not been systematically investigated in previous researches in the field of cultural heritage. The outcomes of multivariate exploratory analysis showed that the NIR region was more effective than the MIR one in describing paint stratigraphies, providing information for the identification of binding media and supporting the characterisation of proteinaceous components at a microscopic level. In fact, MIR data, which were investigated to support the interpretation of NIR spectra and in attempt to define an integrated protocol, resulted to be more affected by distortion of spectra and overlapping of bands.

Moreover, NIR spectra allowed to efficiently distinguish different classes of natural resins, such as sesquiterpenic, diterpenic, diterpenic with polymerised communic acid and triterpenic resins. Such an evidence helped in the chemical characterisation of a mordent layer observed in a real paint stratigraphy, showing that NIR spectroscopy may be extremely useful in an integrated protocol for the recognition of different terpenoid materials within paint layers.

In conclusion, FT-NIR microscopy can be definitely considered as a valuable complementary tool for the characterisation of complex paint stratigraphies. Moreover, it is worth remarking that the exploitation of the enlarged spectral range (NIR-MIR) matched with PCA represents an efficient exploratory procedure for studies on micro-paint samples.

2.4 References

- [1] A. R. H. Cole, R. N. Jones, *JOSA*, 1952, 42, 5, 348-352
- [2] R. J. Gettens, *Science in the art museum*, *Scientific American*, 1952, 187,1, 22-27
- [3] M. R. Derrick, D.C. Stulik, *Infrared spectroscopy in conservation science*, The Getty Conservation Institute: Los Angeles (1999)
- [4] F. Casadio, L. Toniolo, *J. Cult. Heritag*, 2001, 2, 1, 71-78
- [5] M. J. D. Low, N. S. Baer, *Studies in Conservation*, 1977, 22, 116-128
- [6] R. G. Messerschmidt, M. A. Harthcock, *Infrared microspectroscopy. Theory and applications*. Marcel Dekker: New York (1988)
- [7] S. Prati, E. Josph, G. Sciutto, R. Mazzeo, *Accounts of chemical research*, 2010, 43, 6, 792-801
- [8] R. D. Gillard, S. M. Hardman, *Studies in conservation*, 1994, 39, 3, 187-192
- [9] S. Bruni, F. Cariati, *Vibrational Spectroscopy*, 1999, 20, 15-25
- [10] M. Cotte, J. Susini, *Journal of Analytical Atomic Spectrometry*, 2008, 23, 820 – 828

- [11] P. Griffiths, J. A. De Haseth, *Fourier Transform Infrared Spectrometry* 2nd edn. John Wiley & Sons Inc, New Jersey (200)
- [12] F. Rosi, C. Miliani, A. Federici, B. G. Brunetti, A. Sgamellotti, S. Clementi, *Anal. Bioanal. Chem.*, 2010, 399, 9, 3133-3145
- [13] A. van Loon, K. Keune, J.J. Boon, in: *Art'05 – 8th International Conference On The Non Destructive Investigations And Microanalysis For The Diagnostic And Conservation Of The Cultural And Environmental Heritage*, Lecce (2005)
- [14] A. Lins, L. A. Giannuzzi, F. A. Stevie, B. Price, M. Tucker, N. Gutman, *MRS Proc*, 2005, 712, 113-118.
- [15] J. J. Boon, S. Asahina *Microsc and Microanal*, 2006, 12, 1322-1323
- [16] V. Mazel, P. Richardin, D. Debois, D.Touboul, M. Cotte, A. Brunelle, P. Walter, O. Laprèvote, *Anal Chem*, 2007, 79, 9253-9260
- [17] M. Cotte, E. Checroun, V. Mazel, V. A. Solé, P. Richardin, Y. Taniguchi, P. Walter, J. Susini, *e-PS* 2009, 6, 1-9
- [18] S. Bruni, F. Cariati, F. Casadio, L. Toniolo, *Vib Spectrosc*, 1999, 20, 15-25
- [19] J. van der Weerd, H. Brammer, J. J. Boon, R. M. A. Heeren, *Appl Spectrosc*, 2002, 56, 276-283
- [20] H. Dannenberg, J. W. Forbes, *Infrared Spectroscopy of Surface Coatings in Reflected Light*, *Anal. Chem.*, 1960, 32, 3, 365-370
- [21] J. A. Reffner, P. A. Martoglio, *Uniting Microscopy and Spectroscopy*, in *Practical Guide to Infrared Microspectroscopy*, Marcel Dekker: New York, 1995, 41-84
- [22] L. Lewis, A. J. Sommer, *Applied Spectr.*, 1999, 53, 375-380.
- [23] E. N. Lewis, P. J. Treado, R. C. Reeder, G. M. Story, A. E. Dowrey, C. Marco, I. W. Levin, *Anal. Chem.*, 1995, 67, 3377-3381
- [24] K. L. A. Chan, S. G. Kazarian, *Appl. Spectrosc.* 2003, 57, 381-389
- [25] E. Joseph, S. Prati, G. Sciutto, M. Ioele, P. Santopadre, R. Mazzeo, *Anal Bioanal Chem*, 2010, 396, 899-910
- [26] M. Howard, *Fundamentals of Near-Infrared Spectroscopy*, Marcel Dekker, Inc (2001)
- [27] C. Pasquini, *J. Braz. Chem. Soc.*, 2003, 14, 2, 198-219
- [28] M. Blanco, J. Coello, H. Iturriaga, S. Maspoch, C. de la Pezuela, *Analyst*, 1998, 123, 135R–150R
- [29] M. Cruz Sarraguça, J. Almeida Lopez, *Vibrational Spectroscopy* 2009, 49, 204–210
- [30] L. M. Reid, C. P. O'Donnell, G. Downey, *Trends Food Sci Technol*, 2006, 17, 344–353

- [31] R. Karoui, J. de Baerdemaeker, *Food Chem*, 2007, 102, 621–640
- [32] G. Lachenal, *Vibrational Spectroscopy*, 1995, 9, 93–100
- [33] F. Rosi, A. Daveri, B. Doherty, S. Nazzareni, B. G. Brunetti, A. Sgamellotti, C. Miliani, *Appl. Spectr.*, 2010, 64, 956-963
- [34] M. Bacci, D. Magrini, M. Picollo, M. Vervat, *Journal of Cultural Heritage*, 2009, 10, 275–280
- [35] M. Vagnini, C. Miliani, L. Cartechini, P. Rocchi, B. G. Brunetti, A. Sgamellotti, *Anal Bioanal Chem*, 2009, 395, 2107–2118
- [36] F. Rosi, I. Borgia, P. Benedetti, B. G. Brunetti, A. Sgamellotti, *App Spectr*, 2007, 61, 293-299
- [37] E. H. Van't Hul-Ehrnreich, *Stud Conserv* 1970, 15, 175–182
- [38] M. T. Baker, D. W. Von Endt, *Mater Issues Art Archaeol*, 1988, 123, 71–76
- [39] R. D. Gillard, S. M. Hardman, R. G. Thomas, D. E. Watkinson, *Stud Conserv*, 1994, 39, 187–192
- [40] J. Pilc, R. White, *Natl Gallery Tech Bull*, 1995, 16, 73–84
- [41] A. Langley, A. Burnstock, *Proceedings of the 12th Triennial Meeting of ICOM Committee for Conservation*. James & James, London (1999)
- [42] S. Prati, F. Rosi, G. Sciutto, R. Mazzeo, D. Magrini, S. Sotiropoulou, M. Van Bos, *Microchemical Journal*, 2012, 103, 79-89
- [43] C. Miliani, F. Rosi, A. Daveri, B. G. Brunetti, *Appl Phys A* 2012, 106, 295-307
- [44] F. Rosi, A. Daveri, B. Doherty, S. Nazzareni, B.G. Brunetti, A. Sgamellotti, C. Miliani, *Appl. Spectrosc.*, 2010, 64, 956–963
- [45] C. Milani, F. Rosi, A. Burnstock, B.G. Brunetti, A. Sgamellotti, *Appl. Phys. A*, 2007, 89, 849–856
- [46] F. Rosi, A. Daveri, C. Miliani, G. Verri, P. Benedetti, F. Piqué, B.G. Brunetti, A. Sgamellotti, *Anal. Bioanal. Chem.*, 2010, 385, 2097–2106
- [47] T. Trafela, M. Strlic, J. Kolar, D.A. Lichtblau, M. Anders, D. Pucko Mencigar, B. Pihlar, *Anal. Chem.*, 2007, 79, 6319–6323
- [48] A. Nevin, D. Comelli, I. Osticioli, L. Toniolo, G. Valentini, R. Cubeddu, *Anal. Bioanal. Chem.*, 2009, 395, 2139–2149
- [49] K.A. Dooley, S. Lomax, J.G. Zeibel, C. Miliani, P. Ricciardi, A. Hoenigswald, M. Loew, J.K. Delaney, *Analyst*, 2013, 138, 4838-4848
- [50] O. Katsibiri, R.F. Howe, *Microchem. J.*, 2010, 94, 14–23

- [51] S. Prati, G. Sciutto, R. Mazzeo, C. Torri, D. Fabbri, *Anal. Bioanal. Chem.*, 2011, 399, 3081–3091
- [52] T. Poli, O. Chiantore, A. Giovagnoli, A. Piccirillo, *Anal. Bioanal. Chem.*, 2012, 402, 2977–2984
- [53] P. Oliveri, M. C. Casolino, M. Forina, *Chemometric Brains for Artificial Tongues* in: S. Taylor (Ed) *Advances in Food and Nutrition Research*, (2010) , pp. 61 - 2, 57-117
- [54] S. Prati, F. Rosi, G. Sciutto, P. Oliveri, E. Catelli, B. Brunetti, C. Miliani, R. Mazzeo, C. Miliani, *Microchem. J.*, 2013, 110, 314–319
- [55] G. Sciutto, P. Oliveri, S. Prati, M. Quaranta, S. Bersani, R. Mazzeo, *Anal. Chim. Acta.*, 2012, 752, 30–38.
- [56] G. Sciutto, P. Oliveri, S. Prati, M. Quaranta, S. Lantieri, R. Mazzeo, *Anal. Bioanal. Chem.*, 2013, 405, 625–633
- [57] G.R. Hunt, *Geophysics*, 1977, 42, 501–513
- [58] S. Gunasekaran, G. Anbalagan, S. Pandi, *J. Raman Spectrosc.*, 2007, 37, 892–899
- [59] F. van der Meer, *Nonrenew. Resour.*, 1994, 3, 146–164
- [60] S.J. Gaffey, *Am. Mineral.*, 1986, 71, 151–162
- [61] R. Mayer, *The Artist's Handbook of Materials and Techniques*, Faber and Faber, London, 1951.
- [62] M.P. Merrifield, *Medieval and Renaissance Treatises on the Arts of Painting*, Dover Publications, Mineola, New York, 1967
- [63] E.L. Kendix, S. Prati, R. Mazzeo, E. Joseph, G. Sciutto, C. Fagnano, *e-PS*, 2010, 7, 8–13.

Chapter 3

**Discrimination of wool dyed fibers: a
new analytical approach for *in situ*
micro-Raman and SERS spectroscopy**

3.1 Dyeing process and wool dyeing

Dyeing is a textile finishing process of very antique origins [1], that consists in imparting a hue to fibers by means of generally water-soluble coloring organic substances known as dyes, which are able to directly or indirectly interact with the substrate and fix on it in a more or less permanent way.

In ancient times, up to the advent and spread of industrial synthetic dyes, the available molecules for such processes were of natural origin, most of which incapable to fix directly to the substrate [1, 7]. For this reason fibers were mordanted, usually by means of metallic salts able to form complexes with the natural dyes, and act as a 'bridge' between the fiber and the colorant [6].

On the contrary, the vast majority of textile dyes that are nowadays in use possesses what is called a substrate-specificity, that is, the ability to dye a given fiber class without the use of a mordant [6–8]. Such substrate-specificity was discovered early on in the synthetic dyes history, when it was noted that silk fibers were readily dyed by Mauvine (W.H. Perkin, 1856), the first synthetic dye to be ever produced [6]. Through the advances in theoretical and synthetic organic chemistry, it has been made possible the study and investigation of such ability, to a level that eventually allowed the production of the so-called design-dyes, colored molecules intentionally created with the purpose to suit a given substrate, be it a natural or a synthetic fiber, or even a class of food, plastic materials, sensors, and so on [4, 6, 7].

What makes possible for such dyes to directly fix to a substrate is the presence of functional groups able to interact with the constituting chemical units of a textile. In the particular case of wool, as well as for other proteinaceous fibers, its amphoteric character allows the efficient use of both anionic (Acid) and cationic (Basic) dyes, although the former are undoubtedly the most used.

Acid dyes are anionic molecules that are applied in acidic conditions and that usually belong to the monoazo and anthraquinone classes, even though disazo, xanthenes and nitro are also found [6, 9]. The interaction between such molecules and the substrate works by means of their acidic functions, usually one or more sulfonic acid group or less frequently a carboxylic acid, which are mostly encountered as their respective sodium salts [6,9]. Such groups confer to the molecule both water-solubility and a negative charge, the latter being the major driving factor of the dyeing mechanism [4, 6].

As previously stated, this class of dyes is applied to the fibers in acidic conditions, which is to say, in an aqueous dye-bath at low pH values. In such an environment, the protein components of wool acquire a positive charge, principally owed to the protonation of the basic side-chain moieties (amino and imino groups, mainly) and to the neutralization of the carboxylic acid functions [6, 9]. Thanks to the outlined electrostatic change, acid dyes are

attracted from the dye-bath to the fiber by ionic forces (Figure 2.1), and the coloring molecules will migrate and diffuse through the endocuticle towards the rest of the fiber [2, 4, 6, 9, 10].

The extent of such a migration is regulated by both the dimension of the molecule itself and by the other non-ionic forces participating in the process [6, 10]. Indeed, once a dye molecule is inside the fiber, what regulates its inner uptake and circulation, as well as the strength of the bonding are mainly van der Waals' forces due to the aliphatic moieties in the structure. In particular, the more the aliphatic character, the stronger the binding to the substrate [4, 6, 10].

Conversely, the number of sulfonate groups, although representing the amount of possible ionic interactions per dye molecule and the degree of the initial dye uptake [10], also influences the level of hydration, resulting in negatively affecting the quality of the dyeing process by hampering the binding to the fiber [4].

As far as basic dyes are concerned, the way in which they are applied to wool resembles the one just seen for anionic dyes.

Accordingly, their mechanism of fixation to the fiber is propelled by ionic interactions, this time established between the dye cation and the negatively charged moieties within the protein, mainly carboxylate functions (fig. 1).

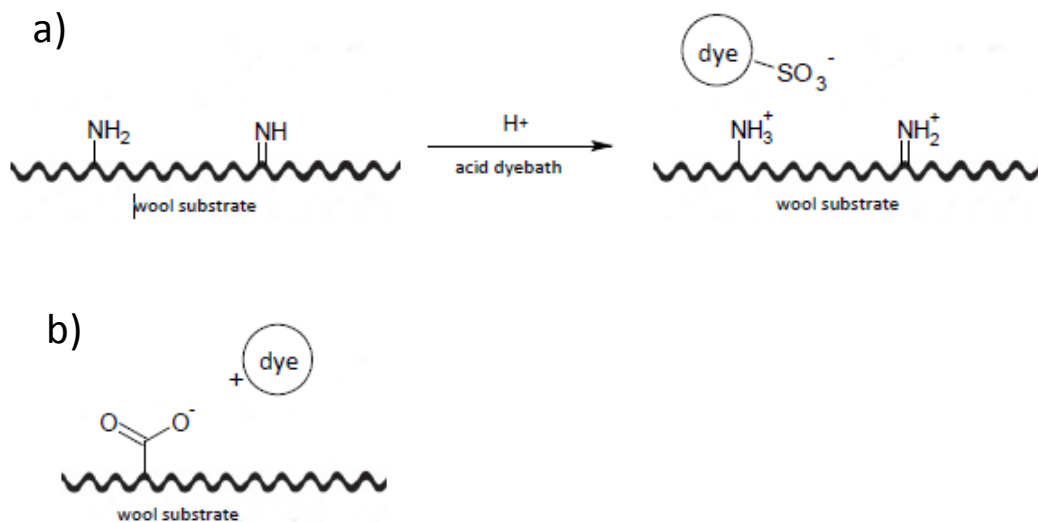


Fig. 12: Wool dyeing with a) acid dyes; and b) basic dyes

3.2 Dyed fibres analysis: an overview

To make a comprehensive analysis of dyes and of dyed fibres, it is often necessary to use several analytical techniques. Indeed, this analytical field is a well-known challenging task, due to dyes inherent high tinting strength and consequently their low concentration in the carrying matrix [1-3], this fact severely limits the number of analytical techniques useful for unambiguous identification [3].

The most common techniques applied for the fibre dyed analysis are micro-spectrophotometry (MSP) which provides a non-destructive and objective measurement of colour, but with little information about the specific dye used [11], and thin layer chromatography (TLC) which provides information about the dyes used, but is semi or completely destructive [12]. Other techniques such as high-performance liquid chromatography (HPLC) and capillary electrophoresis (CE) have been tested for use [13, 14]. Both methods have value for the dye industry in separating dyes but there are a number of practical problems in developing suitable methods for fibre dyed analysis (i.e., variety of dye classes, organic extraction solvent not easily compatible with the CE aqueous buffer) [15].

High performance liquid chromatography (HPLC) is usually the technique of choice also in cultural heritage field, and a comprehensive range of literature can be found on its application to dye analysis, both as standard solutions [16–18] and as mock-ups and real samples from fibre extracts [16–23], with a sample amount in the latter cases ranging from 5 mg to a few millimetres of a single fibre [13,16,17,19]. In order to obtain a viable samples for HPLC, dyed fibres must be pre-treated, a procedure that is generally achieved by treating them with boiling strong inorganic acids such as HCl, and re-dissolving the dye in the mobile phase solvent after removal of the fibre residues and N₂ flux drying of the extract [13,17]. Such treatments are frequently reported to be aggressive with respect to the sample and lead to a significant alteration of its composition [24, 25]. For this reason, protocols including non-destructive investigations such as UV/VIS reflectance or fluorescence measurements directly on the dyed fibre prior to more invasive analyses have been suggested [18,28].

Moreover, when studying works of art, a special consideration is required when choosing methods of analysis: usually, non-invasive analysis are preferred. Hence, it is important to develop and test extractionless in-situ characterization of dyes, pointed at directly analyse the dyed fibres. Characterization of historical dyed fibres with infrared (IR) and reflectance UV/Vis spectroscopy [29], both non-invasive methods, has been also performed. IR spectra are typically dominated by the spectral features of the textile fibre substrate – namely the amide bands from the proteic matrix for wool and silk, or the complex cellulose backbone vibrations in the case of cotton, linen and hemp - often completely obscuring the otherwise sharp absorption bands of the dyes, revealed when analyzed as pure powders. UV/Vis spectra are

broad and undetailed and may suffer from severe interference from the support especially when the latter is aged and has yellowed or deteriorated.

Therefore, dyestuffs must be extracted from the textile support [31], and this is generally performed with the same extracting procedures used for HPLC experiments, with the difference that a greater amount of starting sample must be used because of the higher limit of detection of standard IR spectroscopy with respect to the chromatographic technique. Moreover, strong acid-based extraction procedures frequently lead to the release of components other than the target analyte, such as textile matrix constituents, and the bulk character of the output signal of a standard IR experiment does not allow the dyes to be solely and unambiguously detected, a fact that for separative techniques such as the previously mentioned HPLC can be considered irrelevant.

3.2.1 Raman spectroscopy

Raman spectroscopy is a method based on the Raman effect was discovered in 1928 by Raman who received the Nobel prize for his scientific work in 1930. Over the last 15 years Raman spectroscopy has established as a useful and effective method for the identification of a wide range of materials in art and archaeology [31-35]. Indeed, given its very high spectral resolution, leading to effective discrimination among various species [29] and advantage of allowing non-destructive, *in-situ* detection, it has evolved as an efficient non-destructive technique for the identification of inorganic pigments and other materials in artworks [35].

Micro-Raman spectroscopy (m-RS) has become common practice in many art research laboratories especially for inorganic and, to a lesser extent, synthetic organic pigment identifications. It allows for fast analysis without any sample preparation, and through the use of fibre optics, non-invasive and even *in situ* measurements are possible [36].

Nevertheless, the application of this technique in the characterization of organic dyes has been limited probably due to the interference from fluorescence that often obscures the much weaker Raman signal; only recently a number of spectral databases of synthetic pigments have been published [37-39]. Indeed, the research on early synthetic organic dyes is scarce when compared to the body of literature surrounding synthetic organic pigments and also only few studies – mainly forensic - have been applied to directly characterize the synthetic organic dyes on the textile fibers using Raman spectroscopy [15, 31, 39]. The number of works on natural dyes consistently surpasses the one on synthetic dyes, possibly leading to the misconception of their poor use and diffusion. In fact, thanks to the technological simplifications that such products gave to the textile home and industrial production, their use was rather widespread [40], and a lack of a comprehensive scientific and conservation literature on these molecules could be rather linked to the fact that the attention on the characterisation of contemporary works of art has been paid just relatively recently [40].

Undeniably, Raman spectroscopy presents several advantages for the direct analysis of textile dyed fibers. This technique is non-destructive, the time for analysis is relatively short and also in situ microscopical measures are possible, avoiding any dyes extraction, when the dye concentration on the fiber is sufficiently high. On the other hand, the application of this technique of organic dyes has been limited by two main drawbacks: (1) the intense fluorescence emission which can occur for organic dyes and pigments; and (2) the minute quantities of colored materials, which could be below the detection limit of the Raman technique. As known, excitation in the visible range induces a relevant fluorescence emission from organic molecules, which in the case of dyes can reach very high levels due to their own chemical structure.

For fluorescence problems dispersive Raman is not considered the best technique for detecting synthetic organic dyes and frequently are preferred FT-Raman analysis or SERS techniques. As concern the fluorescence, it can, in some instances, be reduced by changing the laser wavelength [15] or by using SERS techniques, or it can be removed mathematically using post-processing. The use of less energetic laser lines such as those emitting at a NIR wavelength allows a certain degree of reduction of the fluorescence background [42], but a bigger quantity of sample could be necessary, since the sensitivity is lower than when using laser lines in the visible range [41]. Another reported strategy is that of working in resonance conditions that is using a laser line emitting at a wavelength in close proximity to that at which the dye exhibits an absorption maximum. Under this particular set up, some vibrational modes can be selectively enhanced and stand out from the fluorescence background, which however remains a dominant feature of the spectrum [43]. To this end, an optimization of such spectroscopic system has been reported, where the detection of dyes' bands is maximized using post-processing mathematical methods that subtract the background signal [44].

3.2.3 Surface Enhanced Raman Spectroscopy (SERS)

3.2.3.1 General view of SERS

The strong amplification of Raman scattering that we now define as surface enhanced was observed for the first time by Fleischmann et al. in 1974 [45]. In their seminal work, Fleischmann and co-workers reported the enhancement of Raman scattering of pyridine in aqueous solution when adsorbed on a silver electrode previously roughened by means of consecutive redox cycles, and attributed such amplification to the increase in surface area derived from the roughening process, which would have allowed for a larger quantity of analyte to adsorb on the electrode and give rise to a more intense signal. However, Jeanmarie and Van Duyne [46] and Albrecht and Creighton [47] showed that the intensity was due to more than the increase in surface area, comparing that the increase in intensity, attributed to a roughened surface, would be less than a factor of 10, whereas the enhancement obtained was of the order of 10^6 .

It has been demonstrated that silver is a particularly good substrate for SERS but some other metals are also effective: for example gold and copper were widely used giving a good enhancement. Other metals such as lithium and sodium have been established to work well. Many different roughened surfaces have been prepared, the most common being colloidal suspensions, electrodes and cold deposited metal films including silver island films and silver coated beads.

Since this technique was discovered experimentally, many theories were proposed, particularly in the early stages. Although the reasons behind that amplification were soon proven to be unsatisfactory from a quantitative point of view [46], the empirical result on its own constituted a turning point in Raman spectroscopy research and encouraged further exploration on the phenomenon, with particular regard to its theoretical definition [48]. Indeed, as early as in 1977, two research groups, independently, formulated the theories that are now believed to synergistically explain much of the SERS phenomenon. These theories are better known as the electromagnetic mechanism [46] and the charge transfer mechanism [47].

Before briefly describing the theory, it is necessary to understand the nature of the roughened metal surface. Silver surfaces, like the surfaces of other metals, are covered with electrons that arise from the conduction electrons held in the lattice by the presence of positive charge from the silver metal centres. At the surface, the positive charge is only on the metal side of the electrons. Consequently the electron density extends a considerable distance from the surface and there is also freedom of movement in a lateral direction along it. When a light beam interacts with these electrons, they begin to oscillate as a collective group across the surface; these oscillations are termed surface plasmons.

Surface plasmons - from small uniform particles, or from surfaces which have a single periodic roughness feature - have a resonance frequency, called surface plasmon resonance, at which they absorb and scatter light most efficiently. That frequency varies with the nature of the metal surface. Usually both silver and gold plasmons oscillate at frequencies in the visible region. For this reason they are appropriated for use with the visible and NIR laser systems commonly employed in Raman scattering. For SERS analysis are important not only to the ratio of absorption to scattering, but also the nature of the roughness. Usually for a metal surface fabricated by electrochemical roughening of the electrode or by depositing silver onto a surface, there are many different roughness features of varying dimensions. The result of this is that the plasmon on the surface usually covers quite a broad range of wavelengths and this can be determined by measuring the absorption spectrum of the plasmon. However, with nearly mono-dispersed colloids, the range of frequencies covered by the absorption band is very much narrower and usually the half-width is about 50–60 nm indicating a much more defined surface roughness.

3.2.3.2 The SERS effect

There are two primary mechanisms of the enhancement produced by SERS effect described in the literature: an electromagnetic and a chemical enhancement. The electromagnetic effect is dominant, the chemical effect contributing enhancement only on the order of an order or two of magnitude. The electromagnetic mechanism (EM) depends on the presence of the metal surface's roughness features, while the chemical or charge transfer mechanism (CE) involves changes in the adsorbate electronic states due to chemisorption of the analyte.

Electrochemical mechanism

Normally, the collective oscillations, called surface plasmons, couple with the electromagnetic field of the incidence beam, generating the so-called surface-plasmon-polaritons [9chiara]. These specific electromagnetic surface modes are localized at the interface metal-surrounding medium (air, water, . . .) [49] and their field has been reported to be much stronger than the incident field [50]. The simplest description of electromagnetic SERS is based on models of a small metallic sphere. Although this is an approximation to a single colloidal particle, we know that aggregation of suspensions of these particles gives much increased SERS. However the sphere model can be used to explain much of the basic process. When a small metal sphere is subjected to an applied electric field from the laser, the field at the surface is described by:

$$E_r = E_0 \cos\theta + g \left(\frac{a^3}{r^3} \right) E_0 \cos\theta \quad (1.1)$$

E_r is the total electric field at a distance r from the sphere surface,

a is the radius of the sphere,

θ is the angle relative to the direction of the electric field,

g is a constant related to the dielectric constants such that:

$$g = \left(\frac{\varepsilon_1(\nu_L) - \varepsilon_0}{\varepsilon_1(\nu_L) + 2\varepsilon_0} \right) \quad (1.2)$$

ε_0 and ε_1 are the dielectric constants of the medium surrounding the sphere and of the metal sphere respectively; ν_L is the frequency of the incident radiation (Fig. 2).

As Smith [libro] explains, at the metal surface the total electric field is averaged over the entire surface of the small sphere. At any point on the surface the electric field may be described by two components, the average field perpendicular to the surface and the average field parallel to the surface. Clearly, g is dependent on the dielectric constants of the metal and the surrounding medium, and the laser frequency. Since the dielectric constant of the metal is generally about 1, it can be seen by substituting this into Equations (1.1) and (1.2), that the electric field is greater perpendicular to the surface than parallel to it. Thus, the greatest enhancement is observed for a molecule adsorbed on the surface and polarized perpendicular to it. Further, since the field is inversely

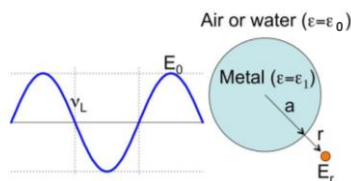


Fig. 2: Schematic representation of the electromagnetic enhancement mechanism in SERS.

proportional to r^3 , the magnitude of the SERS enhancement drops off rapidly with distance from the surface.

Sites metal nanoparticles where the incident light is highly concentrated are called “hot spots” and were defined as subwavelength gaps between clusters of two or more particles where a further coupling of the local electromagnetic fields occurs, generating a region of extra-sensitivity and enhancement [49, 51]. The light scattering in these active sites can be dramatically enhanced. It has been demonstrated that points between particles are extremely active sites, producing an enormous electric fields that give particularly effective SERS. Thus, the excitation frequency the nature of the SERS supports, together with the size and shape of the metal surface will contribute to the SERS enhancement.

Indeed, while the electromagnetic theory explains much of the bulk of SERS, it cannot be accounted for the total magnification of the signal, which is rather the result of additional phenomena independently arising and contributing to the observed enhancement [11 chiara]. Realistic enhancement ratios of up 10^4 can be explained by this mechanism [5 di Lombardi 1985].

Charge transfer mechanism

As opposed to the electromagnetic mechanism, which is based on physisorption and requires that the analyte stays in close proximity to the SERS-active surface [52] without any need of a strictly chemical interaction between them [51, 53, 54], this second mechanism involve direct, chemical interactions [48, 55], and is thus frequently indicated as chemical mechanism [51].

Various effects contribute to the chemical enhancement mechanism: (1) the signal enhancement based on chemical interactions between the molecule and nanoparticle in the ground state, (2) a signal enhancement due to the resonant excitation of a charge-transfer state between the nanoparticle and the molecule, and (3) the resonance Raman enhancement due to the excitation of a higher electronic state of the molecule. More in detail, charge-transfer (CT) processes [51] have been postulated since the very beginning of SERS research by Albrecht and Creighton [47]. Charge transfer or chemical enhancement [52] involves the formation of a bond between the analyte and the metal surface. The formation of this surface species will increase the molecular polarizability of the molecule considerably due to interaction with the metal electrons. Such CT processes can occur both as a molecule-to-metal and as a metal-to-molecule transfer, implying that, thanks to the bond created, an electron can be transferred from the highest occupied molecular orbital in the analyte to the Fermi level of the metal, or from the Fermi level of the metal to the lowest unoccupied molecular orbital in the probing molecule, respectively [15 chiara]. These two types of CT effect can be envisioned for molecules which contain lone pair of electrons available for bonding with the surface. It is important to note that the cases in which a chemical interaction takes place lead to the formation of a metal-analyte complex, causing the resulting SERS spectrum to show different vibrational features, if compared to that of the molecule alone [51, 52]. The possibility of complex formation and the specific kind of complex formed are strongly dependent on the nature of a given molecule, thus variable from analyte to analyte [56]. For

this reason, together with others linked to the existence of specific surface selection rules [57] and to the nature and preparation of the substrates [49], SERS spectra are characterized by a relevant degree of complexity and diversification [52], making it a very demanding technique from an operational point of view. Moreover, although the electromagnetic mechanism predicts an enhancement irrespectively of a molecule's nature [56], it has been experimentally ascertained that only specific classes of substances, in particular those containing functional groups with lone electron pairs, are actually able to undergo such surface enhancement.

However, differentiate these two mechanism is very difficult. Clearly, chemical enhancement should occur only from molecules directly attached to the surface and consequently should increase only up to monolayer coverage. However, electromagnetic enhancement, although a longer range effect, decreases with distance from the surface. The vast majority of evidence suggested that both effects have a part in the enhancement.

The “magnitude” of the enhancement in surface enhanced Raman scattering (SERS) is a difficult issue and different researchers have been discussing this topic. In the earlier correct interpretations [58] based on the “magnitude”, has been observed that the signal increase is due to an increase in the apparent cross-section of the molecules, resulting in the concept of the SERS enhancement factor (EF) [58]. Arguably, the SERS enhancement factor is one of the most important numbers for characterizing the SERS effect. This is especially true for practical applications where the first concern is usually the magnitude of the enhancement factor that can be achieved. It is also important when comparing with theoretical calculations. It is a fact that the EF can strongly depend on the exact SERS conditions: substrate, analyte, excitation wavelength, etc. However, the wide discrepancy in the estimated EFs also comes from the combined result of: (1) a wide variability in the definition of the EF, and (2) the way it is calculated in practice. In general EFs can be divided into:

1. SERS enhancement by a given molecule (SMEF) at a specific point. In general, it is dependent upon the Raman tensor of the probe and its orientation on the SERS substrate and with respect to the local field at that point. It is also dependent upon the orientation of the SERS substrate with respect to the incident laser polarization and direction. Hence, it requires the exact definition of the SERS substrate geometry and the exact position and orientation of the probe on it.
2. SERS substrate enhancement factors (SSEFs), which can be used to compare the average SERS enhancements across different substrates. In fact, most studies of SERS EFs have indeed focused on this aspect and the most widely used definition for the average SERS EF is eq. 2 [58]:

$$EF = \frac{I_{SERS}/N_{Surf}}{I_{RS}/N_{Vol}} \quad (2)$$

where N_{Vol} is the average number of molecules in the scattering volume (V) for the Raman (non-SERS) measurement, and N_{Surf} is the average number of adsorbed molecules in the scattering volume for the SERS experiments. This is normally taken as

representative of a substrate, although it is well known that this equation presents a few problems [58].

The evaluation of SERS EFs can be useful for several reasons: (a) it avoids having to make non-SERS measurements each time a SERS EF is required, (b) it highlights the fact that some non-resonant dyes can still have a larger-than-expected non-SERS cross-section, (i.e., preresonance effects are in general much more common than generally assumed), and (c) it shows that, effectively, different analytes can have widely different intrinsic non-SERS cross-sections as a starting point, which can differ by several orders of magnitude in some cases.

Currently, enhancements $>10^7$ are routinely reported in the literature for plasmonic substrates such as Au and Ag nanoparticle aggregates, Ag film-over-nanospheres (AgFONs), and Ag periodic particle arrays (AgPPAs) [59].

3.2.3.3 SERS active substrates: colloidal dispersions and photoreduced nanoparticles

From a more practical point of view, it has been seen that the condition necessary for the SERS effect to occur is the use of specific surfaces as substrates [52, 52, 57]. Though the choice has been recently extended with the introduction of composite materials such as shell-core nanostructures [60-64], alkali [65, 66], metal oxides [67] and transition metals [64, 68], the most common and efficient SERS substrates remain coinage metals, especially Ag and Au [49, 51, 52].

The physical arrangements in which these metals are used may be classified in three generic groups: roughened electrodes, colloidal solutions and nanostructured films [49]. As previously mentioned, to the first category belong the original substrates on which SERS experiments have been conducted [45-47]. However, in spite of their initial popularity, roughened electrodes have been outdone by other kinds of supports due to the high degree of irreproducibility of their surface roughness and, consequently, of the magnification of the spectral output [52].

To the nanostructured films belong a rather heterogeneous group of enhancing systems, most of which are based on the drop-casting of previously synthesized metallic nanoparticles onto 'bidimensional' supports such as glass slides [49], or on the direct fabrication of the nanostructured material onto those supports, an example of which is the metal island film approach [69]. In some cases, more complex and specifically nano-designed supports have been used, such as those obtained by the numerous lithographic methods that are nowadays available [69-72]. A very important aspect associated to the use of such engineered substrates is the consistent level of reproducibility associated, which has allowed quantitative analytical SERS studies [72-74], reducing the general reputation of it as the major shortcoming of the technique, owed to the already cited difficulties in achieving reliable and homogeneous substrates [51, 73, 75].

Nonetheless, the most common mean to achieve a SERS-active substrate is currently represented by the fabrication of colloidal suspensions [60], due to the possibility of preparing them through relatively simple synthetic routes and cheap starting materials, such as the reduction of a metal salt in aqueous solution (wet chemistry route) [49, 51, 60].

Metal colloids were first introduced as Raman scattering enhancers in 1979 [76], and since then a very wide range of typologies and relative synthetic procedures have been developed, among which the most frequently used are Ag and Au colloidal nanospheres prepared by wet chemistry [51] through the use of trisodium citrate [77, 78], sodium borohydride [76] or hydroxylamine hydrochloride [79] as reducing agents.

Other preparation methods are represented by the photoreduction of metal ions in solution by means of visible laser radiation [80], or higher energy sources such as gamma radiation and electron bombarding [81], and by laser ablation of plate metals in a solvent system [82, 83].

As far as fabrication is concerned, it is of utmost importance to stress that the use of a specific reducing agent over another, be it a chemical compound or a radiation, as well as other experimental parameters such as the metal salt type and concentration, the reaction temperature and environment, the possible addition of capping agents, the radiation exposure time, up to the specific mixing order of the reagents and its modality, heavily influence the physico-chemical properties of the colloid, hence its enhancing performance.

Indeed, as previously outlined, the SERS effect resides at its very basic level on surface plasmons excitation. These quasiparticles have a characteristic resonance frequency at which they absorb light most efficiently, and such frequency varies in function of the chemical nature of the material and the architectural features of the surface - mainly the shape, size and size-distribution of its nanoscale roughness [70]. It follows that this correlation can work to the researcher's advantage if the surfaces are engineered to obtain substrates characterized by a maximum efficiency in a desired operative frequency range (e.g. laser source wavelength). Nanotechnological aids, such as the already mentioned lithographic methods, are able to specifically design and control the morphology of surfaces, thus 'tuning' the plasmonic response to the desired spectral region [70], which lastly results in dealing with better performing systems. Such optimization is possible to a relevant extent with colloidal systems too, by means of the modification of the above listed experimental parameters during synthesis, which allows a very interesting degree of manipulation over the plasmonic response [84-86].

Although the high amount of experimental variables linked to the preparation of colloidal SERS systems through wet chemistry methods can be turned to an advantage, at a practical routine level it often represents a drawback in terms of surface contaminants and others interferences, hence reproducibility of the results [51]. Indeed, synthesis reagents and by-products, as well as other kind of impurities in the final colloidal solution, may sum up to the target spectral output as spurious bands [87], or even possess a higher affinity for the metal nanoparticles than the analyte and directly prevent its interaction with the SERS-active surface [88], making the interpretation of the results a very challenging task. With this respect, the enhancing ability of

the system itself constitutes a disadvantage, in that the low level of concentration at which impurities are present cannot serve as a limiting factor for their detection.

To this end, ways of obtaining purer colloidal systems have been searched out and optimized, ranging from purification methods applied to the wet chemistry colloids themselves, to the use of physical strategies of fabrication in place of chemical ones in order to avoid the introduction of reagents other than the starting materials, such as in the case of photoreduction [80] and laser ablation methods [82, 83, 90].

Another extremely important parameter regarding colloidal solutions and their enhancing performances is the net charge at the interface metal-solvent [51]. Indeed, the electrostatic environment at the nanoparticle surface plays a crucial role not only in the stability of the colloid, that is mainly its ability not to precipitate during a fair amount of time, but also and above all in the possibility to adsorb the analyte, which, as seen, is an essential condition to have a strong SERS signal [51].

Nanoparticles in a colloidal solution are believed to be surrounded by an electric double layer [9], constituted by the naturally developed positive charges at the surface of the metal particles and by the anions present in the solution derived from its synthesis [51], when not purposely added (Fig. 3). These interfacial anions allow a good degree of coulombic repulsion between single metal nanoparticles, and ensure their stability in solution by preventing coagulation and precipitation [2, 9].

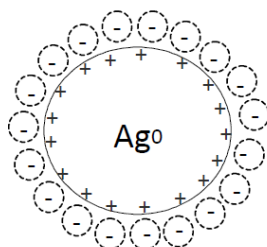


Fig. 3: Electrostatic environment of a model Ag nanoparticle in a colloid.

In addition to the stabilizing effects, it has been reported that such net surface charge highly influences the ability of the nanoparticles to physically and/or chemically adsorb the analyte molecules as well[51, 91].

Indeed, when both nanoparticles and analyte possess the same net charge, coulombic repulsion occurs among them and the adsorption of the target molecule may result partially or totally prevented [51], implying a negligible surface-enhancement of its Raman scattering. On the other hand, if electrolytes are introduced in the colloidal system, a modification in the solution environment - mainly its pH - occurs.

Such alteration results in a different distribution of the surface charges, hence in a different, possibly lower degree of coverage of the metal nanoparticles [91], which favors the interaction of a greater amount of analyte molecules with it. For this reason, studying the surface charge

of a colloidal solution and optimizing it by varying its pH and electrolyte typologies is a very powerful mean for expanding the range of analytes detectable with a given system and further increase its enhancing performance. Lastly, the amplifying power of a colloidal substrate may be incremented the by intentional partial aggregation of the nanoparticles [49, 51], an effect that is routinely achieved by the addition of salts like KNO_3 or KCl to the colloid-analyte system. Such electrolytes produce a decrease in the repulsive barrier surrounding the nanoparticles, which causes an irreversible bonding between two or more units [49]. The amount of magnification that can be attributed to the aggregation process is due to the formation of the hot spots.

It must be stated that a level of aggregation also occurs with the simple addition of the analyte. This is owed to the fact that it causes a modification of the nanoparticles surface charge, due to an actual chemical bonding or to a displacement of the other species owing to a higher affinity with the metal [49]. However, the degree of the modification of the electrostatic environment – hence the resulting aggregation - is highly dependent on the concentration of the analyte, and at the ones generally used in SERS experiments ($\sim 10^{-5}$ M) the effect is marginal, so that further aggregation with salts is regularly performed in order to obtain a better enhancement of the Raman scattering [49].

As mentioned before, both metals colloids and roughened metal electrode are commonly used as SERS substrate, but these substrates present some disadvantages such as: the difficult preparation, the instability for long period of time and the presence of impurities resulted from the synthesis that can be detected appearing spurious bands in the SERS spectra. To avoid these disadvantages, colloids generated in situ by laser irradiation can be exploited.

As the principle of photography underlies, silver metal particles are formed when light impinges upon silver salts [92, 93]. Gao et al. [94] were the first to explore the possibility of combining a photographic process with Raman spectroscopy; and during the past decades Ag photoreduction has been used by several authors to generate AgNPs. In paragraph 4.3.3 a detailed description of this method is reported.

3.2.3.4 SERS on fibres dyed with organic colorants – state of art

Identifying organic colorants is extremely important for the conservation of works of art as well as improving the knowledge on their historical context. To this end several analytical techniques have been utilized, most notably high-performance liquid chromatography (HPLC), UV-Vis absorbance spectroscopy, fluorimetry and Raman spectroscopy [59]. Although HPLC technique have identified the largest number of natural organic colorants in artworks, the analytical method requires a large amount of sample (i.e., ~ 5 mm of fiber) that is problematic for art conservation. Absorbance spectroscopy is also used to identify colorants that cannot be analysed with HPLC, although the broad and featureless UV-Vis spectra render the pigment identification difficult. Colorants and inorganic pigments can be identified using Raman

spectroscopy, but strong fluorescence precludes the measurement of Raman scattering from many organic dyestuffs. Alternatively, SERS fulfills many of the requirements of an ideal analytical technique to detect and identify colorants in artworks. The SERS substrate not only provides enhanced Raman signals, but also quenches the fluorescence generated by many organic dyes. Several groups have demonstrated the applicability of SERS to the detection and identification of colorants with application to art conservation, the results of which are the subject of a review [95].

At the beginning of SERS analysis on organic dyes, harsh chemical extractions were performed in order to remove the colorant from artist substrate, resulting in host material and dye degradation. Although softer extraction procedures have been developed, Zhang et al. [96] reported that a less color removal has been obtained. Ultimately, regardless of the particular extraction procedure the issue of limited sample size often prevents the analysis of actual historical artworks.

To circumvent the problematic issues of aggressive dye extraction and the sample size, different works have been performed using an extractive approaches or *in-situ* analysis, both on microscopic quantities of art samples. As concern the extractive approaches, these can be divided into two categories: solvent/acid extraction or active hydrogels methods. Leona *et al.* [97] reported the application of a hydrogel, functionalized with dimethylformamide and disodium EDTA, directly on the dyed fibre in order to carry out the micro extraction of the dye and directly analyzed the hydrogel with a drop of AgNPs colloid. These active hydrogels were patented on 2008 by M. Leona [98]: a small gel bead loaded with a SERS substrate is used to gently extract microscopic amounts of dyes from works of art, without the need to remove a sample and separately extract the dye by acid hydrolysis of the fiber-mordant-dye system. The gel bead subsequently is examined by SERS in order to identify the dyes. Another micro-extraction method coupled with gels have been presented by Lofrumento et al. [99]: an Ag-agar gel, wet with a drop of ethyl alcohol, was placed in contact with the textile and after the extraction, the cube of gel charged with silver nanoparticles and dye molecules was placed on a microscope glass slide and left to dry. Once dried, SERS measurements were performed achieving good results.

Otherwise, the *in-situ* methods can be divided into non-extractive hydrolysis [100], concentrated silver colloids [89], active hydrogels doped with silver nanoparticles [101] and *in-situ* photoreduction methods [102].

Regarding the non-extractive hydrolysis approach, Leona et al. reported a successful method whereby hydrofluoric acid was used to pretreat (hydrolyze) dyed fibers in order to remove the colorant from the mordanted fiber, and subsequently, Ag nanoparticles were applied to the treated fiber and the predominant dye was detected [100]. The use of concentrated Ag nanoparticles obtained from the centrifugation of Ag-citrate colloid (called AgNPs pastes by other authors [103]), allowed a further reduction of hydrolyzed fibre dimensions decreasing also the spot colloid drops [104]. Moreover, a small quantity of AgNPs paste (i.e., 5 μ L for Brosseau *et al.* [103] and 2 μ L for Wustholz *et al.* [59]) was added directly to the sample. Brosseau *et al.* applied the sample mixed with the colloids to a glass microscope slide (if not

already present on a microscope slide), and the SERS spectra were recorded after the colloid paste had dried onto the sample. Whereas, Wutholz *et al.* deposited a drop of AgNPs paste direct on fibre without any pretreatment procedures and excellent SERS spectra had been obtained from the fibre samples. It is important underline that Brosseau demonstrated that these silver colloidal pastes were stable and once applied, good SERS spectra could be achieved also after several months of storage.

Non-extractive non-hydrolysis SERS was first demonstrated by Chen *et al.* who measured SERS spectra of organic colorants from a Ag nanoparticle-treated dyed fiber taken from a mock artwork [105]. Van Elslande *et al.* reported direct non-extractive non-hydrolysis SERS on pigment grains taken from a Grecian archaeological site, allowing for the identification of the colorants in real historical objects [106]. Doherty *et al.* suggested the employ of active hydrogels doped with silver nanoparticles [101] obtained by adding silver nitrate, glucose and methylcellulose. A drop of this active gel had been applied on unvarnished mock-paintings with red lakes in egg tempera, indicating a possible interaction with the pigments and reproducible SERS activity across the drop. However, on removal of the film from the mock-up, it was noted that the residue from the paint layer was trapped within the film. Thus the formulation must be optimized in order to use this gel satisfactorily.

Finally, Jurasekova *et al.* [102] performed *in situ* on-the-fiber detection of dyed reference fibers using photoreduced Ag nanoparticles. This method has been performed directly on the fibres without hydrolysis pretreatments. Moreover, the use of photoreduced nanoparticles allowed the obtention of SERS spectra without possible spurious bands of impurities resulted from the colloid synthesis.

3.3 A new analytical protocol for dyed fibres analysis

This research is aimed at establish an analytical protocol for dyed fibres, using micro-Raman and SERS spectroscopy applied direct on fibres. Several wool fibres dyed with synthetic organic colorants – belonging to azo, xanthenes, triarylmethane and tiazine classes - have been studied in order to understand their response in Raman spectroscopy and if none spectra allowed from Raman, SERS technique have been tested. The possibility to change Raman parameters and the new SERS procedure accomplished, have allowed to establish a completely new analytical protocol based on the combination of this two techniques.

3.3.1 Raman spectroscopy for wool dyed fibres analysis

The first step of this research is aimed at investigate micro-Raman spectroscopy as a possible technique of examining wool dyed fibres, and at compare different analytical conditions. Indeed, Raman spectroscopy has a large variety of parameters, designs and sampling procedures which has rendered a clear evaluation of the technique difficult until now. For this reasons, the description of the sampling method and the analytical condition used for each classes of dyes are fundamental to create a database. Moreover, the purpose of this study was to generate more analytical knowledge about synthetic colorants used on art objects, focusing on dyes developed and produced in the second half of the 19th century and on synthetic organic pigments developed in the 19th century up to 1940. In that period hundreds of different synthetic colorants were introduced although not all of them turned out to be a commercial success. At this moment, these dyes are not yet well investigated and the studies that have been done are in general on individual basis. This work was possible thanks to the availability of dyed wool fibres belonging to the CHARISMA project.

This study has been conducted and positive results have been achieved for the reason that a sufficient amount of colorant is present on the fibre. This is an essential issue in order to obtain meaningful spectra and to try, for the first time, to identify and distinguish which laser excitation wavelength to apply on the basis of different colour fibres. With the aim at well understand if standard fibres have an excess of colorant, the same procedure have been performed on washed fibres and the results achieved are in agreement with the previous one. For this reason, Raman spectra carried out on standard fibres – not washed – are here presented.

3.3.1.1 Materials and methods

Dyed wool fibres

Dyed wool fibres (belonging to the CHARISMA project) were prepared at the OCW-RCE laboratories. Three recipes were established to obtain the reference materials. For the acid, direct and basic dyes recipes were based on historical recipes given in the sample book developed by Adolf Lehne in 1893 [107]. The quantities and parameters were adapted and laboratory recipes were prepared using analytical grade chemicals and demineralised water. Although these recipes do not completely follow the original historical recipes, by this reproducible dyeings were produced. Prior to dyeing, the wool (Bluefaced Leicester, brand: Rowan, Purelife) was washed with 10% (wool weight) Marseille soap at 40°C for one hour. Next, bundles of 10 g each were made and they were tied with nylon tyrapas to prevent wool from entangling.

The recipe followed to dye wool fibres with acid dyestuffs indicates the use of water heated at 70 °C in which are dissolved 5 g of sodium sulphate and 150 mg of the acid dye consecutively. After, 10 g of wool bundle are soaked in the dyeing solution and 200 µl of concentrate sulphuric acid are added; the dye bath thus prepared is put in oven at 70 °C for 30 minutes. The wool bundle is left to cool down in the dye bath and afterwards it is rinsed with water.

For the basic dyes, the recipe is simpler, due to the fact that the dyed bath is constituted by water at 70 °C and 100 mg of a basic dye only. 10 g of wool bundle are soaked in the dye bath and put in oven at 70 °C for 30 minutes. Finally the bundle is left to cool down in the dye bath and afterwards it is rinsed with demineralized water.

Sample preparation

Dyed wool yarns were sampled by cutting a single fibre from the main wool thread. Such single fibre exhibits a diameter ranging from 20 to 30 µm and a length of about 2 cm was then used.

The sample was prepared taped a single dyed-fibre on top of glass slides and analyzed directly where there was no tape; therefore, no interference from the tape occurred [108]. Differently from Miller et al. [108] the analysis was performed directly on the wool fibre and not on the glass slide (fig. 4). With this method, using the laser at 785 nm, the possible fluorescence from the glass slide that produces a large broad underlying peak near 1400 cm⁻¹, was avoided. Three fibres for each type of dye were prepared and analysed; moreover a fibre of undyed wool was prepared and analysed as reference.

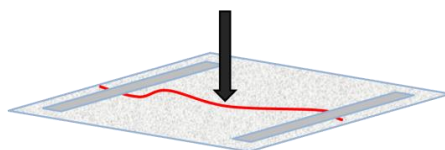


Fig. 4: Sample preparation and side of analysis.

Raman Spectroscopy

The micro-Raman spectra were recorded in a Renishaw inVia Raman spectrometer coupled with a microscope, and fitted with a Peltier-cooled CCD detector and four excitation lines emitting at 532 nm (frequency-doubled Nd-Yag laser) 785 nm (diode laser), 442 nm and 325 nm (He-Cd). Only the former two lines were used for the present study. All measurements were taken using an edge filter, and gratings of 1800 l/mm and 1200 l/mm were used for the set up with laser source at 532 nm and 785 nm, respectively. WIRE software was used to launch the spectral acquisitions. The laser power at the sample was from 0.5 mW to 2.5 mW and 2.5 mW for for the lasers at 532 and 785 nm, respectively. The resolution was set at 4 cm⁻¹ and the geometry of micro-raman measurements was 180°. The measurements were performed using a 100x objective. Three spectra for each fibre were acquired for a total of nine replicas for each dye.

Principal component analysis on single-point spectra

Multivariate data processing were performed by means of in-house Matlab routines (The Mathworks Inc., Natick, USA). PCA on standard dyes spectra was performed in order to verify the possibility of distinguishing in a dye class each single dye. A number of common mathematical pre-processing strategies were applied to the data. The aim of such pre-treatments was the minimisation of unwanted effects – such as baseline variations and global intensity effects – which commonly affect Raman spectra. In more detail, the standard normal variate (SNV) transform, a linear detrending and Savitzky-Golay derivation, using third order polynomials and 11 datapoint gaps [27] were applied in combination, attempting to minimise systematic unwanted variations affecting the signals and to enhance useful features.

3.3.1.2 Results

Seventeen different dyed wool fibres were studied: seven azo dyes, two xantene dyes, seven triarylmethane dye and one thiazine dye (table 1). For each dye, Raman spectra have been acquired both at 532 nm and 785 nm excitation wavelength. The use of two lasers and the large number of wool dyed fibres analysed could permit to create a database on the wool dyed fibres and to promote a new analytical approach direct on fibres.

Table 1 – Information concerning the dyed wool fibres studied, divided by chemical class and preliminary evaluation of achieved Raman spectra according to different excitation wavelengths and the UV-Vis absorption spectra.

| class | colour | name | Raman spectroscopy* | | Max absorbance in UV-Vis |
|-------------|--------|----------------------------|---------------------|---------------|--------------------------|
| | | | Laser 532 nm | Laser 785 nm | |
| Monoazo dye | orange | Orange II (AO7) | No spectrum | Good spectrum | 485 nm |
| | red | Amido Naphthol red G (AR1) | No spectrum | Good spectrum | 503 nm and 529 nm |

| | | | | | |
|--------------------|--------|------------------------|---------------|---------------|---------|
| | red | Cochineal red A (AR18) | No spectrum | Good spectrum | 506 nm |
| | red | Ponceau RR (AR26) | No spectrum | Good spectrum | 504 nm |
| | violet | Azo Fuchsine 6B (AV7) | No spectrum | Good spectrum | 527 nm |
| | yellow | Flavazine L (AY11) | Good spectrum | No spectrum | 391 nm |
| Diazo dye | red | Congo Red (DR28) | No spectrum | Good spectrum | 498 nm |
| Xantene dye | red | Eritrosine (AR51) | No spectrum | Poor spectrum | 524 nm |
| | red | Eosine (AR87) | No spectrum | Poor spectrum | 515 nm |
| Triarylmethane dye | blue | Water blue IN (AB93) | Good spectrum | No spectrum | 574 nm |
| | blue | Vicotria blue R (BB11) | Good spectrum | No spectrum | 611 nm |
| | blue | Victoria blue B (BB26) | Good spectrum | No spectrum | 618 nm |
| | green | Diamond green G (BG1) | Poor spectrum | Poor spectrum | 623 nm |
| | violet | Methyl Violet (BV1) | No spectrum | Good spectrum | 579 nm |
| | violet | Crystal Violet (BV3) | No spectrum | Good spectrum | 586 nm |
| | violet | Fuchsin (BV14) | No spectrum | No spectrum | No done |
| Thiazine dye | blue | Methylene blue (BB9) | Good spectrum | No spectrum | 665 nm |

* The quality of Raman spectra was evaluated using three classification criteria:

- No spectrum: no spectral information obtained due to fluorescence problems;
- Poor spectrum: spectrum of poor quality with only few Raman bands of low intensities;
- Good spectrum: well-defined Raman bands, good spectral quality.

Undyed wool fibre

A single undyed fibre of Bluefaced Leicester wool was analysed with laser sources at 532 nm and 785 nm. The two spectra (Fig. 5) showed the same bands and the same relative intensities although different laser sources have been used. The spectra were in good agreement with which published by H. Liu and w. Yu [109]. The spectra were characterized by the Amide I band at 1652 cm^{-1} due to the C=O elongation vibration of the peptide group and the N-H bonding in plane deformation. A very weak band was also generated from Amide II at 1125 cm^{-1} , due to N-H bonding deformation with minor contribution of C-N bonding elongation. The Amide III Raman band appeared from 1300 to 1240 cm^{-1} generated by a combination of N-H deformation and C-N elongation. The 1448 cm^{-1} peak was originated by CH_2/CH_3 groups. The C-C skeletal stretching vibrations appear at 1002 , 936 and 852 cm^{-1} ; finally the band at 507 cm^{-1} can be assigned to S-S bond.

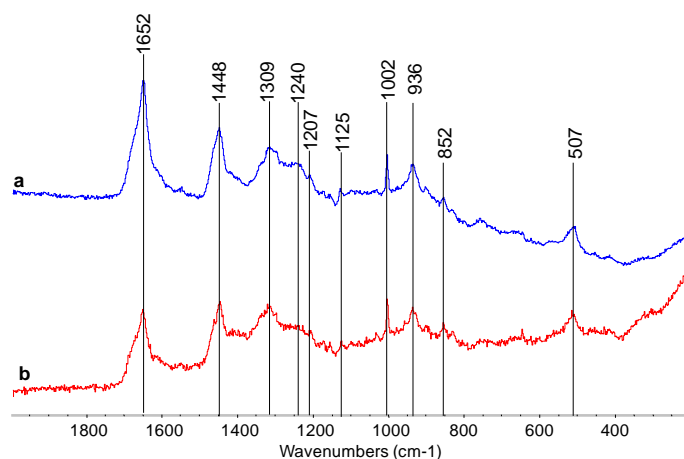


Fig. 5: Raman spectra of wool fiber with different laser excitation: (a) 532 and (b) 785 nm.

Azo dyed wool fibres

Six monoazo dyes and a diazo dye were analysed (table 1); the colours investigated for monoazo dyes were an orange (Orange II - AO7), three red (Amido Naphthol red G - AR1, Cochineal red A - AR18 and Ponceau RR - AR26) a violet (Azo Fuchsine 6B - AV7) and a yellow (Flavazine L - AY11) whereas the diazo dye was a red (Congo Red – DR28). All of this dyed wool fibres were analysed with both 532 nm and 785 nm lasers.

Except the Flavazine L (AY11) which presented a good Raman spectrum with 532 nm laser (fig. 6), all the dyes showed spectra with defined signal of good intensity only with 785 nm excitation wavelength (fig. 7).

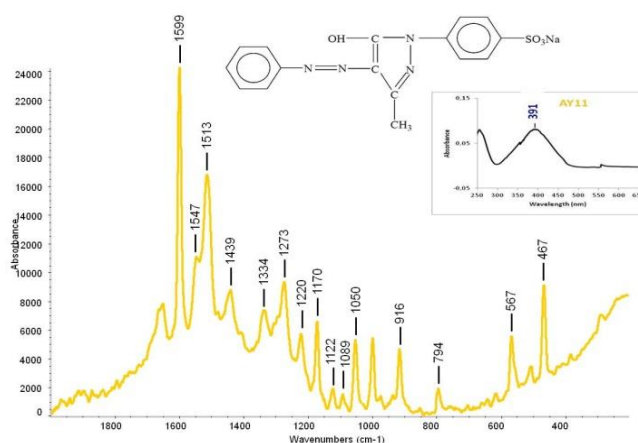


Fig. 6: Flavazine L (AY11) Raman spectrum acquired with 532 nm laser.

Xantene dyed wool fibres

Eritrosine (AR51) and Eosine (AR87) were the two red xantene dyes analysed (table 1), they presented poor spectra when analysed with 785 nm laser. The identified low intensity Raman bands were mainly of the wool substrate and this made the identification of dyes not possible.

Triarylmethane dyed wool fibres

Seven triarylmethane dyes were analysed: three blue (Water blue IN - AB93, Victoria blue R - BB11 and Victoria blue B - BB26), a green (Diamond green G - BG1) and three violet (Methyl Violet - BV1, Crystal Violet - BV3, Fuchsin - BV14). This dyes class presented different results (table 1), except the Fuchsin (BV14) which did not reveal any Raman signal due to fluorescence problems, and except for the Diamond green G (BG1) which showed poor spectra with both excitation wavelengths. The other dyes could be differentiated by the colour. The blue triarylmethane dyes showed high-quality spectra with the 532 nm laser (fig. 8), whereas the violet dyes had good response at 785 nm excitation wavelength (fig. 9).

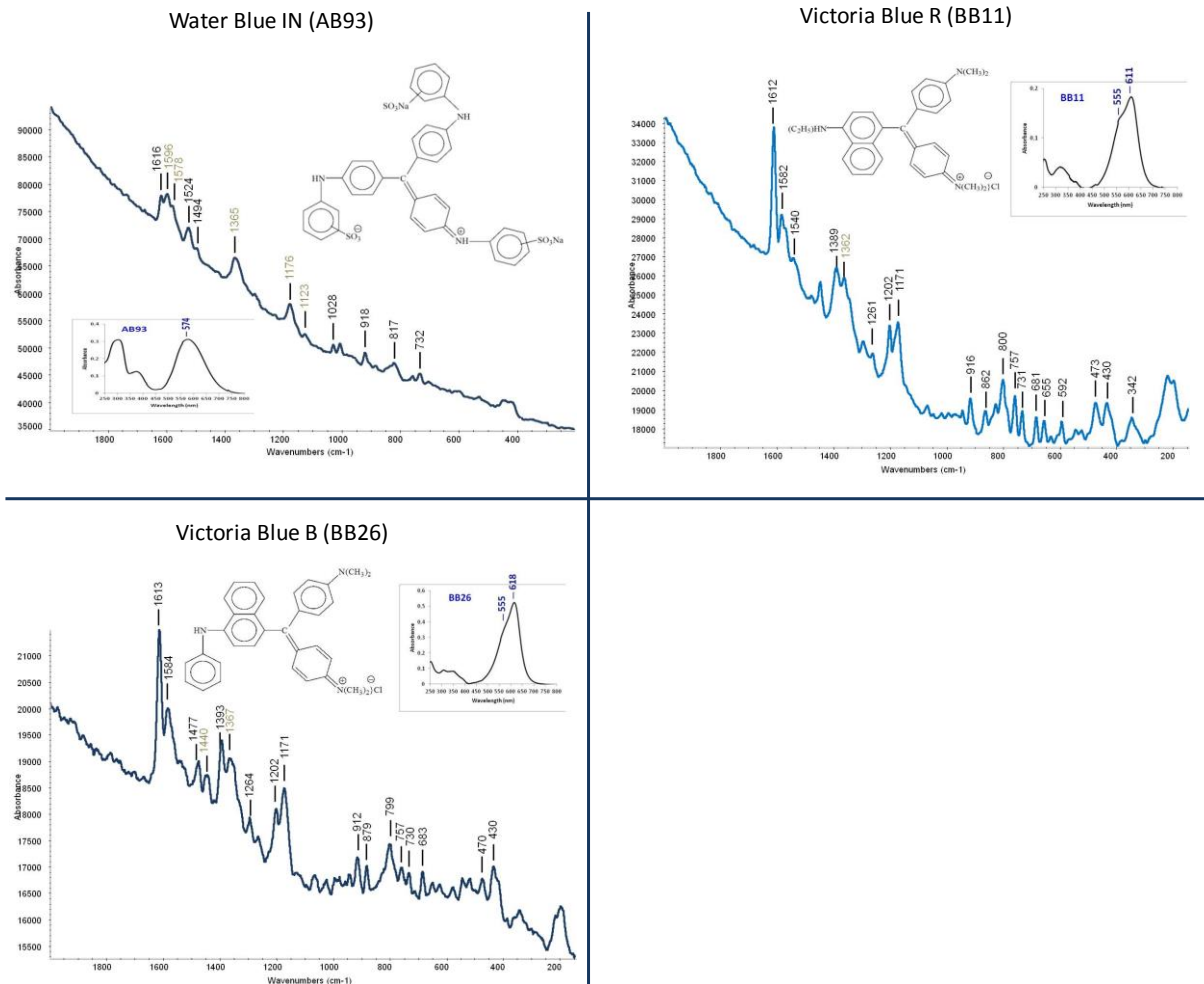


Fig. 8: Raman spectra of blue triarylmethane dyed wool sample acquired with 532 nm excitation wavelength, 100x microscope objective. The spectra were improved with using OMINC software doing smooth of 9 points and baseline correction for BB11 and BB26.

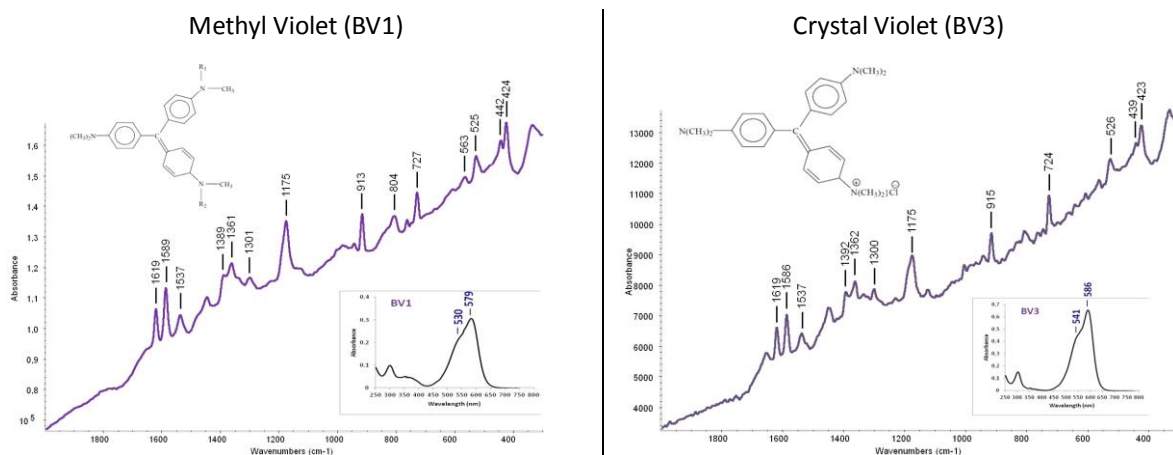


Fig. 9: Raman spectra of violet triarylmethane dyed wool sample acquired with 785 nm excitation wavelength, 100x microscope objective. The spectra were improved with using OMINC software doing smooth of 9 points.

Thiazine dyed wool fibres

The Methylene Blue (BB9) was the blue dye analysed (table 1), which presented a well resolved Raman spectrum at 532 nm (fig. 10).

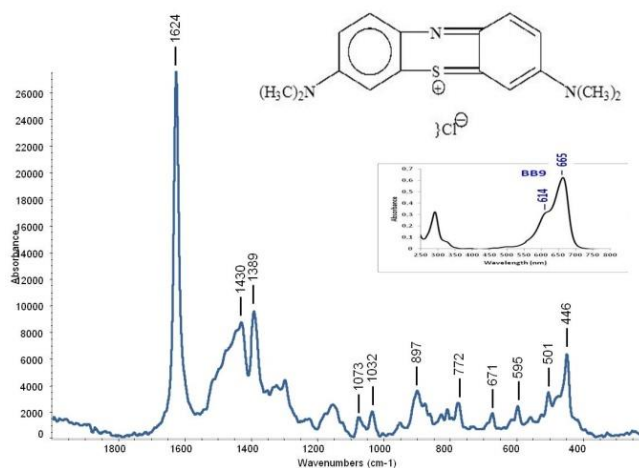


Fig. 10: Methylene blue (BB9) Raman spectrum acquired with 532 nm laser.

3.3.1.3 Discussion

In this study thirteen dyed fibres – on seventeen analysed - gave Raman spectra of a meaningfully quality at 532 nm or 785 nm excitation wavelengths. The signals originating from

the wool matrix were totally obscured or only few peaks, not sufficient for a correct interpretation, were detectable, whereas the bands of the dyes had a good spectral quality allowing the dye identification.

It is well known that, under suitable circumstances, the excitation of electronic molecular states can be reached irradiating fibres with visible light of high intensity. If these states subsequently decay by a radiative process, Raman measurements can be hampered or even rendered meaningless by the superimposition of an intense featureless background (this event is usually named fluorescence). Such problems can be circumvented by a change of the excitation wavelength.

Considerably fluorescence problems on attempting measurements at 532 nm excitation were encountered for the orange, red and violet azo dyes and for violet triarylmethane dyes; whereas good quality Raman data could be obtained readily from the yellow azo dye and the blue triarylmethane and thiazine dyes. On changing to 785 nm excitation detailed spectra could now be acquired from all the fibre samples which were before affected by fluorescence (table 1).

Unexpectedly, the assignation of a functional excitation wavelength to a dyes class or sub-class was not possible and neither the application of an excitation wavelength useful to have resonance phenomena gave positive results. Indeed, in the most of cases, Resonance-Raman spectra acquired were affected by high fluorescence instead of an enhanced signal.

All these differences in Raman responses led to think that the use of a correct excitation wavelength was closely related to the molecular structure of the dyes.

Di and tri-arylmethane dyes

Di and tri-arylmethane dyes belong to the class of polymethine dyes. They could be considered branched polymethines: the branches were created by two aryl rings in which the polymethine chain was incorporated, and by another R group bonded to the central methane carbon (1).

The R group possessed π -electrons or lone pairs of electrons that could interact with the rest of the π -electron system.

The basic chromophores of di and tri-arylmethane dyes were generally considered diphenylmethyl and triphenylmethyl cations [110]. In diarylmethane dye fig. 11 a blue shift of the absorption band was caused by donor substituents (R), whereas a red shift was caused by acceptor groups [110]. The most important electron donor is the amino group.

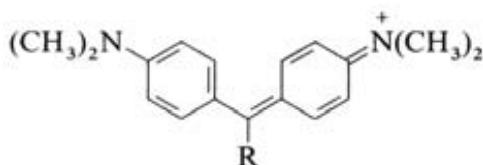


Fig. 11: basic chromophore of di-arylmethane dyes

Triarylmethane dyes were usually divided into mono-, di-, and triaminotriarylmethane dyes. When at least two of the aryl moieties carried electron donating amino group substituents these dyes

were rendered basic. Additional substituents might be located on the aromatic rings such as halogen, alkyl, alkoxy, sulfonic acid and carboxyl; substituents in the meta- and para-positions of the meso-phenyl ring shift the position of the absorption band at longest wavelength, depending on their Hammett constants [110]. Indeed, the nature, the number and the position of substituents influenced not only the dye colour tone but also the type of application of the dyes. For example, sulfonic acid groups converted the basic dyes into acid dyes so they could be used as pigments.

It is well known that triarylmethane dyes were characterized by a highly delocalized positive charge over the aromatic rings, on the central carbon atom and on the nitrogen atoms. When the three rings (C1, C2 and C3) were coplanar, the p orbitals of each carbon atoms were parallel and could efficiently interact allowing a high efficient resonance; nevertheless steric factors were also involved in the final conformation of triarylmethane dyes. Specifically, the presence with respect to the central carbon atom of six hydrogen atoms in ortho position gave rise to a three-blade propeller shape, with each aromatic ring twisted out of the plane [doerty]. Moreover, bulky substituents in the ortho-position caused a steric hindrance, which led to rotation around the central C-C bond, and substituents in the meta-position caused the amino groups to rotate out of the coplanar arrangement. For instance, if a dimethylamino group was introduced into the para position of the meso-phenyl ring, crystal violet was obtained [R = N(CH₃)₂], instead of malachite green [R = H] (fig.12). Indeed, the introduction of a group into the ortho-position of the third – the “meso”-phenyl ring in malachite green – caused rotation of the ring around the central C-C bond. This generally led a colour shift from green to blue.

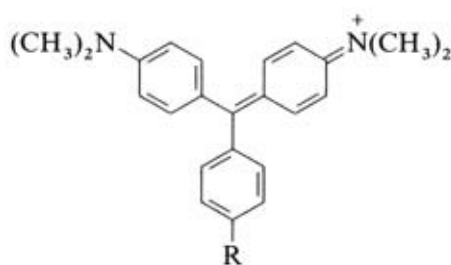


Fig. 113: basic structure of malachite green and/or crystal violet.

The micro-Raman spectra on wool dyed fibres showed a good level of scattering for Water Blue IN (AB93), Vicotria blue R (BB11) and Victoria blue B (BB26) using a 532 nm laser excitation, whereas for Methyl Violet (BV1) and Crystal Violet (BV3) good spectra are acquired with 785 nm laser wavelength; a persisting underlying fluorescence in some cases was observed.

Conversely, for Diamond green G (BG1) and Fucshin (BV14) no spectral information has been obtained due to fluorescence problems with both lasers.

Diamond green G (BG1) spectra showed few peaks not useful for a certain identification of the dyes (table 2); the spectra was affected to high fluorescence, probably due to the broadening of π electron system provided by the diethylamino substituents defined by high electron-

releasing power. Indeed, these substituents for C1 and C3 rings with electron lone pairs were in resonance with the π electron system of phenyl rings. The UV/Vis absorption spectra of BG1 showed two absorption bands in visible region with λ_{max} values of 623 and 423 nm. Hence, its observed green colour was due to the addition of blue and yellow components. The long wavelength band was polarized along the x-axis and the short wavelength band along the y-axis. Therefore, the molecular structure increased not only the polarizability of the molecule and the resonance, but also the probability of internal conversions in the excited state, that gave rise to fluorescence.

Table 2: Tentative band assignment published on “B. Doherty et al. *Spectrochimica Acta Part A: Molecular and Biomolecular Spectroscopy* 121 (2014)”

| BG1 | |
|------------|--------------------|
| 1616 | v(C–C)ring |
| 1430 | |
| 1364 | v(CcenterC) |
| 1219 | |
| 1186 | δ (C-H)ring |

Fuchsine (BV14) spectra were affected by high fluorescence and no peaks were identifiable.

Probably this lack of Raman spectra for Diamond Green (BG1) and Fuchsine (BV14) is due to the high fluorescence background generated using the 532 nm laser due to resonance or pre-resonance phenomena between laser and dyes that caused internal conversion and subsequently fluorescence. On the other hand, employing an excitation wavelength less energetic and not in resonance, as 785 nm, the low Raman cross section of these two dyes does not allow to acquire any meaningful spectra.

The 532 nm laser excitation could be positively applied on wool fibres dyed with di-phenyl-naphthalene dyes (BB11 and BB26) and with the only acidic tri-amino triarylmethane dye (AB93). The presence of bulky substituents as naphthalene or naphthalene-amino-benzene structure in C2 position, or the amino-benzenesulfonate substituents for all the triphenyl rings gave a “positive” geometry with which the p orbitals of substituents were out of the π electron system plane created by the three phenyl rings. This means that fluorescence was quenched by bulky substituents that twisted the molecules reducing resonance between the chromophore and the auxochromes, and also that the 532 nm laser could be positively employed directly on wool fibres dyed, obtaining well resolved spectra, probably thanks to pre-resonance Raman effect.

Victoria blue R (BB11) and Victoria blue B (BB26) spectra achieved with 532 nm laser, presented intense and characteristic peaks of the dyes (table 3). The intense pre-resonance Raman spectrum was achieved thanks to the ethylamino-naphthalene substituent for BB11 and the naphthalene-amino-benzene substituent for BB26 bonded to C2 ring. These bulky substituents increased a steric repulsion that enforces a twist of the naphthalene structure and consequently the resonance was decreased and fluorescence was quenched. Indeed, the BB11 and BB26 spectra were characterised by different peaks: two very strong at 1612 and 1584 cm^{-1}

¹ both due to the stretching of C-C ring bond; two strong at 1390 and 1362cm⁻¹ the least attributed to the stretching of C_{center}-C bond and other two strong bands at 1202 cm⁻¹, due to the bending of C-H bond of the ring and 1171 cm⁻¹ attributable to the (C-C-C) symmetric stretching, (C-C-C) bending and to the CH₃ bending. Other medium or weak peaks distinctive for each dye were appreciable in both spectra.

Using the 785 nm wavelength laser no spectra have been obtained probably due to a reduction in the weakness of the spectrum as a consequence of the lack of Resonance Raman effect

Table 3: Tentative band assignment published on “B. Doherty et al. *Spectrochimica Acta Part A: Molecular and Biomolecular Spectroscopy* 121 (2014)”

| BB11 | BB26 |
|--|---|
| 1612 $\nu(\text{C}-\text{C})_{\text{ring}}$ | 1613 $\nu(\text{C}-\text{C})_{\text{ring}}$ |
| 1582 $\nu(\text{C}-\text{C})_{\text{ring}}$ | 1584 $\nu(\text{C}-\text{C})_{\text{ring}}$ |
| 1540 | 1477 $\delta_{\text{as}}(\text{CH}_3)$ |
| 1389 | 1440 |
| 1362 $\nu(\text{C}_{\text{center}}\text{C})$ | 1393 |
| 1261 | 1367 $\nu(\text{C}_{\text{center}}\text{C})$ |
| 1202 $\delta(\text{C}-\text{H})_{\text{ring}}$ | 1202 $\delta(\text{C}-\text{H})_{\text{ring}}$ |
| 1171 $\nu_{\text{s}}(\text{CCC})/\delta(\text{CCC})_{\text{breathing}}/\delta_{\text{r}}(\text{CH}_3)$ | 1171 $\nu_{\text{s}}(\text{CCC})/\delta(\text{CCC})_{\text{breathing}}/\delta(\text{CH}_3)$ |
| 916 $\nu(\text{CC})_{\text{ring}}$ | 912 $\nu(\text{CC})_{\text{ring}}$ |
| 862 $\delta(\text{CCC})$ | 879 $\delta(\text{CCC})$ |
| 800 $\delta(\text{CH})_{\text{ring}}$ | 799 $\delta(\text{CH})_{\text{ring}}$ |
| 757 | 757 |
| 731 $\nu(\text{CN})$ | 730 $\nu(\text{CN})$ |
| 681 | 683 |
| 655 | 470 $\delta(\text{CC})$ |
| 592 | 430 $\delta(\text{CNC})/\delta(\text{CCC}), \delta(\text{SO}_3)$ |
| 473 $\delta(\text{CC})$ | |
| 430 $\delta(\text{CNC})/d(\text{CCC}), d(\text{SO}_3)$ | |
| 342 $\nu(\text{CNC})/p_{\text{r}}(\text{CH}_3)$ | |

For Water Blue IN (AB93), although fluorescence affects the baseline, characteristics and well resolved peaks were identifiable analysing with 532 nm laser (table 4). This molecule was characterized by three substituents constituted by an aromatic ring with an electron-releasing group (amino group) and an electron-withdrawing group (sulfonate group) both in para-position. The presence of bulky sulphonate groups lead to a quenching of the fluorescence, as in the case of the other blue triarylmethane dyes. The Raman spectrum showed different intense bands due to the stretching of C-C ring bound (1616 cm⁻¹, 1596 cm⁻¹), the stretching of C_{center}-C bound (1365 cm⁻¹), the (C-C-C) symmetric stretching, (C-C-C) bending and to the CH₃ bending (1176 cm⁻¹) and two bands at 1578 and 1524 cm⁻¹.

Also for this dye the reduction of laser frequency probably reduce the intensity of signal and the fluorescence total overlay the dye spectrum.

Table 4: Tentative band assignment published on “B. Doherty et al. *Spectrochimica Acta Part A: Molecular and Biomolecular Spectroscopy* 121 (2014)”

| AB93 | |
|-------------|--|
| 1616 | $\nu(\text{C}-\text{C})_{\text{ring}}$ |
| 1596 | $\nu(\text{C}-\text{C})_{\text{ring}}$ |
| 1578 | |
| 1524 | |
| 1494 | $\delta_{\text{as}}(\text{CH}_3)$ |
| 1365 | $\nu(\text{C}_{\text{center}}\text{C})$ |
| 1176 | $\nu_{\text{s}}(\text{CCC})/\delta(\text{CCC})_{\text{breathing}}/\delta(\text{CH}_3)$ |
| 1123 | $\delta(\text{CCC})/\nu(\text{CN})$ |
| 1028 | |
| 918 | $\nu(\text{CC})_{\text{ring}}$ |
| 817 | $\delta(\text{CH})_{\text{ring}}$ |
| 732 | $\nu(\text{CN})$ |

The Methyl Violet (BV1) and Crystal Violet (BV3) were characterised by di-methyl-amino substituent bonded in para-position to each aromatic ring, and had good spectra at 785 nm laser excitation (table 5). Although the 532 nm laser would be in pre-resonance, this was not sufficient to reduce the fluorescence probably gave by the three donor substituents that had lone pair in direct conjugation with the π -system of each chromophore branch. The Raman spectra these two dyes showed the characteristic bands of the triarylmethane structure: the stretching of C-C ring bond (1616 and 1596 cm^{-1}), the stretching of $\text{C}_{\text{center}}\text{-C}$ bond (1365 cm^{-1}), the (C-C-C) symmetric stretching, (C-C-C) bending and to the CH_3 bending (1176 cm^{-1}). Some typical band of these dyes were observed at 914 (C-C ring stretching and (C- $\text{C}_{\text{center}}\text{-C}$) bending), 724 (C-N bond stretching) and 421 cm^{-1} (C-N-C bond and C-C-C bond bending).

On the other hand, the use of a less energetic laser radiation aids to reduce the fluorescence and distinctive peaks of dyes became visible.

Table 5: Tentative band assignment published on “B. Doherty et al. *Spectrochimica Acta Part A: Molecular and Biomolecular Spectroscopy* 121 (2014)”

| BV1 | BV3 |
|--|--|
| 1619 $\nu(\text{C}-\text{C})_{\text{ring}}$ | 1619 $\nu(\text{C}-\text{C})_{\text{ring}}$ |
| 1589 $\nu(\text{C}-\text{C})_{\text{ring}}$ | 1586 $\nu(\text{C}-\text{C})_{\text{ring}}$ |
| 1537 $\nu(\text{CringN})/\delta_{\text{s}}(\text{CH}_3)$ | 1537 $\nu(\text{CringN})/\delta_{\text{s}}(\text{CH}_3)$ |
| 1389 $\delta(\text{CH})/\delta_{\text{s}}(\text{CH}_3)/\delta(\text{CCC})_{\text{ring}}$ | 1392 $\delta(\text{CH})/\delta_{\text{s}}(\text{CH}_3)/\delta(\text{CCC})_{\text{ring}}$ |

| | | | |
|------|--|------|---|
| 1361 | v(CcenterC) | 1362 | v(CcenterC) |
| 1175 | vs(CCC)/ δ (CCC)breathing/ δ (CH3) | 1300 | vas(CCcenterC)/ δ (CCC)ring/ δ (CH) |
| 913 | v(CC)ring / δ (CCcenterC) | 1175 | vs(CCC)/d(CCC)breathing/ δ (CH3) |
| 804 | δ (CH)ring | 915 | v(CC)ring / δ (CCcenterC) |
| 727 | v(CN) | 724 | v(CN) |
| 563 | γ (CCC)/ δ (CNC)/ δ (CCC) | 526 | δ (CNC) |
| 525 | δ (CNC) | 439 | δ (CC) / δ (CNC) |
| 442 | δ (CC)/ δ (CNC) | 423 | δ (CNC)/ δ (CCC) |
| 424 | δ (CNC)/ δ (CCC) | | |

Xantene dyes

Xantene dyes were obtained if the carbon atoms in ortho position to the central carbon in di- and triarylmethane dyes were bonded via an oxygen atom. Incorporation of this bridge had a pronounced hypsochromic effect: although green and blue dominated in the triphenylmethane series, the characteristic colour of xantene dyes was red [110].

The Eritrosine (AR51) and Eosine (AR87) micro-Raman spectra on wool dyed fibres showed a high fluorescence background without any identifiable dye bands at 532 nm, and poor spectra with only few characteristic peaks of wool substrate with an underlying fluorescence still present at 785 nm. The strong fluorescence feature has been attributed to their structural rigidity ascribed to the dibenzopyran structure resulting from the coordination of the two rings by a heterocyclic system [6]. The structural rigidity causes a decrease of the internal conversion rate, which increases the fluorescence emission.

Azo dyes

Azo colorants contained as their common structural feature the azo (-N=N-) linkage which was attached at either side to two sp^2 carbon atoms. Usually the azo group linked two aromatic rings systems; the monoazo dyes contained a single azo group, whereas which contained two groups were diazo, three azo groups were named trisazo and so on. The presence of the azo group (-N=N-) gave the possibility to provide a more extended electronic conjugation of π electrons and consequently allowing a strong light absorption in the visible region of the electromagnetic spectrum.

The structural chemistry of azo compounds was complicated by the possibilities of isomerism. Two types of isomerism exist, which might commonly be encountered with a certain azo compounds: geometrical isomerism and tautomerism. Many commercial azo colorants contained a hydroxyl group in ortho position to the azo group. This gives rise to intramolecular hydrogen bonding which further stabilised the trans (E)-isomer and effectively prevented its conversion into the cis (Z)-form [6]. Another important feature of azo compounds containing an hydroxy group conjugated in ortho or para position to the azo group, for example, C.I. Orange II, is the possibility to exhibit tautomerism. The hydrogen atom on the hydroxyl group was able to migrate to the nitrogen atom of the azo group and vice versa (Fig. 13). This gives

rise to the coexistence of two distinct chemical structures, called azo (OH) or hydrazo (NH) tautomeric species, where both were stabilized by a strong intramolecular hydrogen bond. The equilibrium between the two species depends on several factors.

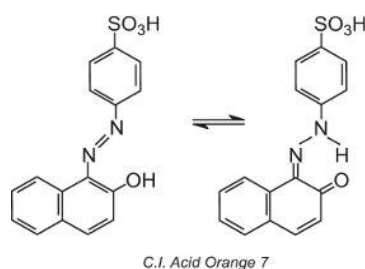


Fig. 13: AO7 tautomerism

This type of tautomerism involves equilibrium between a hydroxyazo tautomer and a ketohydrazone tautomer; in the case that the ketohydrazone tautomer is dominant, the colour observed is of longer wavelength, resulting in a bathochromic shift.

The azo dyes with basic structure as phenyl-azo-diphenyl as Orange II (AO7), Amino Naphtol Red G (AR1), Ponceau RR (AR26) and Azo Fuchsine 6B (AV7) or diphenyl-azo-diphenyl as Conchineal Red A (AR18) and Congo Red (DR28) showed good spectra with 785 nm laser (table 6). Even if these dyes would be in resonance with the 532 nm laser and might expect to obtain resonant Raman spectra, the fluorescence concealed all the possible bands of the dyes. Attempting measurements at 785 nm the fluorescence problems were minimised and good Raman spectra were collected. This is due to the fact that the energy provided by excitation at 785 nm is not enough to promote the system to excited electronic levels.

All these azo dyes presented well resolved Raman spectra with intense and distinctive bands at around 1600 cm^{-1} , attributed to stretching of benzene, naphthalene or conjugated alkene $\text{C}=\text{C}$ bonds, in plane bending of CH, bending of NH and stretching of $\text{C}=\text{O}$ bond for hydrazo forms. The band around 1510 cm^{-1} is assigned to stretching of $\text{C}=\text{O}$ and $\text{C}=\text{N}$ bond, and NH bending for hydrazo form or $\text{C}=\text{C}$ bond for azo structure, and in plane bending of CH. Moreover there were three other characteristics frequency regions in the Raman spectrum: around $1450\text{-}1350\text{ cm}^{-1}$ due to $\text{N}=\text{N}$ stretching mode, around $1400/1450\text{ cm}^{-1}$ attributed to CO stretching, and around $1200\text{-}1300\text{ cm}^{-1}$ with a set of bands assigned to NH bending (in hydrazo form), NN stretching with contributions from CC stretching and CH in plane bending vibrations. Furthermore, for each dye characteristic bands were observed depending on molecular structure.

Table 6: Tentative band assignment. For AR18 dyes have been indicated the assignments published on "M.R. Almeida, The Journal of Physical Chemistry A 114 (2010)"

A07

| | |
|------|---|
| 1598 | $\nu\text{C}=\text{C}$ Bz; $\nu\text{C}=\text{C}$ Conjugate alkene; $\nu\text{C}=\text{C}$ Nph |
| 1553 | δNH |
| 1497 | $\nu\text{C}=\text{C}$ Bz; $\nu\text{C}=\text{C}$ Conjugate hydrazone; $\nu\text{C}=\text{C}$ Nph |
| 1453 | $\nu\text{C}=\text{C}$ Bz |
| 1420 | |

AR1

| | |
|------|---|
| 1596 | $\nu\text{C}=\text{C}$ Bz; $\nu\text{C}=\text{C}$ conjugated alkene; $\nu\text{C}=\text{C}$ Nph |
| 1575 | |
| 1561 | δNH |
| 1492 | $\nu\text{C}=\text{C}$ |
| 1453 | $\nu\text{C}=\text{C}$, asym CH_3 deformation |

| | |
|------|---|
| 1386 | $\nu\text{C-C Nph}$ |
| 1335 | |
| 1259 | In-plane δCH of 1,4-disubstituted Bz |
| 1230 | In-plane δCH of 1,4-disubstituted Bz |
| 1175 | In-plane δCH of 1,4-disubstituted Bz |
| 1119 | In-plane δCH of 1,4-disubstituted Bz |
| 987 | In-plane δCH of 1,4-disubstituted Bz; $\nu\text{N-N}$ |
| 596 | In-plane $\delta\text{C(C=O)C}$ |
| 465 | Out-of-plane δNph ring |

AR18

| | |
|------|--|
| 1589 | (azo form) βCH , νCC /(hydrazo form) βCH , νCC , δNH , $\nu\text{C=O}$ |
| 1572 | δNH , βCH , νCC |
| 1513 | δNH , $\nu\text{C=O}$, $\nu\text{C=N}$, $\beta\text{CH}/\beta\text{CH}$, νCC |
| 1478 | βCH |
| 1458 | βCH |
| 1440 | βCH |
| 1397 | βCH |
| 1362 | νCC |
| 1298 | δNH , $\nu\text{N-N}$, βCH , νCC |
| 1237 | δNH , $\nu\text{N-N}$, βCH , νCC |
| 1215 | |
| 940 | |
| 691 | |
| 496 | Out-of-plane ring deformation |

AV7

| | |
|------|--|
| 1604 | $\nu\text{C=C Bz}$; $\nu\text{C=C conjugated alkene}$; $\nu\text{C=C Nph}$ |
| 1555 | δNH |
| 1515 | δNH , $\nu\text{C=O}$, $\nu\text{C=N}$, $\beta\text{CH}/\beta\text{CH}$, νCC , δNH |
| 1487 | $\nu\text{C=C}$ |
| 1405 | $\nu\text{N=N}$ |
| 1359 | Sym CH_3 deformation |

1405 N=N stretching

| | |
|------|---|
| 1362 | Aromatic ring vibration/ $\delta(\text{CH})\text{ring}$, Sym CH_3 def vib |
| 1330 | |
| 1280 | SO_3^{2-} |
| 1215 | SO_3^{2-} ; OH def vib and C-O str combination |
| 1171 | Aromatic $=\text{C-H}$ in plane def vib |
| 1109 | |
| 998 | SO_3^{2-} , Aromatic $=\text{C-H}$ in plane def vib |
| 986 | |
| 899 | SO_3^{2-} , Aromatic $=\text{C-H}$ out of plane def vib |
| 505 | Out-of-plane ring def vib |
| 484 | Out-of-plane ring def vib |

AR26

| | |
|------|--|
| 1610 | $\nu\text{C=C Bz}$; $\nu\text{C=C conjugated alkene}$; $\nu\text{C=C Nph}$ |
| 1581 | $\nu\text{C=C Bz}$; $\nu\text{C=C conjugated alkene}$; $\nu\text{C=C Nph}$ |
| 1548 | |
| 1493 | $\nu\text{C=C}$ |
| 1415 | $\nu\text{N=N}$ |
| 1380 | Sym CH deformation (C-CH_3), $\delta\text{s CH}_3$ |
| 1342 | δCH |
| 1305 | |
| 1245 | |
| 1226 | SO_3^{2-} , OH deformation and $\nu\text{C-O}$ combination |
| 1171 | |
| 1137 | $\nu\text{C-N}$ |
| 1050 | Methyl benzene CC skeletal vibration rocking |
| 998 | SO_3^{2-} , OH deformation and $\nu\text{C-O}$ combination |
| 938 | δOH |
| 890 | SO_3^{2-} ; γ aromatic $=\text{C-H}$ |
| 744 | |
| 718 | γ C-H |
| 699 | |
| 558 | |
| 493 | γ ring deformation |
| 471 | γ ring deformation |

DR28

| | |
|------|---|
| 1594 | $\nu\text{C=C Nph}$; NH scissor vibration |
| 1453 | $\nu\text{C=C}$, δCH |
| 1402 | $\nu\text{N=N}$ |
| 1374 | |
| 1332 | |
| 1285 | δNH , $\nu\text{N-N}$, βCH , νCC |

| | |
|---|---|
| 1335 | 1248 δ NH, ν N-N, β CH, ν CC |
| 1279 SO ₃ ²⁻ | 1206 |
| 1218 | 1154 |
| 1170 β aromatic =C-H | 1041 |
| 1110 | |
| 1004 | |
| 989 SO ₃ ²⁻ , β aromatic =C-H | |
| 898 γ aromatic =C-H | |
| 502 γ ring deformation | |

The Flavazine L azo dye (AY11) has an opposite behaviour respect the other analysed azo dyes. The complex ring structure with five terms, probably allowed quenching resonance between the two phenyl rings and quenched fluorescence. This permitted to have a spectrum with well-defined Raman bands and good spectral quality using 532 nm laser (table 7).

The very strong Raman band at 1598 cm⁻¹ and the very weak one at 1682 cm⁻¹ were assigned to the stretching of phenyl ring and to the OH group bending mode, respectively. The bands at 1512 and 1438 cm⁻¹ were attributed to the CH in plane bending contribution, and the asymmetrical stretching of N=N, C=C and N-N bond and the CH out-of-plane bending mode of the phenyl rings, respectively.. The medium intensity peak at 1271 cm⁻¹ was assigned to the –N=N=C–C–bending mode. Other characteristic bands were observed at 1170 (phenyl-2 bending mode and C-N stretching mode); 1050 (phenyl-1 bending mode, N-N asymmetric stretching and the C–SO₃-Na symmetrical stretching modes); 997, 916, 566 and 466 cm⁻¹ (CH out-of-plane).

Table 7: Tentative band assignment published on “N.Peica, Journal of Raman Spectroscopy 36 (2005)”

AY11

| |
|--|
| 1651 δ (OH), ν s(C4=C5), δ (ph-1,ph-2) |
| 1599 ν (ph-1, ph-2); β C-H (ph-1,ph-2); δ (OH) |
| 1547 β C-H def. (ph-1); δ (C4–C3=N2); δ (C4=C5-N1) |
| 1519 β C-H def. (ph-1) |
| 1438 γ C-H def. (ph); ν as(N1-N2, C4=C5, N8=N9) |
| 1334 N(-C-N8=N9-C-) |
| 1273 δ (-N1-N2=C3-C4-) |
| 1220 τ (C-H), δ (N2=C3-C4), ν (C4=C5) |
| 1170 δ (ph-2), ν (C4-N8), ν (C10-N9) |
| 1122 γ C-H def. (ph-1, ph-2) |
| 1089 δ (ph-2) |
| 1050 δ (ph-1), ν as(N=N), ν s(C-SO ₃ -Na+) |
| 999 γ C–H def. (ph-1) |

| | |
|-----|---|
| 916 | γ C-H def. (ph-2) |
| 794 | γ pyr.; δ (SO ₃ -) |
| 567 | γ C-H (ph-1,ph-2) |
| 467 | γ C-H (ph-1,ph-2) |

Thiazine dyes

Thiazine dyes were characterised by a heterocyclic ring, having molecular structures that include an aromatic ring containing four carbon atoms, one nitrogen atom and one sulfur atom. One of the most used dyes belonging to this class was Methylene Blue (BB9), which has been used in many different fields such as biology and medicine.

Micro Raman analysis of Methylene Blue (BB9) performed directly on wool fibre showed a well resolved spectrum at 532 nm. The two heteroatoms presented in the heterocyclic ring quenched fluorescence allowing distinguishing intense and characteristics bands of the dye (table 8). The Raman spectrum showed a very strong band at 1624 cm⁻¹ attributed to CC and CN stretching and in plane bending of CH of the ring; some medium bands at 1430 (CC stretching, CN symmetrical stretching and CH out-of-plane bending), and at 1389 cm⁻¹ (stretching of CN lateral and central bond, CC stretching, CH ring in plane bending and CH out-of-plane bending). Moreover, in the region 780-450 cm⁻¹ weak bands were observed that could be assigned to skeletal deformation of CN, CH₃ or CS bonds.

Analyzing the dyed fibre with 785 nm laser, no representative peaks were recognizable due to a high fluorescence effect.

Table 8: Tentative band assignment published on "P.H.B. Aoki, Vibrational spectroscopy 54 (2010)"

| BB9 | |
|------------|--|
| 1624 | vCC; β CH ring; vCN |
| 1430 | γ CH, v CC, vs CN |
| 1389 | vs CN (lateral and center); β CH ring; γ CH; vCC |
| 1298 | vs CN (center); β CH ring; vCC |
| 1073 | v as CS ; β CH ring; γ CH |
| 1032 | |
| 772 | CN and CH ₃ skeletal deformation; β CH |
| 670 | CC skeletal deformation; γ CH |
| 596 | Torsion of molecule; γ CH ring, CC skeletal deformation |
| 503 | CN and CH ₃ skeletal deformation |
| 446 | CN. CS and CH ₃ skeletal deformation |

3.3.1.4 Principal Component Analysis

Multivariate analysis was performed in order to evaluate the data dispersion and to better characterize the different dyes. In more detail, PCA was performed on dyes spectra acquired at 532 and 785 nm laser.. The spectra observed at different excitation wavelengths have been processed in order to understand if the different dye classes and/or each single dye could be differentiated. Moreover, the azo dyes spectra performed at 785 nm have been analyzed with the purpose of underlay the discrimination between each dye. Furthermore a spectrum carried out on a real fibre of Orange II, with the 785 nm excitation wavelength, has been insert in the matrix data to evaluate if the azo dyes discrimination match with a real sample.

Several mathematical pre-treatments for the reduction of unwanted spectral variations were applied, evaluating the effectiveness in the extraction of useful information. For processing the spectra achieved with 785 nm laser and for azo spectral data, a first derivative (Savitzky-Golay method), using first third-order polynomials and 11 datapoint gaps, coupled with SNV transform and linear detrending were finally chosen; for the spectra carried out with 532 nm laser the pre-treatments applied were a first derivative (Savitzky-Golay method), coupled with linear detrending.

Particular attention was devoted to the examination of these results, which were able to provide a satisfactory discrimination of all the different dyes species.

PCA of spectra dyes at 532 nm

The PCA score plot for conventional micro-Raman spectra results in the discrimination of each dye classes (Fig. 14). In particular at positive PC1 and PC2 values was thiazine dye (Methylene Blue BB9) corresponding to the band at 1620 cm^{-1} (ν_{CC} ; β CH ring; ν_{CN}); at positive PC1 and negative PC2 values were triarylmethane dyes, in particular BB11 and BB26. The bands at 1610 cm^{-1} ($\nu(\text{C}-\text{C})_{\text{ring}}$) and 1170 cm^{-1} ($\nu_{\text{s}(\text{CCC})}$ / $\delta(\text{CCC})_{\text{breathing}}$ / $\delta_{\text{r}}(\text{CH}_3)$) differentiated these two dyes; moreover, a distinction between the two triarylmethane dyes were possible thanks to the bands at 1470 cm^{-1} ($\delta_{\text{as}}(\text{CH}_3)$), 880 cm^{-1} ($\delta(\text{CCC})$) and 518 cm^{-1} . The negate values for both PC1 and PC2 corresponded to azo yellow dyes (Flavazine L AY11), characterized by the band at 1596 cm^{-1} attributed to $\nu(\text{ph-1, ph-2})$; β C-H (ph-1,ph-2); $\delta(\text{OH})$. Finally, in the middle, at neutral PC1 and PC2 was the blue azo dye Water Blue IN (AB93) with the bands at $1574, 1523, 1165\text{ cm}^{-1}$ ($\nu_{\text{s}(\text{CCC})}$ / $\delta(\text{CCC})_{\text{breathing}}$ / $\delta(\text{CH}_3)$) and 914 cm^{-1} ($\nu(\text{CC})_{\text{ring}}$).

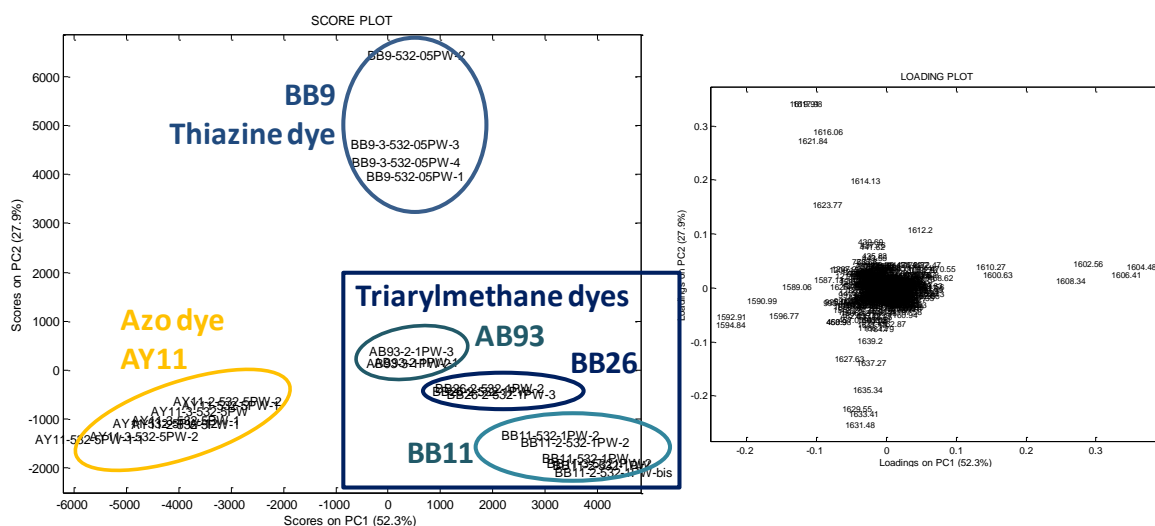


Fig. 14: PCA score and loadings plot of micro-Raman spectra of dyes achieved with 532 nm laser

PCA of dyes obtained at 785 nm excitation wavelength

The PCA score plot for conventional micro-Raman spectra at 785 nm resulted in the potential discrimination of dyes classes (azo and tryarilmethane dyes) and in a sort of differentiation of azo dyes (Fig. 15). In particular at positive PC1 were present Orange II (AO7) with also positive PC2 values and Ponceau RR (AR26) with negative PC2 values; AO7 were distinguished by bands at 1595 ($\nu\text{C}=\text{C}$ Bz; $\nu\text{C}=\text{C}$ Conjugate alkene; $\nu\text{C}=\text{C}$ Nph) and 1450 cm^{-1} . Ponceau RR (AR26) was discriminated by the bands at 1409, 1345 and 1240 cm^{-1} , characteristics of the $\text{N}=\text{N}$ stretching and the CH bending. The negative PC1 values corresponded to Amino Naphtol Red G (AR1), when PC2 values were positive, and Conchineal Red A (AR18), when the PC2 values were negative. AR1 was distinguished thanks to the bands due to NH bending at 1550 cm^{-1} and the $\text{N}=\text{N}$ stretching at 1045 cm^{-1} . On the other hand, the AR18 dye was recognize by the bands at 1510 cm^{-1} , due to NH bending, $\text{C}=\text{O}$, $\text{C}=\text{N}$ and CC stretching and in plane CH bending; 1459 and 1434 cm^{-1} , distinctive for in plane CH bending, and 1236 cm^{-1} attributed to the $\text{N}-\text{N}$ and CC stretching, NH bending and in plane CH bending. In the centre of the plot at neutral PC1 values were triarylmethane dyes (BV1 and BV3) and at positive PC2 values were AV7 and DR28. The two arylmethane dyes were only one group with characteristics bands at 1389 cm^{-1} ($\delta(\text{CH})$, $\delta\text{s}(\text{CH}_3)$, $\delta(\text{CCC})\text{ring}$), and 1180 cm^{-1} ($\nu\text{s}(\text{CCC})$, $\delta(\text{CCC})\text{breathing}$, $\delta(\text{CH}_3)$); AV7: 1480 ($\nu\text{C}=\text{C}$), 1403 ($\nu\text{N}=\text{N}$) and 1110 cm^{-1} ; DR28: 1590 ($\nu\text{C}=\text{C}$ Nph, NH scissor vib) and 1250 cm^{-1} ;

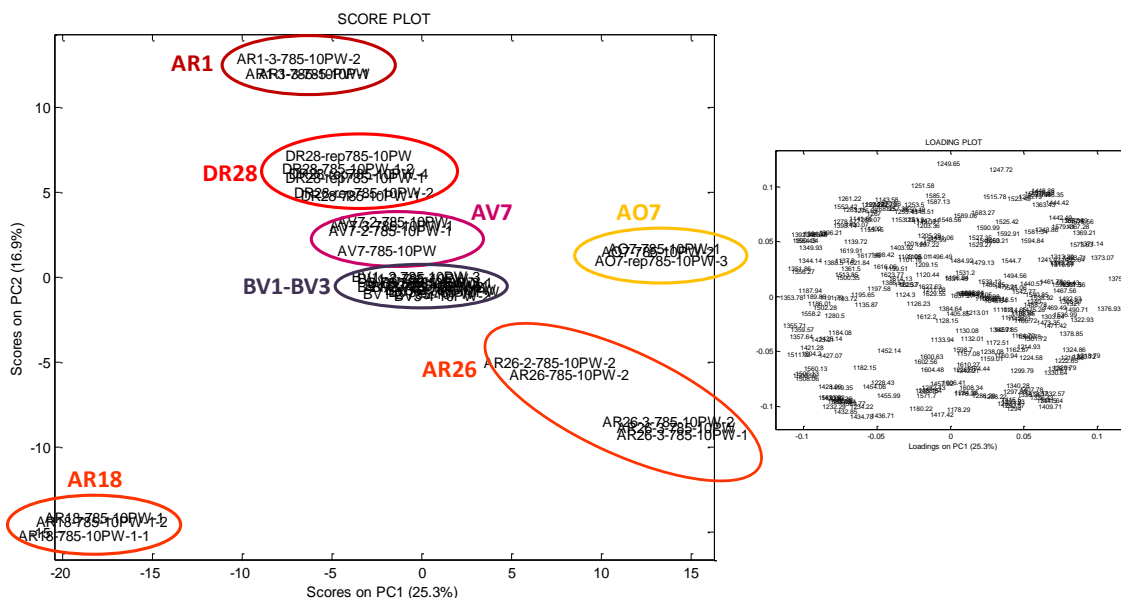


Fig. 15: PCA score and loadings plot of micro-Raman spectra of dyes achieved with 785 nm laser

In this PCA score plot of spectra obtained with the 785 nm laser a good discrimination between each azo dye has been reached. For this reason, a multivariate analysis of only azo dye spectra has been conducted.

PCA of azo dyes obtained at 785 nm

A spectrum of a real fibre sample, coming from a sample book developed by Adolf Lehne and published in 1983, analyzed with the 785 nm excitation wavelength, has been insert in the plot matrix in order to validate this analytical approach and the discrimination also for real samples.

The score plot (fig. 16) showed a possible distinction of each azo dye and a correspondence between the real and the standard samples of the same dye. AR18 was identified at PC1 positive values with characteristics bands at about 1510 cm^{-1} (δNH , $\nu\text{C=O}$, $\nu\text{C=N}$, βCH or βCH , νCC , δNH for azo and hydrazo tautomer, respectively) and 1350 cm^{-1} (νCC). At neutral PC1 and negative PC2 values was AR1 with bands at about 1590 cm^{-1} ($\nu\text{C=C Bz}$; $\nu\text{C=C}$ conjugated alkene; $\nu\text{C=C Nph}$) and 1220 cm^{-1} (SO_3^{2-} ; OH def vib and C-O str combination). On the other hand, at negative PC1 and PC2 values was AO7 standard and real samples differentiated thanks to the band at 1596 cm^{-1} , attributed to the stretching of C=C of benzene, C=C of conjugate alkene and C=C of naphthalene groups. DR28 was identified at neutral PC1 and PC2 score values due to the bands at 1405 cm^{-1} ($\nu\text{N=N}$), and 1150 cm^{-1} ; AV7 is located in the score plot just above DR28 (positive PC2 values) and it was distinguished for the band at 1280 cm^{-1} , attributed to the vibration of SO_3^{2-} , and for the 510 cm^{-1} band, due to the out-of-plane ring deformation. Finally, at negative PC1 and positive PC2 score values AR26 was observed, identifiable for the symmetrical CH deformation of C- CH_3 bond and CH_3 symmetrical bending (1379 cm^{-1}), the CH bending (1340 cm^{-1}) and the 1240 cm^{-1} band.

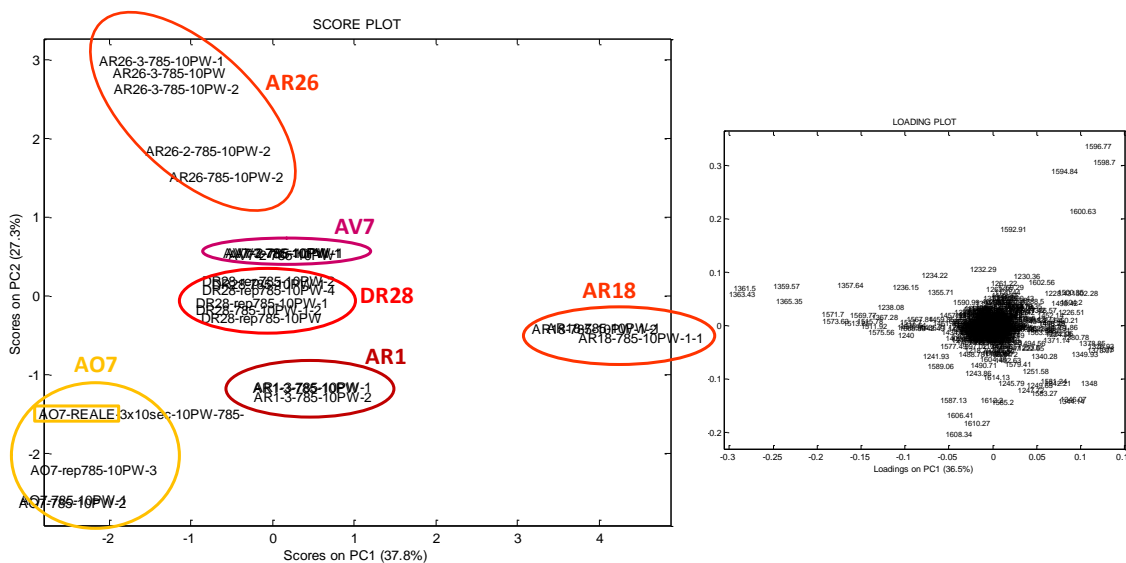


Fig. 16: PCA score and loadings plot of micro-Raman of azo dyes spectra obtained at 785 nm

The multivariate analysis performed on all these different dyes could allow distinguishing not only the dyes classes but also the each dyestuff of standard sample and also on a real one. This demonstrates that this technique could be certainly applied direct not only on standard fibres dyed but also on real fibres. In order to confirm this hypothesis further analysis have to be performed on real samples, but the main point was that also real fibres could contain a great amount of dyestuff not below the LOD.

3.3.1.5 Conclusions

The present study demonstrate the possibility to use micro-Raman spectroscopy as a technique of examining wool dyed fibres, obtaining good and meaningful spectra. First of all, to obtain good Raman spectra the quantities of dyes on the wool fibre have to be enough and not below the detection limit of the Raman technique. Moreover, the sample preparation here proposed has an high importance because it permits to reach a correct in-focus position on the fibre improving Raman spectra. Finally, the possibility to employ different laser wavelength has a great importance in order to determine the best analytical condition for analyze each dye and to create a database.

It is demonstrated that micro-Raman spectra allowed distinguishing not only the different dye classes, but also each single dye belonging to the same class. The PCA analysis underlined this behaviour and clearly divided the triarylmethane, azo and thiazine dye clases and mainly for azo dyes –due to the large number of dyes analysed at the same condition- it was possible to distinguish each colorant based on characteristics bands. In order to better understand and validate the distinction observable with PCA, a new matrix will be calculated including spectra

achieved with both lasers for each dye. This will probably allow to better distinction of dyes classes.

For each organic synthetic dye the best laser to use was indicated, a list of characteristics bands was shown, and a tentative band assignment was proposed. As a general indication for direct analysis on wool fibres dyed with synthetic organic colorants, we can suggest to use the 532 nm excitation wavelength for analysing yellow and blue dyed fibres, whereas for red, orange and violet wool fibres the 785 nm laser could be positively applied.

Finally, it has been also demonstrated that micro-Raman could be also applied on real sample, as the analysis on a real fibre dyed with AO7 revealed. Other real fibres are under investigation in order to confirm what has been observed and suggested from standard fibres analysis.

3.2.2 SERS on wool dyed fibres using photoreduced AgNPs

SERS analysis have been performed as second step in this research and only wool dyed fibres who not present any Raman spectra have been investigated.

SERS is a well known and a powerful technique for examining organic dyes, but the requirement to use metal nanoparticles (Ag is the most used) in colloidal solution makes it expensive and with a certain degree of destructiveness for the sample. Indeed, the area of the fibre investigated with SERS has AgNPs on the surface at least, and this means that further analysis cannot be performed; in this area also a variation in tint is visible. Moreover, the preparation of AgNPs not only require time but also the addition of reagents or stabilizer additives can affect the spectra detecting spurious bands.

All things considering, in this work an analytical approach based on silver photoreduction has been successfully developed. The use of AgNPs photoreduced has a great importance due to a reduction of “contaminated area” that is of about 10 μm , and also due to the exclusion of reagents or stabilizer additives that allowed to acquire SERS spectra free of spurious bands.

3.2.2.1 Ag photoreduction methods

Silver photoreduction methods have been used by several authors to create AgNPs by means of laser photoreduction of a silver nitrate solution on silica colloids [111], on a glass substrate [112], mixed with sodium citrate [113] or directly with the sample [80]. In detail, Muniz-Mirada [111] obtained Ag-doped colloidal silica, irradiating with an argon ion laser a solution in which silver nitrate aqueous solution was added dropwise to colloidal silica. During irradiation, the colourless suspension became brown–yellow, indicative of the presence of silver aggregates on the silica particles. Bjerneld *et al.*[112] used a method for the in situ fabrication of AgNP based on a laser and micro-Raman coupled device. By this system authors were able to fabricate small dimension AgNPs, formed in the area where the laser spot was focused. However, they used a laser to rather enhance the Ag^+ chemical reduction induced by the citrate also existing in the mixture. Moreover, in the latter study citrate was employed as a molecular probe to check the in situ effectiveness of the so-prepared nanoparticles. Sato-Berrù [113] prepared Ag colloids by a direct photoreduction process of the AgNO_3 in sodium citrate solutions, testing different irradiation times. Finally, Ahern *et al.* [80] obtained high-quality surface-enhanced Raman spectra of pyridine, citrate, and biotin from AgNO_3 solutions of the analytes. Ag metal particles were generated in situ by laser illumination of AgNO_3 solutions. Authors underlined that although the quality of the photo-colloid SERS spectra was comparable to that obtained for conventional Ag colloids, the photo-colloids cannot always be used to probe low analyte concentrations.

Recently, Cañamares *et al.* [89] prepared immobilized AgNPs by photoreduction of Ag⁺ by using a 514.5 nm laser/micro-Raman coupled system. The AgNPs preparation was performed in the absence of other reagents (only the counterion of Ag⁺, nitrate, is present in the medium) in order to avoid the appearance of spurious bands in the SERS spectra. In this study, the attention was centered on the morphology and SERS efficiency of AgNPs prepared at different experimental conditions: laser power, laser irradiation time, Ag⁺ concentration, and immobilization substrate (neat compound, normal filter paper, photographic paper and tempera binding medium). The preparation of these photoreduced AgNPs was also aimed to find a sensitive and micro-destructive method for the *in situ* analysis of pigments and dyes in their substrates, with the extra advantage of a high spatial resolution resulting from the combination of micro-Raman and SERS techniques. In this paper, Cañamares *et al.* observed that: (a) hydrophilic surfaces are needed for the immobilization of AgNPs; (b) the size of AgNP aggregates increases with the irradiation time, the laser power and the metallic cation concentration; (c) the nanoparticle morphology, the shape of photoreduced AgNPs can be classified into two classes attending to the morphology: spherical and planar. The latter are likely formed after 15 min of irradiation, and seem to be the responsible for the remarkable SERS intensification observed after this time. Kept this preparation method unchanged, Jurasekova *et al.* [102] exploited photoreduced AgNPs directly on the dyed fibre in order to obtain good SERS dyes spectra and to perform *in situ* detection analysis.

3.2.2.2 Experimental procedure and applied method

The preparation of photoreduced Ag nanoparticles have been clarified in Figure 17 where the experimental procedure followed for the preparation of the immobilized AgNPs on dyed fibres have been displayed.

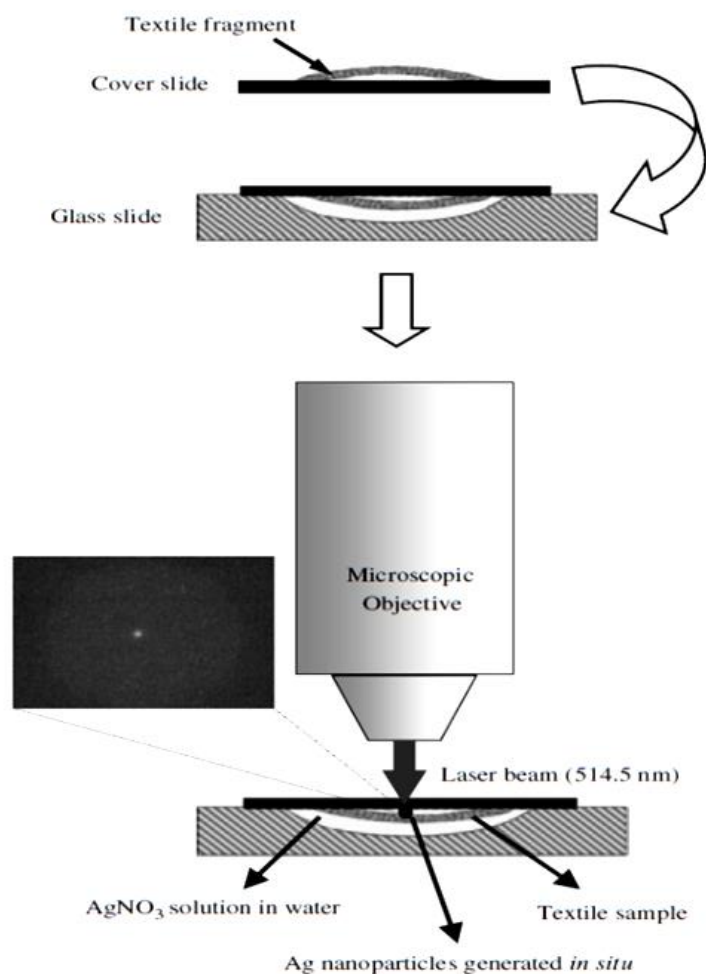


Fig. 17: Method for in situ preparation of photoreduced Ag nanoparticles on textile fibres.

The first step in the experimental procedure was the sampling of 20-mm-length fibre fragment and the fastening of the sample to a cover slide. After, the central well of a glass slide was filled up with 10^{-3} M AgNO_3 solution, and covered with the slide supporting the fixed fibre. Then, a laser beam at 514.5 nm was focused on the surface of the fibre with a 100x objective to induce the formation of immobilised Ag nanoparticles on a spot of approximately $1\ \mu\text{m}$. The irradiation time was 5 and 15 min for silk and wool fibres, respectively. This method was applied on the detection of Luteolin and Apigenin on silk and wool fibres [102] and red and yellow mordant dyes on wool or linen fibers [114].

Starting from this successful method, in the present research work some parameters have been changed in order to optimize an analytical procedure for the SERS analysis of wool fibres dyed with organic synthetic dyestuff.

The established experimental procedure is analogous to that just explained. The aqueous silver nitrate solution was deposited on a glass slide provided with a well in the center (2 cm of diameter and 0.38 mm of depth). The glass slide was previously cleaned with ethanol and milliQ water. A 10-mm-long single dyed fibre fragment was fixed to a cover slide. The solution was then covered with that cover slide. The laser beam at 532 nm or 442 nm was focused in

the internal side of the cover slide corresponding to the surface of the dyed fibre by using an optical microscope with a 100x objective. AgNPs were prepared at different experimental conditions by modifying the excitation wavelength (442 nm or 532 nm); the laser irradiation power on the sample (2.5 mW and 1.5 mW) and the irradiation time. The AgNO₃ concentration remained fixed at 0.1 M.

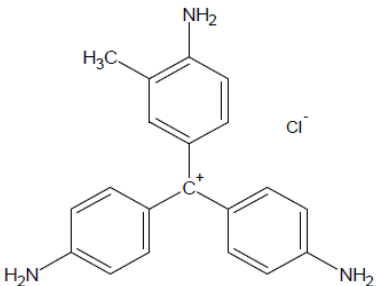
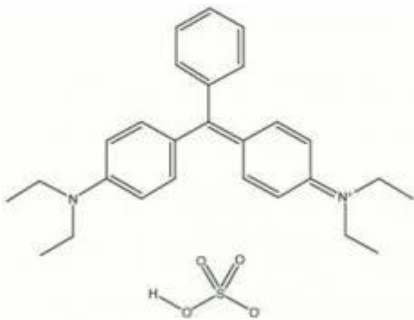
After the preparation of AgNPs, the cover slide was removed and the fibre was thoroughly washed with milliQ water several times. SERS of the fibres was obtained by placing milliQ water in the well of a glass slide and then covered with the washed cover slide containing the wool dyed fibre with immobilized AgNPs.

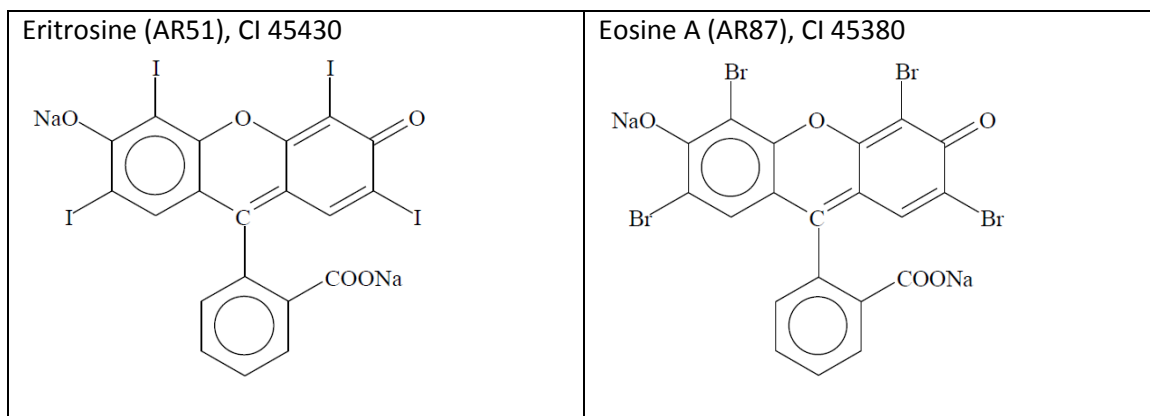
In conclusion, in order to obtain good SERS signals from AgNP prepared by photoreduction and immobilized on fibre without burning the sample, two different experimental methods have been developed. In the first experimental method the the laser at 532 nm excitation wavelength with a power of 2.5 mW was focalized on the fibre for 20 minutes. The second analytical approach was developed with 442 nm laser, the AgNPs were photoreduced using 1.5 mW laser power for 2 minutes.

3.2.2.3 Samples

Proteinic (wool) fibers dyed with triarylmethane and xantene dyes, were analysed. It is the first time that these two classes of dyes were analysed directly on fibre with photoreduced AgNP. The four dyes analysed were: two triarylmethane, Fuchsin (BV14) and Diamond green G (BG1) and two xantene dyes, Eritrosine (AR51) and Eosine A (AR87) (table 9).

Table 9: Molecular structure of analysed dyes.

| | |
|---|---|
| <p>Fuchsin (BV14), CI 42510</p>  | <p>Diamond green G (BG1), CI 42040</p>  |
|---|---|



Dyed wool fibres (belonging to the CHARISMA project) were prepared at the OCW-RCE laboratories. Three recipes were established to obtain the reference materials. The acid, direct and basic dyes recipes were based on historical recipes given in the sample book developed by Adolf Lehne in 1893 [107]. The quantities and parameters were adapted and laboratory recipes were prepared using analytical grade chemicals and demineralized water. Although these recipes do not completely follow the original historical recipes, reproducible dyeings were produced. Prior to dyeing, the wool (Bluefaced Leicester, brand: Rowan, Purelife) was washed with 10% (wool weight) Marseille soap at 40°C for one hour. Next, bundles of 10 g each were made and they were tied with nylon tyrapts to prevent wool from entangling.

The recipe followed to dye wool fibres with basic dyestuff indicated the use of water heated at 70 °C in which 100 mg of a basic dye were dissolved. 10 g of wool bundle were soaked in the dye bath, thus prepared, and put in oven at 70 °C for 30 minutes. Finally the bundle is left to cool down in the dye bath, and afterwards it is rinsed with demineralized water.

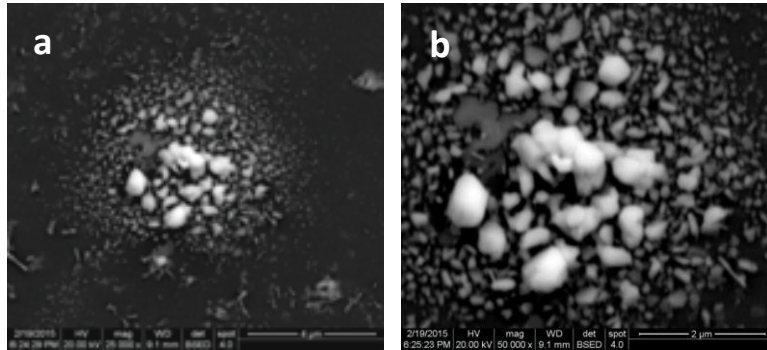
3.2.2.4 Results and Discussion

Effect of laser and irradiation time on AgNPs size

Figure 4 showed the SEM micrographs corresponding to the two different methods developed. As can be seen, the metal spots are actually integrated by a large number of small AgNPs displaying two different characteristic morphologies: spheroids and nanodisks or planar particles, in some cases displaying a triangular shape. In addition, the latter particles seem to be present at both irradiation lasers, as deduced from micrographs 18a and 18c. Planar AgNPs have been obtained by other authors upon Ag^+ photoreduction by means of laser irradiation of AgNP seeds [115]. The fact that only certain AgNPs become planar is attributed to the absorption of 442 nm or 532 nm light by AgNP seeds having an appropriate size to grow with this laser irradiation, because of the selective SPR absorption at this excitation wavelength [115]. The AgNPs photoreduced with 442 nm laser showed various dimensions (fig. 18c,d) probably due to the very short time of photoreduciton. This distribution was well visible also in

the fibre where, even if the AgNPs were dispersed and not all concentrated in the same 10 μm spot, some planar particles, nano-aggregates and spheroids were presented. Moreover, observing SEM images of AgNPs photoreduced with 442 nm laser (fig. 18c,g,e,f), some differences between nanoparticles produced on glass slide or on fibre emerge. Indeed, the AgNPs on the fibre are mainly constituted by spheroidal nano particles or nano-aggregated rather than the great plate or triangular particles observable on glass slide.

Laser 532 nm; 2.5 mW; 20 minutes



Laser 442 nm; 1.5 mW; 2 minutes

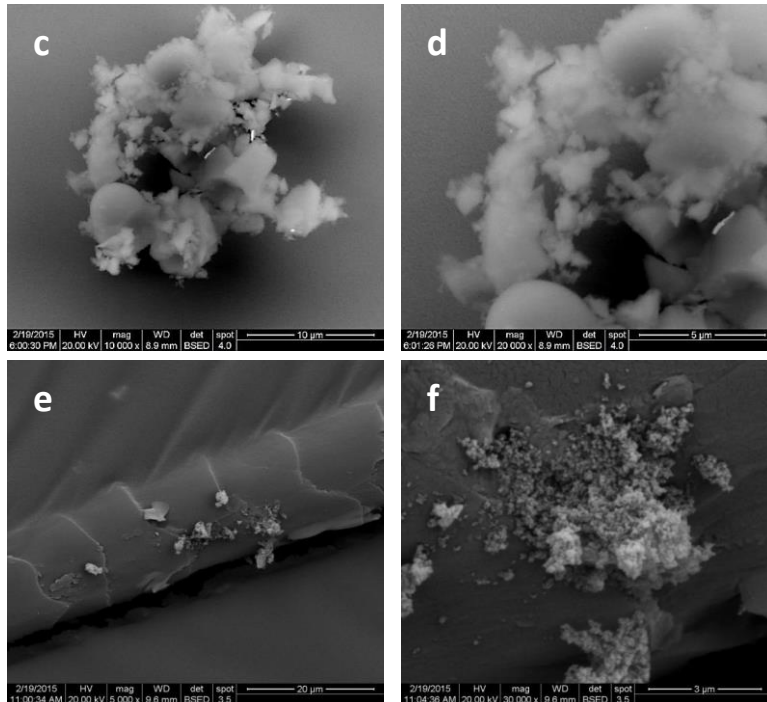


Fig. 18: SEM micrographs of AgNPs registered at the following conditions: 532 nm laser, 2.5 mW, irradiation time 20 min (a and b); 442 nm laser, 1.5 mW, irradiation time 2 min on glass slide (c and d) and on fibre (e and f).

Fuch sine (BV14) SERS spectra

Fuch sine BV14 SERS spectra have been achieved with both AgNPs photoreduced at 532 nm and 442 nm lasers. The first important result reached in this research, was the identification of two behaviours: the photoreduced AgNPs using a 532 nm laser only provided a SERS spectrum with the 532 nm excitation wavelength, while photoreduced AgNPs obtained at 442 nm laser afforded d SERS signal when analyzed with 442, 532 and 785 nm excitation wavelengths.

Considering the SERS spectra achieved with different lasers, some differences in the intensities of peaks were evident (fig. 19).

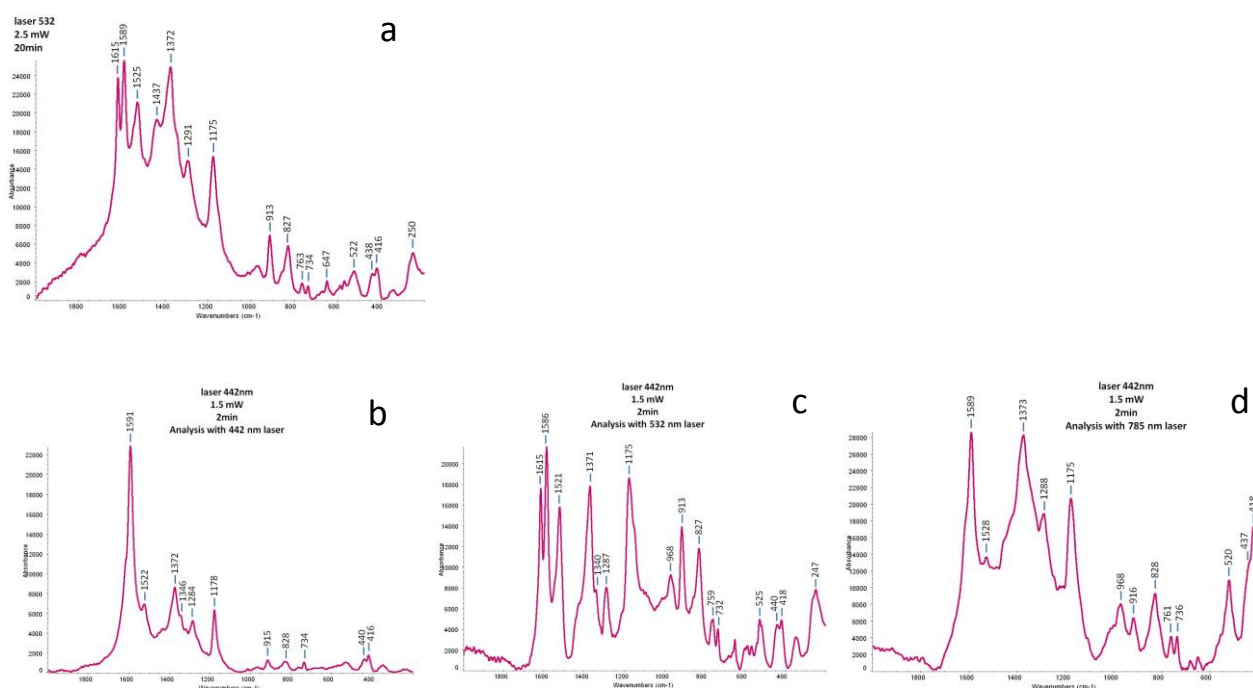


Fig. 19: Fuch sine (BV14) SERS spectra achieved with AgNPs photoreduced with 532 nm laser and analysed with 532 nm laser (a); AgNPs photoreduced with 442 nm laser and analysed with 442 nm laser (b), 532 nm laser (c) and 785 nm laser (d)

This different behaviour regarding the SERS intensification were given by the combined resonance properties of the metal plasmon and the molecule. The structure of the molecule is essential to explain the resonance conditions. Fuch sine is a tri-p-aminophenyl carbonium ion, in which the three rings are arrayed around the central carbonium atom. This structure molecule is analogous to the well described Crystal Violet molecule and we can assume that these two triarylmethane dyes have the same D_3 symmetry point group. The D_3 symmetry group is characterized by an identity (E), a n -fold axis of rotation with n_2 -fold rotations about the axis which is perpendicular to the principal axis. Thus, each of the observed bands can be assigned on the basis of D_3 group to either an a_1 or e irreducible representation. In columns 4 and 5 of table 2 the irreducible representation of each band and benzene mode, which is most closely involved in vibration, are listed according to the published research of Cañameres et al.

[116] and also a brief description of other principal atomic motions involved in the vibration is reported.

Our assignments agree with those of Doerty et al. [117] and are also similar to those done by Cañamares et al. [116] for Cristal Violet molecules.

Table 10: SERS assignment of Fuchsine (BV14)

| photor. λ 532 nm anal. λ 532 nm | photor. λ 442 nm | | | | benzene modes | description of vibration contributing to the normal mode |
|---|-----------------------------|------------------------|------------------------|----|--------------------------------|--|
| | anal. λ 442 nm | anal. λ 532 nm | anal. λ 785 nm | | | |
| 1615 vs | 1617 sh | 1615 vs | 1617 sh | a1 | 8a | v(C-C)ring |
| 1589 vs | 1591 vs | 1586 vs | 1589 vs | e | 8a | v(C-C)ring |
| 1525 m | 1522 w | 1521 s | 1528 w | e | 8b | v(Cring-N) / δ_s (CH3) |
| 1437 vw | 1434 sh | 1428 sh | 1431 sh | | | |
| 1372 s | 1372 m | 1371 vs | 1373 s | e | v0-N | v(CcenterC)/ δ (CCC)ring / δ (CH) |
| 1345 sh | 1346 vw | 1340 vw | | e | δ (ϕ -N) | vas(CCcenterC)/d(CCC)ring/d(CH) |
| 1291 w | 1284 w | 1287 m | 1288 w | e | | vas(CCcenterC)/d(CCC)ring/d(CH) |
| 1175 s | 1178 m | 1175 vs | 1175 s | e | 9a | vs(CCC)/d(CCC)breathing/pr(CH3) |
| 966 w | 968 sh | 968 m | 969 m | a1 | 17a | |
| 913 m | 915 vw | 913 m | 916 w | e | 17a | δ (CCcenterC) |
| 827 m | 828 vw | 827 m | 826 m | e | 17b | d(CH)ring |
| 763 vw | 760 sh | 759 w | 761 w | a1 | 6a | vs(CCcenterC)/v(CN) |
| 734 vw | 734 vw | 732 w | 736 w | e | 4 | v(CN) |
| 647 w | | 650 w | 649 vw | | | |
| 522 w | | 525 w | 520 m | e | 16b | δ (CNC) |
| 438 w | 440 vw | 440 w | 437 sh | a1 | 16a | d(CC) |
| 416 w | 416 vw | 418 w | 418 s | e | 16a | d(CNC)/d(CCC), d(SO3)) |
| 343 vw | 347 vw | 345 w | | e | δ (ϕ -C- ϕ) | γ (CNC)/pr(CH3) |
| 250 m | | 247 m | | e | δ (ϕ -C- ϕ) | γ (CNC)/pr(CH3) |

Although in the four SERS spectra the bands observed are at the same wavenumbers, it is clear that the intensity enhancement differs depending on the excitation line used for the analysis and secondly on the type of photoreduced AgNPs. In particular both the spectra acquired with the 532 nm excitation wavelength present some bands more enhanced compared with the other SERS spectra. This is due to the higher resonance contribution at this excitation. Indeed, the bands mainly enhanced are at 1615 cm^{-1} attributed to the symmetrical 8a benzene mode; 1525 cm^{-1} due to the non-totally symmetric mode of 8b; 915 cm^{-1} produced by the non-totally symmetric 17a benzene mode and 827 cm^{-1} characteristic of non-totally symmetric mode due to a deformation of C-H bond of the ring. The symmetric a1 mode is enhanced thanks to the 532 nm laser resonance contribution through the Frank-Condon mechanism, whereas the non-totally symmetric modes are enhanced probably thanks to the Herzberg-Teller vibronic

coupling. Moreover, all the SERS spectra evidence that the non-totally symmetric bands are predominant and this is probably due to the molecule-metal surface interaction thus charge-transfer contribution [116]. All the SERS spectra present characteristics intense bands of non-totally symmetric stretching of C-C ring bond at 1590 cm^{-1} ; of stretching of $C_{\text{center}}-C$ and bending of C-C-C of the ring and C-H at 1370 cm^{-1} ; and of symmetric stretching of C-C-C combined with C-C-C deformation and CH_3 out-of-plane deformation at 1175 cm^{-1} .

Unfortunately, for this dye no comparison with FT-Raman spectrum can be performed, since only for this dye a high fluorescence effect conceals all the possible FT-Raman bands and finally it is not possible to obtain a meaningful spectrum. For this reason, it is not possible to compare the relative intensities and the wavenumbers of bands and neither suggest if a weak interaction (physisorption) occurs between the molecules and Ag nanoparticles or not.

Brilliant Green or Diamond green G (BG1) SERS spectra

The Diamond Green (BG1) molecule has a reduced symmetry compared with the tryarilmethane dyes class as reported by Beljonne et al. [118] which simulated the TPA spectrum of BG1 and found that the excited states of this dye with the lowest two resonances can unambiguously be associated with $1E'$ and $2A'$ states of the corresponding C_3 -symmetry structure. The doubly degenerate molecules are indicated with the letter E, and this means that there are two wavefunctions for one single energy state. The character for E is 2 because in this case we have two orbitals symmetric with respect to the identity (E) and for each axis of symmetry exist two different modes.

Also for this dyes, SERS spectra have been achieved with both AgNPs photoreduction methods and with the three wavelength lasers (442 nm, 532 nm and 785 nm) for AgNPs produced with 442 nm laser. The SERS spectra display dissimilarities in the intensities of peaks when registered at different excitation lines (fig. 20).

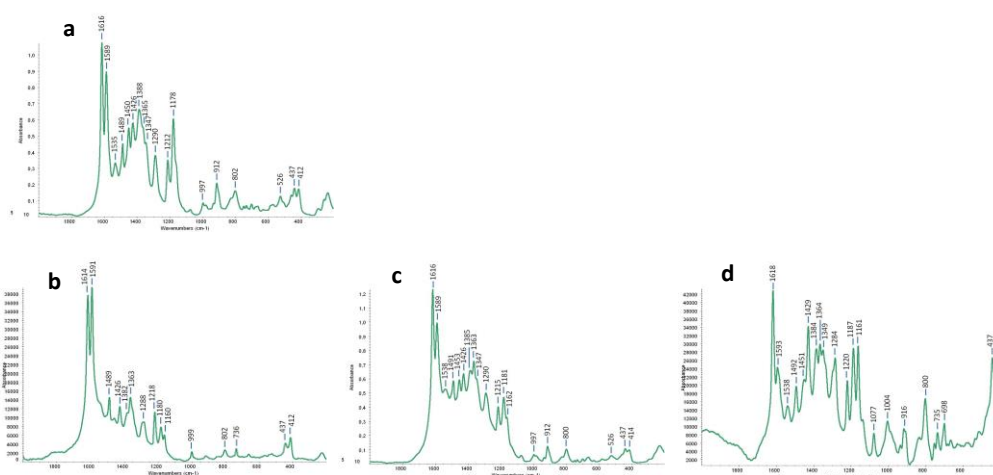


Fig. 20: Diamond Green (BG1) SERS spectra achieved with AgNPs photoreduced with 532 nm laser and analysed with 532 nm laser (a); AgNPs photoreduced with 442 nm laser and analysed with 442 nm laser (b), 532 nm laser (c) and 785 nm laser (d)

As Wu et al. [119] proposed, a characteristics peak of each dye was chosen to calculate each EF. The peak chosen was the 1590 cm^{-1} due to the stretching of the conjugated aromatic C-C bonds. The EF is defined by dividing the intensities of the Raman characteristics peak of the organic dye on the SERS substrate by its intensities on fibre.

$$EF = I_{\text{SERS}} / I_{\text{Raman fibre}}$$

The EF values of the SERS spectra achieved with AgNPs photoreduced with 532 nm laser and analysed with 532 nm wavelength, and with AgNPs photoreduced with 442 nm laser and analysed with 442 nm, 532 nm and 785 nm wavelengths are 4880, 1953, 4060 and 883, respectively. Brilliant green analysed with 532 nm laser resulted in the largest SERS enhancement factor (4880 and 4060 times), because its absorption I_{max} at 623 nm (Fig.21) is close to the line at 532 nm.

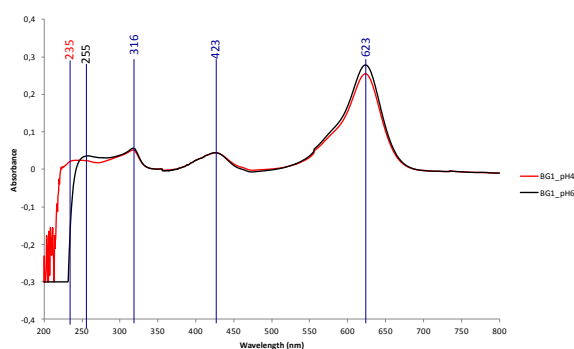


Fig. 21: UV-Vis spectra of BG1 achieved at pH6 (black line) and pH 4 (red line)

Observing the comparison of different SERS spectra and the FT-Raman (Fig. 22), and the table list of all peaks, some features are highlighted. The band at 1590 cm^{-1} , attributed to the stretching of the conjugated aromatic C-C bonds, is enhanced in the SERS spectra carried out at 442 nm and 532 nm. This band is probably due to a symmetric mode and the strong enhancement detectable in the SERS spectrum achieved with 442 nm excitation wavelength probably is caused by an additional resonance effect, proved by a second absorption band present in the UV-Vis spectra at 423 nm (Fig 21). The 1450 cm^{-1} band, probably due to a symmetric mode, is enhanced only for spectra acquired with 532 nm laser. In general, the spectra achieved with 532 nm laser are more enhanced because of the joint contribution of the molecular resonance and, most probably, the surface plasmon resonance in the SERS effect. In addition, the SERS spectra are characterized by medium bands of antisymmetrical CH₃ bending mode at 1489 cm^{-1} , of symmetric C-C_{center}-C stretching, the C-C-C breathing deformation and the C-H bending modes at 1215 cm^{-1} and of antisymmetric C-C_{center}-C stretching and C-H bending modes at 1180 cm^{-1} .

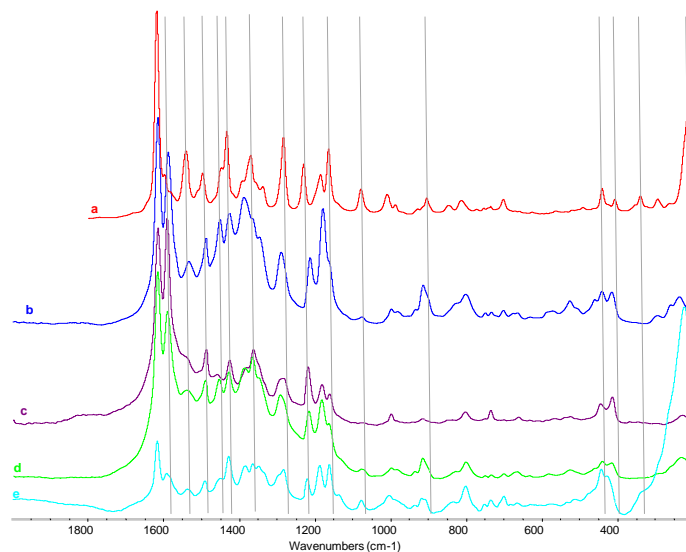


Fig. 22: Comparison between FT-Raman spectrum (a) and SERS spectra achieved with AgNPs photoreduced with 532 nm laser and analysed with 532 nm laser (b); AgNPs photoreduced with 442 nm laser and analysed with 442 nm laser (c), 532 nm laser (d) and 785 nm laser (e).

Moreover, the spectrum acquired with 785 nm excitation wavelength shows a strong enhanced band at 223 cm^{-1} distinctive of the Ag-N stretching, confirming the interaction between the metal nanoparticles and the dye. The spectral features of this 785 nm spectrum are quite similar to those observed for the FT-Raman, revealing the existence on the surface of molecules not bonded or slightly bonded to the metal surface.

Table 11: FT-Raman and SERS assignment of Diamond Green (BG1)

| BG1 Raman FT-Raman powder | BG1 SERS | | | | benzene modes | description of vibration contributing to the normal mode |
|------------------------------|--------------------------|------------------------|------------------------|------------------------|-----------------------|---|
| | photor. λ 532 nm | anal. λ 532 nm | anal. λ 442 nm | anal. λ 532 nm | | |
| 1619 vs | 1616 vs | 1614 vs | 1616 vs | 1618 vs | 8a | v(C-C)ring |
| 1597 sh | 1589 vs | 1591 vs | 1589 vs | 1593 sh | 8a | v(C-C)ring |
| 1542 s | 1535 w | 1539 sh | 1538 vw | 1538 w | 8b | v(Cring-N) / δ_s (CH3) |
| 1495 m | 1489 m | 1489 m | 1491 m | 1492 m | 19a | das(CH3) |
| 1447 sh | 1450 m | 1456 sh | 1453 m | 1451 sh | 19b | |
| 1432 s | 1426 m | 1425 m | 1426 m | 1429 s | | |
| 1389 sh | 1388 s | 1382 sh | 1385 vw | 1384 m | v0-N | δ (CH) / δ_s (CH3) / δ (CCC)ring |
| 1369 m | 1365 sh | 1363 m | 1363 m | 1364 m | v0-N | v(CcenterC) / δ (CCC)ring / δ (CH) |
| 1337 vw | 1345 sh | 1345 sh | 1347 sh | 1347 w | δ (ϕ -N) | vas(CCcenterC) / δ (CCC)ring / δ (CH) |
| 1284 s | 1290 s | 1288 m | 1291 m | 1284 s | | vas(CCcenterC) / δ (CCC)ring / δ (CH) |
| 1229 m | 1212 m | 1218 m | 1215 m | 1220 s | | vs(CCcenterC) / δ (CCC)breathing / δ (CH) |
| 1183 m | 1178 s | 1181 m | 1181 m | 1187 s | 9a | δ (C-H)ring / vas(CCcenterC) |
| 1164 s | 1160 sh | 1160 vw | 1162 sh | 1161 s | 9a | vs(CCC) / δ (CCC)breathing / pr(CH3) |
| 1079 w | 1078 vw | | 1078 vw | 1077 w | | |
| 1009 w | 997 vw | 999 vw | 997 vw | 1004 m | | δ (CCC) |
| 986 vw | | | | | | |
| 903 w | 912 m | 915 sh | 912 w | 916 m | 17a | v(CC)ring / δ (CCcenterC) |
| 847 vw | 832 sh | | 834 sh | 834 vw | | δ (CCC) |
| 815 w | 802 m | 802 w | 800 w | 800 s | 10a | δ (CH)ring |
| 736 sh | 736 vw | 736 vw | | 735 w | | v(CN) |
| 701 w | 701 sh | | 699 sh | 698 w | | |
| | 526 m | | 525 sh | 533 sh | 16b | δ (CNC) |

| | | | | | | |
|-------|--------|--------|--------|--------|------------------------------|---|
| 439 w | 437 w | 442 w | 437 w | 441 s | 16a | $\delta(\text{CC})/\delta(\text{CNC})$ |
| 406 w | 412 w | 411 m | 414 w | 426 w | 16a | $\delta(\text{CNC})/\delta(\text{CCcenterC}), d(\text{SO}_3)$ |
| 338 w | | | | | $\delta(\phi\text{-c-}\phi)$ | $\gamma(\text{CNC})/\rho(\text{CH}_3)$ |
| 294 w | 295 vw | | 295 sh | | | |
| | 236 w | 227 vw | 230 vw | 226 vs | $\delta(\phi\text{-c-}\phi)$ | $\nu\text{Ag-N}/\gamma(\text{CNC})/\rho(\text{CH}_3)$ |
| 215 s | | | | | | |

Eosin Y (AR87) and Erythrosine (AR51) SERS spectra

Eosin Y and Erythrosine are halogenated derivative of the xanthene dye fluorescein. The UV-Vis absorption spectrum of Eosin Y and Erythrosine show intense band at 515 and 524 nm, corresponding to the monomeric form, with a shoulder at 481 and 494 nm, corresponding to the dimeric form of Eosin Y and Erythrosine, respectively.

The dimerization of these dyes is a well known phenomenon. It is reported that most organic dyes will dimerize through hydrogen bond, hydrophobic interaction, dispersion force and electrostatic interaction of zwitterions [120]. Su et al. [121] proposed on the basis of STM experiment and dimeric structure of an Eosin molecule, two possible configurations for the dimer as shown in Fig. 23: (1) two molecules interact with bromine atoms by dipolar–dipolar interaction; (2) the molecules are arranged with hydroxyl paired to carbonyl forming hydrogen bond.

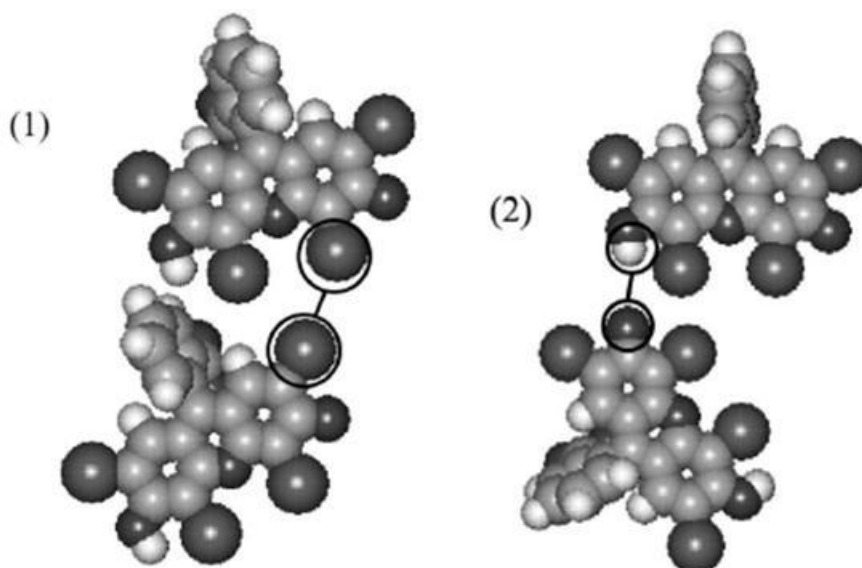


Fig. 23: Two dimeric structures of Eosin molecule optimized by molecular mechanics calculation [121].

Erythrosine is a similar compound with the same behavior as Eosin. In the crystal structure Su et al. [...] reveals the short I-I contact indicating the existence of the Van Der Waals interaction. By comparison, although three xanthene molecules can form dimeric structure as in solution, the configuration of the dimeric structure in the absorbed state is slightly different from that in solution because adsorption can drastically change the geometry due to interaction between molecule and substrate.

SERS spectra have been acquired with both AgNPs photoreduction methods and with the three wavelength lasers (442 nm, 532 nm and 785 nm) for AgNPs produced with 442 nm laser. Considering the SERS spectra achieved, some large bands different from FT-Raman spectra and strange baseline trends are observable (Fig. 24 and 25). These problems are probably due to the use of visible laser irradiation that produces photobleaching [122, 123] and plasmonic

heating [124] which reduce the SERS signal. The plasmonic heating effect can be reduced changing the source intensity and molecular absorption cross-section.

The photobleaching process is driven by the production of singlet oxygen [123]. The laser excites molecules from the ground state to the first excited singlet band following thermalization of the sensitizer to the lowest excited singlet state. Radiative relaxation - spontaneous emission - and internal conversion to the ground state occur from the first excited state band; these processes give rise to the fluorescence as well as nonradiative relaxation - heat generation. In addition, intersystem crossing produces the sensitizer triplet state, thereby allowing this triplet state to generate singlet oxygen through an energy transfer process assisted by collision of the sensitizer with triplet oxygen. The Eosin Y molecules produce on the order of 10^4 molecules of singlet oxygen $^1\text{O}_2$ before being degraded through photobleaching by $^1\text{O}_2$ or through other processes [18]. Xanthene dyes such as Eosin exhibit intense absorption bands in the green area of the visible spectrum (480/550 nm) and produce singlet oxygen with high yields. Increasing the number and atomic mass of halogen substituents on the xanthene skeleton causes the peak maximum to red shift. Likewise, the presence of heavier halogens increases the yield of intersystem crossing to the triplet state of the dye, which is an important criterion for a photosensitizer. For this reason, tetraiodo xanthene derivatives, like Erythrosin B, are generally more efficient photosensitizers than other halogenated derivatives [125].

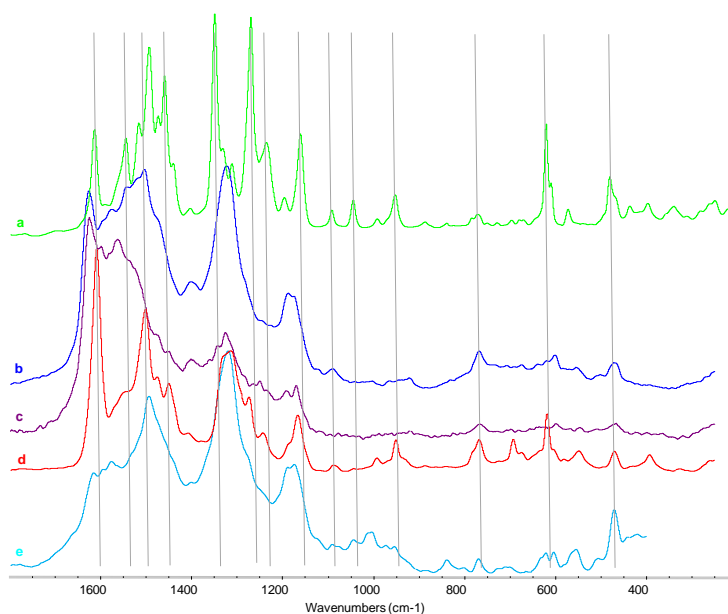


Fig. 24: Erythrosine B (AR51), comparison between FT-Raman spectrum (a) and SERS spectra achieved with AgNPs photoreduced with 532 nm laser and analysed with 532 nm laser (b); AgNPs photoreduced with 442 nm laser and analysed with 442 nm laser (c), 532 nm laser (d) and 785 nm laser (e).

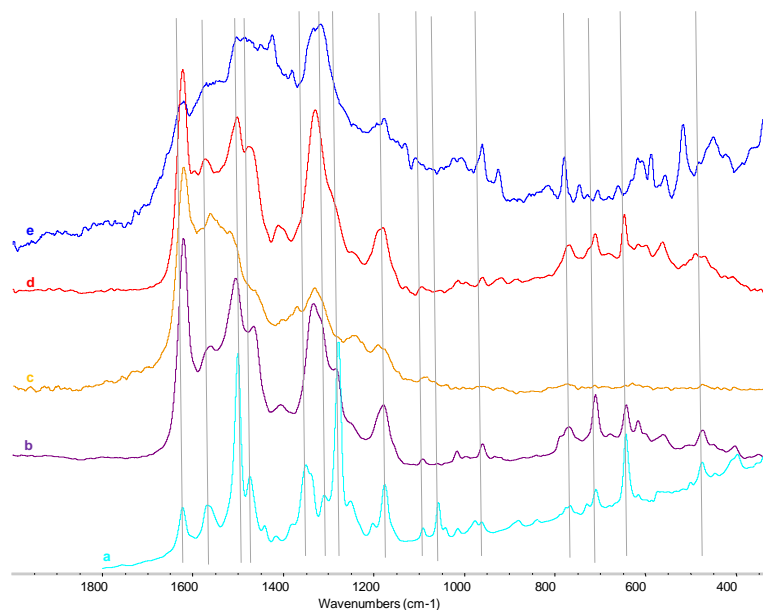


Fig. 25: Eosin Y (AR87), comparison between FT-Raman spectrum (a) and SERS spectra achieved with AgNPs photoreduced with 532 nm laser and analysed with 532 nm laser (b); AgNPs photoreduced with 442 nm laser and analysed with 442 nm laser (c), 532 nm laser (d) and 785 nm laser (e).

The interference of photobleaching effect and the possibility to polymerization of these dyes are well distinguishable in the SERS spectra: SERS spectra differ from the FT-Raman spectra for the bands widening and for the different peak position wavenumbers. Moreover for Erythrosine B changing the laser and the time applied for photoreduction, the spectrum acquired also changes; indeed, the SERRS spectrum achieved analysing AgNPs photoreduced with 532 nm laser for 20 minutes has a worse quality compared to the SERRS spectrum of AgNPs produced with 442 nm laser for only 2 minutes. Although the 442 nm laser is more energetic in respect to 532 nm, the time of irradiation is 10 times reduced and this probably decreases the photobleaching process.

On the other hand, Eosin Y does not show any change in the SERS spectra due to the photoreduction time irradiation. Both SERRS spectra have similar bands intensities and they are placed at about the same wavenumbers. This effect is due to the presence of iodine or bromine substituents in Erythrosine or Eosin, respectively.

The Erythrosine B FT-spectrum (Table 12) shows a very strong band at 1271 cm^{-1} attributed to the asymmetrical stretching mode of C-O-C and to the C-C bridge bond stretching mode. The very strong band at 1490 cm^{-1} was assigned to the in plane C-H deformation mode of the xanthene and benzene rings. The strong peak at 1351 cm^{-1} with the shoulder at 1332 cm^{-1} correspond to the in plane C-C stretching of the xanthene ring. The following strong band at 1474 cm^{-1} corresponds to the C-O-C deformation mode and to the C-C stretching and in plane C-H deformations of the xanthene ring. The xanthenes C-C stretching and the antisymmetrical COO- stretching vibrational modes corresponds to the medium strong band at 1611 cm^{-1} , whereas the xanthenes C-C stretching and the symmetrical stretching mode of COO- functional group was found at 1461 cm^{-1} . Other bands connected with the benzene ring vibrations are the medium band at 1545 cm^{-1} that was assigned to the benzene ring doublet stretching mode.

The weak peak at 1404 cm^{-1} and the medium band at 1237 cm^{-1} can be assigned to the in plane C-OH bending mode belonging to the xanthene ring. The medium band at 1312 cm^{-1} can be due to the stretching of the C-C and CO_2 bonds and in plane C-H deformation mode of the benzene ring. The weak peaks at 1197 and 1046 cm^{-1} were attributed to the symmetrical C-O-C stretching mode and to the C-O-C deformation mode, respectively. The xanthene ring breathing and the xanthenes and benzene C-C and COO stretching modes were observed at 1162 cm^{-1} , while the very weak peak at 992 cm^{-1} was attributed to the trigonal benzene ring breathing mode. Several bands from the FT-Raman spectrum are connected with the xanthene ring deformation modes ($954, 840, 770\text{ cm}^{-1}$), while other bands from this region are associated with the in plane C-H deformation mode of the benzene ring (1092 cm^{-1}). Highly important for the FT-Raman spectrum assignment is the symmetrical C-I stretching modes, which appear in the low wavenumbers region and with low intensities (572 and 479 cm^{-1}) [122, 126].

The Erythrosine B band at 1609 cm^{-1} assigned to the stretching of the C-C xanthenes bond and to the asymmetrical stretching mode of the carboxylate is enhanced in SERRS spectrum achieved with 532 nm laser – with AgNPs photoreduced with 442 nm laser - as N. Peica [126] suggested this probably means that the carboxylate is in the close vicinity of the silver particles with a perpendicular orientation of the ring. Moreover, the shoulder at 1461 cm^{-1} observed in the FT-Raman spectrum becomes a medium strong band in the SERRS spectrum at 1450 cm^{-1} (also red shifted) and can be due to the stretching of the C-C xanthenes bond and to the symmetrical stretching mode of the carboxylate anion [126]. Other remarkable variation in bands intensities for SERS or SERRS spectra have not been evaluated, the bands presents in the SERS spectra achieved with different lasers present broaden and less defines bands with blue or red shifts in the wavenumbers compared to FT-Raman.

The Eosin Y FT-Raman spectrum (Table 13) shows a very strong band at 1278 cm^{-1} attributed to the stretching mode of C-O-C and to the C-C bond stretching mode of the xanthene and benzene rings. The very strong band at 1499 cm^{-1} was assigned to the in plane C-H deformation and C-C stretching modes of the xanthene and benzene rings. The medium peak at 1351 cm^{-1} correspond to C-C stretching of the xanthene and benzene rings. The stretching of C-C bond of xanthenes ring and of xanthene and benzene rings were visible at 1623 cm^{-1} , and at 1474 cm^{-1} , respectively. Other bands connected with the benzene ring vibrations are the medium band at 1569 cm^{-1} . The weak peak at 1441 cm^{-1} and the very weak band at 1252 cm^{-1} can be assigned to the C-OH bending mode belonging to the xanthene ring; moreover the band at 1252 cm^{-1} is due to xanthenes ring stretching of C-C and C-O bonds. The weak band at 1310 cm^{-1} can be due to the in plane C-H deformation and C-C stretching modes of the benzene ring. The C-C stretching of xanthene and benzene ring and the benzene COO symmetric stretching were observed at 1177 cm^{-1} , while the very weak peak at 1015 cm^{-1} was attributed to the trigonal benzene ring breathing mode and to C-Br stretching mode. Several bands from the FT-Raman spectrum are connected with the xanthene ring deformation modes ($962, 776, 710$ and 645 cm^{-1}), while other bands from this region are associated with the in plane C-H deformation mode of the benzene ring (1092 and 618 cm^{-1}) [122, 126].

The Eosin Y SERRS spectra achieved with both AgNPs photoreduced are analogous in bands intensities and wavenumbers. The bands more enhanced are at 1619 cm^{-1} (xanthenes ring C-C stretching and antisymmetrical COO- stretching vibrational mode) and at 1332 cm^{-1} (C-H bending mode of the benzene ring). Due to the similar structure among these two dyes, we can assume -as N. Peica suggested- that the enhancement of 1619 cm^{-1} band probably means that the carboxylate is in the close vicinity of the silver particles with a perpendicular orientation of the ring. Moreover the strong FT-Raman band at 1499 cm^{-1} , attributed to C-H bending and C-C stretching modes of the benzene or xanthenes rings, is still a strong band in SERRS spectra but suffers of a blue shift at 1505 cm^{-1} . Other remarkable variation in bands intensities for SERRS spectra have not been identified, only blue or red shifts in the wavenumbers have been distinguished compared to FT-Raman.

Eosin Y SERS spectrum achieved with 442 nm exhibit a strong antisymmetrical COO- stretching vibrational mode and C-C stretching mode of the xanthene ring band at 1620 cm^{-1} , all the other bands are weak or very weak. The 785 nm SERS spectrum is a poor spectrum with mainly weak bands, the only two medium bands are related to xanthene ring deformation mode at 716 cm^{-1} and in plane C-H deformation mode of benzene ring at 618 cm^{-1} . These features could suggest the orientation of Eosin molecules on AgNPs as planar xanthenes moiety and benzene ring seems to be quite perpendicularly to the silver surface.

Table 2: : FT-Raman and SERS assignment of Erythrosine B (AR51)

| AR51 FT-Raman powder | AR51 SERS | | | | description of vibration contributing to the normal mode |
|----------------------------|--------------------------|--------------------------|------------------------|------------------------|---|
| | photor. λ 532 nm | photor. λ 442 nm | | | |
| | | anal. λ 532 nm | anal. λ 442 nm | anal. λ 532 nm | |
| | 1625 s | 1625 s | | | vCC Xanthene ring/ v(COO) |
| 1615 m | | 1599 sh | 1609 vs | 1615 w | vCC Xanthene ring /va(COO ⁻) |
| | 1577 vw | 1580 sh | | 1578 vw | |
| | | 1564 w | | | v Bz ring |
| 1546 m | 1544 sh | | 1548 sh | | v Bz ring |
| 1517 m | | | | | |
| 1494 vs | 1502 s | | 1501 s | 1493 vs | v(CH)ring Xanthene and Bz |
| 1474 m | 1473 sh | 1477 sh | 1476 w | 1475 sh | vCC Xanthene ring/d(COC)/p(CH) xantene ring |
| 1461 vw | | | 1450 m | | vCC Xanthene ring /vs(COO ⁻) |
| 1404 w | 1401 w | 1401 w | 1407 w | 1402 sh | vCC + d(COH) xantene ring |
| 1351 vs | | | | | vCC Xanthene and Bz ring |
| 1332 vw | 1323 vs | 1326 m | 1314 m | 1320 vs | d(CH) benzene ring |
| 1312 m | | | | | vCC Bz ring/ pCH Bz/ vs CO ₂ Bz |
| 1272 vs | | | 1273 m | | v(COC)/v(C-C) xantene or benzene rings |
| 1237 m | | | 1240 w | | d(COH) xantene ring/ vCO Xanthene ring / vCC |
| 1197 m | 1188 m | | | 1189 m | vs(COC)/ vCC Xanthene ring |

| | | | | | |
|--------|---------|--------|---------|---------|---|
| 1162 m | 1174 m | 1170 m | 1165 m | 1174 m | xanthene ring breathing mode/ ν C-C vs CO ₂ Xanthene and Bz ring |
| 1092 w | 1089 sh | | 1086 sh | | d(CH) benzene ring |
| 1046 w | | | | 1044 sh | d(COC)/ ν CC Bz ring/ vs CO ₂ |
| 992 vw | | | 992 sh | 1002 w | trigonal benzene ring breathing mode trigonal benzene ring breathing mode/ ν Xanthene and Bz ring |
| 954 w | | | 950 w | | xantene + Bz ring deformation mode |
| 840 sh | | | | 837 vw | xantene ring deformation mode |
| 770 vw | 767 vw | 767 vw | 767 vw | 767 vw | xantene ring deformation mode xantene ring deformation mode |
| 620 s | | | 691 w | | |
| 572 | | | 618 m | 622 w | ν Xanthene + Bz ring |
| | | | | 603 | xantene ring deformation mode/ vs(C-I) |
| 479 m | 470 sh | 469 w | 548 | 555 | |
| | | | 471 w | 471 m | skeletal deformation mode/ vs(C-I) |

Table 3: FT-Raman and SERS assignment of Eosin Y (AR87)

| AR87 FT-Raman powder | AR87 SERS | | | | description of vibration contributing to the normal mode |
|----------------------------|--------------------------|--------------------------|------------------------|------------------------|--|
| | photor. λ 532 nm | photor. λ 442 nm | | | |
| | anal. λ 532 nm | anal. λ 442 nm | anal. λ 532 nm | anal. λ 785 nm | |
| 1623 m | 1619 s | 1620 m | 1617 s | 1621 w | vCC Xanthene ring |
| 1569 m | 1561 w | 1560 w | 1572 | | v benzene ring |
| 1499 vs | 1506 s | 1517 sh | 1504 s | 1504 w | vCC Xanthene and Bz ring /d(CH)ring |
| 1474 m | 1466 w | 1463 sh | 1463 w | 1474 sh | vCC Xanthene |
| 1441 w | | | | 1449 vw | d(COH) xantene ring |
| 1416 vw | 1405 w | | 1410 w | | vCC Xanthene |
| 1351 m | | | | | vCC Xanthene and Bz ring |
| | 1332 vs | 1330 m | 1332 vs | 1333 vs | d(CH) benzene ring |
| 1310 w | 1316 sh | | 1317 sh | 1316 vs | vCC Bz ring/ vs CO ₂ Bz |
| 1278 vs | 1284 sh | | 1281 sh | | v(C-C) Xanthene and Bz ring / v(COC) |
| 1252 vw | | 1242 vw | | | v(CC) + v(CO) Xanthene/ d(COH) xantene ring |
| 1177 m | 1178 m | 1175 w | 1175 m | 1177 w | vCC xanthene and Bz ring/ vs CO ₂ Bz |
| 1092 vw | 1091 vw | 1092 vw | 1091 vw | 1089 sh | d(CH) benzene ring |
| 1058 m | | | | | vCC Bz ring/ vs CO ₂ Bz |
| 1015 vw | 1016 vw | | 1015 vw | | Xanthene ring breathing +v C-Br |
| 977 w | | | | | |
| 962 w | 959 w | | 957 w | 962 m | v Xanthene and Bz ring |
| 766 w | 769 w | | 770 w | 779 m | xantene ring deformation mode |
| 710 m | 710 m | | 708 m | | Xanthene out of plane ring deformation |

| | | | | |
|--------|--------|--------|-------|---------------------------|
| 645 m | 641 m | 644 m | | v Xanthene + Bz ring |
| 618 vw | 617 vw | 617 vw | 618 m | d(CH) benzene |
| | 560 w | 562 w | 556 w | |
| 477 w | 474 w | 469 vw | | skeletal deformation mode |

3.2.2.5 Conclusions

SERS is a powerful sensitive technique for the identification of dyes in textile fibres. *On the fibre* SERS method with *in situ* produced photoreduced silver nanoparticles has proved to be a sensitive technique for the detection of triarylmethane and xanthene dyes on dyed fibres. This research project demonstrated the simplicity and effectiveness of the photoreduction procedure.

A visual inspection of the SERS spectra of wool dyed fibres, achieved using photoreduced silver nanoparticles produced *directly on the fibre*, allows us to distinguish the characteristic dye spectrum, and that constitutes a first approach to the diagnosis. Moreover, the AgNPs photoreduced with 442 nm laser can be used to obtain SERS spectra with 442 nm, 532 nm and 785 nm excitation wavelengths, permitting to choose the right laser to develop analysis in more suitable experimental conditions.

The SERS analysis of triarylmethane dyes - Fuschsine and Diamond Green - carried out with the three different excitation wavelengths, allow us to distinguish the different symmetric or non-totally symmetric modes of these two molecules permitting to recognize the unambiguous features of each SERS spectrum and to make an hypothetical bands assignment, based on preview published results. On the other hand SERS spectra of xanthenes dyes underline the reactivity of these molecules when irradiated with visible light. Indeed, the spectra show us that photobleaching process occurred. Moreover, for Erythrosine B a distinction among different photoreduction methods is achievable based on photobleaching process, in particular shorter photoreduction irradiation time allowed to acquire better spectra.

Finally, the authentic novelties of this study are: (I) the use of photoreduced AgNPs that provided the achievement, for the first time, of SERS spectra for different synthetic organic dyes classes; and (II) the photoreduced AgNPs obtained at 442 nm laser have SERS effect when analyzed with 442, 532 and 785 nm excitation wavelengths. This probably occurs because these AgNPs (produced at 442 nm) have various dimensions due to the very short time of photoreduciton and this heterogeneity in nanoparticles dimensions could generate SERS signal with the three different excitation wavelengths.

3.6 References

- [1] E.R. Trotman, *Dyeing and chemical technology of textile fibres*, Griffin London, 1970
- [2] L.N. Jones, D.E. Rivett, D.J. Tucker, Wool and related mammalian fibers, in M. Lewin (ed), *Handbook of fiber chemistry*, CRC Press, 2007
- [3] S. Grishanov, Structure and properties of textile materials, in M. Clark (ed), *Handbook of textile and industrial dyeing*, vol. 1: Principles, processes and types of dyes, Woodhead Publishing, 2011
- [4] K. Hunger (ed), *Industrial dyes - chemistry, properties, applications*, Wiley-VCH, Weinheim, 2003
- [5] H. Höcker, Fibre morphology, in W.S. Simpson, G.H. Crawshaw (eds), *Wool: science and technology*, Woodhead Publishing and CRC Press, 2002
- [6] R.M. Christie, *Colour chemistry*, RSC Paperbacks, London, 2001
- [7] Mansoor Iqbal, *Textile dyes*, Rehbar Publishers Karachi, 2008
- [8] Society of dyers and colourists, *Colour Index*, fourth web edition, www.colourindex.org
- [9] D.P. Chattopadhyay, Chemistry of dyeing, in M. Clark (ed), *Handbook of textile and industrial dyeing*, vol. 1: Principles, processes and types of dyes, Woodhead Publishing, 2011
- [10] W.S. Simpson, Wool chemistry, in W.S. Simpson, G.H. Crawshaw (eds), *Wool: science and technology*, Woodhead Publishing and CRC Press, 2002
- [11] Adolf FP, Dunlop J. Microspectrophotometry/colour measurement. In: Robertson J, Grieve MC, editors. *Forensic examination of fibres*. London: Taylor and Francis; 1999; 251–87.
- [12] Wiggins KG. Thin layer chromatographic analysis for fibre dyes. In: Robertson J, Grieve MC, editors. *Forensic examination of fibres*. London: Taylor and Francis, 1999; 291–310.
- [13] Griffin R, Speers J. High-performance liquid chromatography. In: Robertson J, Grieve MC, editors. *Forensic examination of fibres*. London: Taylor and Francis, 1999; 311–27.
- [14] Robertson J. Capillary electrophoresis. In: Robertson J, Grieve MC, editors. *Forensic examination of fibres*. London: Taylor and Francis, 1999; 328–36.
- [15] G. Massonnet, P. Buzzini, G. Jochem, M. Stauber, T. Coyle, C. Roux, J. Thomas, H. Leijenhorst, Z. Van Zanten, K. Wiggins, C. Russel, S. Chabli, A. Rosengarten, *J Forensic Sci*, 2005, 50, 5

- [16] [14] P. Novotná, V. Pacáková, Z. Bosáková, K. Štulík, *Journal of Chromatography A*, 863, 1999
- [17] J. Orska-Gawrysa, I. Surowiecb, J. Kehlc, H. Rejniakc, K. Urbaniak-Walczakc, M. Trojanowicza, *Journal of Chromatography A*, 989, 2003
- [18] M.R. van Bommel, I. Vanden Berghe, A.M. Wallert, R. Boitelle, J. Wouters, *Journal of Chromatography A*, 1157, 2007
- [19] G.G. Balakina, V.G. Vasiliev, E.V. Karpova, V.I. Mamatyuk, *Dyes and Pigments*, 71, 2006
- [20] K.M. Frei, I. Vanden Berghe, R. Frei, U. Mannering, H. Lyngstrøm, *Journal of Archaeological Science*, 37, 2010
- [21] I. Joosten, M.R. van Bommel, R. Hofmann-de Keijzer, H. Reschreiter, *Microchim Acta*, 155, 2006
- [22] X. Zhang, K. Corrigan, B. MacLaren, M. Leveque, R. Laursen, *Studies in Conservation*, 52, 2007
- [23] X. Zhang, I. Good, R. Laursen, *Journal of Archaeological Science*, 35, 2008
- [24] R. Griffin, J. Speers, High-performance liquid chromatography, in J.R.
- [24] X. Zhang, R.A. Laursen, *Analytical Chemistry*, 77(7), 2005
- [25] F. Pozzi, J.R. Lombardi, S. Bruni, M. Leona, *Analytical Chemistry*, 84, 2012
- [26] D. Fabbri, G. Chiavari, H. Ling, *Journal of Analytical and Applied Pyrolysis*, 56, 2000
- [27] M.J. Casas-Catalán, M.T. Doménech-Carbó, *Analytical Bioanalytical Chemistry*, 382, 2005
- [28] M. Gulmini, A. Idone, E. Diana, D. Gastaldi, D. Vaudan, M. Aceto, *Dyes and Pigments*, 98, 2013
- [29] F. Casadio, K. Mauck, M. Chefitz, R. Freeman, *Appl Phys A* (2010) 100: 885–899
- [30] M.C. Grieve, R.M.E. Gri_in, R. Malone, *Science & Justice*, 38(1), 1998
- [31] F. Casadio, R.P. Van Duyne, *Analyst*, 138, 2013
- [32] L. Bellot-Gurlet, S. Pagès-Camagna, C. Coupry, *J. Raman Spectrosc.* 2006; **37**: 962–965
- [33] Non-destructive Micro Analysis of Cultural Heritage Materials, Ed. K. Janssens, R. Van Grieken, volume XLII, 2004
- [34] P. Colomban, *Journal of Raman Spectroscopy*, 2012. 43, 11, 1529–1535
- [35] P. Vandenabeele, H. G. M. Edwards, L. Moens, *Chemical Reviews*, 2007, 107, 3
- [36] W. Fremout, S. Saverwyns, *J. Raman Spectrosc.* 2012, 43, 1536–1544

- [37] N.C. Scherrer, S. Zumbuehl, F. Delavy, A. Fritsch, R. Kuehnen, *Spectrochim. Acta A, Mol. Biomol. Spectrosc.* **73**(3), 505 (2009)
- [38] F. Schulte, K.-W. Brzezinka, K. Lutzenberger, H. Stege, U. Panne, *J. Raman Spectrosc.* **39**(10), 1455 (2008)
- [38] P. Ropret, S.A. Centeno, P. Bukovec, *Spectrochim. Acta A, Mol. Biomol. Spectrosc.* **69**, 486 (2008)
- [39] P. Vandenabeele, L. Moens, H.G.M. Edwards, R. Dams, *J. Raman Spectrosc.* **31**, 509 (2000)
- [40] J.C. Barnett, *Reviews in Conservation*, **8**, 2007
- [41] H.G.M. Edwards, J.M. Chalmers (eds), *Raman spectroscopy in archaeology and art history - RSC analytical spectroscopy monographs*, Royal Society of Chemistry, Cambridge, 2005
- [42] B. Schrader, H. Schulz, G.N. Andreev, H.H. Klump, J. Sawatzki, *Talanta*, **53**(1), 2000
- [43] P. White, *Surface enhanced resonance raman scattering spectroscopy*, in J.R. Robertson, M. Grieven (eds), *Forensic examination of fibers*, Taylor & Francis Forensic Science Series, Philadelphia, 1999
- [44] F. Rosi, M. Paolantoni, C. Clementi, B. Doherty, C. Miliani, B.G. Brunetti, A. Sgamellotti, *Journal of Raman Spectroscopy*, **41**, 2010
- [45] M. Fleischmann, P.J. Hendra, A.J. McQuillan, *Chemical Physics Letters*, **26**(2), 1974
- [46] D. L. Jeanmaire, R. P. Van Duyne, *Journal of Electroanalytical Chemistry and Interfacial Electrochemistry* Volume 84, Issue 1, 10 November 1977, Pages 1–20
- [47] M.G. Albrecht, J.A. Creighton, *Journal of the American Chemical Society*, **99**(15), 1977
- [48] M. Osawa, N. Matsuda, K. Yoshii, I. Uchida, *Journal of Physical Chemistry*, **98**, 1994
- [49] E. Le Ru, P. Etchegoin, Elsevier, Amsterdam, 2009
- [50] J.R. Ferrero, K. Nakamoto, C.W. Brown, *Introductory Raman Spectroscopy*, Academic Press (Elsevier Science), San Diego, 2003
- [51] R.F. Aroca, *Surface-enhanced vibrational spectroscopy*, John Wiley & sons, Chichester, 2006
- [52] W.E. Smith, C. Rodger, *Surface-enhanced Raman scattering*, in J.M. Chalmers, P.R. Griffiths (eds), *Handbook of vibrational spectroscopy*, vol. 1, Wiley, 2002
- [53] C.A. Murray, D.L. Allara, *Journal of Chemical Physics*, **76**, 1982
- [54] M.E. Abdelsalam, P.N. Bartlett, J.J. Baumberg, S. Cintra, T.A. Kelf, A.E. Russell, *Electrochemical Communications*, **7**, 2005

- [55] J.R. Lombardi, R.L. Birke, T. Lu, J. Xu, *Journal of Chemical Physics*, 84(8), 1986
- [56] M. Moskovits, *Journal of Raman Spectroscopy*, 36(6-7), 2005
- [57] E. Smith, G. Dent, *Modern Raman spectroscopy - a practical approach*, John Wiley & sons, Chichester, 2005
- [58] E. C. Le Ru , E. Blackie , M. Meyer , P. G. Etchegoin, *J. Phys. Chem. C*, 2007, 111 (37), pp 13794–13803
- [59] Kristin L. Wustholz, Christa L. Brosseau, Francesca Casadio, Richard P. Van Duyne *Phys. Chem. Chem. Phys.*, 2009, 11, 7350–7359
- [60] R.F. Aroca, R.A. Alvarez-Puebla, N. Pieczonka, S. Sánchez-Cortés, J.V. García-Ramos, *Advances in Colloid and Interface Science*, 116, 2005
- [61] R.A. Alvarez-Puebla, J.P. Bravo-Vasquez, P. Cheben, D-X. Xu, P. Waldron, H. Fenniri, *Journal of Colloid and Interface Science*, 333(1), 2009
- [62] S. Wojtysiak, M.S. Walczynski, A. Kudelski, *Vibrational Spectroscopy*, 57(2), 2011
- [63] D. Huo, J. He, S. Yang, Z. Zhou, Y. Hu, M. Epple, *Journal of Colloid and Interface Science*, 393, 2013
- [64] Z-Q. Tian, Z-L. Yang, B. Ren, D-Y. Wu, SERS from transition metals and excited by ultraviolet light, in K. Kneipp, M. Moskovits, H. Kneipp (eds.), *Surface enhanced Raman scattering: physics and applications*, Springer-Verlag, Berlin Heidelberg, 2006
- [65] A. Lund, R.E. Tevault, R.R. Smardzewski, *Journal of Chemical Physics*, 88, 1984
- [66] B. Bozlee¹, S. Clark, C. Marr, S. Slaughter, M. McWaffers, Y. Choi, R.L. Garrell, *Journal of Raman Spectroscopy*, 27(1), 1996
- [67] Y. Wang, Y. Wang, J. Zhang, H. Hu, J. Zhang, B. Zhao, B. Yang, J.R. Lombardi, *Journal of Raman Spectroscopy*, 40(8), 2009
- [68] Z-Q. Tian, B. Ren, D-Y. Wu, *Journal of Physical Chemistry B*, 106(37), 2002
- [69] K.M. Kosuda, J.M. Bingham, K.L. Wustholz, R.P. van Duyne, Nanostructures and surface-enhanced Raman spectroscopy, in D.L. Andrews, G.D. Scholes, G.P. Wiederrecht (eds), *Comprehensive nanoscience and technology*, vol 3, Academic Press, Oxford, 2011
- [70] T.R. Jensen, R.P. Van Duyne, S.A. Johnson, and V.A. Maroni, *Applied Spectroscopy*, 54(3), 2000
- [71] N.G. Greeneltch, A.S. Davis, N.A. Valley, F. Casadio, G.C. Schatz, R.P. Van Duyne, N.C. Shah, *Journal of Physical Chemistry A*, 116, 2012
- [72] N.A. Abu Hatab, J.M. Oran, M.J. Sepaniak, *ACS Nano*, 2(2), 2008

- [73] Q. Tao, J. Dong, W. Qian, *Progress in Chemistry*, 25(6), 2013
- [74] M. Sackmann, S. Bom, T. Balster, A. Materny, *Journal of Raman Spectroscopy*, 38(3), 2007
- [75] M. Sackmann, A. Materny, *Journal of Raman Spectroscopy*, 37(1-3), 2006
- [76] J.A. Creighton, C.G. Blatchford, M.G. Albrecht, *Journal of the Chemical Society, Faraday Transactions 2*, 75, 1979
- [77] P.C. Lee, D. Meisel, *Journal of Physical Chemistry*, 86, 1982
- [78] C.H. Munro, W.E. Smith, M. Garner, J. Clarkson, P.C. White, *Langmuir*, 11, 1995
- [79] N. Leopold, B. Lendl, *Journal of Physical Chemistry B*, 107, 2003
- [80] A.M. Ahern, R.L. Garrell, *Analytical Chemistry*, 59, 1987
- [81] Z. Jurasekova, S. Sánchez-Cortés, M. Tamba, A. Torreggiani, *Vibrational Spectroscopy*, 57, 2011
- [82] J. Neddersen, G. Chumanov, T.M. Cotton, *Applied Spectroscopy*, 47(12), 1993
- [83] M. Procházka, J. Štěpánek, B. Vlčková, I. Srnová, *Journal of Molecular Structure*, 410-411, 1997
- [84] A. García-Leis, J.V. García-Ramos, S. Sánchez-Cortés, *Journal of Physical Chemistry C*, 117, 2013
- [85] J.E. Millstone, S.J. Hurst, G.S. Métraux, J.I. Cutler, C.A. Mirkin, *Small*, 5(6), 2009
- [86] J. Silva, J. Saade, P. Farias, E. Falcão, *Advances in Nanoparticles*, 2, 2013
- [87] S. Sánchez-Cortés, J.V. García-Ramos, *Journal of Raman Spectroscopy*, 29(5), 1998
- [88] S-Y. Fu, P-X. Zhang, *Journal of Raman Spectroscopy*, 23(2), 1992
- [89] M.V. Cañamares, J.V. García-Ramos, J.D. Gómez-Varga, C. Domingo, S. Sánchez-Cortés, *Langmuir*, 23, 2007
- [90] V. Amendola, M. Meneghetti, *Physical Chemistry –Chemical Physics*, 11, 2009
- [91] S. Sánchez-Cortés, J.V. García-Ramos, *Surface Science*, 473, 2001
- [92] C. E. K. Mees *The Theory of the photographic Process*; Macmillan: New York. 1942; Chapter IV.;
- [93] Walls. J. H.; Amdge, A. A. *Basic Photo Science*; Focal Press: London, 1977; pp 93-118.
- [94] X. Gao; C. Wan; T. He; J. Li; H. Xin; F. Liu; *Chem. Phys. Lett* 1884. 112. 465-468.
- [95] K. Chen, M. Leona and T. Vo-Dinh, *Sens. Rev.*, 2007, 27, 109–120

- [96] X. Zhang and R. A. Laursen, *Anal. Chem.*, 2005, 77, 2022–2025
- [97] Marco Leona, Peter Decuzzi, Thomas A. Kubic, Glenn Gates, John R. Lombardi *Anal. Chem.* 2011, 83, 3990–3993
- [98] M. Leona patented US 20070035729 A1 Non-Invasive Identification of Fluorescent Dyes in Historic Textiles By Matrix Transfer-Surface Enhanced Raman Scattering
- [99] C. Lofrumento, M. Ricci, E. Platania, M. Becuccia, E. Castellucci, *J. Raman Spectrosc.* 2013, 44, 47–54
- [100] M. Leona, J. Stenger and E. Ferloni, *J. Raman Spectrosc.* 2006; **37**: 981–992
- [101] B. Doherty, B. G. Brunetti, A. Sgamellotti, C. Miliani *J. Raman Spectrosc.* 2011, 42, 1932–1938
- [102] Z. Jurasekova, C. Domingo, J. V. Garcia-Ramos, S. Sanchez-Cortes *J. Raman Spectrosc.* 2008; 39: 1309–1312
- [103] Christa L. Brosseau, Alessa Gambardella, Francesca Casadio, Cecily M. Grzywacz, Jan Wouters, Richard P. Van Duyne, *Anal. Chem.*, 2009, 81 (8), pp 3056–3062
- [104] M. V. Canamares, M. Leona, M. Bouchard, C. M. Grzywacz, J. Woutersd, K. Trentelmanc. *J. Raman Spectrosc.* 2010, 41, 391–397
- [105] K. Chen, K. C. Vo-Dinh, F. Yan, M. B. Wabuyele and T. Vo-Dinh, *Anal. Chim. Acta*, 2006, 569, 234–237
- [106] E. Van Elslande, S. Lecomte and A. S. Le Ho, 4th International Conference on the Application of Raman Spectroscopy in Art and Archaeology, Modena, Italy, 2007
- [107] Dr. A. Lehne, *Tabellarische Uebersicht über die künstlichen organischen Farbstoffe und ihre Anwendung in Färberei und Zeugdruck*, 1893, Verlag von Julius Springer, Berlin
- [108] J. Miller, E. G. Bartick, *Appl. Spectr.*, 2011, 55, 12
- [109] H. Liu, W. Yu, *Journal of Applied Polymer Science*, Vol. 103, 1–7 (2007)
- [110] T. Gessner, U. Mayer, *Ullmann's Encyclopedia of Industrial Chemistry*, 2012 Wiley-VCH Verlag GmbH & Co. KGaA, Weinheim
- [111] Muniz-Miranda, M. *J. Raman Spectrosc.* 2004, 35, 839.
- [112] Bjerneld, E. J.; Murty, K. V. G. K.; Prikulis, J.; Kañll, M. *Chem. Phys. Chem.* **2002**, 1, 116
- [113] R. Sato-Berru, R. Redón, A. Vázquez-Olmos, J.M. Saniger *J. Raman Spectrosc.* 2009, 40, 376–380

- [114] Z. Jurasekova, E. del Puerto, G. Bruno, J. V. García-Ramos, S. Sanchez-Cortes, C. Domingo J. Raman Spectrosc. 2010, 41, 1455–1461
- [115] Maillard, M.; Huang, P.; Brus, L. *Nano Lett.* 2003, 3, 1611
- [116] M. V. Cañamares, C. Chenal, R. L. Birke, J. R. Lombardi, *J. Phys. Chem. C* 2008, 112, 20295–20300
- [117] B. Doherty, M. Vagnini, K. Dufourmantelle, A. Sgamellotti, B. Brunetti, C. Miliani, *Spectrochimica Acta Part A: Molecular and Biomolecular Spectroscopy* 121 (2014) 292–305
- [118] D. Beljonne, *Adv. Funct. Mater.* 2002, 12
- [119] M.C. Wu, M.P. Lin, S.W. Chen, P.H. Lee, J.H. Li, W.F. Su, *RSC Adv.*, 2014, 4, 10043–10050
- [120] G. J. Su, S. X. Yin, L. J. Wan, J. C. Zhao, C. L. Bai *Chemical Physics Letters* 370 (2003) 268–273
- [121] G. J. Su, S. X. Yin, L. J. Wan, J. C. Zhao, C. L. Bai, *Surface Science* 551 (2004) 204–212
- [122] N. G. Greeneltch, A. S. Davis, N. A. Valley, F. Casadio, G. C. Schatz, R. P. Van Duyne, N. C. Shah, *J. Phys. Chem. A* 2012, 116, 11863–11869
- [123] L. S. Herculano, L. C. Malacarne, V. S. Zanuto, G. V. B. Lukasiewicz, O. A. Capeloto, N. G. C. Astrath, *J. Phys. Chem. B* 2013, 117, 1932–1937
- [124] A. O. Govorov, H. H. Richardson, *Nano Today* 2007, 2, 30–38
- [125] DeRosa, M. C.; Crutchley, R. J. *Photosensitized Singlet Oxygen and Its Applications.* *Coord. Chem. Rev.* 2002, 233–234, 351–371
- [126] N. Peica *Vibrational spectroscopy and density functional theory calculations on biological molecules*, 2006

Chapter 4

Surface Enhanced Vibrational Spectroscopy (SEVS). Development of two innovative approaches in the IR range.

Vibrational spectroscopy has a great importance in the characterization of structure, bonding and reactivity of different compound and molecules. In the past decades, vibrational enhanced spectroscopic techniques become more and more important allowing the observation of enhanced spectra of an absorbed analyte on metal surfaces [1]. Indeed, SEVS spectra resulted of the molecule-light interaction when a molecule is near or attached to a nanostructure supporting surface plasmons.

SEVS consists of two main branches: SERS (Surface Enhanced Raman Scattering) and SEIR (Surface Enhanced Infra Red). As concern the selection rules, for highly reflecting surfaces in the infrared region, only vibrational mode with a component of the dynamic dipole perpendicular to the surface are observed. Although the relative intensities of the achieved IR spectra can be limited, these spectra provides new information about the molecular orientation and the molecule-surface interaction. Moreover, the surface selection rules generally applied to IR and Raman spectroscopy are extended to SEVS with additional peculiarity due to the nature of the local field and/or the roughness of the surface used for SEVS.

The presence of metal noble nanostructure is also an important subject in SEVS analysis due to the fact that these nanostructures have intrinsic properties of enhancing signals and, furthermore they may leave its own footprints in the SEVS spectra. Indeed, the interference of nanostructures can be detected as a characteristic band caused by a surface complex, a frequency shift and a changes in relative intensities. In the course of time different nanostructures have been produced and tested, as isolated particles, nanorods, nanowires or aggregates. In many SEVS analysis, the nanostructures are created directly on to a solid substrates allowing possible reflections and refraction phenomena on the surface detectable in the spectral features [1].

In summary, SEVS is a new molecular spectroscopy class that is highly dependent on the optical properties, size and shape of metallic nanostructures. Of particular interest for this part of research work are those configurations resulting in the magnification of the IR signal as Reflection-Absorption IR spectroscopy (RAIRS) coupled with ATR method and Surface Enhanced IR Absorption spectroscopy (SEIRA).

4.1 Surface Enhanced Infrared Absorption (SEIRA)

4.1.1 SEIRA effect

In 1980 Harstein et al. [2] discovered that when a molecule was absorbed on metal surfaces, its infrared absorptions appeared more intense than what would be expected for traditional measurements. This effect was named Surface-Enhanced Infrared Absorption (SEIRA), to recall the analogy with SERS (Surface Enhanced Raman Spectroscopy), which was already known since the beginning of 70th [3,4]. Many papers have been published trying to explain the enhancement mechanism which may be related to the result of the enhanced optical field at the surface of metal nano-particles when illuminated at the phonon resonance frequencies. In analogy with the interpretation of the SERS effect, Osawa [5] suggested that the total enhancement is produced by the combination of electromagnetic and chemical mechanisms. Moreover, it was noticed that the enhancement was significant for the first monolayer directly attached to the metal surface and decayed sharply within 5 nm from the surface. In addition, vibrational modes that have dipole moment derivative components perpendicular to the surface were preferentially enhanced [5]. Indeed, for aggregated nanostructures, the plasmonic effect is relevant in the MIR region: the metal islands are polarized by the incident infrared photon field through the excitation of collective electron resonance, or localized plasmon modes, and the dipole (p) induced in an island generates a local electromagnetic (EM) field stronger than the incident infrared photon field around the island. This is the EM contribution to SEIRA effect; intensity of enhanced EM field decays with the distance of analyte from metallic surface. In proximity of nanoisland, local EM field is polarized normal at every point along the surface. The scheme reported in figure 1 explains the short enhancement and the surface selection rules.

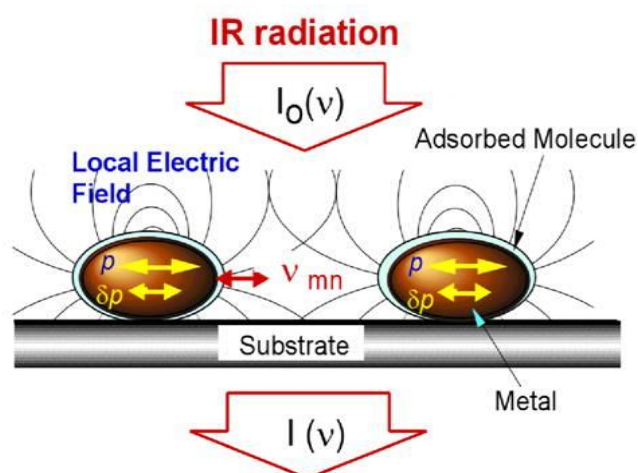


Fig. 14: Schematic representation of the EM mechanism of SEIRA on metal island films [6].

Moreover, if the molecules strongly adsorb at the metal surface, additional dipoles are induced in the metal islands. Dipoles perturb optical properties of metal nanostructures: since the perturbation is larger at vibrational frequencies of the molecule than at other frequencies, the spectrum of the metal island film should result very similar to the spectrum of the molecule. These kind of effects, generated by the strong interaction between analyte and metal surface, are considered the chemical contribution to SEIRA effects, due to chemisorbed molecules that have larger absorption coefficient than those of condensed overlayers [6]. The enhancement factor and the prevalence of electromagnetic or chemical contributions must be evaluated in every specific case, according to the nature of SEIRA support used and molecular species investigated.

Enhanced infrared spectra can be obtained in transmission, ATR (attenuated total reflection), external reflection and diffuse reflection mode [7] and mainly depend on the morphology of the metal surface.

Different types of enhancing surfaces can be successfully applied in order to obtain SEIRA effect. The most used and useful support was found to be island film coinage metals [8-11], but also other surfaces as Pt [12], Sn [9], Pd, Ru [13]. With the advent of nanotechnology, a lot of enhancing surfaces have been made available for SEIRA spectroscopy [14,15]; it may be interesting a brief description of different SEIRA-active substrates.

The first SEIRA surface was composed by silver and gold metal film, sputtered on silicon plate in order to perform ATR measurements [2].

Thin film evaporation has been demonstrated to be an effective way to obtain irregular surfaces (also applied for SERS analysis), the typical preparation of such film is performed with vacuum evaporation [16, 17]. This is a simple and non-expensive procedure that provides a disordered, rough, thin film of metal on suitable holder. The deposition rate of the metal and film thickness are crucial parameters in this technique in order to obtain an active surface: it was found that slow rate of deposition generally provides the best enhancement [14, 17],

whereas the thickness of film depends on deposition rate. Indeed, it doesn't exist an unified protocol for the best thin film preparation, but it must be evaluated for each particular case.

An alternative method to obtain a metal film is electrochemical deposition: a suitable potential of current is applied to electrolyte solution of salts of the metal to be deposited, either under potentiostatic, galvanostatic or potential cycling condition. In this case the parameters controlled are: concentration of solution, voltage or current applied, time of deposition. Further additives can be used to control morphology. Using this procedure, rough electrodes for SEIRA analysis have been proposed as low cost substrates [18].

Metal colloids can also be used in order to obtain SEIRA-active substrates. Metal colloids have become the most commonly used substrates, both in SERS and in SEIRA, thanks to their easy preparation and the possibility of inducing aggregation, during and post-synthesis [19, 20]. In more detail, metal colloidal nanoparticles may be produced using the chemical (reactions in solution), the physical (laser ablation) or the photophysical (photoreduction of Au and Ag salts) methods.

In 1979 the first report describing the use of metal colloids for SERS analysis was published [21] proposing Ag and Au solutions obtained by reduction of AgNO_3 and $\text{K}(\text{AuCl}_4)$ with NaBH_4 . Only a year later, in 1980, Kerkel et al. [22] reported the use of citrate ions as reducing agent. According to the literature, silver colloids seem to produce the largest enhancement effect among metal colloids, although their oxidation represents an intrinsic limitation .

In particular the citrate – reducing method, proposed by Lee and Meisel [23], has been widely used for SERS analyses. However, the synthesis generates by-products that could be enhanced in surface-vibrational spectroscopies, as spurious peaks, interfering with the detection of the analytes. Recently, the hydroxylamine hydrochloride reducing method [24] has been considered the most effective system for the production of colloidal solutions to be employed for spectroscopic applications [25] because most of the reaction byproducts are gaseous and leave the system.

Laser ablation synthesis in solution (LASiS) is the methodology which allows to synthesize nanoparticles without interfering molecules. From the pioneering work of Fojtik and Henglein [26], the methodology has been improved as reported in a recent review [27]. With LASiS, stable colloidal solutions can be obtained in pure water and other solvents without the presence of any stabilizing agents due to the charges produced on the nanoparticles by the ablation. Moreover, the nanoparticles, presenting a clean surface, can be easily reached by molecules, assuring a good interaction, which is mandatory for observing an enhanced signal. This type of nanoparticles shows, therefore, an advantage over those obtained by chemical reduction of salts in solution, in particular for the absence of interfering species in the colloidal solution.

For SEIRA analysis the sample can be placed on the active substrates using different methods. Using the “drop-drying method” a dilute solution of the analyte is applied on the support and analysed after drying. Another possibility is to form a thin film of the sample on the metal

surface by evaporation under vacuum. SEIRA analyses can be performed also on Langmuir films obtained by horizontal deposition in a Langmuir balance which are then transferred to the SEIRA substrate [14]. Moreover, depending on the type of support, different configurations such as sample-metal, metal-sample and metal-sample-metal have been successfully adopted.

Since the enhancement factors (about 10-1000 times) of SEIRA is not competitive when compared with those of SERS, few attention has been dedicated to possible applications. However the cross sections for absorption in the infrared are order of magnitude higher than the corresponding Raman cross sections. Thus even if SEIRA enhancement is modest it can have effect in practical applications so that both the two techniques are under development as promising "optical sensor technology" [14]. Nevertheless, few analytical applications of SEIRA have been reported up to now since the main concern is related to the poor reproducibility of the substrates [28]. However, SEIRA has been used in the analysis of environmentally hazardous chemicals in waste waters [18], as a detector coupled to chromatographic techniques, such as liquid and gas chromatography [29] or to immunological techniques [30, 31]. In the biochemical field the application of this technique was considered particularly useful to obtain information on the structural changes at a molecular level [30]. Moreover, one field in which SEIRA has been widely employed is the study of the molecular organization of thin films formed with different preparation methods [32-34]. SEIRA has been also successfully proposed to study the catalytic behavior of metal particles [35]. Several papers have been published concerning the combination of SEIRA with electrochemical methods, employing the metal islands as electrodes [28]. In particular, the ATR Kretschmann configuration in which the metal islands are deposited directly on the crystal is a successful tool for electrochemical dynamic studies.

4.1.2 Materials and methods

4.1.2.1 Materials

The selected dye, Acid Orange 7 (AO7), and the dyed wool were kindly provided by RCE (Rijksdienst voor het Cultureel Erfgoed / Cultural Heritage Agency of the Netherlands) in the frame of the European project CHARISMA.

Hydroxylamine hydrochloride (HONH₃Cl), silver nitrate (AgNO₃), sodium chloride (NaCl), sodium nitrate (NaNO₃), sodium sulfate (Na₂SO₄), sodium iodide (NaI), and sodium hydroxide (NaOH) were all purchased from Sigma. Tri-distilled water was used for all solutions preparation.

4.1.2.2 Silver colloid preparation

Silver colloidal solution was prepared according to the Leopold and Lendl method [24]. In more detail an aqueous solution of silver nitrate (AgNO₃) was reduced by hydroxylamine hydrochloride (HONH₃Cl) in a weakly alkaline ambient and let under vigorous stirring at environmentally temperature.

Reaction mechanism is complex and provides various kind of intermediate, and Ag---HX complexes formation. By-products are: N₂ and NO_x, in gas phase, that easily leave the reaction mixture. For this reason, this kind of synthesis is preferred to lee and Meisel method for spectroscopic purposes. Using FTIR characterization of two different sols, it could be found that citrate colloid is affected by a larger number of spurious pecks in FTIR spectrum, as also reported in previous work [25].

The aggregation of colloid has been conducted by addition of sodium chloride. Aggregation procedure was found to be effective to obtain the best performances in SERS experiments, for this reason in this work we try to evaluate if the contribution of aggregates formation improve also SEIRA activity.

4.1.2.3 Gold colloid preparation

The synthesis of gold nanoparticles (AuNPs) was obtained by LASiS according to previous reports [36, 37]. Briefly, a bulk metal target was immersed in NaCl 10⁻⁵ M water solution and irradiated with 9 ns pulses of a Nd:YAG laser (Quantel YG-981E-10) at 1064 nm using a fluence of 10 Jcm⁻². The colloidal concentration was monitored with UV-vis extinction spectroscopy [37]. In this way a dispersion of nanoparticles with diameters between 18 and 20 nm was obtained.

The colloidal solution was used as obtained or after a controlled aggregation, with centrifugation at 30000 RCF for 10 minutes of the AuNPs . In this way an active substrate, made up of aggregates of 100–150 nm, was obtained without introducing other interfering material. The aggregated AuNPs were then dispersed in pure water by sonication.

4.1.2.4 UV-Vis spectroscopy

UV-vis spectra of colloidal suspensions were recorded between 200 and 800 nm, using a Varian Cary Bio UV – Vis Spectrophotometer (Varian, Palo Alto, CA, US), single beam. The reference was taken on a quartz cell filled with tridistilled water. Measurements were performed using a 1 cm quartz cell.

4.1.2.5 FTIR spectroscopy

The FTIR measurements were performed on gold coated glass slides for RAS (Reflection Absorption Spectroscopy) analysis, using a Thermo Nicolet iN™10MX raster scanning microscope, fitted with an MCT detector cooled by liquid nitrogen. Spectra were recorded in the range 4000–675 cm⁻¹ with an aperture 50 × 50 μm, spectral resolution 4 cm⁻¹ and 128 or 512 number of scans. Data collection and post-run processing were carried out using the OMNIC Picta™ software (Thermo).

Gold coated glass slides were ultrasonicated in ethanol and dried under ambient conditions before the application of the analyte. Unaggregated and aggregated Ag and Au nanoparticles were immobilized by direct deposition on a glass slide for RAS. An aliquot of 5 μl of unaggregated and aggregated colloidal solutions were deposited over the slide forming a circle

of almost 2 mm diameter. Subsequent depositions of the colloidal solution were performed applying 3, 5, 8 drops of 5 μl each in order to produce a more homogeneous distribution. The dried drops were characterized by RAS spectroscopy to define spurious peaks, then washed with tridistilled water and characterized once again to evaluate the effectiveness of washing.

1 μL of 10^{-4} M AO7 solution was deposited both on the naked gold coated slide and over the different types of colloidal depositions, in order to compare the spectra and to verify the presence of surface enhancement effects. SEIRA spectra were registered on the external profile of the drop of the colorant applied over the colloidal deposition, on points in which the borders of the colorant were not superimposed to the one of the colloid.

In the second protocol, the interaction of the colorant with the nanoparticles (aggregated and unaggregated) was obtained in solution. In this case, 10 μl of 10^{-4} M AO7 solution were dried and 10 μl of aggregated or unaggregated gold colloid solutions were added. After sonication, 1 μl of the obtained solutions was spotted on the gold coated glass slide. 1 μl of 10^{-3} M AO7 solution was deposited on the gold coated slide in the absence of AuNps and used as reference for peak attribution.

4.1.2.6 Extraction method

Extractions were performed employing mild methods in order to avoid hydrolysis of the wool and thus the presence of spurious bands due to the presence of by-products, in the FTIR spectra. Preliminary tests were performed with 1 mg of dyed wool (corresponding to 6 mm of a woolen yarn). Then, the amount of wool was reduced to just a few pieces of fiber (less than 0,01 mg, which were not possible to be weighted corresponding to few mm in length of a single fiber), using a reduced amount of solvents.

The following methods were compared:

Formic acid method: 1 mg of the dyed wool was added with 40 μl of a mixture 85:15 (v / v) methanol-formic acid for 60 minutes at 50°C [38]. After removing the wool, the extract was evaporated to dryness under ambient conditions for a night and then reconstituted in a small amount (10 μl) of demineralized water.

Ethylenediaminetetraacetic acid (EDTA) method: 1 mg of the dyed wool was added with 40 μl of a mixture 2: 10: 88 (v/ v/ v) 0,001 M aqueous H₂EDTA / acetonitrile / methanol for 30 minutes at 60°C [26]. After removing the wool, the extract was evaporated to dryness under ambient conditions for a night and then reconstituted in a small amount (10 μl) of demineralized water.

Methanol (MeOH) method: 1 mg of the dyed wool was added with 40 μl of methanol for 30 minutes at 60°C After removing the wool, the extract was evaporated to dryness under ambient conditions for a night and then reconstituted in a small amount (10 μl) of demineralized water.

For comparison, a small amount (1 μL) of each reconstituted solution was deposited on a gold coated slide for RAS measurements.

4.1.2.7 SEIRA analyses on micro extractions

The developed SEIRA protocol was applied for the analyses of few pieces of fiber extracted with the MeOH method. The fiber was extracted employing 3 aliquot of 10uL of MeOH over a time of 30 min at 60°C. Every 10 minutes, approximately, the solvent dried and a new aliquot of MeOH was added. The extract was reconstituted with 5uL of water and 5uL of the unaggregated colloidal solution. After sonication, 1 μL was spotted on a gold coated glass slide and analyzed in RAS mode.

4.1.3 Results and discussion

4.1.3.1 Characterization of the colorant

In order to obtain a reference spectra, 1 μL of the 10^{-3} M AO7 solution was spotted on a gold coated glass slide and RAS measurements were performed on the external profile of the drop (Fig. 2, band assignment is reported in Table 2 (par. 4.1.5.3).

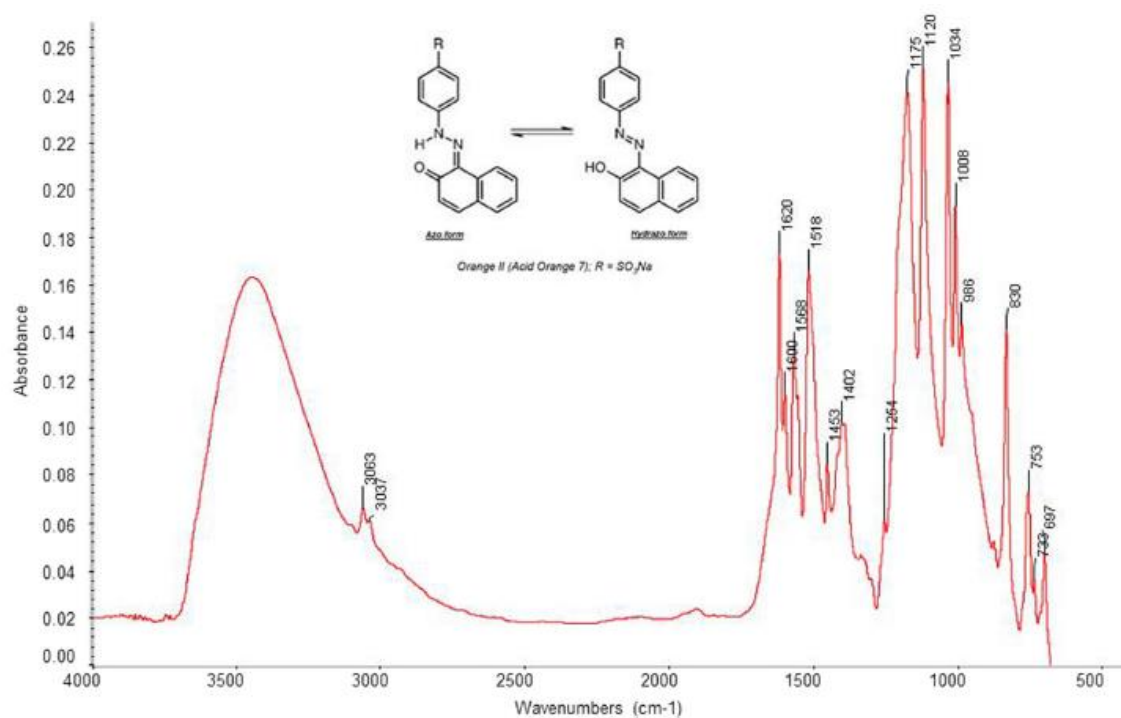


Fig. 2: RAS spectrum registered on the border of a drop obtained spotting 1 μL AO7 10^{-3} M solution.

4.1.3.2 Ag colloidal solutions (unggregated and aggregated)

UV-Vis spectroscopy

The UV Vis spectra of aggregated and not aggregated Ag colloidal solution are reported in figure 3. The spectrum was already characterized in previous works [24, 25].

In the spectrum of the not aggregated solution the main peak at approximately 420 nm is due to the plasmonic oscillation of silver nanoparticles as reported by Leopold and Lendl [24]. Moreover the estimated FWHM (full – wide half maximum) value of about 66 nm calculated is in good agreement with the data previously published [24].

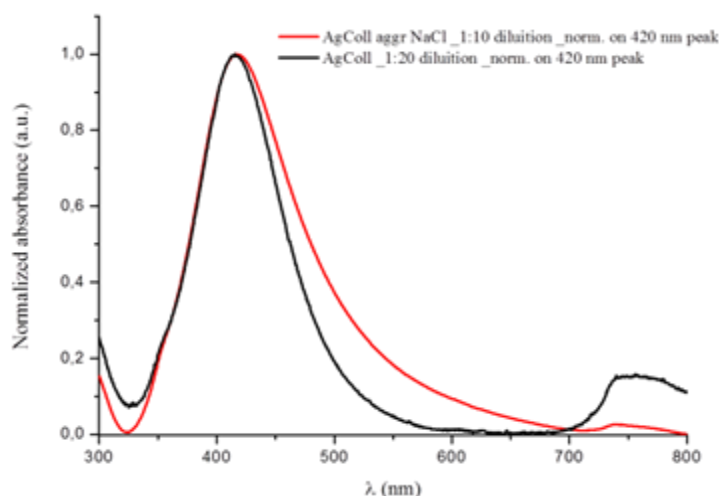


Fig. 315: UV – Vis spectra for AgColl unaggregated (black line) and aggregated with NaCl (red line).

In UV spectra of aggregated solution a broad band appears in 700 – 800 nm, corresponding to the longitudinal oscillation modes of surface silver plasmons. This absorption increases with the nanoparticles domains dimensions.

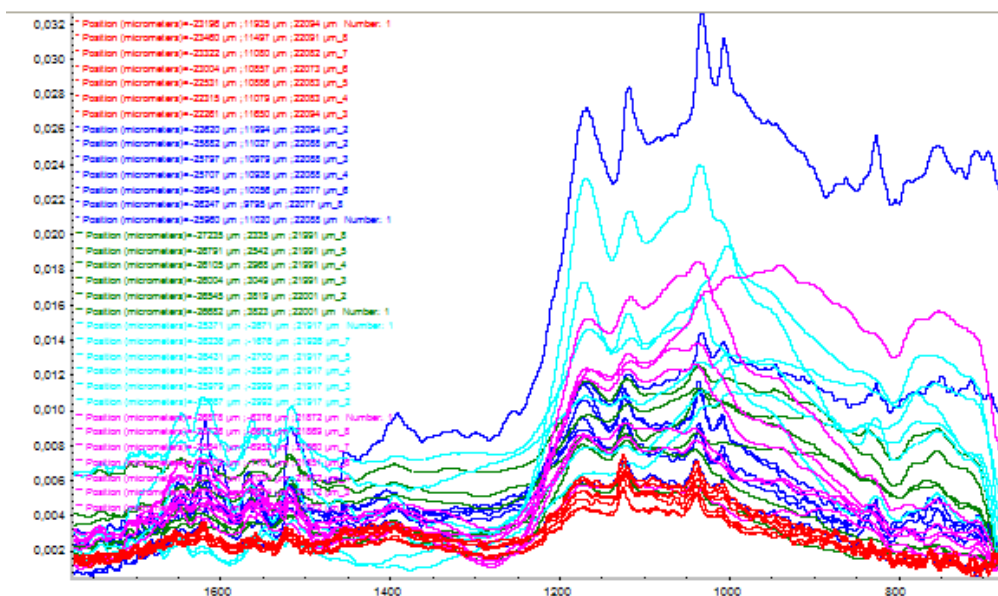
The transversal oscillation mode, represented by 420 nm peak, undergoes an enlargement on FWHM; this means that the size distribution of nanostructures in solution becomes larger, as expected.

SEIRA analysis

Even if spurious peaks related to the presence of nitrates were detected, both in the aggregated and in the not-aggregated Ag solution, after a washing treatment the signals can be mostly eliminated. After the evaluation of colloidal washing effectiveness, a drop of AO7 10^{-4} M, 0,5 ul, was deposited over every colloidal depositions, to evaluate the different enhancement effects. A drop of simple AO7 solution, 0,5 ul, is deposited and used like reference standard. FTIR analysis have been performed on several points for each drop.

The SEIRA analysis of AO7 on Ag colloid unaggregated (fig. 4) showed that the average intensity of spectrum increase increasing the number of depositions, an estimation of the effective peak heights and areas is necessary in order to evaluate the enhancement effect,

because a significant contribute to intensity is given by scattering effects, that means growth of baseline, due to scattering of metal nanostructures.



- = AO7, ref, 10-4M, 0,5 μ l
- = AgColl not aggr. 5 μ l + AO7 10-4M, 0,5 μ l. Inner area of colloid deposition.
- = AgColl not aggr. 3x5 μ l + AO7 10-4M, 0,5 μ l. Inner area of colloid deposition
- = AgColl not aggr. 5x5 μ l + AO7 10-4M, 0,5 μ l. Inner area of colloid deposition
- = AgColl not aggr. 5x5 μ l + AO7 10-4M, 0,5 μ l. Inner area of colloid deposition

Fig. 4: SEIRA spectra of AO7 on Ag unaggregated colloid

Besides it, high frequency are not effective to evaluate enhancement, because variable amounts of humidity in air may affect the intensity of OH bands in progressive measures. For this reason, we focus on 1700 – 700 cm^{-1} region.

Analyzing different bands an anomalous trend is observed: the peak height medium value growth from reference to 1 AgColl deposition, to decrease in a sudden for three depositions, growth again slowly for 5 deposition and finally slowly decrease for height depositions. There is not apparent consequentiality in this trend. An explanation could be that a significant scattering contribution is present that tends to affect the baseline and to decrease the resolution of those peaks.

Also for Ag aggregated colloid, SEIRA experiments are performed over 3, 5 and 8 colloid depositions. The drops were washed with distilled water and the analyte solution was deposited over. Spectra obtained are superimposed to qualitatively estimate the enhancement effect (fig. 5).

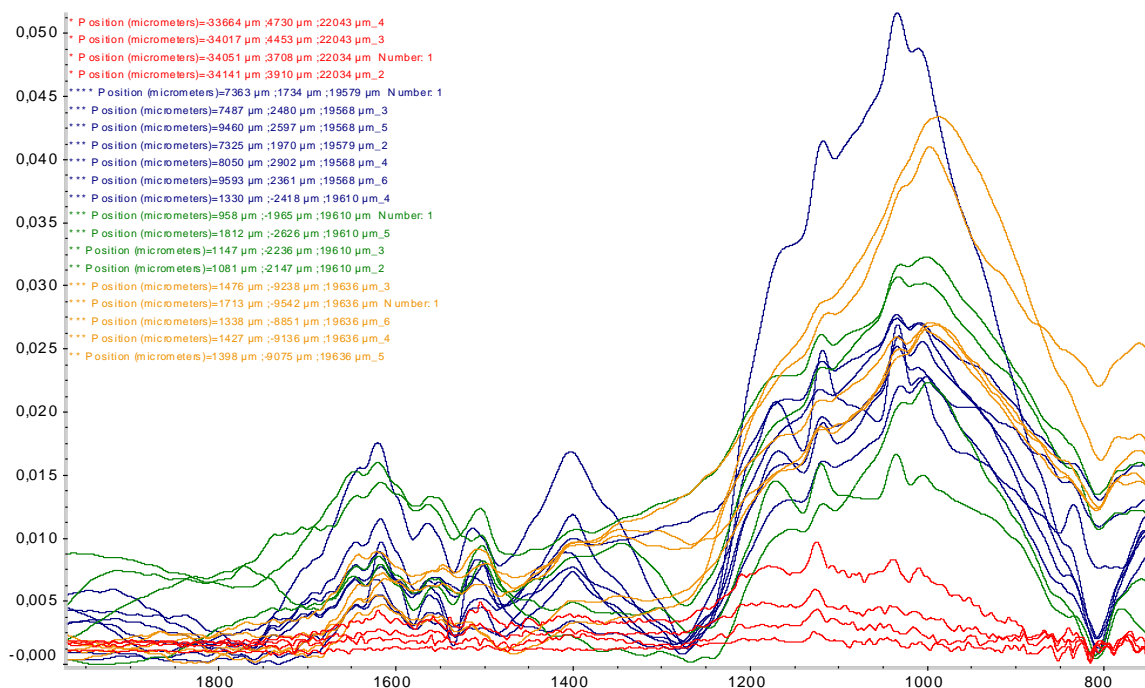


Fig. 5: comparison between SEIRA spectra at different rate deposition of Ag colloid: AO7, reference (red), AO7 + AgColl, 3x5ul (blue), AO7 + AgColl, 5x5ul (green), AO7 + AgColl, 8x5ul (yellow).

Also for these spectra the effective intensities and areas of the peaks have been evaluated in order to identify the enhancement. The data evaluation shows the existence of more homogeneous trend for aggregated colloid, and a significant enhancement for 3 and 5 colloid depositions.

In conclusion, analyses performed in RAS on the not aggregated Ag colloid did not provide the evidence of enhancement neither in the drops obtained after three depositions nor in the ones with five depositions as expected observing the morphology of the deposited aggregates. Spectra registered on the eight deposition drop showed a slight increase mainly ascribable to an increase of the baseline, and a change in the spectral shape.

On the other hand spectra registered on the drops obtained with the Ag aggregated colloidal solution showed an enhancement. The intensity of the spectra was highly variable on all the spotted areas and it did not seem to be affected by the number of depositions. As far as spectral resolution is concerned, it tended to decrease passing from three to eight deposition. Moreover bands tended to enlarge with the increasing of their intensity, even if in few cases it was obtained a reasonable spectral resolution in medium intense spectra.

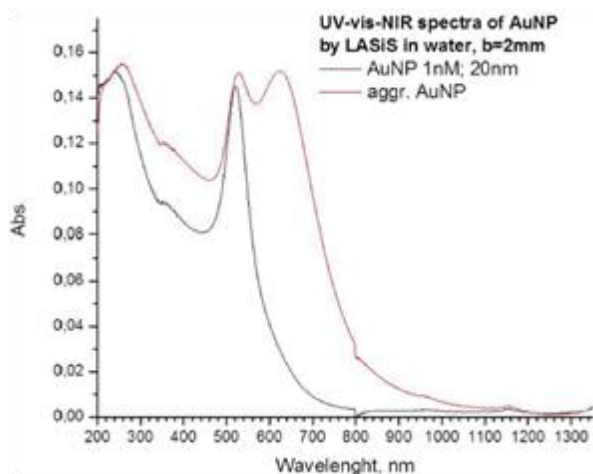
4.1.3.3 Au colloidal solutions (unggregated and aggregated)

More attention has been paid to SEIRA analysis performed with Au colloid due to the fact that this colloid has been obtained without addition of reagents or stabilizer additives. This means that the spectra are hypothetically free of spurious bands and, moreover, it is no necessary wash the colloid before the application.

Concerning this part of research project, we have published an article [39]

Characterization of Au colloid

The UV-vis-NIR spectra recorded for unaggregated and aggregated AuNPs are reported in Figure 6. The localized surface plasmon resonance (LSPR) of unaggregated AuNPs is useful for its characterization using the Mie-Gans model [37]. By fitting this spectrum one estimates that



the average dimension of the AuNPs is 20 nm and their concentration 10^{-9} M. The aggregated AuNPs present a characteristic red-shifted plasmon resonance band, according to the Mie-Gans model used for size and concentration evaluation of gold colloidal solution [37]. Aggregates composed by few tens of nanoparticles, 10–20 AuNPs, cause a typical band at 600–800 nm, as just reported before [40, 41].

Fig. 6: UV – Vis spectra of the AuNPs unaggregated (black line) and aggregated (red line).

RAS analyses of the two colloidal solutions showed the presence of bands with very low intensity probably due to some residual environmental pollutants, which, however, didn't affect the SEIRA spectra (Fig. 7).

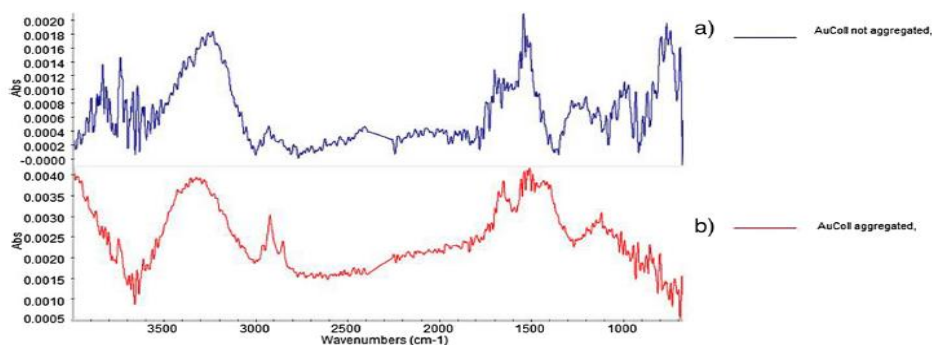


Fig. 7: RAS spectra registered on the border of a drop obtained spotting 1 μ L of a) unaggregated AuNPs b) aggregated AuNPs.

SEIRA on multiple depositions of the colloidal solutions

Multiple depositions of the colloidal solutions, as recalled in the experimental part, were applied on a RAS gold coated glass slide. A drop of colorant was then deposited over the AuNPs and the spectra were recorded on the border of the colorant drop, in correspondence of the inner part of the colloid substrate (Fig. 8a).

Spectra of AO7 deposited on the unaggregated AuNPs drops showed an enhancement of the signal in few points, probably depending on the local formation of aggregates. It was observed that increasing the number of colloid drops depositions an increase of the signal is observed just in few areas, probably due to the formation of aggregates with a more efficient geometry. In Figure 8b one of the enhanced spectra is compared with the RAS spectrum obtained applying the same volume of AO7 10^{-4} M solution directly on a gold coated glass slide. It can be noted that without the nanoparticles the signals of the colorant can be hardly distinguished from the background. In the presence of the AuNPs an increasing in signal intensity was detected (Fig. 8b) and the main features of the colorant can be distinguished from the background. However spectra were characterized by a high variability of the intensity and by a worsening in the definition of the absorption bands as it can be evinced comparing the spectrum reported in Figure 8 with a reference spectrum of a more concentrated solution of AO7 (10^{-3} M) acquired in RAS (Fig. 8c). The enlargement of the bands and the shift in some maximum positions may be ascribable either to scattering events or to the presence of some pollutants derived either by the colloid or by the water employed to prepare the dye solution.

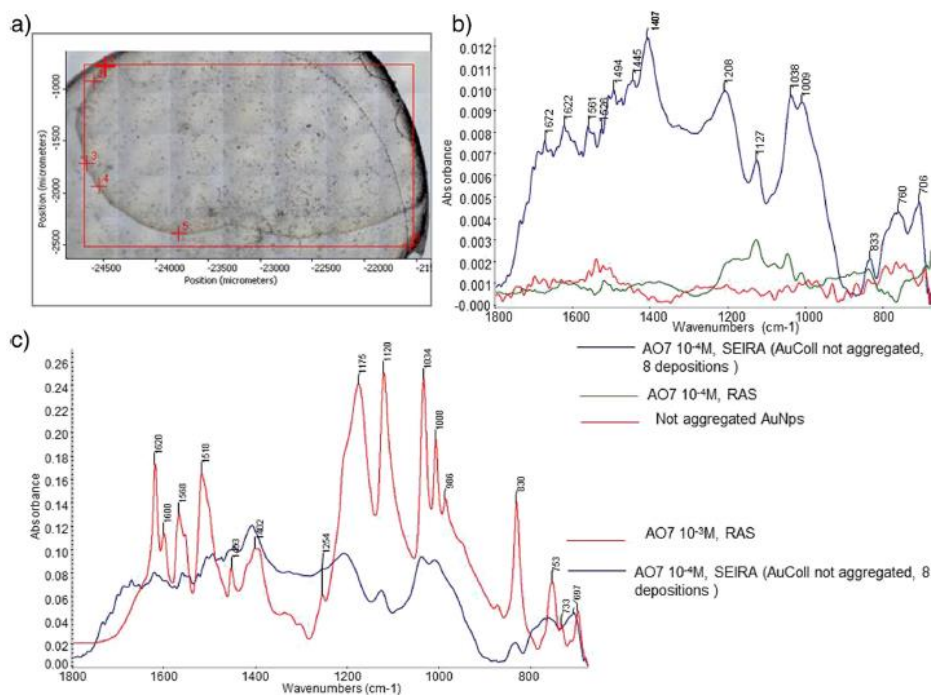


Fig. 8: SEIRA analyses performed applying 1 μ L of 10^{-4} M AO7 solution over the unaggregated AuNPs spot obtained after 8 depositions. a) Photo of the colorant spot, numbers refer to points of analysis b) SEIRA spectrum registered in position 4 (blue profile), RAS spectrum of AO7 10^{-4} M (green profile) and RAS spectrum of 1 μ L of the unaggregated AuNPs solution (red profile), common scale c) SEIRA spectrum registered in position 4 (blue profile) and RAS spectrum of AO7 10^{-3} M solution (red profile), full scale.

On the other hand, spectra registered on the colorant deposited on the aggregated AuNPs showed an enhancement for all the three types of multiple depositions (mainly on the three depositions), even if they were characterized by a variable intensity, depending on an inhomogeneous distribution of the colloidal aggregates.

As an example, a spectrum of medium enhancement from the ones obtained on the three depositions is reported in Figure 9 and compared with the reference RAS spectrum of the AO7 10^{-4} M solution applied directly on a gold coated glass slide and with the RAS spectrum registered on the AuNPs. Also in this case, in all the enhanced spectra an enlargement of peaks can be noted and the definition of the bands was worse than in the spectra registered on a more concentrated solution without AuNPs (Fig. 9b). Nevertheless, the identification of the colorant absorption bands was not compromised.

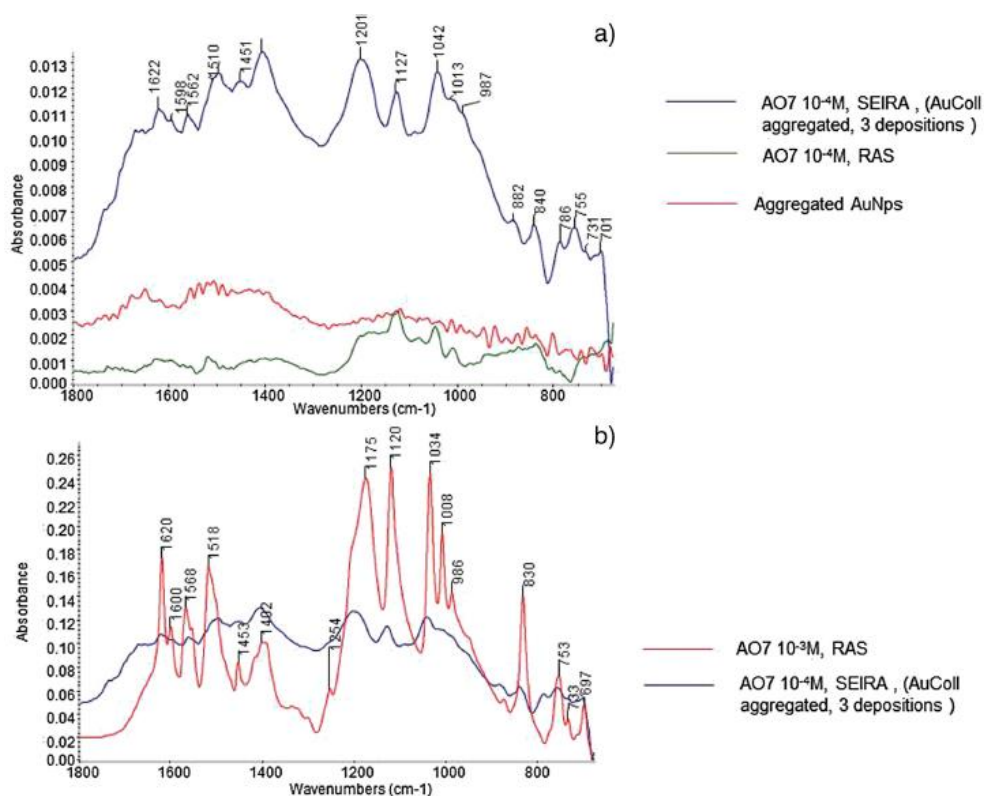


Fig. 9: SEIRA analyses performed applying 1 μL of 10^{-4} M AO7 solution over the aggregated AuNPs spot obtained after 3 depositions. a) SEIRA spectrum registered on the border of the drop (blue profile), RAS spectrum of 1 μL AO7 10^{-4} M solution (green profile) and RAS spectrum of 1 μL of the aggregated AuNPs solution (red profile), common scale b) SEIRA spectrum registered on the border of the drop (blue profile) and RAS spectrum of 1 μL AO7 10^{-3} M solution (red profile), full scale.

Deposition of the mixture colloid-colorant

The second evaluated protocol, performed with AuNPs, was based on the preparation of a mixture between the colloidal solutions and the colorant which is subsequently applied on the RAS support. FTIR analyses were performed on the external profile of the drop, which was characterized by a higher concentration of the mixture components (Fig. 10a). Figure 10b shows one of the spectra registered for the 10^{-4} M solution of AO7 mixed with the unaggregated AuNPs. It can be noticed that a remarkable enhancement of the signal is obtained without compromising the resolution of the absorption bands present in the spectra. Indeed comparing the obtained FTIR spectrum with the RAS spectrum on a 10^{-3} M AO7 solution a better correspondence of the band can be observed (Figure 10c). Conversely, band resolution of spectra registered on the 10^{-4} M solution of AO7 mixed with the aggregated

AuNPs was worse than that obtained with the previous method, even if a significant enhancement was obtained.

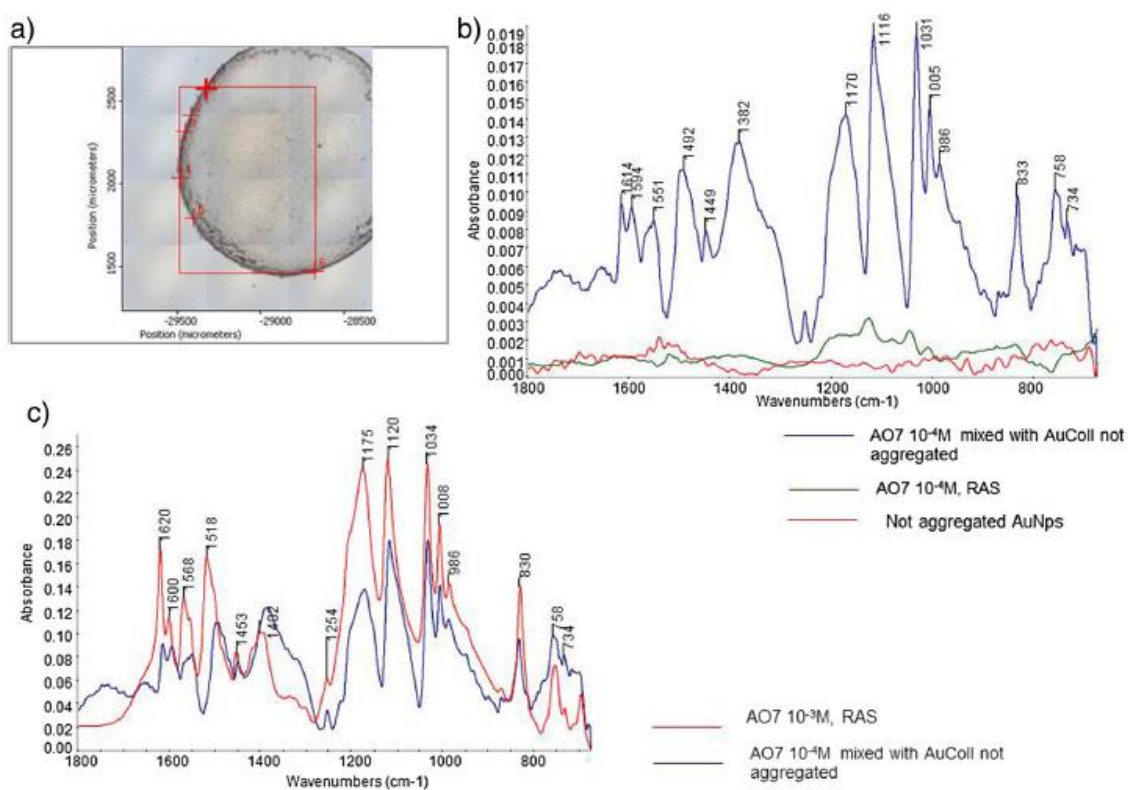


Fig. 160: SEIRA analyses performed after spotting 1 μL of the AO7 10^{-4} M solution containing the unaggregated AuNPs. a) Photo of the drop, numbers refer to points of analysis b) SEIRA spectrum registered in position 3 (blue profile), RAS spectrum of 1 μL AO7 10^{-4} M solution (green profile) and RAS spectrum of 1 μL of the unaggregated AuNPs solution (red profile), common scale c) SEIRA spectrum registered in position 3 (blue profile) and RAS spectrum registered on the border of a drop obtained spotting 1 μL AO7 10^{-3} M solution (red profile), full scale.

Therefore, the unaggregated colloid-colorant mixture procedure was selected as the most efficient approach for an easier identification of the colorant. To verify the performances of the method, $5 \cdot 10^{-5}$ M and 10^{-5} M solutions were also analyzed.

Spectra registered on the drops obtained with the $5 \cdot 10^{-5}$ M solution showed characteristic bands of the colorant (Fig. 11), which were not detected in the reference spectrum obtained in RAS mode on the dye solution at the same concentration. However, for the 10^{-5} M solution, any diagnostic AO7 absorption bands were identified, even with the addition of the AuNPs, due to the high noise of the spectra.

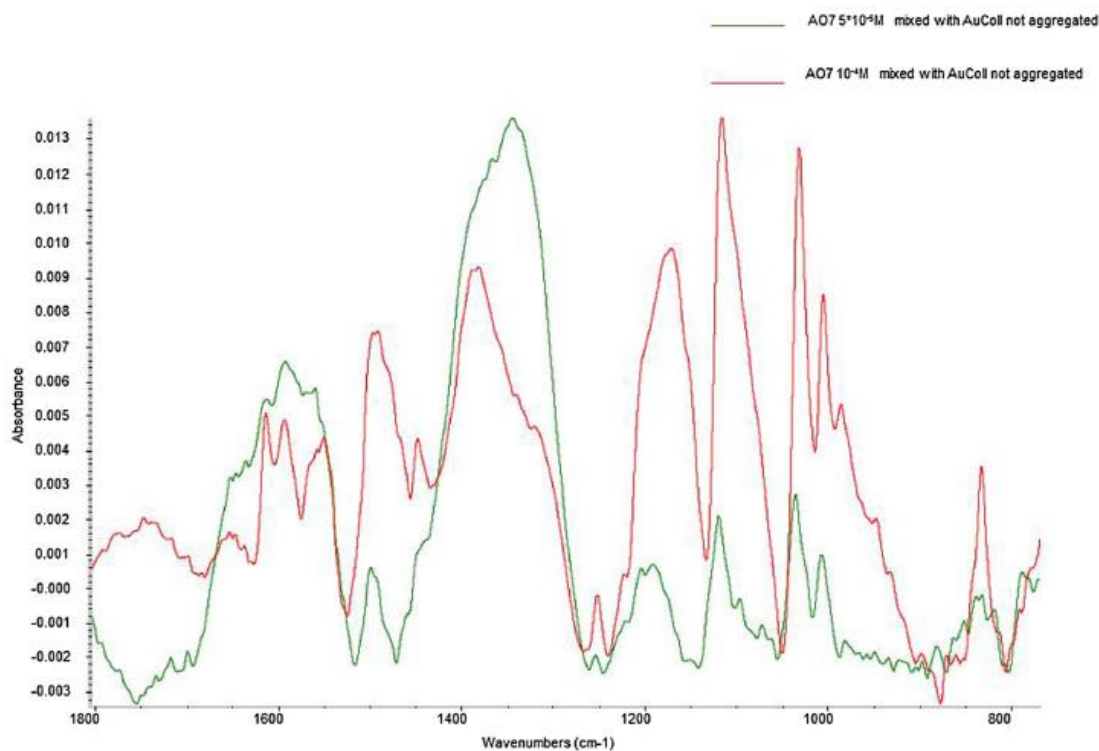


Fig. 11: SEIRA spectrum registered on the border of the drop obtained spotting 1 μL AO7 $5 \cdot 10^{-5}$ M solution containing the unaggregated AuNPs (green profile) and SEIRA spectrum registered on the border of the drop obtained spotting 1 μL AO7 10^{-4} M was mixed with the unaggregated AuNPs solution (red profile), full scale.

Extraction tests

Different extraction procedures were tested as mentioned in par 3.1.2.6. Preliminary investigations were carried out on a measurable amount of dyed wool (1 mg), then the most promising procedure was employed on just a few pieces of fiber (less than 0.01 mg, which were not possible to be weighted).

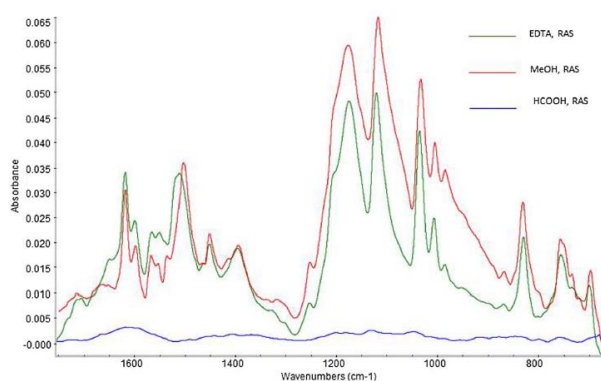


Fig. 12: Comparison between the extraction methods. RAS spectra of 1 μL of the solution extracted from wool with the: EDTA (green profile), MeOH (red profile), HCOOH (blue profile) methods, common scale.

Comparing the three procedures (Fig. 12) the HCOOH method appeared to be the less effective in extracting Acid Orange 7. The EDTA method showed an optimal extraction capability. Intense and well resolved spectra were obtained without the presence of spurious peaks. However, reducing the amount of wool, spurious peaks connected to EDTA appeared in the spectrum (data not shown). The methanol (MeOH) method provided results similar than EDTA with the advantage to be completely eliminated when the sample

was dried and, therefore, it was selected for SEIRA analyses.

SEIRA on the extracted colorant

The MeOH extraction method was employed for the extraction of a few pieces of fiber. Then, as described in par. 3.1.2.7, the extract was mixed with unaggregated AuNPs and analysed in RAS mode. The obtained SEIRA spectra were characterized by a weak intensity of the signal (Fig. 13) and even if bands resulted enlarged by the presence of other contaminants, diagnostic absorption bands, related to the presence of AO7, resulted identifiable as peaks or shoulders, allowing the identification of the colorant used in the dyeing process.

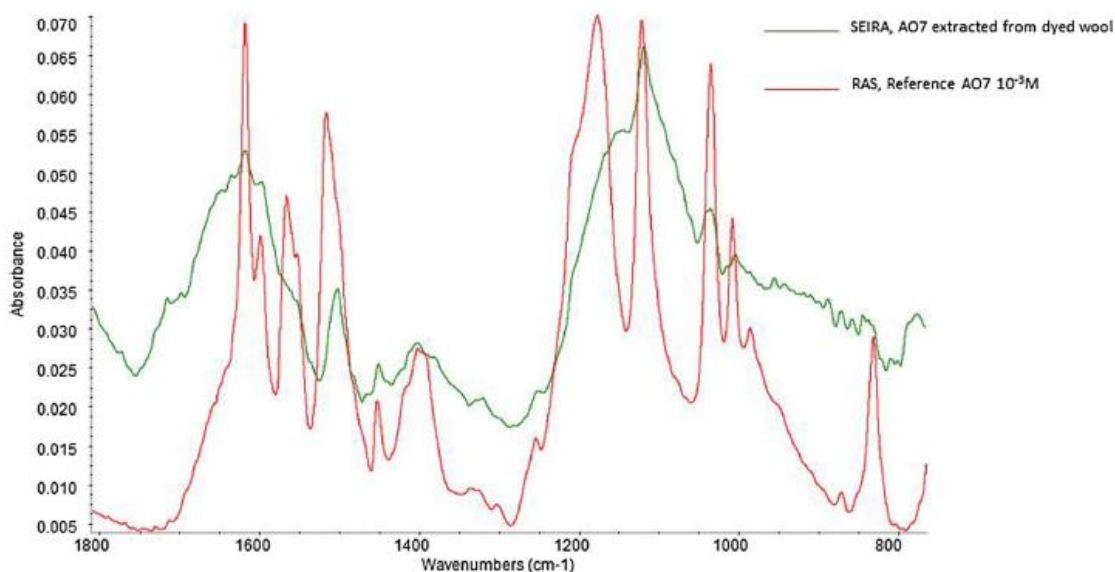


Fig. 13: SEIRA spectrum registered on the border of the drop obtained spotting 1 μL of the solution extracted with the MeOH method from few fibers (few mm of a single fiber) dyed with AO7 and mixed with the unaggregated AuNPs (green profile) and RAS spectrum of 1 μL of AO7 10^{-3} M solution (red profile), full scale.

4.1.4 Conclusions

It is here proved that SEIRA can be used as an analytical method to analyze small quantities of colorants. The method set up using naked AuNPs produced by means of laser ablation, allowed strong enhancements of the signals, without the presence of spurious by-products which may affect the results. On the other hand, applying the method performed using AgColl, worse results have been achieved due to the lower enhancement and mainly due to the presence of spurious bands – generated by the Ag colloid - and a low spectra resolution caused by a considerable growth of the baseline.

The best results in term of enhancement and spectral resolution were obtained mixing the colorant solution with the Au unaggregated particles. The analyses were then performed on a drop deposited on a gold coated glass slide after drying in RAS mode on the borders of the spot, which contain the highest quantity of colloid and colorant. This method allowed to analyze solution down to $5 \cdot 10^{-5}$ M and has been applied for the analyses of extracted dyed wool samples after the setting up of a suitable micro extraction method aimed at avoiding

hydrolysis of wool and the presence of by-products which can hinder the colorant absorption bands. The extraction with MeOH, which provided the most effective results among three extraction methods tested, was applied for the analysis of a few pieces of fiber. SEIRA spectra obtained mixing the extract with the unaggregated AuNPs allowed to recognize bands of the colorant, even if present in low concentration.

Further efforts will be devoted to optimize the micro extraction procedure in order to improve the detection limit. Moreover the method will be applied for the analyses of several types of colorants in order to understand the limits of the proposed methodology in the discrimination among different compounds. The micro-extraction SEIRA analyses of small amount of colorants may find several applications for the study of artistic samples as well as those coming from the forensic and the environmental fields.

4.2 ATR-RAIRS

4.2.1 Reflection Absorption InfraRed Spectroscopy (RAIRS) and Grazing Angle (GA)

The technique of Reflection Absorption InfraRed Spectroscopy was first described both theoretically and experimentally in 1958 by Francis and Ellison [42]. It is performed on thin samples physically or chemically adsorbed on a highly reflective surface, generally a metal support. The main idea is already suggested by the name of the technique: the incident IR beam has to pass twice through the sample; first it is transmitted through it, then, as it reaches the metal support, it is reflected back. In this way, it has to pass a second time through the sample; as a consequence, the sampling occurs twice, leading to a doubling of the spectral output.

Given the importance of high reflectivity of the support on which the thin sample is in contact for the occurrence of this phenomenon, the metals that are more commonly used are gold, silver and copper, being them excellent reflectors in the mid-IR range [42]; in spite of this, even dielectric materials (non-conducting materials with small absorption index and refractive index between 1.3 and 4.0) have been used sometimes, which can be a very useful alternative, although less performing, for some technological applications [42].

Concerning the thickness of the samples to be analyzed, RAIRS nomenclature refers to the specific case in which the thickness of the sample is smaller than the interacting wavelength, while for samples having comparable or higher thickness, the technique is referred to as *transfection* spectroscopy [42]. Such discrimination must be stressed because the thickness of the sample analyzed plays a crucial role in determining the associated physical phenomena, hence the resulting IR spectra.

Indeed, if the thickness is smaller than the wavelength of the interacting IR light, it is possible to enhance even more the obtainable spectral signal by setting the source at grazing angle incidence and by polarizing it to its parallel component. It is well known that a molecule is able to absorb infrared radiation only if the molecular vibration is associated with a simultaneous change in the dipole moment; in addition to this fundamental selection rule, Francis and Ellison [43] predicted that the molecule needed to have a component of its transition moment (the change in the dipole moment) normal to the metal surface in order to be infrared active. This is due to the fact that the perpendicular component of the radiation undergoes an approximate phase shift of 180° for all angles of incidence upon a direct reflection, which is equivalent to say that the electric field has a node at the surface for the perpendicular component. Accordingly, no net electric field can interact with the oscillating dipole at the metal surface and thus no absorption can be observed. The parallel component, however, do

not cancel because of the finite phase shift between the incident and the reflected components upon reflection [44]. This is the reason why, for very thin samples, a bigger enhancement can be obtained by using p-polarized light at grazing incidence (where the grazing angle can be defined as the angular value as closest as possible to the critical angle for total internal reflection). This can be maybe more easily understood observing figure 1, published in 1985 by Liedberg et al. [44]:

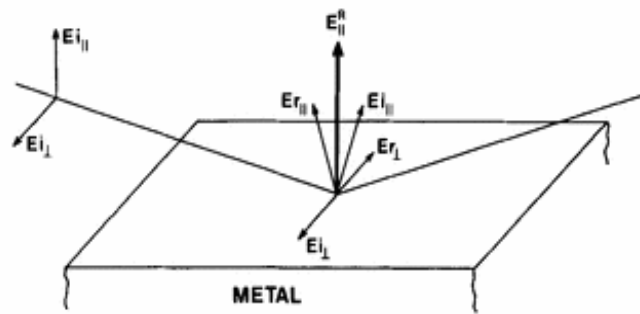


Fig. 17: The electric field at the metal surface for a high angle of incidence and for both parallel and perpendicular polarization of the IR radiation. $E_{||}^R$ = electric field normal to the metal surface; the electric fields in the plane of the metal surface is almost zero since $E_{ij} = -E_{rj}$

Another excellent publication about the topic was presented by R. Greenler in 1965 [45], who calculated the phase shift for light reflected from a metal surface, for light polarized both parallel (p) and perpendicular (s) to the plane of incidence, as he displayed in the reported figure 2:

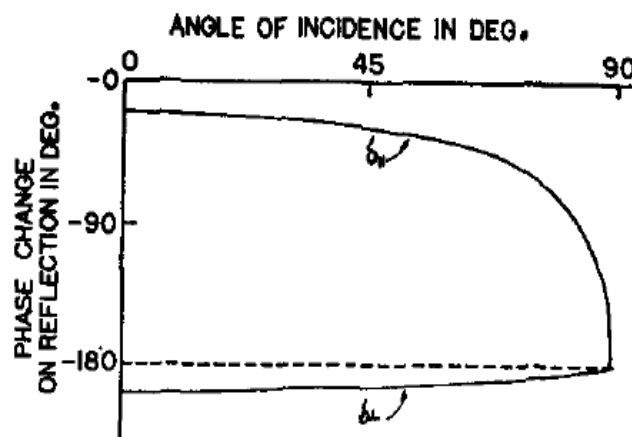


Fig. 18: Phase shift for light reflected from metal surface. $\delta_{||}$ is the phase shift for light polarized parallel to the plane of incidence; δ_{\perp} is the light polarized perpendicular to the plane of incidence

Thanks to this graph it is easy to visualize how the phase shift, for the light component polarized parallel to the plane of incidence, changes rapidly at high angles of incidence [45]. Indeed, at increasing angular incidence from the surface normal, that is, at values progressively reaching the grazing angle condition, the behavior of s and p polarized light drastically changes. Specifically, while for the s component the phase shift is always approximately

constant at 180° for each angle of incidence, meaning that this component will hardly contribute to the spectral signal whichever the angular configuration of the source is, the phase shift associated to the p polarized light ranges instead from the already stated 180° for an angle of incidence of 0 , to 90° for an angle of incidence of about 87° from the surface normal [42, 45]. At such angular value, the electric vectors of the p polarized impinging and reflected IR radiation progressively sum up, generating a strong electric field at the metal surface [42].

Since the intensity of the thin film absorption is proportional to the field strength, it follows that an increasing amplification of the spectral output will occur at increasing incidence angle values, and that the sensitivity of the system to very thin, up to sub-monolayer samples will as well benefit from it [42, 46].

From all this, it follows that only vibrational modes with transition moment normal to the surface can be excited by infrared radiation. This additional requirement for excitation of adsorbed molecules on metal surfaces is normally summarized in the “surface selection rule” [4]. A visualization of it has been proposed by Liedberg [44] and it is presented in figure 3:

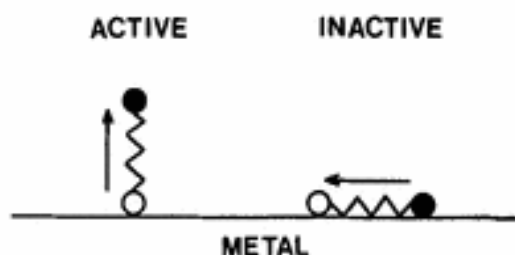


Fig. 19: two hypothetical dipoles adsorbed in different orientations on the metal surface. The “surface selection rules” allows only the vibration with dipole moment change normal to the metal surface to be IR active. The arrows indicate the direction of the transition moment.

Group theory tells us which vibrations have components in x, y and z directions, allowing us to predict which molecules will be active in RAS conditions.

Moreover, it is right to point out, as suggested by Francis and Ellison [43], that the selection of p-polarized light as a source offers the possibility to study ordered molecular structures and their orientation at reflective surfaces. The surface selection rule can indeed be exploited to infer molecular organization of a film at an interface.

4.2.2 Attenuated Total Reflection (ATR)

As just briefly introduced in Chapter 2, par. 2.2, it is known that when a propagating wave, be it an electromagnetic or an acoustic one, passes through the boundary between two materials having different indices of refraction, there will be a critical angle of incidence with respect to

the boundary normal above which total internal reflection occurs, that is, all the radiation is reflected back into the first medium [42]. The critical angle may be calculated according to the Snell law [42]:

$$n_1 \sin \theta_i = n_2 \sin \theta_r \quad (2.1)$$

$$\theta_c = \arcsin \left(\frac{n_2}{n_1} \right) \text{ when } \theta_r = 90^\circ \quad (2.2)$$

If the first medium is characterized by a higher refractive index n_1 (optically dense medium) than the second n_2 (optically rare medium), and it is placed in intimate contact with it, then the conditions for the phenomenon of attenuated total reflection are fulfilled, and part of the propagating wave enters the second, optically rare medium in the form of an evanescent wave [42] (Fig. 4). Such evanescent wave exhibits an exponential decay character as a function of the distance from the refractive boundary [47], with the exact penetration depth value depending on the radiation wavelength, on the precise angle of incidence and on the ratio between the indices of refraction of the two media [48, 49] – as explained in chapt.2, par 2.1, eq. 1.2 of this thesis.

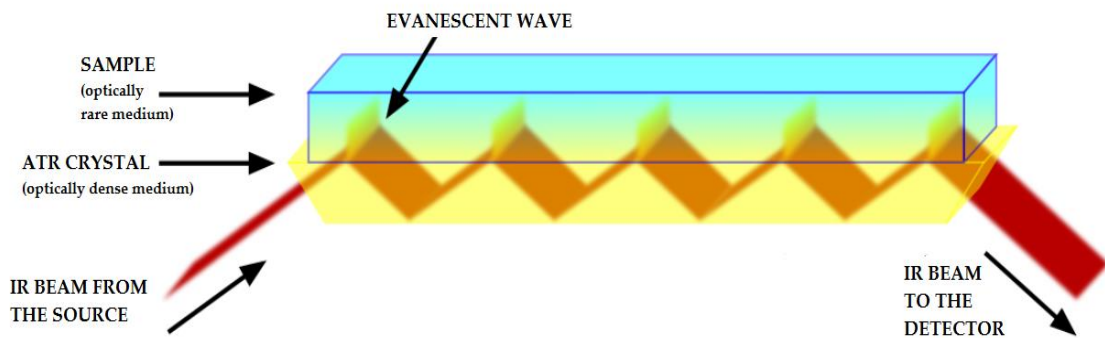


Fig. 20: ATR configuration

Provided that the passing wave is an IR beam, and that the optically rare medium is IR-active, the ATR phenomenon can be spectroscopically exploited in the IR region to study its chemical composition and structure, due to the fact that the evanescent wave can be absorbed by the material [50], and this absorption can be recorded in terms of the occurring attenuation of the total internally reflected radiation [51].

The experimental arrangement is such that the infrared radiation passes through an infrared transmitting crystal with a high refractive index that allows the radiation to reflect at least once off the internal surface in contact with the sample. More often, the beam reflects several times, and this precise number, together with the internal angle of incidence, is a function of the material chosen and of the geometry it has been cut. Especially the particular number of internal reflections is a very important parameter concerning the signal to noise ratio obtainable, since as this number increases, the spectral signal carried through the evanescent wave gets multiplied and consequently amplified [42]. It must be pointed out that such

amplification is not correlated to the abnormal increase of bands at lower wavenumbers which is always observed in unprocessed ATR spectra.

Moreover, the ATR conditions are achieved with the aid of an internal reflection element (IRE) placed between the IR source exit - in the case of IR microscopy, the microscope objective - and the sample, with which it is placed in tight contact [50]. The IRE is an IR-transparent, inorganic crystal of higher refractive index than the sample, the most common being made of ZnSe or Ge. [42]. Silicon, diamond and the so-called KRS-5 crystals (red thallium bromiodides) are also used, but their application is limited due to interfering impurities contained, to the high costs associated and to the toxicity of the material, respectively [50, 51].

4.2.3 Enhanced IR: Grazing Angle Attenuated Total Reflection (GAATR) and ATR-RAIRS

ATR technique has been often used for examining very thin films on substrates: in more detail, films, whose thickness is less than the employed wavelengths, are applied on a semiconductor or a metallic surface and analysed by ATR. In such conditions a sort of "tunneling effect" is observed and the total reflection conditions are accomplished considering a system composed by the IRE (n_1) and the support on which the thin layer is applied (n_3) [53] such as the film was not present.

Several papers have been published, for instance, on the use of silicon as support [52, 54-56]. Harrick and du Pre developed formulae for ATR analysis of very thin weakly absorbing films, presenting a thickness much less than the wavelength, deposited on a silicon substrate [57]. In these conditions the evanescent wave propagates parallel to the surface, hence cannot reflect from the film-silicon interface. This greatly enhances the electric field strength within the film and since the absorption is proportional to the square of the electric-field amplitude, an enhancement in the electric-field strength of ten times results in a hundredfold enhancement in absorption [52].

The technique has been named Grazing Angle Attenuated Total Reflection (GAATR) because high incident angles have to be used (i.e. for the system germanium-silicon $\theta_c > 59.6^\circ$) to accomplish the total reflection conditions. Indeed, using a lower angle (even if bigger than the θ_c for the system IRE-thin film) the evanescent wave would be refracted at the interface between the thin film and the support (for example, silicon) following the Snell law. Moreover, another spectroscopic technique that yields high sensitivity to small amount of sample is known as SuGARS (Super Grazing Angle Reflection Spectroscopy) [48]. The difference between this technique and GAATR has been recently described by Milosevic [48]. Both the two techniques use a germanium ATR element on a very thin sample. The difference is that SuGARS uses metallic substrate instead of silicon. Because of the metallic substrate this technique is not an ATR technique because the substrate has a much higher refractive index than germanium. Nevertheless, the metal substrate confines the transmitted wave to the film, which has for a consequence that the intensity of the wave in the film is highly enhanced.

SuGARS shows a slightly different dependence of the enhancement on film thickness than GAATR [48].

It has also been found by numerical analyses that the more is the refractive index n_3 related to the support for the thin film, the more is the enhancement of the signal [54]. Indeed, a peculiar enhancement effect occurs when GAATR is performed applying a thin film on a metallic support [54]. Moreover, it was interesting to note that the absorbance at a fixed wave and at a fixed incident angle – greater than the critical angle - increases with the film thickness since at a certain extent (i.e. 10 nm) and then tends to decrease [52]. Normally for very thin films, compared to the wavelength of light, the absorbance and film thickness are proportional. As the film thickness reaches the penetration depth, the linear relationship becomes saturated and further increases in film thickness bring no increase in the measured absorbance. When silicon is present the decrease of absorbance after a certain film thickness is certainly ascribable to a decrease of the electric-field strength of the evanescent wave, which dominates over the increase in the film thickness.

Initially researchers tried to explain this effect through the enhancement of the electric field generated by the superficial plasmonic resonance of metallic nanoislands in parallel to what happened in SERS (Surface Enhanced Raman Spectroscopy). The term Surface Enhanced InfraRed Absorption (SEIRA) has been coined referring to the analyses of thin layers either in ATR or in transmission employing metal over layers or under layers geometry obtained using metallic support, sputtering of the IRE or of the film or deposition of metallic nanoparticles [58]. This explanation was not accepted by Ishino and Ishida [59] which stated that the enhancement was not attributed to the metal island effect, but depended on the refractive index of the IRE.

Milosevic et al. underlined that a sensible enhancement is obtained when the film is applied on gold, even if due to the higher refractive index of the metal compared to the one of the IRE, it cannot be possible to obtain an internal total reflection [54]. Thus, the explanation of this phenomenon from a theoretical point of view is still difficult. Mulcahy et al. [60] explained intuitively the reasons of the increased sensitivity, which was related to the reflectivity of the metallic surface. Indeed for film whose thickness is less than the depth of penetration and using an incident angle bigger than the critical one for the system IRE-film, the evanescent wave is established in the metallic layer. However, the attempted transmission into the third medium is thwarted by its reflectivity, which allows total reflection to be restored. Such type of configuration was evaluated and compared with RAIRS on the same substance by Davies and Yarwood [61], demonstrating that by using the ATR-metal over layer configuration with a fixed incident angle (45°), an enhancement of the signal employing p polarized light was obtained.

Even if these hybrid configurations have been theoretically studied, they have not been extensively exploited from a more applicative point of view and no applications to the field of cultural heritage analysis has been so far reported. However this type of approach may be extremely interesting in this field in which the amount of samples may be extremely limited.

Since in commercial instrumentations available in conservation departments incident angle is commonly fixed, we tried to verify if with this type of set up it is possible to obtain an enhancement with respect to RAIRS for the detection of colorants extracted from dyed wool fibres. Considering the above mentioned literature we choose a germanium IRE ($n_1=4$) and a gold glass slide as support for the application of the sample. Standard solutions of different synthetic colorants were spotted on the support and ATR-RAIRS analyses were performed on the coffee rings formed after solvent evaporation. AFM analyses were also done to measure the film thickness.

4.2.4 Materials and methods

4.2.4.1 Materials

Synthetic colorants, standard dyed fibers and real samples (see table 1) were kindly provided by Dr Martaan van Bommel (Ministry of Education, Culture and Science Cultural Heritage Agency of the Netherlands) in the frame of the European project CHARISMA.

Solution at different concentration up to 10^{-6} M were prepared with demineralized water.

Real samples come from a sample book developed by Adolf Lehne published in 1893 which contains more than 300 wool samples dyed with dyes available in the second half of the 19th century.

4.2.4.2 Micro extraction procedures

Extractions were performed employing a mild method in order to avoid hydrolysis of the wool and thus the presence of spurious bands due to the presence of by-products in the FTIR spectra.

The colorant was extracted from few fibers (less than 0,1 mg) employing 3 aliquot of 10uL of methanol over a time of 30 min at 60°C. Every 10 minutes, approximately, the solvent dried and a new aliquot of methanol was added. The extract was reconstituted with 10uL of deionized water.

4.2.4.3 Substrate preparation

Different substrates for the coupling with the Ge IRE were tested and chosen among those showing the following physical properties: transparency to the mid-IR radiation and/or a high IR-reflectivity. Hence, Silicon wafer, AgCl (Thermo, smooth surface), BaF₂ (Thermo, smooth surface), and an Au-coated glass slide optimized for RAS measurements (Thermo, smooth surface, 200 nm coating thickness) were selected.

Measurements were taken on the supports as purchased. Au-coated slides were additionally cleaned through ultrasonic bath cycles with MilliQ water and ethanol (Sigma-Aldrich, ~96%) and dried under warm air flux.

4.2.4.4 ATR/RAIRS measurements

1 μL of standard colorant solutions at different concentrations and dye extracts were spotted on gold glass slides and let to dry. ATR-RAIRS and RAIRS analyses were performed on the coffee rings formed after evaporation using a Thermo Nicolet iNTM10MX Raster scanning microscope, fitted with an MCT detector cooled by liquid nitrogen. Spectra were recorded in the range 4000–675 cm^{-1} with an aperture 200 x 200 μm , spectral resolution 4 cm^{-1} and 128 number of scans and using a fixed incident angle at 45°. Data collection and post-run processing were carried out using the OMNIC PictaTM software (Thermo).

4.2.4.5 PCA evaluation

Multivariate data processing were performed by means of in-house Matlab routines (The Mathworks Inc., Natick, USA). Spectral data set were submitted to row and column pretreatments. In particular, the standard normal variate (SNV) transform and first Savitzky-Golay derivative was calculated using third order polynomials through 15 datapoint gaps, attempting to minimize systematic unwanted variations affecting the signals and enhance useful features. The spectral regions were then reduced to the range 1790-700 cm^{-1} .

4.1.4.6 AFM measurements

AFM analyses have been performed with a NT-MDT Ntegra, Smena head microscope. The investigated areas were 75 μm x 75 μm and in each area 256 points per scan were acquired.

4.2.5 Results and discussion

4.2.5.1 AO7 FTIR spectra references acquired both in transmission and RAS mode

A reference spectrum of AO7 as a powder sample has been acquired through conventional FT-IR spectroscopy in transmission mode (Fig. 5).

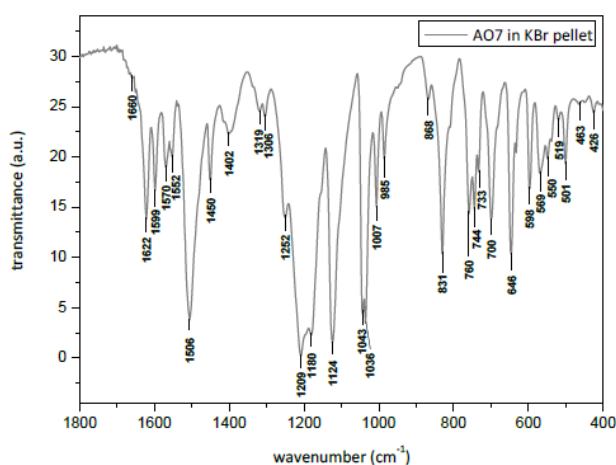


Fig. 21: Transmission infrared spectrum of the AO7 powder sample.

The spectral profile shows a clear preponderance of the hydrazone tautomer over the azo one, in that the band at 1506 cm^{-1} corresponding to the $\nu\text{C}=\text{N}$ of conjugated hydrazones is one of the most intense in the spectrum. The stated equilibrium can also be confirmed by the presence of the sharp band at 1620 cm^{-1} assigned to the ketonic $\text{C}=\text{O}$ stretching characterizing the hydrazone form, as well as the in-plane δ of the $\text{C}(\text{C}=\text{O})\text{C}$ moiety at 598 cm^{-1} . Other important bands for the elucidation of the structure are the one at 1209 cm^{-1} and the doublet at $1043\text{-}1036\text{ cm}^{-1}$ due to the asymmetric and symmetric stretching modes of the SO_3^{2-} group on the benzene ring, respectively. Most of the remaining bands are due to the stretching and deformation modes of the aromatic moieties, and a full assignment can be found in Table 2.

Moreover, also RAIRS spectrum of a $1\text{ }\mu\text{L}$ dried drop of a 10^{-4} M solution of AO7 have been acquired. As can be seen in Figure 6, the quality of the signal is very poor, and most bands result scarcely discernible from the background noise. In addition, the overall intensity is very low, so that a lower concentration, such that of a possible micro-extract, could very likely result unquantifiable with this approach.

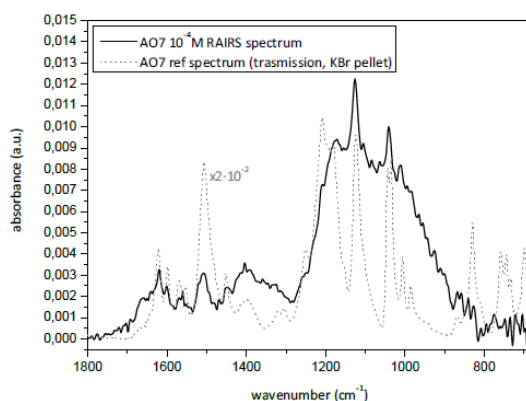


Fig.6: RAIRS spectrum of a $1\text{ }\mu\text{L}$ dried drop of a 10^{-4} M solution of AO7. The reference transmission spectrum is shown in dashed line. Its intensity has been reduced of a $2\cdot 10^{-2}$ factor to be fitted in the RAIRS spectrum scale.

Indeed, the monolayer sensitivity reported for RAIRS can only be achieved at grazing angles, while the present work has been optimized using a 45° geometry, which is the most frequently encountered configuration in standard $\mu\text{FT-IR}$ equipments.

4.2.5.2 AFM analyses

In order to evaluate the enhancement mechanism of the proposed analytical configuration, Atomic Force Microscopy (AFM) analyses were performed to estimate the thickness of the coffee rings of AO7 solutions at different concentrations. A high variability of thickness was observed in different points of the coffee rings. Indeed, the coffee ring formation is a well-known phenomenon which depends on the solvent superficial tension and on the variation of microclimatic conditions [62] during the evaporation.

In figure 7 the 3D atomic force microscopy image of one point analysed in the coffee ring obtained after spotting the 10^{-5} M solution is reported showing a thickness rate moving from

the internal to the external part. Decreasing the concentration of the spotted solution also this thickness rate is reduced.

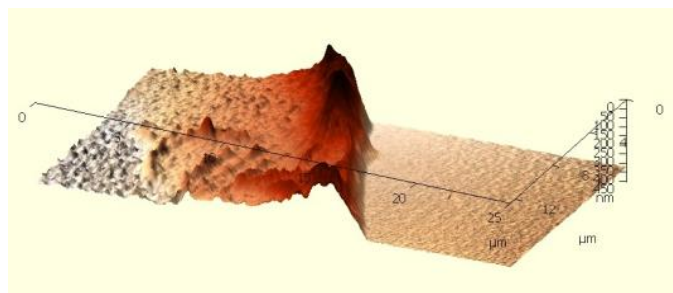


Fig. 7: Thickness rate in the coffee rings obtained after spotting 1 μL AO7 10⁻⁵M solution on a gold glass slide

The first set of measurements were performed on a single drop obtained after spotting a 1 μL 10⁻⁴ M AO7 solution in four different areas position. In each position at least 7 measurements were undertaken.

In Table 1 the minimum and maximum thickness observed for the different AO7 solution are reported. Analyses performed in other two drops confirmed a similar behavior.

Increasing the dilution of the spotted solution the thickness of the coffee ring decreased and was more variable from a drop to the other. It can be noted that for high wavenumber the penetration depth is of the same order of magnitude of the thicker AO7 10⁻⁵M points and is lower than the AO7 10⁻⁴ M points.

However, it is worth to underling that using a germanium (Ge) IRE with an incident angle of 45° the penetration depth was superior than the film thickness even for the 10⁻⁴ M drops for most of the mid IR range. Indeed, penetration depth calculated applying the formula reported in the Chapter 2, par. 2.1 [62] in the range 3000-650 cm^{-1} increases from 0,2 μm to 0,9 μm .

Table 4: Coffee ring thickness

| Drop | Minimum thickness (nm) | Maximum thickness (nm) |
|------------------------|-------------------------------|-------------------------------|
| AO7 10 ⁻³ M | 500 | 1800 |
| AO7 10 ⁻⁴ M | 250 | 600 |
| AO7 10 ⁻⁵ M | 120 | 300 |
| AO7 10 ⁻⁶ M | 50 | 160 |

4.2.5.3 ATR-RAIRS analyses of AO7

Analyses of standard AO7 solutions from 10^{-4} M to 10^{-6} M were performed in ATR-RAIRS. Spectra obtained on the coffee rings spotting the 10^{-4} M solution appeared similar to those obtained in transmission mode, unless some shifts which can be observed in the right part of the spectra and which can be ascribable to typical ATR deformation; a full assignment can be found in Table2.

Table 5: Bands assignment attempt for Acid Orange 7 FTIR spectra [56-59, 61, 62]

| Band frequency_%T (cm ⁻¹) | Band frequency_RAS (cm ⁻¹) | Assignment attempts |
|---------------------------------------|--|---|
| 3453 (m, broad) | 3453 (m, broad) | v OH |
| 3054 (m) | 3063 (m) | v (CH) aromatic |
| 1665 (sh) | 1665 (sh) | v (C = O) |
| 1621 (s) | 1619 (s) | v (C = O), δ(NH), δ(naph) |
| 1598 (m) | 1600 (m) | v (Ph) 8a, δ(Ph) 9a, δ(NH) |
| 1568 (m) | 1567 (m) | v (Ph) 8b, δ(Ph) 3, δ(NH), v (NN), δ(naph) |
| 1551 (m) | 1551 (m /w) | δ(naph), δ(naph) |
| 1507 (vs) | 1516 (s) | δ(NH), δ(naph), v(CN) |
| 1483 (sh) | 1484 (sh) | δ(naph), v (NN) |
| 1451 (m) | 1453 (m) | δ(naph) |
| 1416 (sh) | – | v (Ph) 19b, δ(Ph) 18b, v(CN), δ(NH), δ(naph) |
| 1391(w) | 1393 (m) | v (Ph) 19b, δ(Ph) 18b, δ(NH), v(CN), |
| 1398 (m) | 1402 (m) | v (Ph) 19b, δ(Ph) 18b, δ(NH), v(CN) |
| 1338 (sh) | 1338 (sh) | δ(naph), δ(Ph), v (NN) |
| 1303 (m/w) | 1303 (m/w) | v (Ph) 8b, δ(Ph) 3, δ(naph) |
| 1249 (m) | 1254 (m) | v (NN), δ(NH), δ(naph), δ(Ph) 9a |
| 1181 | 1178 | v _{as} (SO ₃ ⁻) |

| | | |
|-----------|-----------|---|
| 1124 | 1122 | ν_s (SO ₃ ⁻), δ (Ph)1 |
| 1038 (vs) | 1035 (vs) | ν_s (SO ₃ ⁻), δ (Ph)1 |
| 1006 (s) | 1010 (s) | δ (Ph) 18a |
| 986 (m) | 986 (s) | |

In figure 8 spectra of 10⁻⁴ M drops analysed in ATR-RAIRS and RAIRS with an aperture 200 x 200 μ m are reported. It is worthy to note that in the two set up the same aperture was maintained even if in ATR-RAIRS the investigated area is only 50 μ m x 50 μ m as it is equal to the ratio between the aperture and the refractive index of the IRE. A good enhancement of the signal was observed in the region in which the colorant absorbed unless at higher wave numbers. Indeed bands related to the CH stretching are not enhanced with respect to what observed in RAIRS because at that

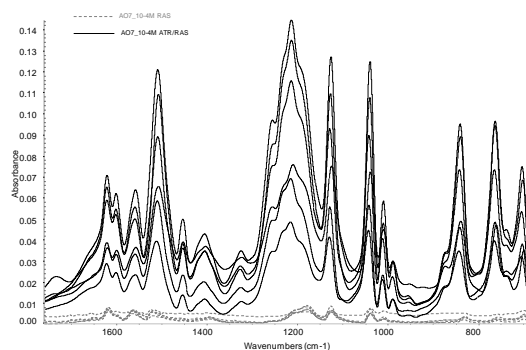


Fig. 8: ATR-RAIRS and RAIRS spectra of AO7 10⁻⁴ M

wavenumbers the penetration depth is in media lower than the film thickness and the evanescent wave cannot be influenced by the metal layer. RAIRS spectra acquired on 10⁻⁵ and 10⁻⁶ M drops were too noisy under the limit of detection.

Comparing ATR-RAIRS signals at different concentrations it can be observed that the signal decreased with the decrease of the concentration of the spotted solution (fig. 9). Indeed the thickness of the coffee ring tends to decrease such as the optical path. Spectra obtained on 10⁻⁶ M spotted solution were weak and noisy even if the colorants characteristic bands can still be recognized. Thus as normally observed for very thin films compared to the wavelength of light, the absorbance and film thickness are proportional. As the film thickness reaches the penetration depth, the linear relationship becomes saturated and further increases in film thickness bring no increase in the measured absorbance. This behavior suggested that the mechanisms responsible of the signal enhancement when thin films are spotted on metallic surfaces is different from what observed GAATR and on SuGARS. Indeed when silicon is present the absorbance reaches a maximum for very thin thickness and then decreases. This behavior is certainly ascribable to a decrease of the electric-field strength of the evanescent wave, which dominates over the increase in the film thickness [14]. In our experiments, the enhancement is observed when thin film thicker than monolayers, but thinner than the penetration depth are applied on a metallic surface and analyzed in ATR.

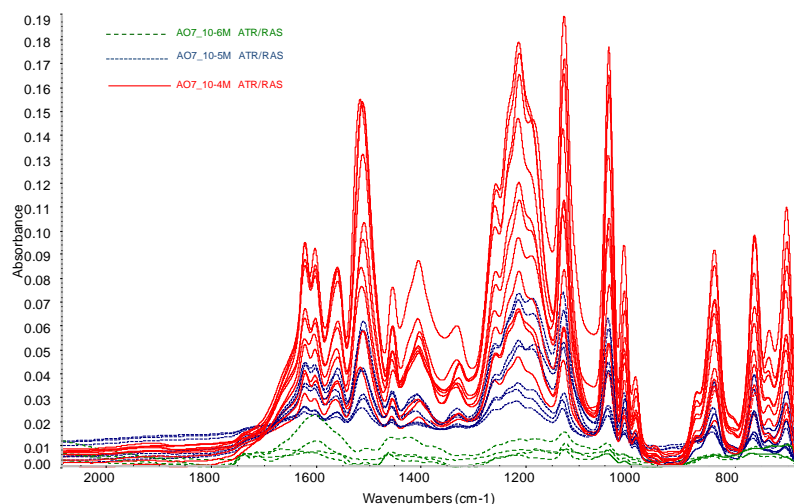


Fig. 9: ATR/RAIRS spectra of AO7 10^{-4} M (red profile), 10^{-5} M (blue profile) and 10^{-6} M (green profile), full scale.

Spectra of variable intensities were registered in the different analyzed points which may depend on the variability of the film thickness and on the contact between the IRE and the film.

When a 10^{-3} M solution was spotted the ATR-RAIRS spectra were less variable (fig. 10a) with an higher intensity with respect to 10^{-4} M drops even if the averaged gain obtained in particular for absorption in the between $1700 - 1000 \text{ cm}^{-1}$ is less compared to what observed in figure 8. On the other end a significant difference occurs when the 10^{-3} M and the 10^{-4} M drops are analysed in RAIRS modes (fig. 10b). Thus probably the film thickness of the 10^{-3} M drops coffee rings begins to be higher than the penetration depth for a wider range of wavelength and in ATR-RAIRS mode the evanescent wave is less influenced by the metal. In RAIRS mode the thickness of the film is still enough small to allow the wavelengths to be reflected back from the metal underlayer leading to a bigger optical path with respect to the thinner drops.

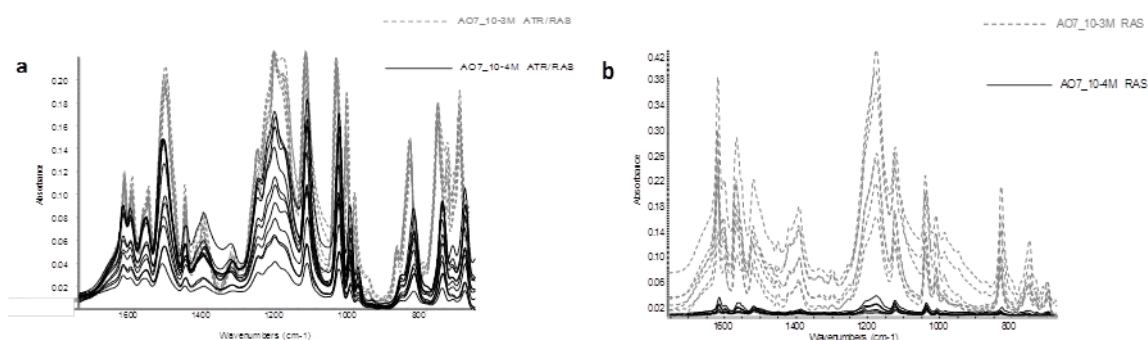


Fig. 10: AO7 solution spectra acquired with a) ATR/RAIRS spectra of 10^{-3} M (dashed line) and 10^{-4} M (black line); b) RAIRS spectra of 10^{-3} M (dashed line) and 10^{-4} M (black line); full scale.

Thus for film thickness higher than the penetration depth it is not possible to obtain an enhancement of the signal with the ATR-RAIRS configuration and if the film is thin enough the RAIRS mode provide higher signals. This may support the hypothesis of Mulcahy et al. [60] which explained the enhancement mechanism of ATR-RAIRS analyses performed on thin films applied on a metallic support with a combination of the ATR and RAIRS mechanisms: with an

incident angle bigger than the one for the system IRE-film internal total reflection occurs. The signal is further enhanced when the penetration depth is bigger than the film thickness because the attempted transmission into the third medium is thwarted by the metal reflectivity which allows total reflection to be restored [60].

To evaluate the performance of the system from an analytical point of view other types of supports were tested (fig. 11). The same aliquot of AO7 10^{-4} M solution was spotted on a silicon wafer and on IR transparent windows made of AgCl and BaF₂.

Spectra acquired on silicon appeared distorted (fig. 11a). Indeed the incident angle used is above the critical angle of the system IRE-silicon and the conditions for obtaining a total internal reflection are not fulfilled. In particular with a germanium IRE and an incident angle of 45° the refractive index of the support must be less or equal to 2.8. The other two materials respected this restriction (the refractive indexes for AgCl and BaF₂ are about 2 and 1,46 respectively). It is interesting to note that spectra on AgCl are more intense than the ones registered on BaF₂ (fig. 11b). Indeed it is known from numerical simulations and theoretical studies that an increase in the refractive index of the support lead to an increase of the signal unless the conditions of total internal reflection are maintained [52, 54].

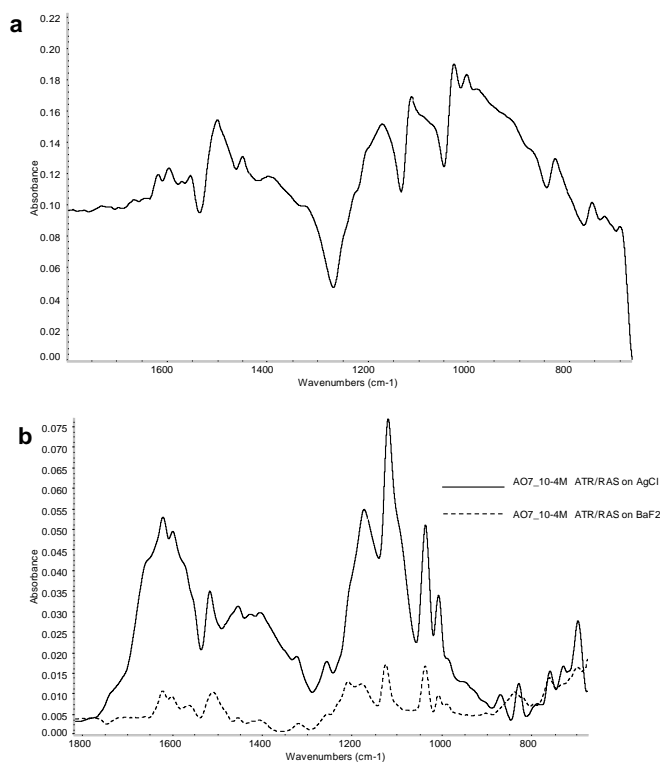


Fig. 22: ATR7RAIRS spectra of AO7 10^{-4} M solution acquired on a) silicon wafer; b) BaF₂ (dashed line) and AgCl (black line); full scale.

However, the enhancement was not comparable from what observed for the gold glass slides, and for this the ATR/RAIRS set up has been selected for developing an analytical approach for the analyses of diluted colorant solutions.

4.2.5.4 ATR-RAIRS for the analyses of colorants

Solution 10^{-4} M of different synthetic colorants were analysed in ATR-RAIRS with the previously described method. Several drops have been spotted on gold glass slides and on each of them several spectra have been recorded. The huge amount of data was treated using PCA in order to verify if the proposed method was able to distinguish the class to which the single colorants belong. A preliminary investigation on the pure colorants analysed in transmission on KBr pellets confirmed that FTIR spectroscopy can hardly distinguish the different colorants belonging to the same class but that it is a suitable technique for identifying the class to which the colorant belongs.

ATR-RAIRS analyses on the spotted 10^{-4} M solutions allowed to maintain the separation of the different colorant classes observed on pure colorants as reported in figure 12.

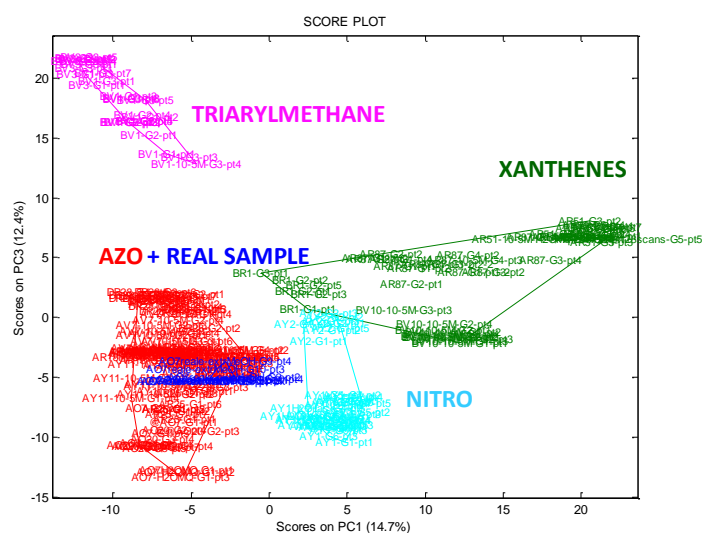


Fig. 23: PCA score plot of ATR-RAIRS of several standard dyes diluted at 10^{-4} M solutions and of a real sample micro extracted from AO7 wool fibres.

Thus the method appeared suitable for the analyses of dyed extracted from fibers.

4.2.5.5 ATR-RAIRS for the analyses of dyes extracted from fibers and validation of the method on real samples

ATR-RAIRS analyses were tested on micro-extracts obtained from few not weighable fibers dyed with standard colorants. Several mild micro extraction procedures were tested. In particular, extraction methods based on the use of (i) formic acid, (ii) Ethylenediaminetetraacetic acid (EDTA) and (iii) methanol were compared. Even if the extraction appeared effective to the naked eye the main concerns in the use of mild acids or complexing agent is the remaining of such IR active compounds in the micro extracts.

Based on these results, methanol extraction method was selected in order to avoid spurious signals in the FTIR spectra. The extraction procedure was applied on a wide selection of fibers dyed with standard colorants belonging to different classes, obtaining promising results. PCA

analyses performed on the extracted dyes allowed to maintain a good separation between the different classes (fig. 13).

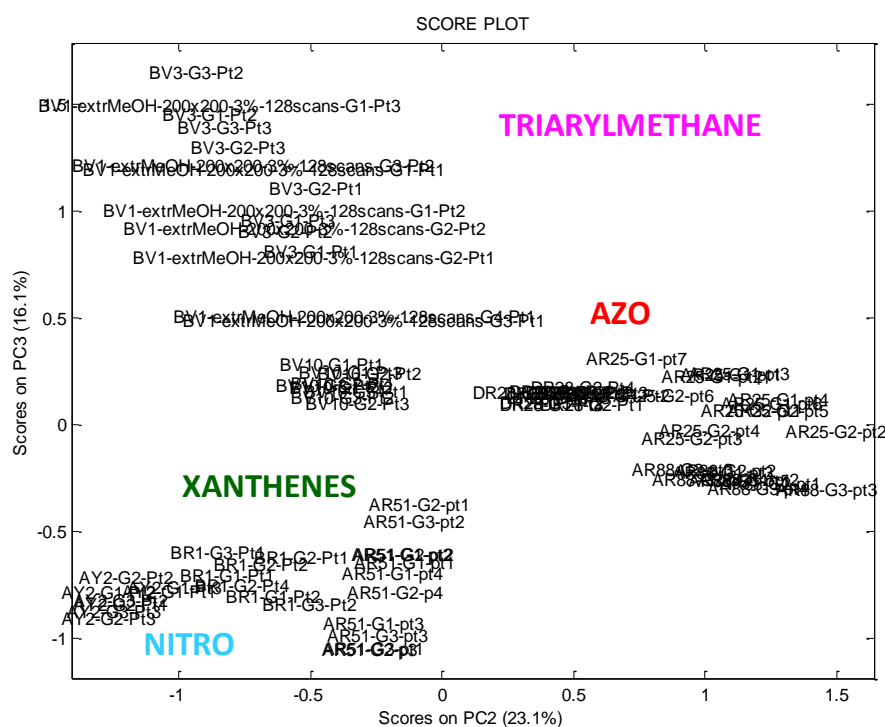


Fig. 13: PCA score plot of ATR-RAIRS spectra of several dyes micro-extracted from standard dyed wool fibres.

Moreover, a comparison between spectrum of AO7 extracted from dyed fibers and the spectrum acquired on the 10^{-4} M standard solution is reported (fig. 14a). It can be noted that the extraction seemed effective and the spectrum is clearly correlated to the one registered on the standard solution. It is worthy to note that when reducing the concentration of the solution to be analysed the occurrence of IR active contaminants, especially arising from the extraction of the fibers, may hinder the identification of the extracted colorant.

The method was tested on a known real sample dated back to 1893 and belonging to the sample book developed by Adolf Lehne. The orange fibers were dyed with AO7 which was identified by HPLC analysis in the frame of the FP7 funded European project CHARISMA. The ATR/RAIRS spectra performed on the micro extract allowed the clear identification of diagnostic bands related to the AO7 (fig. 14b). Furthermore, in attempt to clearly validate the results, a multivariate comparison was performed. In particular, PCA was applied on standard colorants belonging to all the different classes, including spectra of the extracted real ample. As expected, the obtained score scatter plot revealed the identification of the extracted orange colorant as an azo dye (fig. 12).

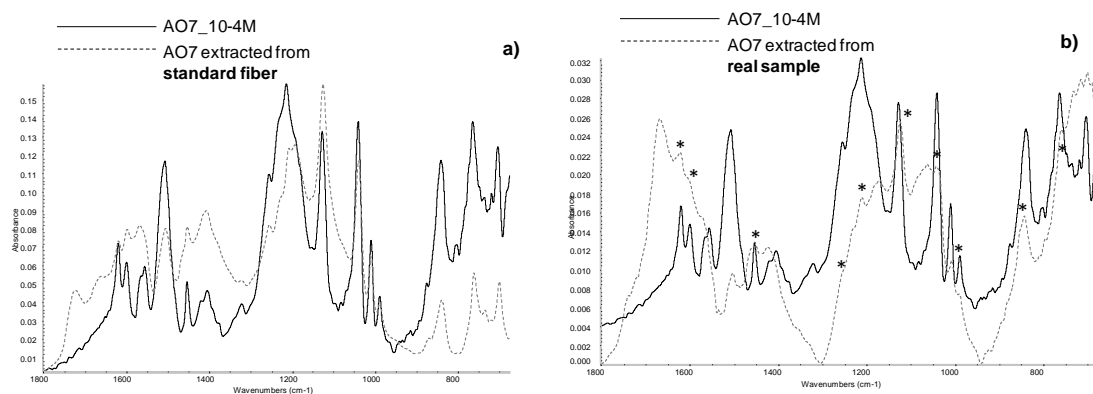


Fig. 24: comparison between ATR/RAIRS spectra of AO7 standard 10-4M solution (black line) and a) AO7 extracted from standard fibre (dashed line) or b) AO7 extracted from real sample.

4.2.6 Conclusions

A significant enhancement has been obtained by this analytical technique, the methodology has been especially implemented for standard μ FT-IR equipments, which are characterized by a 45° geometry that does not yield the high sensitivity level achievable when working at grazing angles. A preliminary optimization phase resulted fundamental, since it allowed the definition of the coupled ATR-RAIRS analytical mode that has been successively employed to characterize the dye both as a standard solution and as a micro-extract from the fiber.

As demonstrated, this technique works on solution, this means a necessary sample pretreatment for dyed fibres. Using the micro extraction method, the limitations inherent to IR spectroscopy which do not allow the obtainment of clear vibrational spectra from minor analytes in a protein matrix such as wool, has been overcome.

A good reproducibility of the proposed analytical approach have been revealed for the analysis on AO7; and a the good consistency with conventional IR reference data when concentrations in the range of 10^{-4} - 10^{-5} M was observable. Moreover, several other solution of synthetic organic standard dyes belonging to xanthene, triarylmenthane, nitro and azo classes have been successfully analysed. The spectra achieved from the analysis of these standard dyes solution have been processed with PCA. The multivariate analysis demonstrate that all these dyes categories can be correctly discriminate. The positive results obtained on standard solution, have been encouraged to further explore this method on micro-extraction of standard and real fibres samples, and, also for micro-extraction on standard fibres, a worthy degree of discrimination identified with PCA have been achieved.

The overall information may support the hypothesis that the enhancement mechanism is due to a combination of ATR and RAIRS: with an incident angle bigger than the critical angle for the system IRE-film internal total reflection occurs. The signal is further enhanced when the penetration depth is bigger than the film thickness because the attempted transmission into

the third medium is thwarted by the metal reflectivity which allows total reflection to be restored.

In conclusion, also the ATR-RAIRS method can be used as an analytical method to analyze small quantities of colorants. The method has been set up without using any type of metal nanoparticles colloid and the enhancement is achieved only coupling two techniques: ATR and RAIRS.

ATR-RAIRS analysis totally avoid the use of metal NPs, to produce a good enhancement. It is here demonstrated that these are powerful sensitive techniques for the identification of small amount of colorants and they may find several applications for the study of artistic samples as well as those coming from the forensic and the environmental fields.

4.3 Conclusions

Both the innovative IR approaches here presented allowed to analyse small quantities of synthetic organic dyes due to the enhancement in the acquired spectra.

Even though SEIRA method has been demonstrated to be useful in the identification of small quantities of synthetic organic dyes of standards solutions and also, micro extracted from standard fibres, the necessary use of metal colloids and the spectra resolution to be improved make this analytical approach difficult and costly due to the employment of naked AuNPs created by means of laser ablation. Indeed, only these NPs allowed strong enhancements of the signals, without the presence of spurious by-products which may affect the results. On the other hand, applying the method performed using AgColl, worse results have been achieved due to the lower enhancement and mainly due to the presence of spurious bands generated by the Ag colloid.

For these reasons another approach have been experimented, with the aim of reach the enhancement without the use of metal colloids. Experimental data allowed to identify a new enhanced vibrational technique which we have named ATR-RAIRS: this technique is performed with commercial instrumentations available in conservation departments, coupling ATR and RAIRS methods with a fixed incident angle (characterized by a 45° geometry).

The enhancement is observed when thin film thicker than monolayers, but thinner than the penetration depth are applied on a metallic surface and analyzed in ATR. Indeed, drops of solutions of standard dyes or micro-extraction from standard or real fibres have been successfully analysed. These results allowed to assume that the enhancement mechanism is due to a combination of ATR and RAIRS: with an incident angle bigger than the critical angle for the system IRE-film internal total reflection occurs. The signal is further enhanced when the penetration depth is bigger than the film thickness because the attempted transmission into the third medium is thwarted by the metal reflectivity which allows total reflection to be restored.

In conclusion although it has been here demonstrate that good results arise from both the techniques, ATR-RAIRS analysis seems to be easier to perform - without the use of metal colloids - and with better enhancement and spectral resolution compared to SEIRA. Moreover, these analytical approaches can be conducted with a standard μ FT-IR equipments without any specific slide and also without the necessity of samples preparation or with an easy and quick extraction procedure.

4.3 References

- [1] R.F. Aroca, *Surface-enhanced vibrational spectroscopy*, John Wiley & sons, Chichester, 2006
- [2] A. Hartstein , J.R. Kirtley , J.C. Tsang, . *Phys Rev Lett* 1980, 15,201–204.
- [3] M. Fleischmann, P.J. Hendra, A.J. McQuillan, *Chem Phys Lett* 1974, **26**,163–166.
- [4] D.L. Jeanmaire, R.P. Van Duyne, *J Electroanal Chem* 1977, **84**,1–20.
- [5] M. Osawa, N. Matsuda, K. Yoshii, I. Uchida, *Phys Chem* 1994, 98,12702–12707.
- [6] M. Osawa, M. Ikeda, J. *Phys Chem*, 1991, 95, 24, 9914-9919
- [7] M. Osawa, *Topics Appl Phys* 2001, **81**,163–187
- [8] A. E. Bjerke, P.R. Griffiths, W. Theiss, *Anal. Chem.*, 1991, 71, 1967-1974
- [9] R. Aroca, B. Price, *J. Phys Chem.* 1997, 101, 6537-6540
- [10] F. Hahn, C.A. Melendres, *Electrochimica Acta* 2001, 46, 3525-3534
- [11] J.A. Seelenbinder, C. W. Brown, P. Pivarnik, A. G. Rand, *Anal. Chem.* 1999, 71, 1963-1966
- [12] A. Miki, S. Ye, M. Osawa, *Chem Commun*, 2002, 1500-1501
- [13] D.A. Heaps. P.R. Griffiths, *Vibr. Spectr.*, 2006, 42, 1, 18, 45-50
- [14] F. Aroca, J. Ross, C. Domingo, *Appl. Spectr.* 2004, 58, 11, 324A-338A
- [15] J. F. Masson, M. P. Murray-Méthot, L.S. Live, *Analyst*, 2010, 135, 1483-1489
- [16] Y. Saito, J.J. Wang, D.A. Smith, D.N. Batchelder, *Langmuir*, 2002, 18, 8, 2959-2961
- [17] G.D. Sockalingum, A. Beljebbar, H. Morjani, J.F. Angiboust, M. Manfait, *Biospectroscopy*, 1998, 4, S71–S78
- [18] H.D. Wanzenböck, B. Mizaikoff, N. Weissenbacher, R. Kellner, *Fresenius' Journal of Analytical Chemistry*, 1998, 362, 1, 15-20
- [19] A.M. Polubotko , *Phys Lett A* 1993, 173:424–432.
- [20] S. Badilescu , P.V. Ashrit , V.V. Truong , L. Badilescu , *Appl Spectr* 1989, 43,549–551.
- [21] J.A. Creighton , C.G. Blatchford , M.G. Albrecht , *J Chem Soc Faraday Trans* 1979, 2,790–798.
- [22] M. Kerke, O. Siiman, L.A. Bumm , D.S. Wang, *Appl Optics* 1980, 19,3253–3255.

- [23] P.C. Lee , D. Meisel , *J Phys Chem* 1982, 86,3391–3395.
- [24] N. Leopold , B. Lendl , *J Phys Chem B* 2003, 107,5723–5727.
- [25] M.V. Canamares , J.V. Garcia-Ramos , J.D. Gomez–Varga , C. Domingo , S. Sanchez-Cortes , *Langmuir* 2005, 21,8546–8553.
- [26] A. Fojtik , A. Henglein , *Ber Bunsen Ges Phys Chem* 1993, 97,252–254.
- [27] V. Amendola , M. Meneghetti , *Phys Chem Chem Phys* 2013, 15,3027–3046.
- [28] L.H. Wang , X.E. Jiang , *Chin J Anal Chem* 2012, **40**,975–982.
- [29] E. Sudo , Y. Esaki , M. Sugiura , *Bunseki Kagaku* 2001, 50,703–707.
- [30] K. Ataka , J. Heberle , *Anal Bioanal Chem* 2007, 388,47–54.
- [31] A.G. Rand , J. Ye , C.W. Brown, S.V. Letcher, *Food Technol* 2002, 56,32–39.
- [32] M. Osawa : *Surface-Enhanced Infrared Absorption Spectroscopy*. In *Handbook of Vibrational Spectroscopy*. Edited by Chalmers JM, Griffiths PR. New York: John Wiley and Sons; 2002,785.
- [33] T. Imae : *Molecular Organization in Monolayers – Surface Spectroscopy and Sensing*. In *Encyclopedia of Surface and Colloid Science*. Edited by Hubbard AT. New York: M. Dekker; 2002,3547.
- [34] A. Ulman : *Ultrathin Organic Films*. Boston: Academic Press; 1991.
- [35] R. Nakamura , K. Ueda , S. Sato , *Langmuir* 2001, 17,2003–2298.
- [36] V. Amendola , M. Meneghetti , *J Mater Chem* 2007, 17, 4705–4710
- [37] V. Amendola , M. Meneghetti , *J Phys Chem C* 2009, 113,4277–4285.
- [38] . Brosseau CL, Gambardella A, Casadio F, Grzywacs CM, Wouters J, Van Duyne RP, *Anal Chem* 2009, 81,3056–3062.
- [39] S. Prati, M. Quaranta, G. Sciutto, I. Bonacini, L. Litti, M. Meneghetti, R. Mazzeo, *Heritage Science* 2014, 2,28
- [40] G. Sciutto , L. Litti C. Lofrumento S. Prati, M. Ricci , M. Gobbo, A. Roda, E. Castellucci , M. Meneghetti, R. Mazzeo , *Analyst* 2013, 138,4532–4541.
- [41] M. Meneghetti, A. Scarsi, L. Litti , G. Marcolongo , V. Amendola , M. Gobbo , M. Di Chio , A. Boscaini , G. Fracasso , M. Colombatti , *Small* 2012, 8,3733–3738.
- [42] P.R. Griffiths, J.A. de Haseth, *Fourier transform infrared spectrometry*, John Wiley & sons, Hoboken, New Jersey (2007)

- [43] S. A. Francis, A. H. Ellison, *J. of the Optical Soc. of America*, vol. 49 number 2 (1958)
- [44] B. Liedberg, B. Ivarsson, I. Lundstrom, W. R. Salaneck, *Progress in Colloid and Polymer Science*, Vol. 70 (1985) 67-75
- [45] R. G. Greenler, *The Journal of Chemical Physics* 44, 310 (1966)
- [46] B.L. Frey, R.M. Corn, S.C. Weibel, *Polarization-modulation approaches to reflection-absorption spectroscopy*, in J.M. Chalmers, P.R. Griffiths (eds), *Handbook of vibrational spectroscopy*, vol. 2, Wiley, 2002
- [47] N.J. Harrick, *Journal of the Optical Society of America*, 55(7), 1965
- [48] M. Milosevic, *Internal Reflection and ATR Spectroscopy*, John Wiley & sons, Hoboken, New Jersey, 2012
- [49] F.M. Mirabella, Principles, *Theory and practice of internal reflection spectroscopy*, in J.M. Chalmers, P.R. Griffiths (eds), *Handbook of vibrational spectroscopy*, vol. 2, Wiley, 2002
- [50 10] M. Derrick, D. Stulik, J.M. Landry, *Infrared spectroscopy in conservation science*, The Getty Conservation Institute, Los Angeles, 1999
- [51 11] J. Fitzpatrick, J.A. Re_ner, *Macro and micro internal reflection accessories*, in J.M. Chalmers, P.R. Grffiths (eds), *Handbook of vibrational spectroscopy*, vol. 2, Wiley, 2002
- [52] M. Milosevic, S. L. Berets, A. Y. Fadeev, *Soc. for Applied Spectr.* 2003,57, 6
- [53] J.E. Olsen, F. Shimura, *Appl. Phys. Letters* 1988, 53, 1934
- [54] M. Milosevic, V. Milosevic, S.L. Berets, *Appl. Spectrosc.* **61**, 530 (2007)
- [55] J.E. Olsen, F. Shimura, *Appl. Phys. Letters* **53**, 1934 (1988)
- [56] S. Ekgasit, J. Vongsvivut, P. Thongnopkun, *Anal. Sciences* **23**, 847 (2007)
- [57] N.J. Harrick, F.K. duPre, *Appl. Opt.*, 5, 1739 (1966)
- [58] A.Hartstein, J.R. Kirtley, J.C. Tsang, *Phys. Rev. Lett.* **3**, 201 (1980)
- [59] Y. Ishino, H. Ishida, *Appl. Spectrosc.* **42**, 1296 (1988)
- [60] M.E. Mulcahy, S.L. Berets, M. Milosevic, J. Michl, *J. Phys. Chem. B* **108**, 1519 (2004)
- [61] G.H. Davies, J. Yarwood, *Langmuir* **5**, 229 (1989)
- [62] B.M Weon, J.H. Je, *Phys. Rev. E* **82**, 015305-1 (2010)
- [63] N.J. Harrick, N.H. Riederman, *Spectr. Acta* 21, 2135 (1965)

Chapter 5

**New development of TLC-SERS and
TLC-FTIR methods.**

3.1 Thin-Layer Chromatography (TLC) and coupled TLC-SERS and TLC-FTIR methods

The term TLC stands for Thin Layer Chromatography, a kind of separation technique based on the different polarity of the analytes and the substrate. Usually the substrate, or stationary phase (SP), is constituted by a layer of adsorbent inorganic compound applied on a solid support (glass, plastic, aluminium), while the unknown mixture to be solved is deposited as drops on the substrate. The separation of the mix in single analytes is performed using a solvent of chosen polarity grade (mobile phase MP) which flows up by capillarity through the stationary phase. On the basis of the polarity of the SP and of the mobile one, some analytes will remain more attached to the substrate, while others will follow with their own speed the uprising of the solvent.

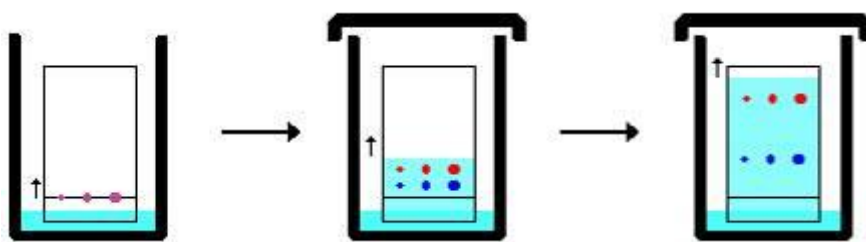


Fig. 25: Schematic representation of TLC technique

The first experiments in liquid chromatography were performed by using highly polar SP and a relatively non polar solvent as hexane or isopropyl ether [1]. For historical reasons this kind of chromatography is today defined as normal phase chromatography. Of course, in this case, the less polar analyte is eluted firstly while the most polar will remain anchored at the baseline of the SP.

The other kind of TLC, defined as reversed phase, deals with a stationary non polar phase and a polar MP. Here, the elution order is exactly the opposite as the one in the normal phase, but in both cases to perform a optimal separation is important to balance the intermolecular forces between analytes, SP and MP.

In TLC is not only important the partition equilibrium, but also the adsorption one. The SP is a solid finely dispersed so analytes compete with the MP for the sites available on the solid surface. This produces retention of the analytes that tend to be more adsorbed on the SP (equilibrium).

Silica and alumina are widely used for their adsorbent properties as SP. For both of them retention times increase with the increasing polarity of analytes.

Sometimes, the separated analytes are colourless and to visualize them can be exploited their fluorescent property (or the one of the SP) or particular colour reagents can be sprayed on the plate.

The TLC technique is very fast and cheap; therefore is widely used especially in the industrial, pharmaceutical, biochemical and biological fields [1]. The technique can be used to monitor a reaction, determine the grade of purity, identify a specific analyte in a mixture, determine the appropriate conditions for a column chromatographic separation, etc.

As concern the stationary phases, the most important adsorbent for TLC separation was and still is silica gel, followed by alumina, other mineral oxides, cellulose, ion-exchanger, polyamide and other new developed phases [1,2].

In most of the cases the SP is applied on the solid support as an aqueous dispersion of inorganic particles and a inert organic or inorganic binder, as gypsum or a polymer, to increase the cohesion between particles themselves and between particles and the solid support [2]. The TLC plate is then warmed until dried.

Nowadays many TLC plates are commercially available with standard particle size and purity. Usually the substrate is constituted by 12 μm particles, while for high-performance thin-layer chromatography (HPTLC) the stationary phase is composed by 5 μm particles with a narrow particle size distribution [2].

To whom it concerns the analysis of organic colorants, it is well known that dyes are used for many different applications in which purity may be important, or the presence/absence of certain impurities/intermediates, or uniformity, etc. In all these instances TLC has proved to be the ideal solution with the separation power and spot/zone capacity necessary to solve dyes with similar chemical structures and intermediates [3]. Thus, thin-layer chromatography (TLC) is an efficient, inexpensive and effective approach to separate different components from a given mixtures [4]. Concerning the detection and characterization of dyes from mixtures, already some examples are available in literature; some of them involve TLC separation coupled with FTIR analysis [4, 5], while more common are the publications about TLC-SERS coupling, with applications in various field [6,11].

Concerning the development of TLC-FTIR techniques, great efforts have been made in the last 50 years [4]. In the 60's, TLC-FTIR analysis was carried out via solvent elution transfer approach: analytes were separated on the TLC plate, each spot was then dissolved and transferred to an IR-transparent pellet or powder for the identification by spectral analysis [12, 13]. This was a time-consuming procedure which also could encounter sample loss, contamination and other problems. As changes in the chemical environment were made to bring about analytes isolation, the unknown material often decomposed, changed physical form, or underwent further reactions [4]. Consequently, the spectral results arising from these isolates tended to be misleading. A more desirable approach would have been to obtain infrared spectra in situ from TLC unknown spots and then to use this information in the subsequent characterization of the material. It was in this direction that C.J. Percival and P.R.

Griffiths moved, and in 1975 they developed an in situ TLC-FTIR technique, preparing a TLC plate with an infrared transmitting material as stationary phase (AgCl) [14]. They separated and analysed amino acids, but also some dyes: methylen blue and Stahl's test dye solution which was a 0.1% solution of butter yellow, Sudan red G and indophenol blue.

Subsequently, M. P. Fuller et al. [15, 16] and G. E. Zuber et al. [17] adopted various spectral techniques to develop in situ TLC-FTIR techniques. They did some work with diffuse reflectance infrared Fourier transform (DRIFT) spectrometry to directly analyze spots, while Lloyd et al. [18] used Fourier transform infrared photoacoustic spectroscopy. However, the biggest problem of the in situ TLC-FTIR technique is that traditional TLC stationary phases, such as silica and alumina, exhibit a strong background absorption that can bring about significant interference to sample identification. To solve the problem, Danielson et al. [19] proposed to use DRIFT (diffuse reflectance infrared Fourier transform) spectrometry on self-produced zirconium oxide TLC plates that has no mid-IR absorption between 4000 cm^{-1} and 1000 cm^{-1} . DRIFT is a technique applicable on rough samples that when irradiated by the IR beam produce diffuse reflection, collected by a detector. In Danielson work were separated with different solvents the dyes: rhodamine B, methylen blue, methylen green, methyl orange and methyl red. For each one the retention factor was measured and DRIFT spectrum acquired. Unfortunately, zirconium oxide stationary phase tended to absorb a great amount of water giving interference [19].

During the years continued the research for inorganic materials transparent to IR and suitable as TLC supports. Inorganic halides with characteristics of IR-transparency and insolubility, as silver iodide and barium fluoride, have been recently used by many Chinese researchers. In particular F. Wang et al. [4] used self-produced AgI plates to separate a mixture of the dyes rhodamine B and bromocresol green, and then analyse it by FTIR-ATR. Compared to BaF_2 , silver iodide has the advantage of retaining a lower amount of water, which makes of it a more suitable TLC stationary phase. The only drawbacks are that the AgI is more expensive and photosensible.

Moreover, concerning the field of cultural heritage materials, TLC coupled with SERS analysis has been widely applied especially for the analysis of organic synthetic colorants. The first TLC-SERS coupling was reported in 1984 when three cationic dyes (crystal violet, malachite green and basic fuchsine) were separated by paper chromatography, and after solvent drying were sprayed with a silver colloid to perform a SERS analysis [20]. Silver was, and actually still is, the most used metal for surface enhancement and the commonest form is the colloid suspension [21]. In some cases analytes were mixed with the silver colloid and spotted on the TLC plate, but this method is appropriate just for pre-TLC Raman analysis. To record SERS spectra after separation is necessary to add the silver colloid afterwards, although also the use of some pre-activated plates has been reported [21]. For example, in 1997, using crystal violet as analyte, Szabo and Winefordner precoated a TLC plate via a Brashear reduction and compared it with commercially available argentation plate (with silver salts contained in the stationary phase) [22]. Poor quality SERS spectra were obtained, clearly showing that this method has major drawbacks and only the post-addition of a colloid gives good results [21 da 39 lara]. More

recently, K. Herman et al. [23] treated a normal silica TLC plate by impinging it into an AgNO_3 solution before performing the separation of three of binary mixtures of cresyl violet, bixine, crystal violet, and Cu(II) complex of 4-(2-pyridylazo)resorcinol. The presence of AgNO_3 permits a direct SERS analysis on the plate thank to the photoreduction of the silver contained within.

During the years, in most studies, TLC plates have been used only for deposition and merely a few separations have been reported. Regarding dyes, G.W Somsen, P.G.J.H. ter Riet, et al. [24] performed TLC-SERS on a mixture of green and violet aminotriphenylmethane dyes. More recently I. Geiman, M. Leona, and J.R. Lombardi investigated synthetic dyes found in ballpoint inks achieving separation on a silica gel TLC plate and Raman analysis of a blue ink [25]. Strictly regarding the field of cultural heritage it's of noticeable importance the coupling TLC-SERS performed by C.L. Brosseau, A. Gambardella, et al. [10]. They developed silica gel substrates to be used as stationary phases to perform TLC separation of mixtures of dyes; after developing and drying of the TLC plate, the spots corresponding to the dyes have to be each treated with citrate reduced silver colloid before recording SERS spectra. By using this method, they obtained good preliminary results by TLC-SERS coupling in the field of art conservation and restoration [10].

Coupling TLC-FTIR and TLC-SERS have proved to be a valuable analytical tools. FTIR and Raman analysis are complementary since IR absorption and Raman scattering have different selection rules, hence what is frequently strong in a Raman spectrum is weak in an IR spectrum and vice versa [26]. For this reason, a combined IR and Raman system offers a complete vibrational information from numerous compounds.

In this work different stationary phases, whose composition is suitable to perform enhanced vibrational analyses without the addition of colloidal solutions, have been tested to separate mixtures of standard dyes: silver iodide (AgI), and two kinds of hydroxyapatite substrates enriched with gold nanoparticles. AgI was chosen because of its known transparency in the mid-IR range, already exploited for TLC-FTIR analysis of dyes [4]. In the frame of this research AgI was deposited over gold slides in order to perform ATR-RAIRS analyses. This mode is known to produce an enhancement of the IR signal as explained in Chapter 4, par 4.1. Moreover, AgI belongs to the class of silver halides which have been lately used as SERS active substrates [27].

3.2 Materials and Methods

3.2.1 Materials

Synthetic colorants were kindly provided by Dr. Martaan van Bommel (Ministry of Education, Culture and Science Cultural Heritage Agency of the Netherlands) in the frame of the European project CHARISMA.

The proposed methodology has been optimized on different synthetic dyes belonging to the classes of triarylmethane dyes: Brilliant Green (BG1); xanthenes dyes: Rhodamine B (BV10); and tiazine dyes: Methylen Blue (BB9). All the used dyes were in the form of aqueous solutions 10^{-4} M prepared with H₂O MilliQ,

Different TLC Stationary Phases have been used: AgI self-produced and deposited on different substrates and nano-silica gel produced by Fluka with layer thickness of 0,2 mm and medium pore diameter of 60 Å.

The AgI method was tested on a mixture of three standard dyes: brilliant green (BG1), rhodamine B (BV10) and methylen blue (BB9). Silver iodide was also deposited on different metallic supports, glass slides and silicon to explore if and how different TLC supports can impact on vibrational spectra.

To compare the obtained results, also standard nano-silica gel HPTLC plates were analysed with the mixture: BG1, BV10 and BB9.

3.2.2 AgI synthesis

The synthesis procedure of silver iodide (AgI) has been optimized with the aim of having the final product in the form of small particles, easy to bring into suspension, in order to facilitate the subsequent deposition of the salt and to have a substrate as more homogeneous as possible.

The most suitable preparation procedure for the present application resulted to be the following precipitation method:

- preparation of 0,1 M AgNO₃ and 0,1 M KI aqueous solutions in 50 ml backers; the backer containing the AgNO₃ solution has to be wrapped with aluminium foil to protect the reagent from the light, being it photosensitive;

- resting of the solutions in a refrigerator for 30 minutes, to allow them to reach a temperature around 4°C;
- adding of the AgNO₃ solution to the KI solution, keeping the new one closed in the aluminium foil;
- resting of the new solution in a refrigerator for 1 hour;
- resting of the new solution at ambient temperature for a time ranging from 45 minutes to 1 hour, in dependence on the external temperature (increasing of the resting time for colder temperatures);
- filtering of the precipitate under vacuum and rinsing of the obtained product with H₂O milliQ several times, to remove the remains of the chemical reactions, such as KNO₃;
- drying in a oven at the temperature of 40°C for 20 minutes;
- removal of the final product from the filter and weighing;
- two successive cycles of sonication of 15 minutes each of AgI in ethanol or pronanol, in order to produce a surnatant;
- deposition of the surnatant on slide through micro-pipette dropping dropwise.

3.2.3 AgI deposition methods

In order to obtain reproducible results in terms of AgI film homogeneity, efficiency of chromatographic separation and suitable spectroscopic signals, different deposition methods have been tested.

3.2.3.1 Deposition in ultrasonic bath:

- Adding of 0,100 g of AgI in 5ml of ethanol poured in a 50 ml backer;
- Two sonication cycles of 15min;
- Drop-wise deposition of 1ml of surnatant on the TLC support while sonicating and system enveloping with parafilm;
- Resting of the self-produced TLC plates inside the sonicator for 24 hours or until the solvent has evaporated.

The key point of this deposition method is the ethanol evaporation which strongly affects the homogeneity of the AgI forming layer. To vary the speed of evaporation some modification to the deposition were fruitlessly tried: sonicator filled with ice and water, pierced parafilm envelop, and substitution of the sonicating deposition with a bath deposition in oven or environmental conditions.

3.2.3.2 Deposition in ethanol saturated atmosphere:

- Adding of 0,100 g of AgI in 7ml of ethanol poured in a 50 ml backer;
- Two sonication cycles of 15min;
- Drop-wise deposition of 1ml of surnatant on the TLC support in an ethanol chamber;

- Resting of the self-produced TLC plates for 24 hours or until the solvent has evaporated.

The ethanol chamber is a closed system in which is present a watch-glass containing 2ml of ethanol to obtain a saturated ethanol atmosphere. As mentioned previously, it's on the ethanol evaporation conditions that the attention has been focused to optimize the deposition. In this case, the presence of a saturated atmosphere permits a slower ethanol evaporation from the TLC support.

3.2.3.3 Deposition in propanol saturated atmosphere:

To reach an even slower evaporation of the surnatant solution, ethanol has been substituted with propanol which is less volatile because of its longer aliphatic chain. In this case the procedure is the same as the one developed for the ethanol saturated atmosphere. The only adjustments regard the sonication, which has been divided into three cycles of 10 min instead of two of 15min, and the propanol saturated chamber, that contained three backers with 30ml of propanol each.

3.2.3.4 Spin-coating

- Adding of 0,100 g of AgI in 3,5 ml of ethanol poured in a 50 ml backer;
- Two sonication cycles of 15min;
- Deposition of 0,5 ml of surnatant on the slide, rotating at low speed;
- Increasing of the speed to 400 rpm until complete removal of the solvent;
- Repetition of the last two steps multiple times to obtain a layer of the desired thickness.

Spin-coating was performed at the Department of Industrial Chemistry of the Bologna University in Bologna, Italy.

3.2.4 TLC

Dyes mixtures 10^{-4} M were deposited on the different SP using a Hamilton syringe or a micropipette and let dry. TLC separations were performed in a glass backer closed with parafilm as elution chamber, with typical developing times ranging from a few minutes for nano-silica and HAPAA to a maximum of 15 minutes for AgI. Eluent mixture was optimized for the different SP.

Table 6: TLC conditions for the different SP

| <i>SP</i> | <i>Dyes Mixture</i> | <i>Deposited Volume</i> | <i>Eluent</i> | <i>Eluent Ratio</i> |
|-----------|---------------------|-------------------------|----------------------|---------------------|
| AgI | BG1, BV10, BB9 | 0,5 μ l | EtOH+NH ₃ | 9:1 |

| | | | | |
|-------------|-----------------|-------------|--|-----------|
| HA/ HAPAA | AO20, BV1, AR87 | 1,0 μ l | EtOH+NH ₃ | 9:1 |
| Nano-silica | BG1, BV10, BB9 | 0,5 μ l | EtAc+ MeOH+ NH ₃ +H ₂ O | 35:11:5:5 |

3.2.5 Optical Microscope and SEM

AgI TLC plates with metallic and glass supports have been characterized with the Olympus Optical Microscope (Olympus Optical, Tokyo, Japan) BX51 microscopy equipped with a digital scanner camera Olympus DP70, of the Microchemistry and Microscopy Art Diagnostic Laboratory (M2ADL) of the Bologna University in Ravenna, Italy .

SEM analysis have been conducted both at the Department of Cultural Heritage of the Bologna University in Ravenna, Italy using a Fei Quanta instrument; and at the Department of Industrial Chemistry of the Bologna University in Bologna, Italy using a ZEISS instrument coupled with a Raman probe Renishaw with an excitation wavelength of 514nm.

AgI TLC plates were analysed without coating to keep untouched the SP. In the case of conductive metal supports this wasn't a problem, while in the case of glass support it resulted in poor quality images.

3.2.6 FTIR-ATR and ATR-RAIRS

FTIR analysis were executed at the Microchemistry and Microscopy Art Diagnostic Laboratory (M2ADL) of the Bologna University in Ravenna, Italy. A Thermo-Nicolet iN10MX micro-spectrometer filled with a nitrogen-cooled mercury cadmium telluride (MCT) detector was employed for RAS measurements using a 45° geometry. This setup regarded only AgI-TLC plates in which the highly reflective surface generating the enhancement was constituted by the already mentioned metallic supports.

Enhanced-ATR spectral data were acquired using a slide-on ATR device by Thermo-Nicolet, provided with a conical Ge IRE having an index of refraction in the mid-IR range of 4,00. An aperture of 200x200 μ m was used for all measurements, which resulted in an investigated area of 50x50 μ m.

Spectra were recorded in the range 4000 - 675 cm^{-1} at a resolution of 4 cm^{-1} , using a co-addition of 128 scans. Background acquisition, at the interface Ge-air in the case of ATR measurements, was taken with the same parameters before each set of acquisition.

ATR-RAIRS analysis were performed only on AgI TLC plates with golden support after the separation of the mixture BG1, BV10 and BB9. Also single colorant spots were analysed on AgI TLC plates and on plain gold slides in order to build a library of standard spectra for each dye.

In this case too, colorants solutions 10^{-4} M were deposited as 0,5 μ l drops using a Hamilton syringe and let dry.

3.2.7 Raman-SERS

Raman-SERS experiments were conducted at the Pinacoteca of Bologna in Bologna, Italy. Analyses were performed with a Bruker SENTERRA Raman microscope, fitted with a diode laser excitation source emitting at 785 nm.

Raman-SERS measurements were executed for the separated mixture BG1, BV10, BB9 on AgI TLC plates on gold support. On this, others AgI supports (glass, Cu, Al, SiO₂) and on plain Au slides also spot analysis of the dyes was performed. As for ATR-RAIRS, the 10^{-4} M dyes solutions were prepared using milliQ water and exactly the same deposition procedure was adopted.

The Raman-SERS measurements have successively been performed on the solid residues of the drops of dyes themselves or in the separated spots after the TLC elution. These analyses have been executed on the following substrates:

- golden slides, performing measurements only on spotted dye solutions (no TLC elution is possible on such a substrate);
- golden slides coated with AgI, performing measurements on the substrate itself and both on spotted dye solutions and on separated spots after the TLC elution;
- glass slides coated with AgI, performing measurements both on spotted dye solutions and on separated spots after the TLC elution.

Additionally some investigations on the same AgI TLC-plates were completed with the deposition on dyes spots of 1 μ l of silver citrate colloid (AgCt) prepared by reduction of silver nitrate with trisodium citrate dihydrate, according to the Lee-Meisel's procedure [30]. The propriety of AgCt solution was verified by UV-Vis-NIR spectroscopy by checking the presence of the absorption maximum around 421 cm⁻¹.

Concerning standard nano-silica HPTLC plates, Raman-SERS measurements were performed after separation of the mixture BG1, BV10, BB9 and on dyes spots with and without AgCt colloid application (1-4 μ L). Furthermore, some analysis were taken after deposition of a AgCt paste, used also in literature [31], obtained from the colloid following this procedure:

- Placing of 1mL of colloid solution in a eppendorf;
- Centrifuge for 10 min at 3600 rcf;
- Removal of the limpid supernatant solution, avoiding to remove any of the concentrated paste present at the bottom of the eppendorf;
- Addition of another 1mL of colloid solution;
- Repetition of last three steps five times, remembering to completely discard the supernatant at the end of the last cycle to obtain the paste.

Another AgCt paste was also produced in the same way, but centrifuging 15 min for ten times. Concerning the application of these pastes usually was spotted on the sample in the following order: 1 μ l of paste, 0,25 μ l HNO₃ 0,2M and 0,25 μ l NaNO₃ 0,5M. These additions were necessary to accomplish the acidification and aggregation of pastes.

3.3 Results and discussion

3.3.1 AgI

Different synthesis and deposition routes were tested for AgI and its morphology was characterized by optical microscopy and scanning electron microscopy (SEM). The method was tested on a mixture of three standard dyes: BG1, BV10 and BB9.

ATR-RAIRS and Raman-SERS analysis were performed on AgI TLC plates with golden or glass support after the separation of the mixture and on single dyes spots.

3.3.1.1 Deposition Approaches and TLC Results Comparison

Different deposition methods were compared to each other in order to identify the most suitable to obtain a homogeneous SP with high separation power, reproducibility and optimal analytical signal of the selected organic dyes.

Deposition in ultrasonic bath

TLC separation of the dyes mixture was well achieved on AgI on gold support TLC plates prepared in ultrasonic bath, with eluent EtOH:NH₃ 9:1.

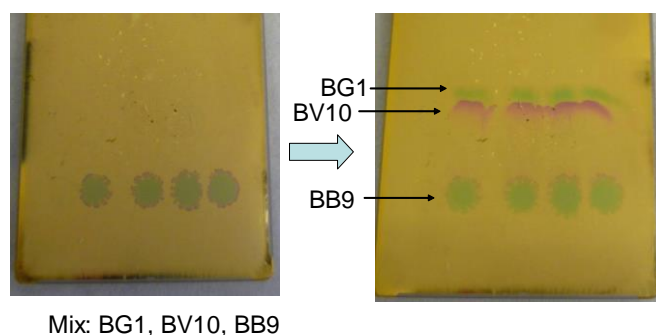


Fig. 26: TLC separation of the mixture BV10, BG1, BB9 on AgI coated gilded slide prepared through ultrasonic bath deposition. The TLC plate is shown before and after the separation.

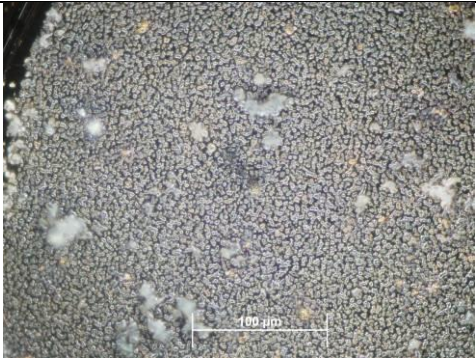
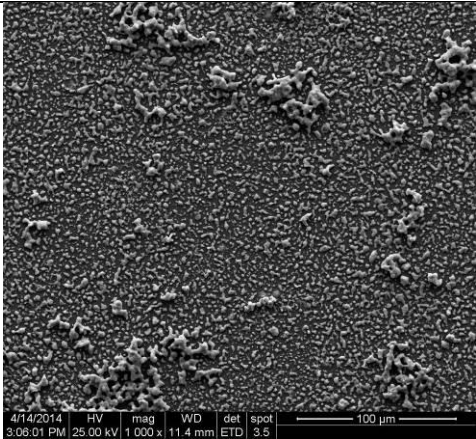
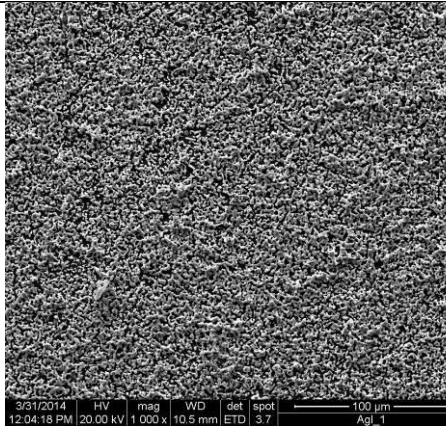
As shown in figure 6, during TLC separation BB9 remained in the same spot where the drop was deposited, while BV10 and BG1 migrated following the eluent. Due to their different

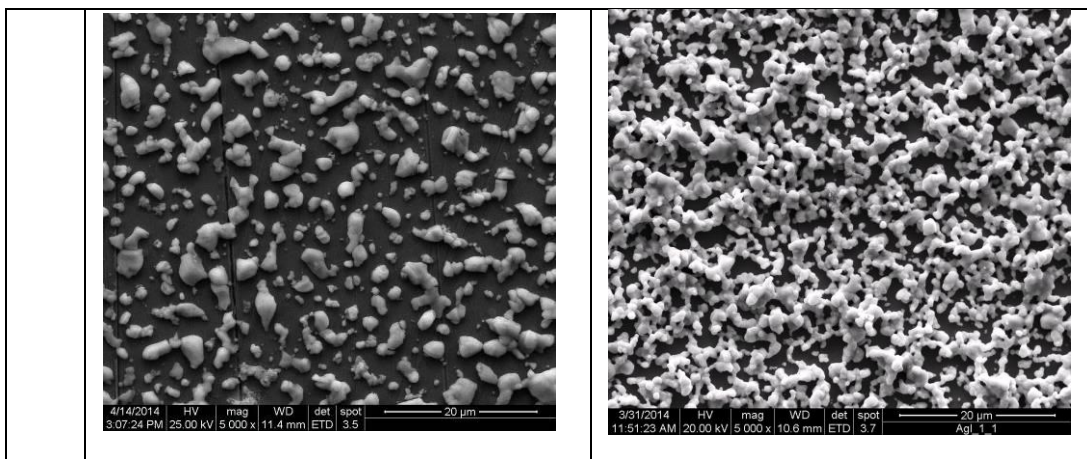
structure BG1 tended to migrate a little further than BV10, allowing the separation of these last two dyes too.

The main problem regarding this deposition protocol were the difficulties to obtain a reproducible AgI layer with homogeneous distribution of the stationary phase and a regular thickness. It was very common to notice, after deposition, big particles accumulation or a different concentration of AgI on the gold support in arbitrary areas. On these TLC plates was impossible to perform a TLC and had to be discarded. Certainly a lot of variables were very difficult to be tuned during the deposition: parafilm coverage function, environmental conditions of evaporation inside the sonicator, need of planar water surface and stillness of gold slides during sonication.

To better appreciate the variations in structure and morphology of AgI deposited on gold supports, optical microscopy (OM) and SEM were employed.

Table 7: Camera, OM and SEM (magnification 1000x, 5000x) images of two different AgI TLC plates on Au support obtained by ultrasonic bath deposition

| | AgI-Au_1 | AgI-Au 2 |
|-----|---|--|
| |  |  |
| OM |  |  |
| SEM |  |  |



AgI-Au_1 and AgI-Au_2 exemplify the two types of TLC plates obtained on which was possible to perform a TLC separation:

- AgI-Au_1 covered with a thin AgI layer, reflected in OM and SEM images as more rarefied and sparse AgI particles
- AgI-Au_2 characterized by a thick AgI layer that completely overcomes the reflectivity of the gold support and by a higher particle density shown in OM and SEM images

Nevertheless shapes and sizes of particles on AgI-Au_1 and AgI-Au_2 appear very similar, and some aggregates reach in both cases nano-dimensions, a very important aspect concerning SERS active substrates. Regarding this kind of analysis, has to be outlined the big variability in terms of Raman output reported for these inhomogeneous layers.

As mentioned previously, due to the reproducibility problem of the ultrasonic bath deposition method, the attention was focused on changing the deposition system aiming to better control evaporation of the solvent in which AgI supernatant was dispersed.

Deposition in ethanol saturated atmosphere

AgI TLC plates obtained following this protocol had more uniform AgI layers and permitted a successful separation of the dyes mixture in the order of elution already described.

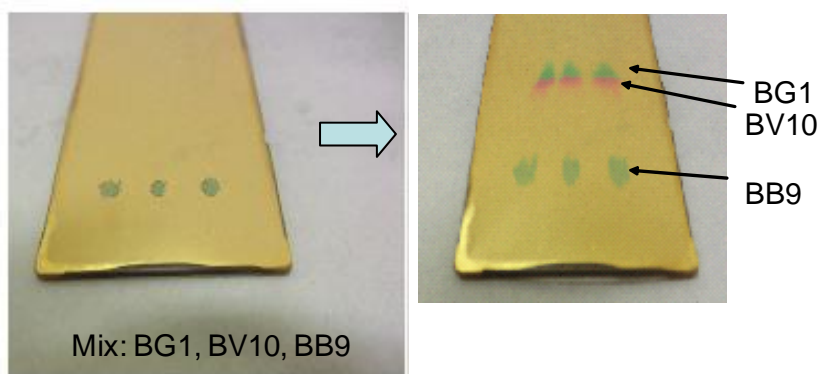
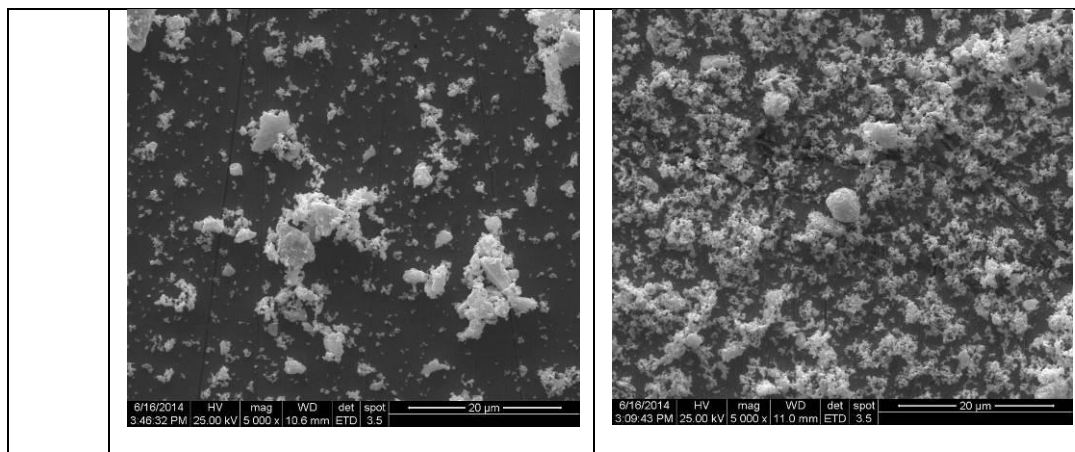


Fig. 27: TLC separation of the mixture BV10, BG1, BB9 on AgI coated gilded slide prepared through ethanol saturated atmosphere deposition. The TLC plate is shown before and after the separation.

To characterize AgI particles morphology and distribution, SEM was employed, still showing some density differences between a TLC plate and the other. As reported in table 4 AgI-Au_3 shows more rarefied particles compared to AgI-Au_4, while morphology and dimension of AgI particles are very similar.

Table 8: Camera and SEM (magnification 1000x, 5000x) images of two different AgI TLC plates on Au support obtained by ethanol saturated atmosphere deposition

| | AgI_Au 3 | AgI_Au 4 |
|-----|----------|----------|
| | | |
| SEM | | |



Employing this new protocol better reproducible TLC plates were obtained, probably thank to the ethanol saturated system in which the deposition took place. Ethanol vapour already present in the system slowed down the evaporation of ethanol dispersed with AgI surnatant on the gold support, allowing a more uniform drying process. In most of TLC plates obtained with ethanol saturated atmosphere method, was possible to perform TLC separation and only a few were discarded. Concerning Raman analysis, the variability in terms of Raman output was diminished, as TLC plates became more similar in density and morphology passing from ultrasonic bath to ethanol saturated atmosphere deposition.

A significant advantage of this deposition technique is the lower amount of AgI surnatant necessary for the deposition: 0,100 g AgI in 7ml of ethanol instead of 0,100 g of AgI in 5ml of ethanol used for the ultrasonic bath deposition. More TLC plates can be prepared following the deposition in ethanol saturated atmosphere.

Deposition in propanol saturated atmosphere

A further improvement was the substitution of ethanol with propanol vapours to saturate the deposition system to obtain an even slower evaporation, and hence a more homogeneous layer. Propanol has a longer aliphatic chain which implies a lower volatility compared to ethanol. Effectively, AgI TLC plates obtained had a high level of reproducibility and could all be utilized for dyes mixture separation.

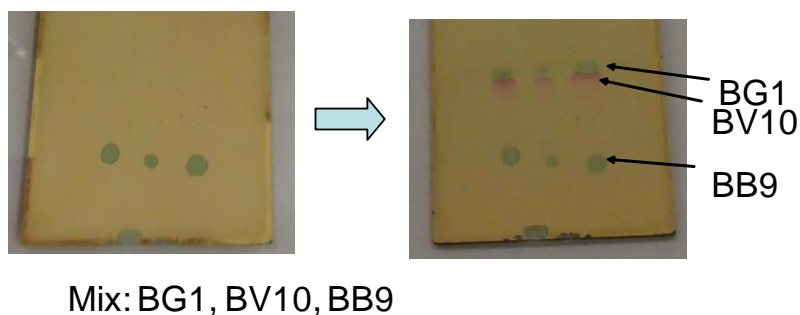


Fig. 28: TLC separation of the mixture BV10, BG1, BB9 on AgI coated gilded slide prepared through propanol saturated atmosphere deposition. The TLC plate is shown before and after the separation.

As shown in the above figure the separation always follows the same elution order: BG1, BV10, BB9

SEM characterization of these TLC plates in figure 4.6 shows a dense and uniform layer with AgI aggregates with comparable shapes and sizes.

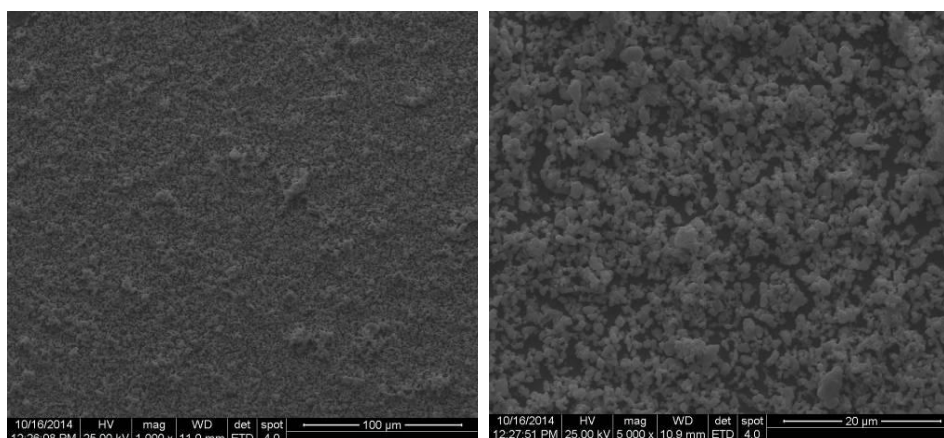


Fig. 29: SEM (magnification 1000x, 5000x) image of an AgI TLC plate on Au support obtained by propanol saturated atmosphere deposition.

In conclusion propanol saturated atmosphere deposition allowed for a high reproducibility of AgI TLC plates, reflected also on SERS signals. Furthermore, as for ethanol saturated atmosphere deposition, this protocol doesn't require a high amount of AgI to cover the TLC plates.

Spin-coating

Also by spin-coating was possible to achieve a homogeneous and reproducible coverage with AgI of gold supports, which resulted in an optimal TLC separation of the dyes mixture. Only BB9 streaked a little following the eluent uprising, as displayed in figure 10.

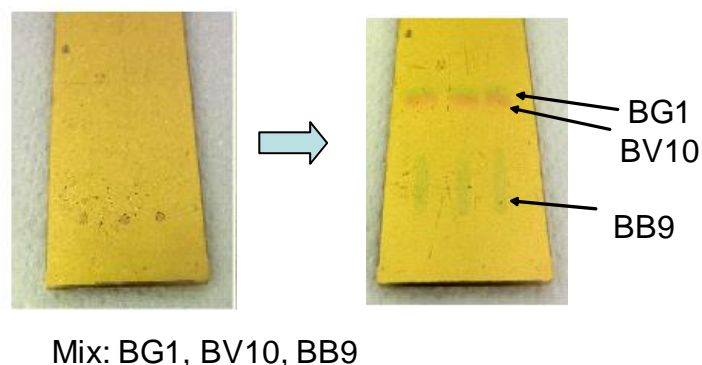


Fig. 30: TLC separation of the mixture BV10, BG1, BB9 on AgI coated gilded slide prepared through spin coating. The TLC plate is shown before and after the separation.

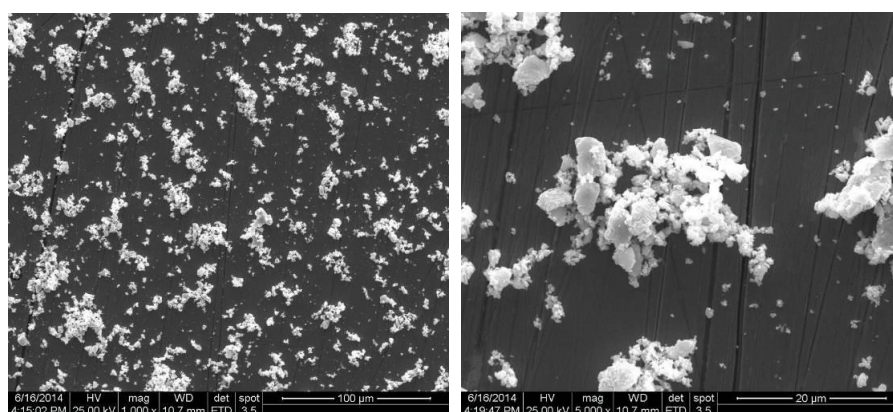


Fig. 31: SEM (magnification 1000x, 5000x) images of AgI TLC plates on Au support obtained by spin coating.

SEM images illustrate the uniform distribution of AgI particles and the presence of some nanostructures.

By comparing spin coating with the developed deposition technique, it's clear that is necessary to use a higher amount of AgI (0,5 μ l of supernatant for ten times) to obtain a complete coverage of the TLC plate, but the protocol is so much more faster, avoiding the evaporation step of 24 hours. In spin coating the solvent in which is present the supernatant is lost in the radial liquid flow, as also some of the AgI.

In conclusion, deposition in propanol saturated atmosphere was chosen as proper method because of its high reproducibility, low AgI amount to obtain homogeneous TLC plate coverage and high TLC separation power coupled with optimal Raman-SERS signals.

3.3.1.2 ATR-RAIRS

ATR-RAIRS analyses have been performed on AgI TLC plates with golden support after the separation of the mixture BG1, BV10 and BB9. Also single colorant spots were analysed on AgI TLC plates and on plain gold slides in order to understand if there were any signal differences due to the presence of the AgI layer and, especially, to build a library of standard spectra for each dye.

Reference spectra library

Reference spectra of BG1, BV10 and BB9 10^{-4} M were taken on naked gold slides and covered with AgI by mean of ATR-RAS configuration, already proved to produce more intense signals than a simple ATR configuration (Chapt. 4, par. 4.1). The deposited solution drops, after drying, formed the so-called coffee-ring.

ATR-RAIRS analyses of dyes spots on AgI TLC plates deposited on gold supports were performed with the aim of checking that the AgI layer on gold and the presumed complex between AgI and basic dyes didn't impede the enhancement due to the presence of the gold support. Effectively, as shown in figures 12, no significant differences were noticed in terms of bands position and intensity. As a consequence Au slides covered with an AgI layer resulted a good combination to obtain a TLC plate suitable for FTIR analysis.

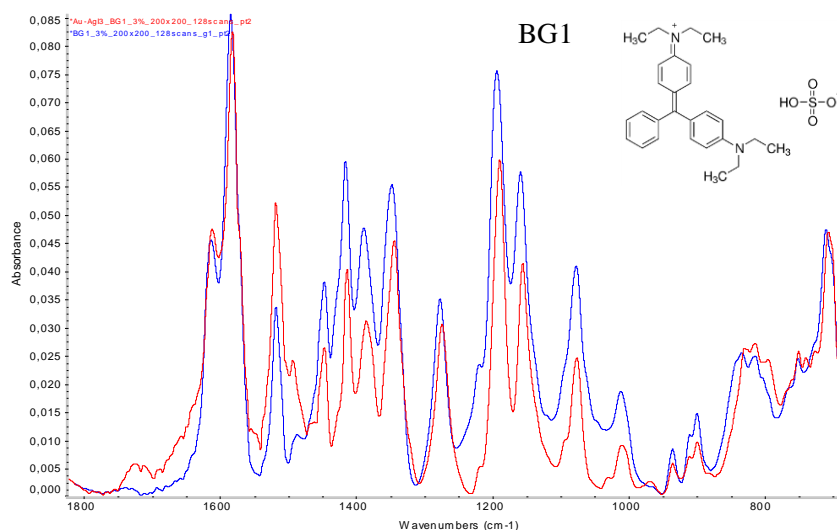


Fig. 32: FTIR-ATR-RAS spectra of BG1 recorded on gold slide (blue profile) and on AgI TLC plate on gold support (red profile)

Thanks to these comparisons, it is possible to demonstrate that the inorganic salt silver iodide synthesized does not absorb in the mid-IR range as expected, and that it can therefore be used in FTIR analyses. Moreover, it can be seen that, in our ATR-RAIRS configuration, AgI does not affect the enhancement given by the Au underlayer and it is therefore sensible, at least from this point of view, to carry out the research for the development of such a TLC substrate to be analyzed also by means of enhanced FTIR spectroscopy.

In table 4, 5 and 6 are reported the FTIR bands assignments of BG1, BV10 and BB9.

Table 9: Bands assignment attempt for FTIR-ATR-RAS spectrum of BG1, where ν = stretching, δ =bending, s = symmetric, as = asymmetric, $i.p$ = in plane [32]

| Band frequency (cm ⁻¹) | Assignment attempt |
|------------------------------------|---|
| 1618 | |
| 1587 | $\nu(C=C)$ of para-disubstituted ring (C-Ph-N) aromatic $\nu(C=C)$ |
| 1449 | CH ₃ def |
| 1419 | CH ₂ scissoring def, N-H i. p. def |
| 1389 | CH ₃ def, N-H i. p. def |
| 1350 | |
| 1279 | |
| 1220 | |
| 1193 | $\nu(C-C)$, CH ₂ wag |
| 1159 | |
| 1078 | $\delta i.p.(CC)$, NH ₂ rock |
| 1009 | $\delta as(C-C-N)$ ring |
| 937 | vs CArCArN of Ar-N(CH ₃) ₂ |
| 900 | vs CArCArN of Ar-N(C _x H _x) ₂ |
| 832 | |

Table 10: Bands assignment attempt for FTIR-ATR-RAS spectrum of BV10, where ν = stretching, δ =bending, XR= xanthene ring, PR= phenyl ring, A= NHC₂H₅ [33-36]

| Band frequency (cm ⁻¹) | Assignment attempt |
|------------------------------------|---|
| 1714 | PR vibrations |
| 1649 | $\nu(CC)$ of XR |
| 1594 | $\nu(XR)$ |
| 1555 | XR-A |
| 1530 | XR-A [3], $\nu(CC)$ of XR [4] |
| 1493 | $\nu(XR)$ |
| 1466 | XR-A |
| 1414 | XR |
| 1394 | |
| 1381 | |
| 1348 | |
| 1276 | P group [1], $\delta(CH)$ of XR [2] |
| 1247 | A+PR [1], X+PR [3] |
| 1182 | XR+A [1, 3], $\delta(CH)$ of XR [2] |
| 1134 | XR+A [1], $\delta(CH)$ of XR [2], XR+A+PR [3] |
| 1077 | A+PR [1, 3], $\nu(PR)$ [2] |
| 1014 | vibr. P |
| 980 | |
| 925 | X+A+P [1], $\nu(X+PR)$ [2] |
| 831 | X+A+P |

Table 11: Bands assignment attempt for FTIR-ATR-RAS spectrum of BB9, where ν = stretching, δ =bending, s = symmetric, as = asymmetric, $i.p.$ = in plane, $o.o.p.$ =out of plane [37-39]

| Band frequency (cm ⁻¹) | Assignment attempt |
|------------------------------------|--|
| 1601 | aromatic $\nu(C=C)$ [1], $\nu(CN_{center} \text{ and lateral}) + \nu(CC) + \delta i.p.(CH)_{ring}$ [3] |
| 1490 | vibr. heterocycle skeleton [2], $\nu(CN_{center}) + \nu(CC) + \delta o.o.p.(CH) \text{ of } CH_3 + \delta i.p.(CH)_{ring}$, vibr. of arom. ring [3] |
| 1441 | $\delta as(CH_3)$ [2], $\nu(CN_{center}) + \delta i.p.(CH)_{ring} + \delta o.o.p.(CH) \text{ of } CH_3$ [3] |
| 1392 | $\delta s(CH_3)$ [2], $\nu(CN_{center}) + \delta i.p.(CH)_{ring} + \delta o.o.p.(CH) \text{ of } CH_3$ [3] |
| 1355 | $\nu(CN_{center}) + \delta i.p.(CH)_{ring} + \delta o.o.p.(CH) \text{ of } CH_3$ [3] |
| 1337 | $\nu(CN_{center}) + \delta i.p.(CH)_{ring} + \delta o.o.p.(CH) \text{ of } CH_3$ [3] |
| 1250 | $\delta i.p.(CH)_{ring}$ |
| 1220 | vibr. heterocycle skeleton [2], $\nu(CN_{lateral}) + \delta i.p.(CH)_{ring} + \delta o.o.p.(CH) \text{ of } CH_3$ [3] |
| 1178 | vibr. heterocycle skeleton |
| 1145 | $\delta i.p.(CH)_{ring}$ |
| 1042 | vibr. heterocycle skeleton [2], $\nu(CS) + \delta i.p.(CH)_{ring}$ [3] |
| 957 | skeletal deformation (CC and CH ₃), $\delta o.o.p.(CH)$ |
| 887 | $\delta(CH)$ in heterocycle [2], skeletal deformation (CC and CH ₃), $\delta o.o.p.(CH)$ [3] |
| 833 | $\delta(CH)$ in heterocycle |

Post-TLC spectra

Post-TLC dyes spectra were widely identifiable and matched with the reference spectra acquired previously, with no noticeable shifts in wavenumbers (fig. 13). As expected the intensities were reduced because of dyes dilution during the elution process of the chromatographic separation. Therefore it was demonstrated that also after TLC was possible to identify the different dyes, starting from a really low dye amount (0,5 μ l of a 10⁻⁴M solution).

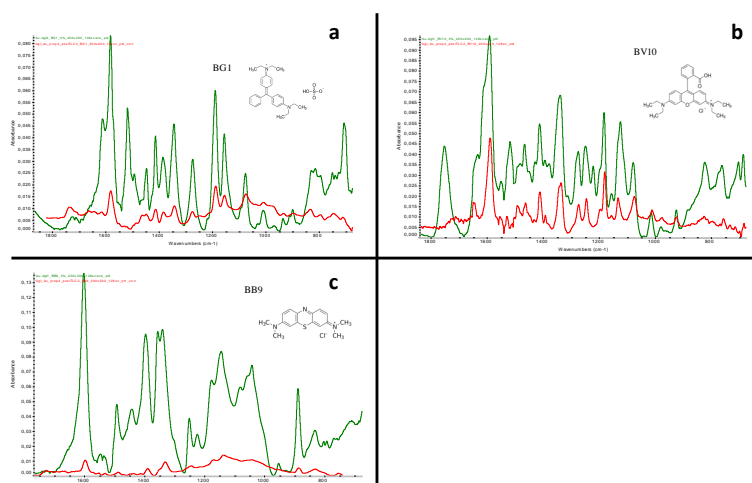


Fig. 33: FTIR-ATR-RAS spectra recorded on AgI TLC plate on gold support before (green profile) and after TLC separation (red profile) of BG1 (a); BV10 (b); and BB9 (c) . The former spectra is in common scale, while the latter is in full scale.

3.3.1.3 Raman-SERS

The interpretation of Raman-SERS presented many more difficulties in comparison with that of enhanced IR, due to the big variability of the obtained outputs; this constituted a serious problem of reproducibility which however seems to be a quite common feature when dealing with SERS and developing of new substrates for it. Experimentally, differently from enhanced IR, also the substrate constituted by glass slide coated with AgI has been tested and, in order to have more spectral material available to assess the extent of the enhancement, some analyses have been performed also after the deposition of 1.0 ml of silver colloid (called AgCt) on the point under investigation. Some of the spectra collected will be here on reported in figures showing the signals in common scale, after having performed the automatic baseline correction of the software.

Raman-SERS measurements were executed for the separated mixture BG1, BV10, BB9 on AgI TLC plates on gold support. As for ATR-RAIRS, also single dyes spots were analysed on naked gold and on AgI TLC plates on gold support.

Spectra on Au vs spectra on AgI_Au

As previously described for ATR-RAIRS, spectra of BG1, BV10 and BB9 10^{-4} M were taken on naked gold slides and covered with AgI. By comparing the results obtained, it was noticed an enhancement of SERS output for AgI deposited on gold support with high signal to noise ratio (fig. 14). Therefore these AgI TLC plates resulted interesting not only for the separation power, ATR-RAIRS and Raman dyes identification but also for an enhancement of SERS signal.

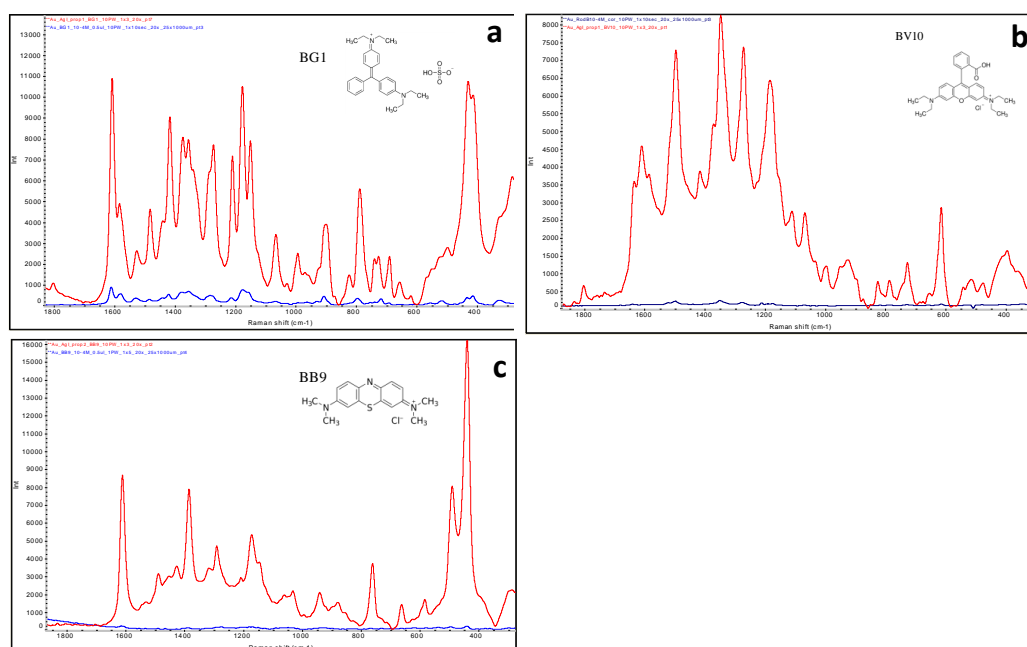


Fig. 34: SERS spectra recorded on gold slide (blue profile) and on AgI TLC plate on gold support (red profile) of BG1 (a); BV10 (b) and BB9(c).

It has been here reported here only the bands assignments of BV10 for the reason that the Raman and SERS bands assignments of BG1 and BB9 are reported in Chapter 4.

Table 12: assignment attempt for Raman spectrum of BV10, where ν = stretching, δ =bending, i.p.= in plane, o.o.p.= out of plane, XR= xanthene ring, PR= phenyl ring, A= NHC_2H_5 [33,34, 40]

| Band frequency (cm^{-1}) | Assignment attempt |
|-------------------------------------|---------------------------------|
| 1634 | $\nu(\text{XR})$ |
| 1611 | $\nu(\text{XR})$ |
| 1496 | X+A [1] $\nu(\text{XR})$ [2] |
| 1417 | X |
| 1347 | $\nu(\text{XR})$ |
| 1272 | $\delta(\text{CH})$ of XR |
| 1186 | $\delta(\text{CH})$ of XR |
| 1111 | A |
| 1068 | $\nu(\text{P})$ |
| 1002 | |
| 941 | $\nu(\text{XR}+\text{P})$ |
| 823 | P |
| 728 | δ o.o.p.(CH) of PR |
| 678 | δ o.o.p.(CH) of PR |
| 614 | XR deformation i.p. |
| 541 | X+P |
| 481 | |
| 398 | |

Post-TLC spectra

Post-TLC dyes spectra were identifiable and matched with the spectra acquired previously from the dyes spotted on AgI TLC plates with gold support. Thank to SERS effect, after TLC, dyes spectra still had a high signal to noise ratio (fig. 15) allowing easy dyes identification starting from a low dye amount ($0,5\mu\text{l}$ of a solution 10^{-4}M).

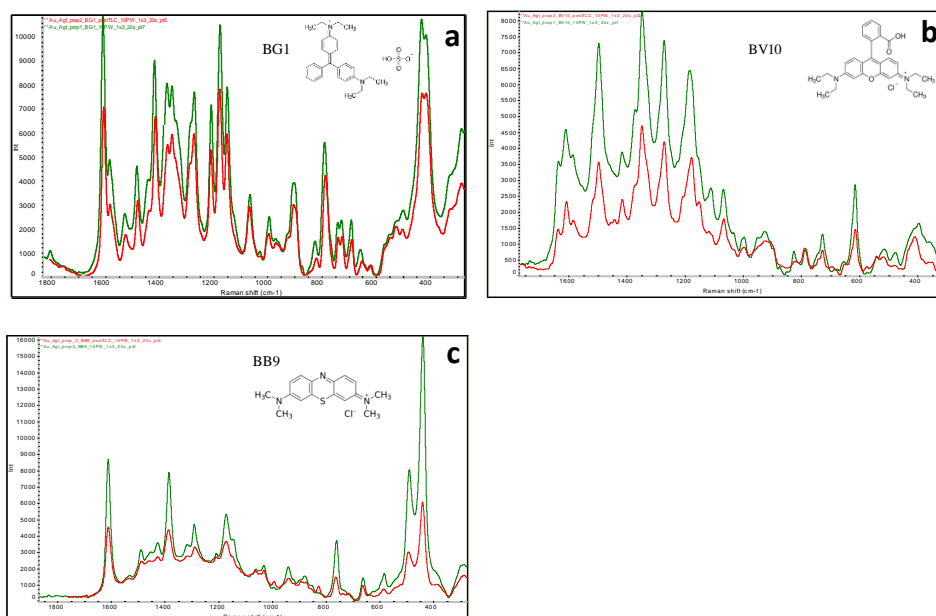


Fig. 35: Raman-SERS spectra recorded on AgI TLC plate on gold support before (green profile) and after TLC separation (red profile) of BG1 (a); BV10 (b); and BB9 (c). Experimental parameters: power 10 mW, acquisition time 1x3s, objective 20x.

3.3.1.4 Insight into Raman-SERS on AgI TLC Plates

Some investigations on AgI-Au TLC-plates were completed with the deposition on dyes spots of 1µl of silver citrate colloid to understand if it was possible to gain a further signal enhancement. Moreover silver iodide was also deposited on different metallic supports, glass and silicon to explore if and how different TLC supports can impact on Raman-SERS spectra.

Deposition methods and spectra

As previously described, the two most interesting AgI deposition methods developed during this project were the one in propanol saturated atmosphere and the spin-coating. They resulted both reproducible and the only drawback of spin coating was the higher quantity of AgI necessary to cover the gold support. In this section are reported Raman-SERS spectra obtained with the two protocols, showing that results are equivalent for the analysed dyes (fig. 16).

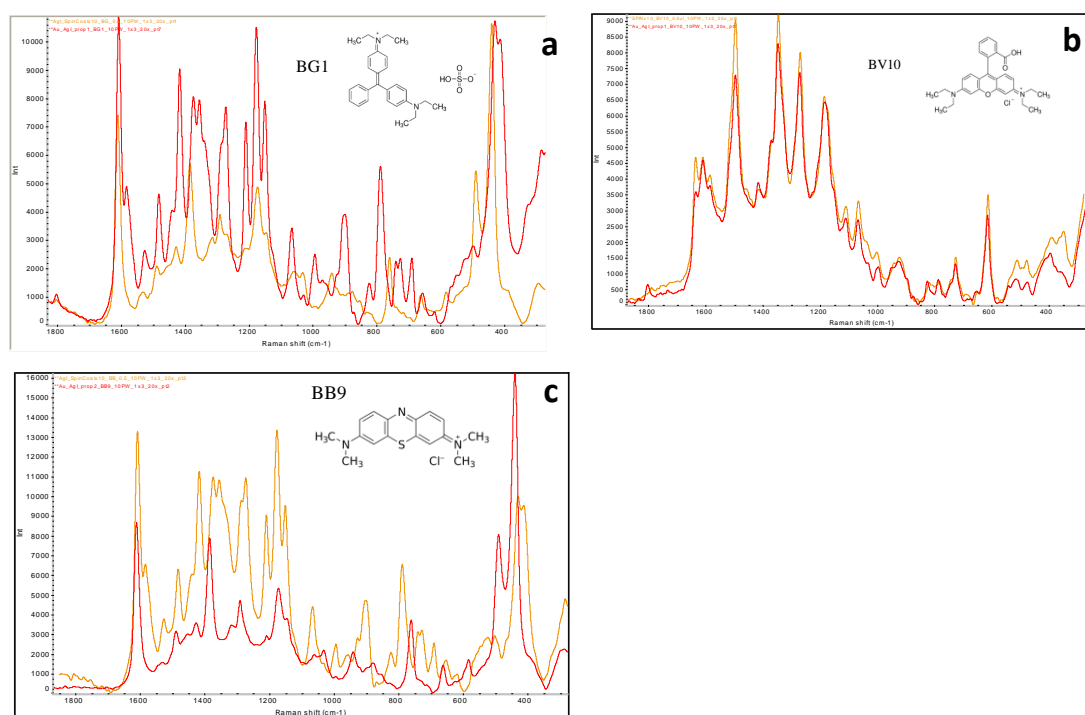


Fig. 36: Raman-SERS spectra recorded on AgI_Au TLC plate obtained through propanol saturated atmosphere deposition (red profile) and by spin coating (orange profile) of BG1 (a); BV19 (b), and BB9 (c). Experimental parameters: power 10 mW, acquisition time 1x3s, objective 20x.

Spectra with silver colloid

Raman-SERS analyses performed on AgI_Au TLC plates of single dyes spot in presence of silver citrate colloidal solution showed an increased enhancement, but not as important as in the case of plain gold. Since dyes spots adsorbed on AgI probably formed complexes and were less available for interacting with the colloid, the enhancement didn't boost as much as for gold, on which the colorant deposited couldn't interact with any compound (fig. 17).

From a practical point of view, colloidal solutions presented some drawbacks: first of all they had to be prepared in a proper manner and not always was possible to obtain a colloid with the desired properties; and second the colloidal solution applied on dyes spots didn't spread homogeneously, not interacting in the same way in different micro-areas of dyes spots. The results were that sometimes the colloid had to be prepared several times and Raman output was very variable, depending on which micro-area the analysis was performed. Moreover colloidal solutions presented some peaks in Raman spectra and, during application on TLC separated dyes, colloid drops applied may lead to contamination between different dyes spots.

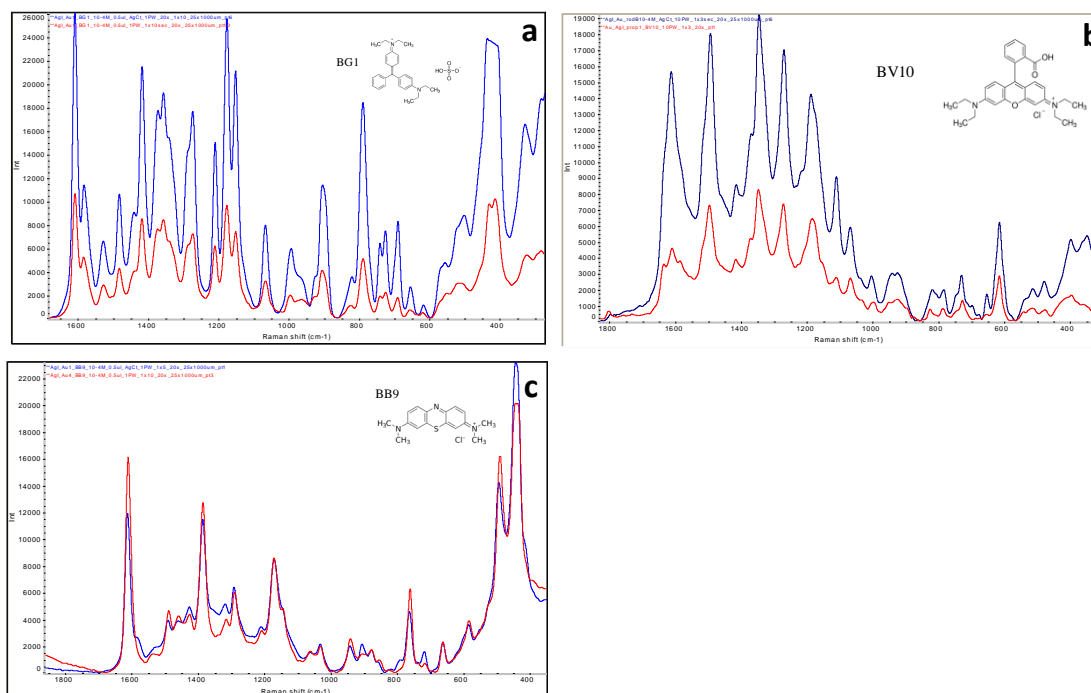


Fig. 37: Raman-SERS spectra recorded on AgI TLC plate on gold support (red profile) and after addition of silver citrate colloid solution (blue profile) of BG1 (a); BV10 (b) and BB9 (c).

Spectra on different supports

Aiming to understand the enhancement observed on AgI₂/Au TLC plates, silver iodide was deposited also on other kinds of supports: silicon, glass, copper and aluminum. BG1 and BV10 dyes spots were analyzed and it was found that only AgI TLC plates on metallic supports were suitable to produce a dye signal enhancement.

3.3.2 NANO silica

HPTLC plates were used to separate the mixture BG1, BV10 and BB9 and SERS analyses were performed after adding on the dyes spots silver colloidal solution or paste.

3.3.2.1 TLC results

Dyes separation on HPTLC plates resulted in really band-shaped and concentrated dyes spots (fig. 5). The order of elution remained the same as for AgI_Au TLC plates: immovable BB9, BV10 in an intermediate position and BG1 at the top.

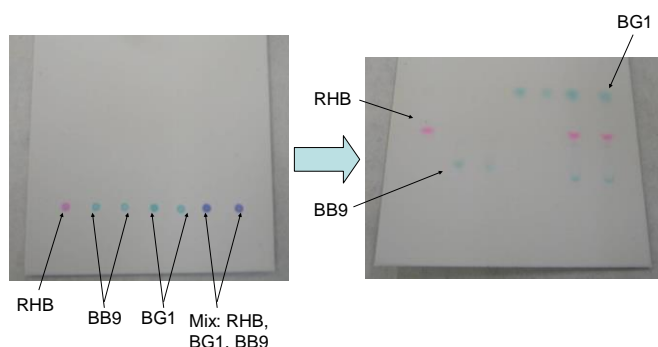


Fig. 38: TLC separation of the mixture BV10, BG1, BB9 on nano-silica HPTLC plate. The plate is shown before and after the separation.

FTIR-ATR analysis weren't performed on these plates because of the known FTIR spectra of silica.

3.3.2.2 Raman-SERS with Silver Citrate Colloid

Raman-SERS measurements were executed for single deposited dyes spots and for the separated mixture BG1, BV10, BB9. Different trials with the addition of increasing volumes of silver citrate colloid were experimented.

On HPTLC plates the addition of silver citrate colloid resulted essential to obtain an identifiable Raman spectra of the different dyes.

By comparing dyes spectra recorded on nano-silica TLC plates in presence of silver citrate colloid with spectra on AgI-Au, the enhancement due to the presence of the silver halide still remains the major one.

3.3 Conclusions

The present research was aimed at developing a new SP suitable to couple TLC with enhanced vibrational techniques to separate and identify mixtures of organic synthetic dyes.

Silver iodide deposited on gold glass slides provided very promising results. Synthesis and deposition protocols were optimized to obtain homogeneous layers and reproducible TLC separations. Furthermore ATR-RAIRS and Raman analyses allowed the detection and identification of low concentrated dyes after TLC separation and without addition of colloidal solutions.

ATR-RAIRS configuration wasn't disturbed by the presence of the AgI layer deposited on the reflective gold glass slide and dyes IR spectra resulted equivalent to the ones detected on naked gold glass slides.

SERS spectra of green and blue dyes showed the higher enhancement, in particular BB9. This molecule absorbs principally red light at a wavelength of 670 nm, which is not so far from the one of laser excitation, 785 nm (near IR). In decreasing order the second profitable dye is Brilliant Green, whose has its absorption maximum at 623 nm, slightly more distant than Methylene Blue from the laser source wavelength. The lowest Raman intensities are finally showed by Rhodamine B, whose absorption maximum lays around 553 nm, lightly raised by the complex with AgI up to 580 nm. It therefore seems that, at increasing distance of the absorption maximum of the dye from the laser wavelength, there is a decrease in the extent of the enhancement. This could be interpreted in terms of pre-resonance; in fact it is known that using a laser line emitting at a wavelength in close proximity to that at which the dye exhibits an absorption maximum can enhance some vibrational modes (as explained in Chapter 3). In none of our cases it is possible to talk about SERRS (Surface Enhanced Resonance Raman Scattering), since not even BB9 dye exhibits an absorption maximum close enough to the laser wavelength, but we can support the thesis that dyes absorbing at longer wavelengths produce a Raman signal that is improved through the SERRS effect, being our spectra collected using a NIR excitation source.

Concerning the understanding of the enhancement mechanism in Raman analyses we supposed that AgI may be partially photoreduced by the laser used and that this reaction may occur at the relatively weak conditions employed for the analyses thanks to the presence of the metallic underlayer. Indeed in literature photo-reduction of silver halides is promoted employing more energetic laser in the visible range for a longer time [41]. The enhancement of the signal cannot be obtained when AgI is deposited on glass slides or silicon. However this hypothesis has still to be confirmed. Different working conditions, as laser power and wavelengths, are going to be tested in order to better understand how the AgI photoreduction works. Moreover morphological observation of the particles before and after the laser irradiation, such as investigation on the silver speciation in Raman analysed area will be performed.

Nano-silica gel on HPTLC plates, widely used as SP, consented to separate and identify dyes mixtures by SERS spectroscopy after addition of silver citrate colloid. The enhancement obtained wasn't as marked as for AgI deposited on gold glass slides and, moreover, colloids fabrication still remains a challenging task.

In conclusion AgI deposited on gold glass slides resulted more efficient and functional than nano-silica HPTLC plates, allowing for dyes separation and complementary vibrational enhanced spectroscopy analyses. It has also to be outlined the fact that ATR-RAIRS and Raman analyses can be performed on the same AgI coated gold glass slide. With only one chromatographic separation is possible to gain many valuable information about dyes contained in the mixture under analysis.

3.4 References

- [1] D.A. Skoog, D.M. West, F.J. Holler, *Fundamentals of analytical chemistry*, Edises, 2002
- [2] S. Gocan, *Journal of Chromatographic Science*, Vol 40, Nov/Dec 2002
- [3] P.E. Wall, *Thin-Layer (Planar) Chromatography*, Academic Press, 2000, 2619-2631
- [4] F. Wang, H. Wu, Q. Zhu, K. Huang, Y. Wei, C. Liu, Y. Zhai, Z. Yang, S. Weng, Y. Xu, I. Noda, J. Wu, *Anal. Methods* 2013, 5, 4138-4144.
- [5] K. Tsutsumi, K. Ohga, *Analytical Sciences*, 1998, 4
- [6] N. J. Szabo, J. D. Winefordner, *Society for Applied Spectroscopy*, 1997, 51, 7
- [7] L. Kocsis, E. Horvath, J. Kristof, R.L. Frost, A. Redey, J. Mink, *Journal of Chromatography A*, 1999, 845, 197–202
- [8] K. Herman, N. E. Mircescu, L. Szabo, L. F. Leopold, V. Chiş, N. Leopold, *Journal of Applied Spectroscopy*, 2013, 80, 2
- [9] Q. Zhu, Y. Cao, Y. Cao, Y. Chai, F. Lu, *Anal Bioanal Chem*, 2014, 406, 1877–1884
- [10] C. L. Brosseau, A. Gambardella, F. Casadio, C. M. Grzywacz, J. Wouters, R. P. Van Duyn, *Anal. Chem.*, 2009, 81, 3056–3062
- [11] A. V. Whitney, F. Casadio, R. P. Van Duyn, *Appl Spectrosc*, 2007, 61, 994
- [12] R. N. McCoy, E. C. Fiebig, *Anal. Chem.*, 37, 593-597 (1965)
- [13] P. A. Sturm, R. M. Parkhurst, W. A. Skinner, *Anal. Chem.*, 38, 1244-1247 (1966)
- [14] C. J. Percival, P. R. Griffiths, *Anal. Chem.*, 50, 1906-1910 (1975)
- [15] M. P. Fuller, P. R. Griffiths, *Anal. Chem.*, 1978, 50 (13), pp 1906–1910
- [16] M. P. Fuller, P. R. Griffiths, *Appl. Spectrosc.*, 1980, 34, 533–539.
- [17] G. E. Zuber, R. J. Warren, P. P. Begosh, E. L. O'Donnell, *Anal. Chem.*, 1984, 56 (14), pp 2935–2939
- [18] L. B. Lloyd, R. C. Yeates, E. M. Eyring, *Anal. Chem.*, 1982, 54 (3), pp 549–552
- [19] N. D. Danielson, J. E. Katon, S. P. Bouffard, Z. H. Zhu, *Anal. Chem.*, 64, 2183-2186 (1992)
- [20] C.D. Tran, *Journal of Chromatography*, 292, 1984, 432-438

- [21] R.J. Dijkstra, F Ariese, C. Gooijer, U.A.Th. Brinkman, *Trends in Analytical Chemistry*, Vol. 24, No. 4, 2005
- [22] N. J. Szabo, J. D. Winefordner, *Applied Spectroscopy*, 1997, 51, 7, 965-975
- [23] K. Herman, N. E. Mircescu, L. Szabo, L. F. Leopold, V. Chiş, N. Leopold, *Journal of Applied Spectroscopy*, 2013, 80, 2
- [24] G. W. Somsen, P. G. J. H. Ter Riet, C. Gooijer, N. H. Velthorst; A. T. Brinkman, *JPC. Journal of planar chromatography, modern TLC*, 1997, 10, 1, 10-17
- [25] I. Geiman, M. Leona, J.R. Lombardi, *Journal of Forensic Science*, 2009, 54, 4
- [26] E. Koglin, *Academic Press*, 2000
- [27] X. Wang, W. Shi, G. She, L. Mua, *Phys. Chem. Chem. Phys.*, 2012, 14, 5891–5901
- [30] Lee PC, Meisel D, *J Phys Chem* 1982, 86,3391–3395.
- [31] F. Casadio, M. Leona, J. R. Lombardi, R. Van Duyne, *Acc. Chem. Res.*, 2010, 43 (6), pp 782–791
- [32] B. Doherty, M. Vagnini, K. Dufourmantelle, A. Sgamellotti, B. Brunetti, C. Miliani, *Spectrochimica Acta Part A: Molecular and Biomolecular Spectroscopy* 121, 2014, 292-305
- [33] S. Sharma, A., Kumar; *Greener Journal of Physical Sciences* 3(6), 2013
- [34] J Sarkar, *Vibrational Spectroscopy* 41, 2006
- [35] H Watanabe, *Journal of Physical Chemistry B* 109, 2005
- [36] D Sternik, M. Majdan, G Derylo-Marczewska., G. Zukocinski, A. Gladysz-plaska, V. M. Gun'ko, *Journal of Thermal Analysis and Calorimetry*, 103 (2), 607-615, 2011
- [37] E.I. Saez, R. Corn, *Electrochimica Acta* 38 (12), 1993
- [38] O.V. Ovchinnikov, *Journal of Applied Spectroscopy* 74(6), 2007
- [39] P.H.B Aoki, *Vibrational Spectroscopy* 54, 2010
- [40] L. Jensen, G. Schatz, *Journal of Physical Chemistry A*, vol.110, no. 18, 2006
- [41] K. Herman, S. Szabo, L.F. Leopold, V. Chis, N. Leopold, *Anal. Bioanal. Chem.* 2011, 400, 815-820.

Chapter 6

**Infrared spectrum Grinding Curves
method on MIR and FIR ranges**

In this chapter a new method for calcite analysis has been performed with the aim to investigate the crystals size, the atomic order and to differentiate morphological structure arising from different crystallization process. Even though this is an inorganic material, calcium carbonate in various forms has had from earliest times a wide role in art as a pigment (i.e. Saint Jhon's white), as a raw matter in sculptures (i.e. marble as Carrara marble), as a substrate for wall paintings and also as a treatment for artworks restoration in consolidation procedure for wall or stones and in paper de-acidification practice. For this reason, it was decided to develop also new spectroscopic approaches, in order to improve knowledge on this mineral.

6.1 Calcium carbonate in cultural heritage

Calcite is the most common mineral form and stable polymorph of calcium carbonate, CaCO_3 ; also two less common polymorphic forms exist and they are aragonite and vaterite. Calcite generally occurs in large single transparent cubic crystals and the especially pure variety is called Iceland spar. Marble is metamorphosed limestone which is re-crystallized calcite, in which the calcite crystals size can reach considerable dimensions, on the other hand some concretionary calcite is composed by minute crystals. Calcite can be divided from geogenic origins that forms in karstic caves and around springs, biogenic origins derived from skeletal fragments of ancient marine organisms, or pyrogenic origins. All these forms of calcite may be found in paintings, in the pictorial layers as well as in the support structures, along with varying amounts of common impurities.

Natural stones constituted by calcium carbonate has been largely employed for sculptures or many different constructional purposes since ancient time. The splendour of Greek and Roman civilisation largely depend on them and during time innumerable artworks all over the world have been created using marble or limestone. Indeed, limestone is a very common sedimentary rock usually of biological origin and it makes up about 10% of the total volume of all the sedimentary rocks; it is almost composed by calcite and it is easily weathered by acidic conditions.

Calcite can also be found in wall paintings, indeed a typical wall painting, belonging to the classic tradition, consists of roughly three layers whose main structural component is calcium carbonate. The inner layer, which is laid on the wall, is called *arriccio* and is the richest in sand necessary to avoid cracks that form upon drying. Moving towards the surface, the *intonaco* layer is found, consisting of a plaster that often contains an equal amount of lime and sand. The third and outer one is the paint layer, which is a thin film made by a mixture of pigments and calcium carbonate. In the so-called *buon fresco* technique, the pigments (dispersed in water or lime water) are directly applied on the wet intonaco layer, and upon carbonation are embedded into the crystalline carbonate network forming a smooth surface. The paint layer is at the interface between the wall and the surrounding environment and it is strongly susceptible to degradation caused by the mechanical stresses that arise from salt crystallization, usually occurring at the surface [1]. With the aim of solving the problem of the degradation of wall paintings caused by the presence of sulphates and to achieve a good

consolidation, in the mid-seventies Enzo Ferroni and Dino Dini [2] developed a conservation treatment based on the application of ammonium carbonate and barium hydroxide solutions. Recently, starting from this procedure calcium hydroxide nanoparticles or calcium and barium hydroxide nanoparticles, are used for consolidation on fresco due to their re-carbonation effect.

Moreover, when limestone or marble or any form of calcium carbonate is strongly heated or calcined at 800-900 °C, carbon dioxide is driven off as gas, leaving a white residue of calcium oxide or 'quicklime' (CaO). Freshly calcined lime reacts vigorously with water to form calcium hydroxide, Ca(OH)₂, simultaneously producing an exothermic reaction. If just the correct amount of water is added under carefully controlled conditions, the calcium hydroxide is formed as a fine white powder. After a long exposure to air the calcium hydroxide combines with atmospheric carbon dioxide to form calcium carbonate, thus in effect reversing the lime-burning process. This causes the setting and hardening of mortar with age.

Cennino Cennini uses the name *Bianco di San Giovanni* to describe the preparation of a white lime pigment in his book *Il Libro dell'Arte* [3]. He does not explain the name used for this lime white, and it is probable therefore, this important white pigment was in use by artists before Cennini's time. D. V. Thompson says it gets its name after the patron saint of Florence [4]. Bianco di San Giovanni is a pigment of inorganic, natural mineral origin from limestone (calcium carbonate) deposits. Not to be confused with simple lime white or chalk, Bianco di San Giovanni, as Cennino Cennini reports, is dried lime which is reduced to powder and then immersed in the water for eight days that is changed each day. It is then made into small cakes that are left to dry in the sun. It is then grounded finely. Bianco di San Giovanni primarily consists of calcium carbonate plus calcium hydroxide. It is considered the white pigment par excellence for fresco painting. It is used also in tempera and grounds while it is not advised in oil and encaustic painting techniques [5].

Another white pigment composed of calcium carbonate is "white shell", with this term two different pigments are indicated depending on geographical location. The term 'shell white' is usually used in European literary sources to describe white made from crushed egg shells. The most often quoted reference is to Lomazzo's 'Trattato' of 1584 in which finely ground egg shell (*il guscio delle uova tridato minutamente*) is recommended as a white pigment for mixing with other colours in fresco painting. Egg shell white and a white made from cuttlefish bone are also mentioned in the Paduan MS. (c. mid-seventeenth century) transcribed and translated by Mrs Merrifield. In Japan unique use of white shell has been made of sea shells, mostly oyster shells, to produce a white pigment for artists' use called *gofun*, which has been widely employed. The shells of molluscs are nearly pure calcium carbonate and for the preparation of *gofun* they are used for a simple mechanical process which involves selection, crushing, grinding and pulverizing in a ball or stamp mill, followed by particle-size classification by several steps of water levigation in concrete tanks [6].

It has been presented the main applications of calcite in cultural heritage but, calcium carbonate polymorphs can be found also on other artistic fields as mosaics manufacturing, archaeological, etc...

6.2 Grinding curves method

The presence of many different genesis and formation mechanism of calcite affects the crystals atomic order playing an important role in the mineral's chemical and mechanical properties. In general, geogenic, biogenic and pyrogenic calcites are formed by different mechanism, and this can influence different properties such as crystallinity, coherence length, domain size, and crystal habit. Large geogenic calcite crystals, with well-defined crystal habits, are presumed to form slowly from saturated solutions. In contrast, many biogenic calcites are thought to form via an amorphous calcium carbonate precursor phase that crystallizes *in vivo* [7-10]. Chalk and limestone typically originate as biogenic calcite, but they have often undergone dissolution and reprecipitation processes to different extents [11]. The two main forms of pyrogenic calcites found in archaeological sites are wood ash and lime plaster/mortar, each with a different formation pathway.

Infrared spectroscopy is a well-established method for identify and characterise different mineral and organic components. Moreover, it is well documented that differences in particle sizes and morphologies can also affect the sizes and shapes of IR absorption peaks [11-13]. An infrared spectrum is therefore affected by order within a material, both at the local atomic level and at longer length scales.

Calcite has three characteristic IR absorption peaks in the range between 400 and 4000 cm^{-1} : ν_3 at 1420 cm^{-1} , ν_2 at 874 cm^{-1} , and ν_4 at 713 cm^{-1} . All of these absorptions are influenced by the different ways in which the C=O bonds of the carbonate unit interact with the IR radiation. It has been shown experimentally [7, 8, 15, 16] and theoretically [17] in biogenic calcite from the sea urchin, that the ratio of the ν_2/ν_4 peak heights decreases as the initially deposited amorphous calcium carbonate crystallizes into calcite. Chu et al. [18] used the ν_2/ν_4 peak heights ratio to distinguish between geogenic and pyrogenic calcites in archaeological contexts. The same study also showed that the calcite ν_3 absorption peak narrows with increased grinding of the sample as the ν_2/ν_4 ratio increases. Moreover, previous studies on calcite analysed in FTIR in transmission mode, revealed that the peak height was influenced by the extent to which the sample was ground [19]. Indeed, Regev et al. [20] introduced a method, using FTIR spectroscopy, that can provide a way of characterising atomic order of calcite formed by different mechanism. He suggestes a method to calculate the "grinding curves" based on the variation in the intensity of the FTIR bands in function of the intensity of grinding. This method consists in repetitive grinding of the same sample, in acquiring the IR spectrum after each grinding and in plotting the heights of the ν_2 peak (875 cm^{-1}) versus the ν_4 peak (712 cm^{-1}), both normalized to the ν_3 peak (1420 cm^{-1}) height. A characteristic grinding curve with a distinctive trend line was formed for each calcite particles types [17, 20-22]. The obtained curves were reproducible, and the position of the so-called grinding curve on the graphic depended on the formation mechanism and on the local atomic order of the sample [20]. According to their research, there is no need to measure the particle size of the

specimen, and a routine IR spectroscopy can reveal the differences in the degree of intrinsic order among calcites formed by different mechanism. The research shows how by this simple method, slight changes in the trend lines derived from different formation mechanism can be documented [22].

By implementing this new method for different calcite samples, promising results on different types of crystals of calcite with also different crystallisation origins, can be achieved.

Moreover, a totally new approach have been experimented here, applying grinding curves on calcite FTIR spectra achieved in Far Infrared (FarIR) range.

FarIR spectroscopy is widely employed in different fields, such as astrophysics, cation exchange and interactions in ceramics, as well as lattice vibrations in the field of polymer crystallization. Since 1969, several studies have highlighted the analytical potential of FarIR spectroscopy for the investigation of minerals in the 200-50 cm^{-1} region [23]. Furthermore, recent studies document the application of FarIR spectroscopy in both transmission [24] and ATR modes [25-28] as a valid alternative method for the characterization of the compounds inactive in the MidIR (different inorganic pigments and corrosion products). In the FarIR spectroscopy are detected lattice or crystal vibrations. Lattice vibrations have lower frequencies than the internal vibrations, in particular, those for organic compounds are usually at frequencies lower than 400 cm^{-1} . Inorganic compounds absorb at even lower frequencies due to the presence of heavier atoms. In general, as the atomic mass is increased the bond length between the atoms will be longer, and the vibrational excitation energy becomes lower (this corresponds to higher wavelength and lower wavenumbers).

The Far-IR region is defined as below 400 cm^{-1} . Indeed, FarIR spectroscopy is a well known technique used as an alternative way for collecting spectra of many inorganic pigments and corrosion products found on art objects. Among the available techniques, the far infrared region is accessible by employing either transmission spectroscopy or attenuated total reflection (ATR).

Due to the possibility to detect lattice vibrations, grinding curves in FarIR range have been successfully tested on different types of calcite samples.

6.3 Materials and Methods

6.3.1 Materials

Different calcite samples of different origins have been analysed. As geogenic calcite, Iceland Spar have been selected for both MIR and FIR grinding curves; a biogenic sample as Sea Urchin spine have been selected for both MIR and FIR grinding curves whereas Scallop shells have been analysed only in FIR spectroscopy and a synthetic calcite constituted by nanoaggregates have been synthesized and analysed with both FTIR ranges.

6.3.1.1 Synthetic calcite

Analytical grade calcium chloride bi-hydrate and mono-ethanolamine were obtained from Sigma-Aldrich chemical company; sodium carbonate was purchased from Labochimica. MilliQ water was used for the preparation of aqueous solutions; all chemicals were used without further purification.

Synthesis:

The precipitation of CaCO_3 was carried out in a glass vessel at room temperature (ca. 22°C). Aqueous solutions of CaCl_2 (0.5M) with mono-ethanolamine (4.73M) and of Na_2CO_3 (0.5M) were prepared and mixing together under vigorous stirring by using a magnetic stirrer. The mixture was let under stirring for different times 1 hour, closed with parafilm to avoid interactions with atmospheric CO_2 , then filtered and dried in a 105°C drying oven.

The presence of Ethanolamine (ETH) distinctly affected the morphology of precipitated calcium carbonate and an unusual structure constituted by regular assembly of rhombohedral crystallites having an average size from 210 to 640 nm. These crystallites appeared as nanoaggregates with an average size of about 3.3 μm (Fig. 1).

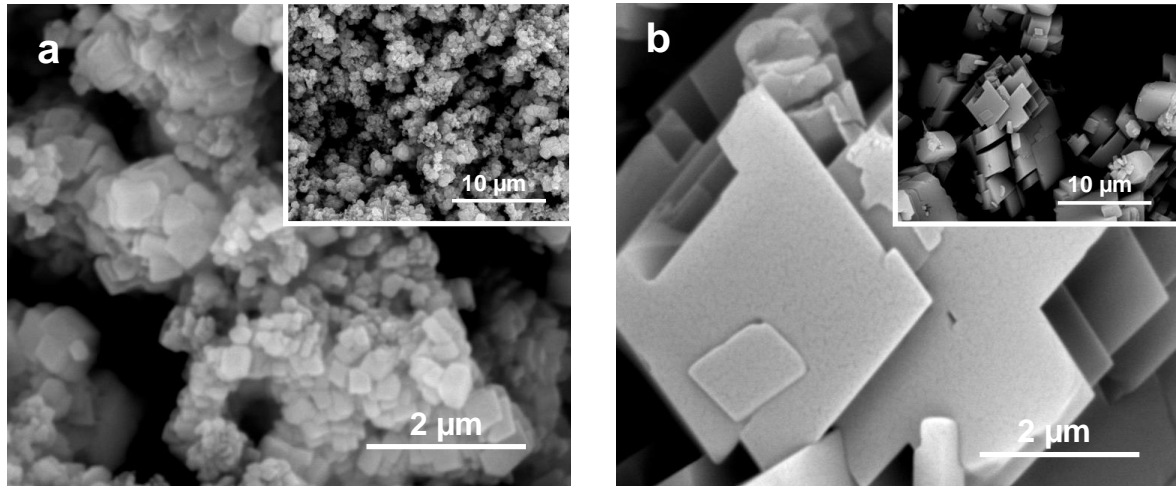


Fig. 39: SEM pictures of synthetic calcite crystallized a) in presence of additive (ETH) for 1 hour and b) in absence of additive for 24 hours

Moreover, a control samples synthesized with the same procedure in absence of additive (ETH) has been analysed. This sample obtained after 24 hours synthesis, only pure calcite rhombic and cubic particles, with well define growth planes and geminates and great sizes have been analysed with SEM.

6.3.1.2 Iceland Spar

Iceland Spar is a transparent variety of calcite, generally used in demonstrating the polarization of light and well known also for its double refraction. It has rhombohedral and scalenohedral crystals, with different size depending on the growth conditions.

6.3.1.3 Scallop shell

Scallop shell (*Pecten maximus*) presented calcitic foliated microstructure in the internal layer constituted by parallel, flat elongated blades regularly fan-arranged in large groups usually oriented to the growing edge of the shell [29].

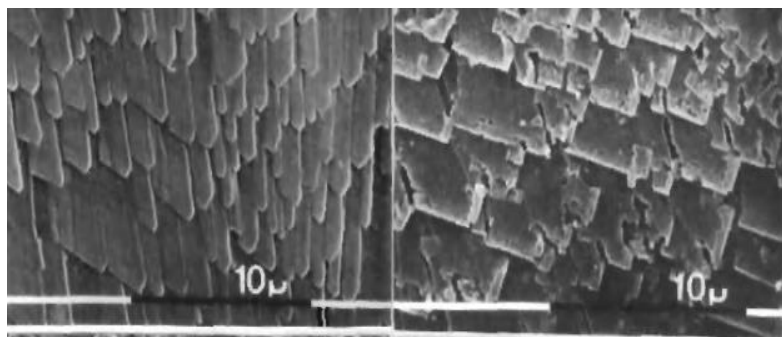


Fig. 40: *Pecten maximus* shell SEM pictures [29]

6.3.1.4 Sea Urchin spine

As described by F. Meldrum [30] the first deposit in the formation of a sea urchin larval spicule is a regular rhombohedral calcite and as growth continues, the organism actively modulates the crystal morphology to generate a single crystals with tri-radiate structure.

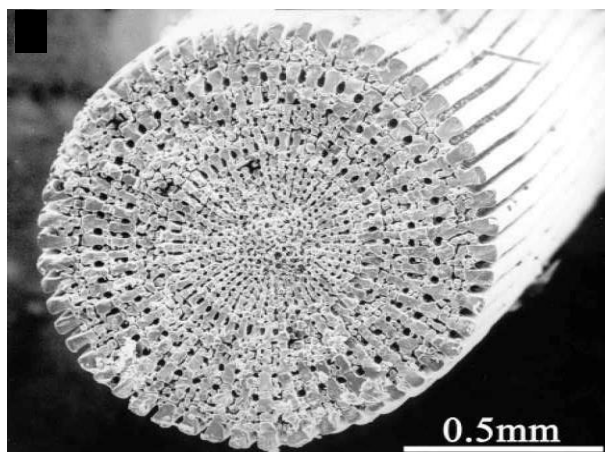


Fig. 41: Micrographs of sea urchin *Heliocidaris erythrograma* spine [30]

6.3.2 Methods

6.3.2.1 Grinding curves in MIR range

About 750 μg of powdered sample were placed in an agate mortar with 150 mg of KBr (from Sigma-Aldrich), manually ground for 1 minute and put under a 3 tons pressure for 1 minute using a manual hydraulic press. The 13 mm KBr pellet was analysed by FTIR in transmission mode using a Thermo Nicolet Avatar 370 instrument with a resolution of 4 cm^{-1} and 64 scans for each acquisition. The baselines for heights measurement of ν_2 , ν_3 , ν_4 were determined using the line tool in the OMNIC software. We will call normalised absorption unit (n.a.u.) the unit in which $\nu_3 = 1000$.

After the analysis the same pellets were ground again for 2 minutes, put under the same pressure for the same time as before, and then spectra were reacquired. These operations were then iterated with grinding times of 5 and 10 minutes. The comparison of the 4 spectra allows the construction of a grinding curve.

6.3.2.2 Grinding curves in FIR range

For the analysis in transmission in FIR range, polyethylene (PE) pellets are required. To prepare PE pellets, the normal procedure for preparing KBr pellets is followed, however, with a few modifications.

5 mg of calcite sample were placed in agate mortar and were grinded for 1 minutes. After this time, 1 mg of sample were collected and simply mixed with 75 mg of PE using a spatula. The metallic anvil die accessory (in this case, a 13-mm die from SPECAC, Kent, UK, with a maximum load of 10 tons), used for making the KBr pellets, is also used in this case. Unlike KBr pellets, the die is heated on a heater until its red light turns off. The temperature is expected to be approximately 130–150 °C (the melting temperature of PE is 120–130 °C). The mixture of PE and the sample are quickly added in the die, which is assembled and put under 5-ton pressure for 2 min. Following this, the die is disassembled and the resulting PE pellet is put in the sample pellet holder into the IR spectrometer and an FIR spectrum is recorded in the 650–50 cm^{-1} region.

The remaining sample already grinded for 1 minutes was grinded for another 1 minutes and after 1 mg of sample was taken and mixed with PE in order to produce the second pellets with 2 minutes grinded sample. This procedure was repeated also grinding the remaining sample for another 3 minutes in order to reach 5 minutes grinding and then 1 mg of sample was mixed with PE to obtain the third PE pellet.

The FIR spectrometer used is a Thermo Nicolet 5700, which has a spectral resolution of 4 cm^{-1} and is attached with a Parker/Balston Self-Contained FT-IR PurgeGas Generator; this prevents water and carbon dioxide in the atmosphere from interacting with the PE pellet and creating interference bands in the FIR spectra. The baselines for heights measurement of E_u 311 cm^{-1} , E_u 227 cm^{-1} and 106 cm^{-1} were determined using the line tool in the OMNIC software. We will call normalised absorption unit (n.a.u.) the unit in which E_u 311 cm^{-1} = 1000.

6.4 Results and discussion

The different calcite samples have been analyzed employing the FTIR grinding curve method, and as previous studies revealed, the peak height is influenced by the extent to which the sample was ground [20]. Indeed, the increase of the grinding time results in sharpening and in the enhancement of the bands intensity (Fig. 4).

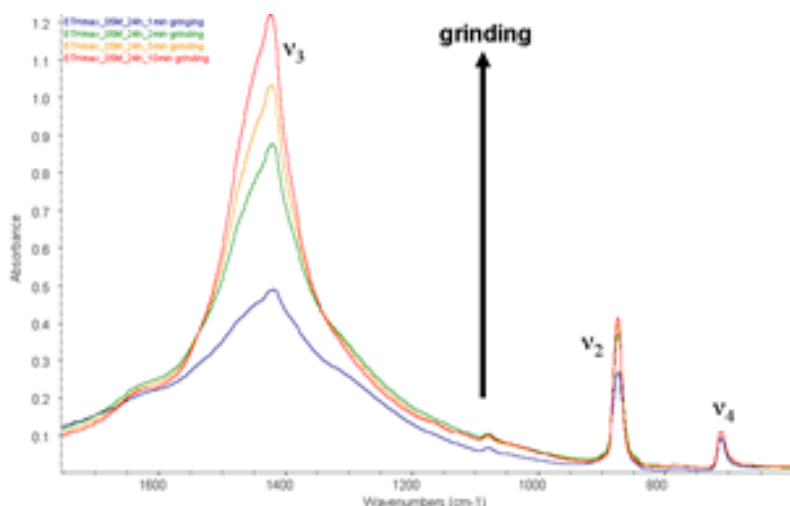


Fig. 4: FTIR spectra illustrate that peak sharpening occurs with grinding, leaving peak position unchanged. A single specimen was ground and re-pressed; spectra are shown with common absorbance scale.

Once the FTIR spectra have been acquired the grinding curves have been calculated, as illustrated in Figure 5. The biogenic calcite samples have a different trend line compared with geogenic and synthetic samples. The difference trend lines show that there are a systematic difference in the v_2 versus v_4 peak heights for calcites that presented different crystal morphologies not strictly depended on crystallization origins. Indeed, Iceland spar and synthetic calcite produced in absence of additives present the same shallowest trend line probably due to the same rhombic and cubic particles morphology, even though the origin is completely different. Moreover, biogenetic calcite samples present the same trend line, a little more sloping than geogenic sample.

The calcite obtained after 1 hr of crystallization in the presence of ETH have a steepest slope than the one observed for geogenic calcite. It can be noted that the position of the curve achieved just considering the points obtained on the 1 hr ETH calcite is shifted in the left lower part of the graphic with respect to the geogenic curve.

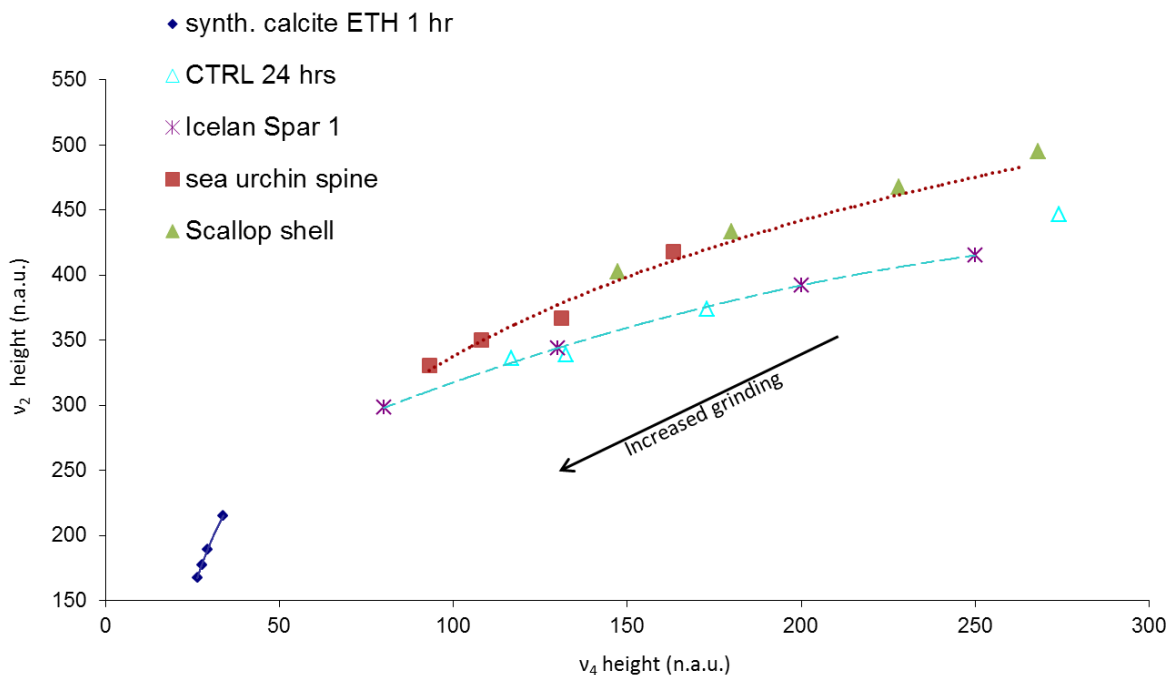


Fig. 5: Plot of the v₂ versus v₄ peak heights of geogenic, biogenic and synthetic calcites, after each spectrum was normalized to the corresponding v₃ peak height. For each type of calcite, data points correspond to successive grindings of the same specimen.

The distance of synthetic calcite grinding curve from the grinding curve of a geogenic and biogenic calcite is a measure of the reduction of the crystalline perfection of the crystals, which can be generally associated with the presence of entrapped additives. The trend line shows also that the particles precipitated after 1hr are characterized by lower values of the v₂/v₃ and v₄/v₃ ratios, when compared to those for geogenic particles, due to the intensification and narrowing of the v₃ band. Moreover, the shift of the v₃ band from 1420 to 1447 cm⁻¹ is evident (Fig. 6).

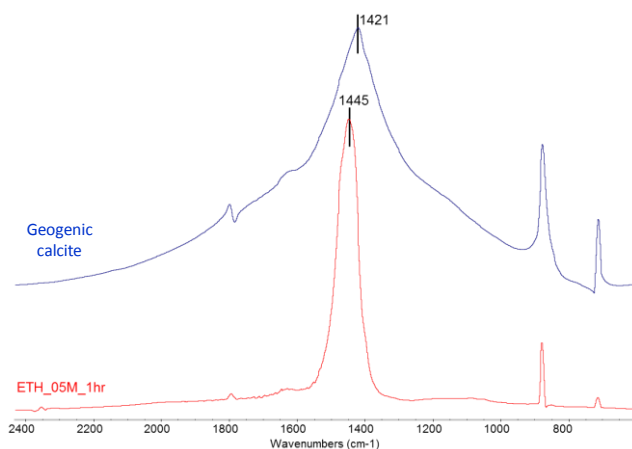


Fig. 6: FTIR spectra of synthetic calcite sample (named ETH_05M_1hr) and geogenic sample

These unusual narrowing and the shift of the ν_3 band were reported to be due to a reduction of the size of the mineral particles [31, 32] and this is in good agreement with the observed considerable reduction of crystals size when synthesis in presence of ETH has been conducted. Indeed, H.L. Yue et al. [31, 32] studied three ultra-fine calcite samples having similar particle size but presenting different agglomeration state. They suggested that the size effect and crystal distortion in the lattice of nanoparticle CaCO_3 weaken the crystal field effect and lattice vibrations, and finally result in the abnormal IR behaviour. The main peak positions of the three nanoparticle CaCO_3 samples, analysed by H.L. Yue, were estimated at 1465 cm^{-1} , 875 cm^{-1} and 713 cm^{-1} , respectively. The ν_3 band has a 40 cm^{-1} blue shift compared with the reference and contrary to previous reports of broadened assimilation bands in nanomaterials, it was unusually narrow. The fact that the ν_2 and ν_4 bands are not split denotes that the crystal structures of the three nano-particle CaCO_3 samples were calcite. Andersen et al. [33] suggested that the strong and broad ν_3 assimilation band originated from several overlapping bands resulted from the combination of lattice vibration of A_{2u} (354 cm^{-1}), E_u (311 cm^{-1} , 227 cm^{-1}) and ν_2 , ν_4 bands. C. N. R. Rao [34] suggested that the crystal field effect often caused the broadened absorption bands. Therefore, H.L. Yue et al. [31, 32] suggested that many defects or relatively large strains in the crystal lattice of nanoparticle calcite weaken the crystal field effect and, weaken the lattice vibrations of A_{2u} and E_u in the far infrared region as well. Consequently, the overlapping peaks around the ν_3 band disappeared and this band seemed narrow. Moreover, the absorption intensities of the lattice modes for the ultra-fine calcite samples are much weaker than that to the reference calcite.

Thus, it seems that the reduction of the crystal size and a consequently variation in the lattice, might have an effect in the blue shift of ν_3 band and in the ν_3 narrowing due to the intensities variations of A_{2u} (354 cm^{-1}) and E_u (311 cm^{-1} , 227 cm^{-1}) vibrations.

To verify our hypothesis, far infrared (FIR) spectra have been acquired on particles synthesized in presence of ETH at 1 hour crystallization and on particles produced with the control experiment at 24 hours crystallization time similar to Iceland spar. Considering the height ratio of peaks $E_u\ 311\text{ cm}^{-1}$ versus $E_u\ 227\text{ cm}^{-1}$ of the particle synthesizes in presence of ETH and the particles obtained by control experiment, grinded at different times, it's possible find a trend.

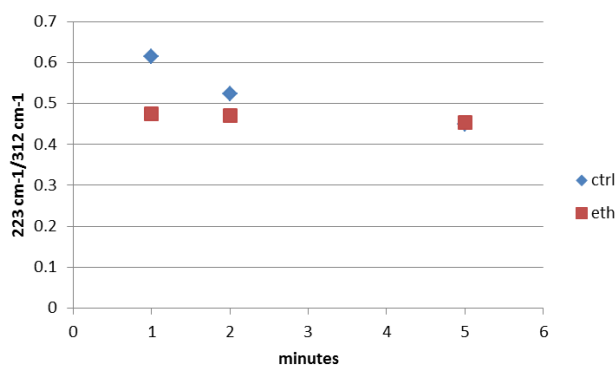


Fig. 7: 223/312 cm^{-1} ratio at 1, 2 and 5 minutes

As Figure 7 shows, at low grinding time the ratio of $311/227\text{ cm}^{-1}$ is different for the two samples, this is probably due to the differences in particles size. Increase the grinding time the differences between the ratio of the two samples decrease progressively up to reach the same ratio value at 5 minutes grinding. The $223/312\text{ cm}^{-1}$ ratio of calcite/ETH sample does not change increasing of grinding times, on the other hand the ratio values of control sample decrease, increasing the grinding time. These two trends highlight the differences in size of particles (Fig. 1): while calcite/ETH sample has constituted by nano-aggregates, the control has rhombic particles greater than $10\text{ }\mu\text{m}$, with well-defined growth planes and geminates. Grinding the sample, a reduction of crystal sizes occurs with a consequent variation in intensity of E_u (311 cm^{-1} , 227 cm^{-1}) vibration; the control sample reveals mainly this tendency since it has greater size crystals. The decrease of E_u ratio at variance of grinding time produces a narrowing in ν_3 band, and this is evident also in mid-infrared spectra of control experiment.

Grinding curves have been calculated also for FIR spectra, due to their capacity to clearly reveal different intensities in 311 cm^{-1} , 227 cm^{-1} and 106 cm^{-1} peaks caused by a possible variations in lattice vibrations (Fig. 8).

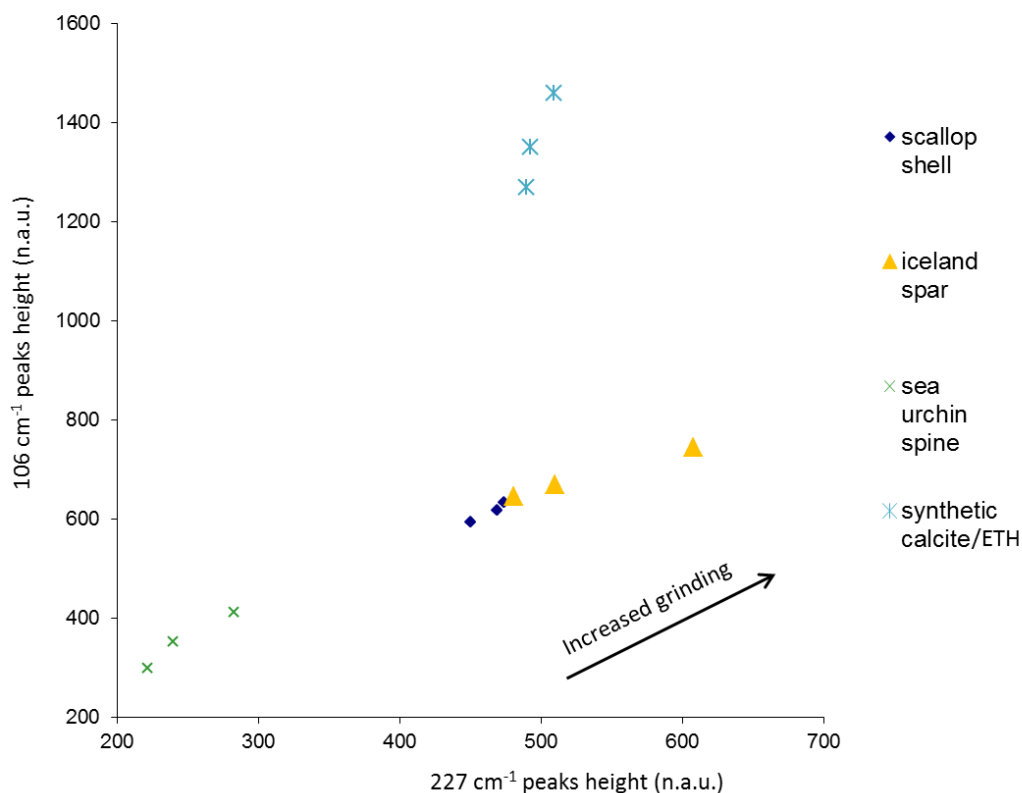


Fig. 8 : Plot of the 227 cm^{-1} versus 106 cm^{-1} peak heights of geogenic , biogenic calcite and synthetic calcite synthesized at 1 hr in presence of additives (ETH) after each spectrum was normalized to the corresponding 311 cm^{-1} peak height. For each type of calcite, data points correspond to successive grindings of the same specimen.

A differentiation between all the analyzed calcite samples is detectable in figure 8.

Iceland spar and Scallop shell present the same shallowest trend line probably due to the same rhombic and cubic particles morphology, even though the origin is completely different.

Moreover, biogenetic calcite of sea urchin spine is positioned in the left lower part of the graphic with respect to the Scallop shell calcite. Indeed, sea urchin spines have crystal morphology constituted by a single crystals with tri-radiate structure.

The calcite obtained after 1 hr of crystallization in the presence of ETH have a steepest slope than the one observed for geogenic and biogenic calcites. It can be noted that the position of the is shifted in the higher part of the graphic. This totally different trend for calcite/ETH sample has already been observed in MIR grinding curves, and it is probably due to the morphology of precipitated calcium carbonate: an unusual structure constituted by regular assembly of rhombohedral crystallites appeared as nanoaggregates.

Also applying this second method, a good distinction between different calcite samples can be reached.

In order to first validate the obtained results and then to better understand this phenomenon in FIR region, further analysis on calcites samples will be planned mainly using XRD.

6.5 Conclusions

A new approach to study crystals morphology, atomic disorder and genesis in calcite samples is here successfully tested.

As concerned grinding curves achieved in MIR region, the normalized v_2 versus the v_4 peaks height trend lines for samples ground to different extents is an efficient, rapid, and effective tool to distinguish between calcites formed by different processes. The basis for this differentiation correlates with characteristic differences of local and extended atomic order in the calcite.

Moreover, the possibility to use grinding curves method also in spectra acquired in FIR region is the real novelty. FIR grinding curves might allow to differentiate calcite samples depending on their lactone vibrations.

The described methods due to their routine advantages such as measurement simplicity, can be implemented easily on large amount of samples. This opens possibilities for identifying calcites produced under different conditions. In the field of cultural heritage this could allow higher suitability in preservation techniques and also study on raw materials provenance could be conducted. This may well have application not only in the field of archaeology and cultural heritage, but also in biomineralization, geology and materials sciences.

6.6 References

- [1] R. Giorgi, M. Ambrosi, N. Toccafondi, P. Baglioni, *Chem. Eur. J.* 2010, 16, 9374 – 9382
- [2] E. Ferroni, V. Malaguzzi, V. Rovida, *Proceedings of the ICOM-CC Plenary Meeting*, The International Council of Museums-Committee for Conservation, Amsterdam, 1969.
- [3] C. Cennini, *Il libro dell'arte*, ed. Neri Pozza (coll. I colibri)
- [4] D. V. Thompson, *The materials and techniques of medieval paintings*, 1956
- [5] E. Denninger, *Studies in Conservation*, 1974, 19, 185-187
- [6] R.J. Gettens, E. West Fitzhugh, R. L. Feller, *Studies in Conservation*, 19 (1974), 157-184
- [7] L. Addadi, S. Raz, S. Weiner, *Advanced Materials*, 2003, 15, 959-970.
- [8] E. Beniash, J. Aizenberg, L. Addadi, S. Weiner, *Proceedings of the Royal Society of London Series B-Biological Sciences*, 1997, 264 (1380), 461-465.
- [9] L. Gago-Duport, M.J.I. Briones, J.B. Rodríguez, B. Covelo, *Journal of Structural Biology*, 2008 162, 422-435.
- [10] Y. Politi, R.A. Metzler, M. Abrecht, B. Gilbert, Wilt, F.H. Sagi, I. Addadi, L. Weiner, S. Gilbert, *Proceedings of the National Academy of Science (USA)*, 2008, 17362-17366.
- [11] F. Pettijohn, 1957. *Sedimentary Rocks, second ed.* Harper & Row, New York.
- [12] G. Duyckaerts, *Analyst* 1959, 84, 201-214.
- [13] M.D. Lane, *Journal of Geophysical Research, Planets*, 1999, 104 (E6), 14099-14108.
- [14] R. Ruppin, R. Englman, *Reports on Progress in Physics*, 1970, 33 (2), 149-196.
- [15] J. Aizenberg, J. Hanson, T.F. Koetzle, S. Weiner, L. Addadi, *Journal of the American Chemical Society*, 1997, 119 (5), 881-886.
- [16] Y. Politi, T. Arad, E. Klein, S. Weiner, L. Addadi, *Science*, 2004, 306 (5699), 1161-1164.
- [17] R. Gueta, A. Natan, L. Addadi, S. Weiner, K. Refson, L. Kronik, *Angewandte Chemie International Edition*, 2007, 46, 291-294.
- [18] V. Chu, L. Regev, S. Weiner, E. Boaretto, *Journal of Archaeological Science*, 2008, 35, 905-911.

- [19] M.D. Lane, *Planets* 104 (1999), 14099-14108.
- [20] L. L. Regev, K. M. Poduska, L. Addadi, S. Weiner, E. Boaretto, *Journal of Archaeological Science*, 2010, 37, 3022-3029
- [21] M. Suzuki, Y. Dauphin, L. Addadi, S. Wainer, "Atomic order of aragonite crystals formed by mollusks", *CrystEngComm*, 2011, 13, 6780-6786
- [22] K. M. Poduska, L. Regev, E. Boaretto, L. Addadi, S. Weiner, L. Kronik, S. Curtarolo., *Advanced Materials*, 2011, 23, 550-554
- [23] C. Karr, J.J. Kovach (1969) *Appl Spectrosc* 23,219-223
- [24] E. Kendix, G. Moscardi, R. Mazzeo, P. Baraldi, S. Prati, E. Joseph, E. Capelli, (2008) *J Raman Spectrosc.* 39: 1104-1112;
- [25] E.L. Kendix, S. Prati, E. Joseph, G. Sciutto, R. Mazzeo, (2009) *Anal. Bioanal. Chem.* 394, 1023-1032;
- [26] J.A. Reffner, P.A. Martoglio (1995) In: H.J. Humecki (ed) *Practical Guide to Infrared Microspectroscopy*. Marcel Dekker, New York, pp 41-84;
- [27] L.A. Averett, P.R. Griffiths, K. Nishikida (2008) *Anal. Chem.* 80,3045-3049
- [28] S. Nunn, K. Nishikida (2003) *Thermo Scientific Application Note* 01153
- [29] H. Larvor, J. P. Cuif, N. Devauchelle, Y. Dauphin, A. Denis, P. Gautret, F. Marin, *Bulletin de l'Institut océanographique*, Monaco, n° special 14, 4 (1996)
- [30] F. C. Meldrum, *International Materials Reviews* 2003, 48, 3, 187-224
- [31] L.H. Yue, M. Shui, Z. Xu, *Journal of Zhejiang University (SCIENCE)* (2000), 1, 2,178-183
- [31] L.H. Yue, M. Shui, Z. Xu, *Spectroscopy letters* (2001) 34, 6, 793-802
- [32]: Sadtler *Research Laboratories. Standard Infrared Collection*. Sadtler: Philadelphia, PA, 1980 - 1996.
- [33]: F. A. Andersen, L. Brecevic, *Infrared spectra of amorphous and crystalline calcium carbonate*, *Acta Chemica Scandinava* (1991), 45, 1018-1024.
- [34]: C. N. R. Rao, *Chemical Applications of Infrared Spectroscopy*, Academic Press (1963), 23.

Acknowledgements

My sincerest thank to all who have helped and supported me in this research work

Dr.ssa Silvia Prati

Dr.ssa Giorgia Sciutto

Prof. Rocco Mazzeo

Dr.ssa Marta Quaranta

Prof. Santiago Sanchez Cortés

Dr.ssa Maria-Vega Cañamares

Prof. Giuseppe Falini